Block Copolymer Self-assembly: From Process Optimization to Optical Properties

by

Gayashani Kanchana Ginige

A thesis submitted in partial fulfillment of the requirements for the degree of

Doctor of Philosophy

Department of Chemistry
University of Alberta

© Gayashani Kanchana Ginige, 2022

Abstract

Molecular self-assembly is the basis of structure in Nature. While of far less complexity than a natural system, the same physical rules apply to simple synthetic designed systems that spontaneously form self-assembled structures and patterns. The self-assembly of block copolymers (BCPs) is an interesting example, as it can be harnessed to form both 2D (in thin films) and 3D (in bulk) porous and chemically controlled morphologies at scale. The self-assembly of BCPs on surfaces is of interest for a range of applications, but due to the enormous economic driver that is the computer industry, this direction has been pushed most strongly. Self-assembly of BCPs has been described in the International Technology Roadmap for Semiconductors (the ITRS, and now the IDRS) for almost two decades for lithography on semiconductors and for patterning the magnetic material of hard drives. As a result, there has been much academic interest, both fundamental and applied, to meet the challenges as outlined in the ITRS/IDRS due to the promise of this scalable and low-cost nanopatterning approach. More recently, the remarkable work harnessing BCP self-assembly has been directed to other applications, one being optical metamaterials; this thesis will add to this growing body of science. One aspect holding BCP self-assembly back is the defectivity in the patterned material or surface; some applications are more defect tolerant than others, but hard drive and other computer-industry applications have very low tolerance for defects. It is, therefore, important to have systematic control over the self-assembly process as well as quality of the final patterns generated by BCP self-assembly for these applications and others not yet imagined. This thesis examines the defectivity of the hexagonal nanoscale patterns derived from BCP self-assembly and looks at extending them to produce nanoscale patterns of native and non-native morphologies that have plasmonic properties.

This thesis is divided into two parts. The first part deals with optimization of solvent vapor annealing of BCP self-assembly, the critical step in which the actual nanoscale phase segregation takes place; in this case, it uses a controlled solvent vapor flow annealing apparatus, design of experiment and machine learning approaches. In this work, it was discovered that slight variations in the initial film thickness on the

order of even a couple of nanometers and the final swelling degree have a huge influence on the defectivity and the quality of the resulting patterns. Next, machine learning approaches are applied to compile qualitative and quantitative defect analysis into a single figure of merit that is mapped across an experimental parameter space. This approach enables faster convergence of results to arrive at the optimum annealing conditions for the annealing of thin films of BCPs of PS-*b*-PDMS that generate nanoscale hexagonal patterns of silica dots with a minimum number of defects.

In the second part of the thesis, mixed metal/oxide double layer patterning was studied using sequential self-assembly of BCPs. The second part of the thesis starts with optimization of reactive ion etching (RIE) for producing single layer metal nanopatterns from metal ion-loaded thin films of PS-*b*-P2VP BCPs to generate single layers of hexagonal metal nanopatterns that can withstand a second consecutive reactive ion etching step. The goal of this work is to enable density doubled and/or Moiré pattern formation via self-assembly of a second layer of BCP on the initial pattern prepared by self-assembly of either the same or different BCP, as will be described in Chapter 4. Therefore, the initial pattern produced via BCP self-assembly and RIE etching would need to withstand a second treatment step of BCP self-assembly and RIE. While single layer nanopatterns of Au and Pt nanoparticles can be produced without much trouble, these resulting patterns could not be applied for density multiplication of metal–metal nanopatterns since the metal dots become too small and disordered. To demonstrate that metal nanoparticles derived from BCPs could be used, at least, to produce a mixed metal oxide/metal patterns, arrays of SiO_x dots were first produced from PS-*b*-PDMS BCPs and then layered a BCP of PS-*b*-P2VP that was subsequently loaded with gold or platinum ions. Upon RIE etching, the BCP is removed and the SiO_x/Au or Pt nanoparticle arrays were produced.

Based upon the outcomes of the optimization of the etching work, mixed Au-Pt commensurate and incommensurate hexagonal lattice patterns were produced on both silicon and quartz substrates. Finally, the optical properties of these mixed metal Pt-Au bilayer patterns were studied. They demonstrated interesting plasmonic properties of the bilayer patterns, including consistent observation of extended plasmon bands that suggest coupling of the localized surface plasmon resonances (LSPRs) of

the gold nanoparticles through proximal platinum nanoparticles when arrayed in periodic patterns.

Preface

This thesis is arranged into five chapters. Chapter 1 gives a brief overview about the lithographic techniques and role of directed self-assembly using block copolymers in patterning, along with the concepts of polymer chemistry and self-assembly. Chapter 2 discusses how to use machine learning approaches to analyze and quantify defects observed in block copolymer self-assembled patterns and optimize the solvent vapor annealing parameters in an effective and efficient way. Optimization of reactive ion etching for deposition of a single layer of metal nanopattern using several methods was explained in Chapter 3 in order to fabricate metal–metal bilayers. Chapter 4 contains the generation of mixed metal/oxide double layer patterns and investigates their optical properties.

The work presented in Chapter 2 is published as Gayashani Ginige, Youngdong Song, Brian C. Olsen, Erik J. Luber, Cafer T. Yavuz, Jillian M. Buriak, "Solvent Vapor Annealing, Defect Analysis, and Optimization of Self-Assembly of Block Copolymers Using Machine Learning Approaches" *ACS Appl. Mater. Interfaces* **2021**, *13* (24), 28639–28649. I designed the experiments and conducted them together with Dr. Youngdong Song, who was a visiting graduate student in our group from the Yavuz group at KAIST in Korea, and now at KAUST in Saudi Arabia. I wrote the initial text draft and analyzed the data with Dr. Erik J. Luber and Brian C. Olsen. The solvent vapor flow annealing system was designed by Dr. Erik J. Luber and Brian C. Olsen. The control software, machine learning algorithms, and all the images were processed by Brian C. Olsen. All the authors contributed to the discussion and text editing.

All the experiments in Chapter 3 were designed and conducted by me under the guidance of Dr. Erik J. Luber, Brian C. Olsen, and Prof. Jillian M. Buriak. All the image processing and data analysis were carried out by me. I wrote the discussion part and Prof. Jillian M. Buriak contributed to the writing of the text.

Chapter 4 is being restructured as a manuscript that will be co-authored with Brian C. Olsen, Dr. Erik J. Luber, Prof. Mark T. McDermott, and Prof. Jillian M. Buriak. I performed all the experiments, created each figure, and analyzed most of the data. Dr. Erik J. Luber, Prof. Mark T. McDermott, and Prof. Jillian M. Buriak

contributed to the analysis of UV-vis spectroscopy data. I wrote most of the text, and Prof. Jillian M. Buriak contributed to writing and editing the text.

Chapter 5 is the thesis summary and outlook for several future research directions in the field.

Acknowledgements

First of all, I would like to convey my profound acknowledgement to my supervisor, Professor Dr. Jillian Buriak, for her enormous support, guidance, and encouragement. Not only has her knowledge, passion, and attitude towards science influenced me, but also her sparkling nature and great personality as a human being always inspired me to follow her footsteps. She is not only a respectful supervisor but also a great mentor and a close friend. Your help and encouragement helped me go through a hard time during the pandemic with my daughter at home and writing a thesis as an expecting mother. I am very grateful to have joined the Buriak group and be one of her students.

I would like to thank my committee members: Prof. Eric Rivard, Prof. Julianne Gibbs, Dr. Lingzi Sang, and Prof. Douglas Barlage from the Department of Electrical and Computer Engineering for their valuable advice and guidance. In addition, I would like to thank Prof. Matthew Moffitt from University of Victoria for agreeing to be my external examiner. Thanks to Prof. Steven Bergens for chairing my candidacy examination. I also would like to thank collaborators for their kind help and support to my projects, including Dr. Youngdong Song from Korea Advanced Institute of Science and Technology (KAIST) and Prof. Cafer T. Yavuz from King Abdullah University of Science and Technology (KAUST),

I would like to express my sincere gratitude to previous and current members from the Buriak group. Thanks to Dr. Erik Luber and Brian Olsen for your tremendous support and valuable advice with my research and papers writing. Tate Hauger, thank you for your generous technical support and teaching of new instruments used in my experiments. Again, Brian Olsen and Dr. Erik Luber, thank you for offering help with figure drawing and manuscript revision. My special thank goes to Dr. Cong Jin for his guidance and shared knowledge about block copolymer self-assembly with me as a senior graduate student. I would also like to thank Dr. Hezhen Xie, Dr. Chengcheng Rao, Dr. Bing Cao, Dr. Minjia Hu, Dr. Peter Kalisvaart, Dr. Christopher Fetterly, Dr. Mahmoud Almadhoun, Dr. Hao Wang, Dr. Sayed Youssef Sayed, Jasper Woodard, Aaron Kirkey, Kelli Luber, Jennifer Ozdoba, and Adrian Velazquez for providing some

useful suggestions for my research, along with a rich and colorful experience during my Ph.D. studies.

I also would like to thank the following staff members of the Department of Chemistry, nanoFAB, and Nanotechnology Research Centre: Ryan Lewis, Michael Barteski, Andrew Yeung, Dr. Aaron Hryciw, Peng Li, Stephanie Bozic, Melissa Hawrelechko, Scott Munro, Shiau-Yin Wu, Dr. Nancy Zhang, Dr. Shihong Xu, Dr. Mike Xia, and Paul Concepcion for the technical support and kind help. Also, a special thanks to Dr. Anna Jordan for her patience and expertise in editing my thesis.

Lastly, I would like to thank my parents, siblings, and in-laws for their unconditional love and support throughout my life. A special thanks is reserved for my husband, Sumal Wattegedara. I couldn't have gotten so far without you. Finally, my daughter Yenaya who has been such an angel during the tough time of writing this thesis and studying.

Table of Contents

Abstract ii
Preface v
Acknowledgements vii
List of Tables xiii
List of Figures xiv
List of Abbreviations xxxiii
CHAPTER 1 1
Introduction 1
1.1 Moore's Law and Its Limitations 1
1.2 Next Generation Nanolithography (NGL) 6
1.2.1 Extreme UV (EUV) 6
1.2.2 Electron Beam Lithography 8
1.2.3 Nanoimprint Lithography 9
1.2.4 Directed Self-assembly (DSA) 11
1.3 Block Copolymer Self-assembly 14
1.3.1 Polymer Chemistry 15
1.3.2 Block Copolymers 18
1.3.2 Phase Behavior of BCPs - The Basis of Self-assembly 19
1.3.3 High χ BCPs 24
1.4 Annealing 26
1.4.1 Thermal Annealing 26
1.4.2 Solvent Annealing 29
1.4.3 New Trends in Annealing 31
1.5 Applications of BCP Based Nanopatterning 32
1.5.1 FinFET Fabrication 33
1.5.2 Bit-patterned Media Fabrication 34
1.6 Scope of the Thesis 36
CHAPTER 2 38
Machine Learning Approaches for Solvent Vapor Annealing Process Control [a] 38
2.1 Introduction 38

2.2 Apparatus for Solvent Vapor Annealing 39
2.3 Design of Experiment and Machine Learning 44
2.4 Experimental Methods 46
2.4.1 Materials 46
2.4.2 Silicon Wafer Dicing and Cleaning 46
2.4.3 BCP Thin-film Self-assembly 46
2.4.4 Controlled Solvent Vapor Flow Annealing System 47
2.4.5 PS-*b*-PDMS Thin Film Reactive Ion Etching (RIE) Process 48
2.4.6 Film Characterization 48
2.4.7 Data Processing 49
2.5 BCP Pitch and Cell Orientation 50
2.6 Point Defects 54
2.6.1 Registration Error (R_e) 55
2.6.2 Defect Distance 58
2.6.3 Phase defects 60
2.7 Figure of Merit (FOM) 63
2.8 Conclusions 67
CHAPTER 3 69
Reactive Ion Etching of Metal-loaded Self-assembled Block Copolymer Thin Films 69
3.1 Introduction 69
3.2 Experimental 76
3.2.1 Materials 76
3.2.2 Substrate Preparation 76
3.2.3 BCP Thin-film Self-assembly 76
3.2.4 Metallization 77
3.2.5 Reactive Ion Etching and Thermal Annealing 77
3.2.5 Formation of Au@Ag Core-shell Nanoparticle Arrays 78
3.2.6 Film Characterization and Data Processing 78
3.3 Sequential Self-assembly of BCPs 78
3.4 Optimization of the Reactive Ion Etching 85
3.5 Optimization of Thermal Annealing 91

3.6 Au@Ag Core-shell Nanoparticle Arrays 98
3.7 Conclusions 101
Chapter 4 103
Incommensurate Block Copolymer Self-assembly for Photonic Mixed Metal Nanopatterns 103
4.1 Introduction 103
4.2 Introduction to Moiré Patterns 108
4.3 Optical Metasurfaces 110
4.4 Experimental Methods 113
4.4.1 Materials 113
4.4.2 Substrate Preparation 113
4.4.3 BCP Thin Film Self-assembly by Solvent Annealing 114
4.4.4 Metallization and Reactive Ion Etching 116
4.4.4 Characterization 118
4.4.5 Ellipsometry and UV-vis Spectroscopy Analysis 118
4.4.5 Data processing 118
4.3 Multicomponent Block Copolymer Self-assembly 118
4.4 UV-vis Spectroscopic Analysis of the Localized Surface Plasmon Resonance of the Metal Nanoparticle Arrays 132
4.5 Conclusion 151
Chapter 5 153
Thesis Summary and Outlook 153
5.1 Thesis Summary 153
5.1.1 Chapter 1 153
5.1.2 Chapter 2 153
5.1.3 Chapter 3 154
5.1.4 Chapter 4 154
5.2 Future Research Directions 155
5.2.1 Effect of Bottom Layer Height on Pt−Au Nanoparticle Overlap 155
5.2.2 Finite-difference Time-domain (FDTD) Simulation of Pt−Au Bilayers .. 157
5.2.3 Mixed Metal-metal Nanopattern and Their Optical Properties 158
5.2.4 Application of Mixed Metal–metal Bilayer Patterns 159

References 162

List of Tables

Table 1.1. Flory-Huggins Interaction Parameters for Different Block Copolymers.. 25

Table 3.1. Pitch, Dot Diameter and Calculated β of the Different BCPs Used in This Study 79

Table 4.1. Experimental Parameters for Preparation of SiO_x, Pt and Au Nanopatterns from BCP with Different Molecular Weights.. 117

Table 4.2. Pitch and Dot Diameter of the Different BCP Used in This Study......... 120

Table 4.3. Native Pitch of the Bottom and Top Layer BCPs and the Corresponding Pitch Ratios for Six Different Configurations of Sequentially Deposited BCP Bilayers 123

Table 4.4. Native Pitch Ratios Calculated from a Single Layer of Pt and Au Nanopatterns and Diameters of Pt and Au Nanodots in Single Layers and in Their Corresponding Double Layer Patterns for Each Combination of BCP Patterns 138

Table 4.5. Native Pitch Ratios Calculated from a Single Layer of Pt and Au Nanopatterns and Diameters of Pt and Au Nanodots in Single Layers and the Estimated Edge to Edge Distance Between Two Nanoparticles for Each Combination of BCP Patterns and Single Layers of Nanoparticles 148

Table 4.6 Native Pitch Ratios Calculated from a Single Layer of Pt and Au Nanopatterns, the Estimated Center to Center Distance Between Two Nanoparticles, Radius of Au Nanodots in Single/Double Layers and Calculated Interparticle Separation for Each Combination of BCP Patterns and Single Layers of Nanoparticles ……………………………………………………………………………………151

List of Figures

Figure 1.1. Moore's Law: The number of transistors on a chip doubles about every two years. Reprinted with permission from De Gruster, from reference 2......................... 1

Figure 1.2. Schematic representation of the lithographic techniques. (a) Serial patterning using direct laser writing (DLW). (b) Parallel patterning using UV, extreme UV, and X-ray lithographies. Reprinted from reference 19. 2

Figure 1.3. Schematic representation of a photolithographic process with an (upper) positive and (lower) negative photoresist, where the irradiated polymer molecules decompose to become either more soluble in a specific developer solution than the unexposed regions (positive photoresist) or less soluble due to crosslinking of the photoresist (negative photoresist) to render the exposed regions insoluble in the developer.. 3

Figure 1.4. International Roadmap for Devices and Systems (IRDS) predictions for semiconductor product nodes and expected production timeline with respect to next generation lithography techniques. The image is from reference 40. Reprinted with permission from IOP Publishing... 5

Figure 1.5. (a) Schematic illustration of the EUV system. The image is from reference 47 with permission from SPIE-The International Society for Optical Engineering. (b) Standard cell pattern of metal layer in 7 nm logic produced by ArF immersion multipatterning and single exposure EUV. Reprinted from reference 45 with permission from SPIE... 7

Figure 1.6. e-beam exposed resist for high resolution patterning (a) 9 nm CD isolated pattern. (b) 10 nm line to space ratio = 5 (L/5S). (c) 11 nm L/4S. (d) 12 nm dense L/S patterns. (a-d) Adapted from reference 55. Copyright © 2020 American Chemical Society. (e) Schematic representation of electron beam lithography setup: side view.

The figure has been reprinted from reference 56 with permission from Springer Netherlands. 9

Figure 1.7. The basic process steps of all categories of nanoimprint lithography. Figure reproduced from reference 48 with permission from IEEE. 10

Figure 1.8. (a) SEM micrographs for patterns produced using DSA of BCPs that form cylindrical and lamellar structures using chemoepitaxy and graphoepitaxy. The images are adapted from references 69,71-73. Copyright © 2008 Wiley, 2016 SPIE, 2009 American Chemical Society and 2015 American Chemical Society. Schematic diagram of (b) chemoepitaxy and (c) graphoepitaxy. Figure has been reproduced from reference 74 with permission from Elsevier BV. 12

Figure 1.9. (a) Schematic representation of top and side view of the PS-*b*-PDMS arranged in the region surrounding a single HSQ nanopost chemically modified surface by a monolayer of short-chain PDMS brush. (b) SEM image of spherical microdomains without a guiding template. (c-d) SEM images of ordered spheres directed self-assembly within the sparse 2D lattice of HSQ nanopost (brighter dots). The substrate and nanopost surface functionalized with (c) PDMS brush and (d) PS brush. Images are from reference 76 with permission of the American Association for the Advancement of Science. (e) Schematic and SEM image of square arrays of nanopost template. (f) Commensurability of the spacing between nanoposts and native pitch of the BCP generated two equally probable orientations (parallel to the x- and y- axes). Bends and terminations appear when the orientation of the BCP changes. Adopted from reference 77 with permission from the Nature Publishing Group. 13

Figure 1.10. The schematic diagrams of synthetic polymerization processes, step-growth polymerization and chain-growth polymerization (non-living and living). The letters A, B, C, D, E represent different monomers. The symbols r_A and r_B represent the reactivity of the monomers A and B respectively. Diagram is from reference 105 with permission from the Royal Society of Chemistry. 16

Figure 1.11. Common examples of block copolymer architectures. 18

Figure 1.12. Diblock copolymer bulk phase behavior. (a) Schematic illustration of diblock copolymer equilibrium morphologies as a function of volume fraction of block A. (b) Theoretical phase diagram of diblock copolymer predicted by SCFT. (c) Experimental phase diagram of PS-*b*-PI. The phase diagram is from reference125 adapted with permission from the American Institute of Physics. 20

Figure 1.13. Theoretical phase diagram of AB diblock copolymer in a thin film, where χN is fixed at 20 as a function of volume fraction of A and film thickness w in the units of radius of gyration (R_g), and the resulting morphologies formed. Reprinted from reference 136 with permission from the American Chemical Society. 23

Figure 1.14. Schematic illustration of different surface affinities of lamellae forming AB diblock copolymers. 24

Figure 1.16. (a) Controlled solvent vapor annealing using nitrogen inlet and outlet. (b-d) SEM micrographs of silica nanostructures formed by PS-*b*-PDMS with different solvent annealing conditions with corresponding toluene:hexane (T:H) and swelling ratios (SR). Adopted from reference 182 with permission from IOP Publishing. (e) Schematic representation of processing steps for DSA of cylinder forming PS-*b*-PDMS on topographically patterned substrate annealed using mixed solvent vapors and SEM micrographs of resulting patterns. Image is from reference 183 and is reprinted with permission from Wiley-VCH... 30

Figure 1.17. Scanning electron micrographs of (a) Poly(styrene-*b*-trimethylsilylstyrene-*b*-styrene) (PS-*b*-PTMSS-*b*-PS) with a water soluble topcoat after thermal annealing. Inset is without the topcoat. (b) Poly(trimethylsilylstyrene-*b*-d,l-lactide) (PTMSS-*b*-PLA) topcoat after thermal annealing. Inset is without topcoat. The images are from reference 200. Copyright American Association for Advancement of Science. (c) Process flow of DSA with BCP using chemoepitaxy and topcoat via iCVD. (d-f) SEM micrographs of (d) e-beam resist pattern after trim etch (e) DSA pattern after sequential infiltration and synthesis and removal of the topcoat with reactive ion

etching (RIE). (f) Alumina line/space pattern after removal of organic components by RIE. Image is from reference 199 with permission of the Nature Publishing Group. 32

Figure 1.18. Fin formation by PS-*b*-PMMA. (a) Process flow diagram of graphoepitaxy based fiFET fabrication. Reprinted from reference 82. American Chemical Society. (b) Comparison of pattern quality between self-aligned quadruple patterning (SAQP-baseline) and DSA-based finFET fabrication. Reprinted from reference 83 Nature Publishing Group. 34

Figure 1.19. (a) Using double imprinting to create rectangular bits by intersecting circumferential and radial line space patterns. Reprinted from reference 219 with permission from IOP publishing. (b-e) SEM micrographs of bit media patterns from DSA of PS-*b*-PDMS on nanoimprint template. Images are from reference 86 with permission from the American Chemical Society. 35

Figure 2.1. Topological defects found in line patterns generated from BCP PS-*b*-P2VP self-assembly. The positive phase is the P2VP block and the negative phase is the PS block. The image is from reference 224 with permission from the Public Library of Science. 39

Figure 2.2. Examples of general solvent vapor annealing apparatus. (a) “Jar” annealing using a Petri box. Schematic is from reference 232 with permission of Elsevier. (b) Static solvent vapor apparatus, and (c) static solvent vapor apparatus with gas flow. Adapted from reference 155 with permission from the American Chemical Society. 40

Figure 2.3. Profile and plan view of terraced phases of a thin film of PS-*b*-PB-*b*-PS with 14k-73k-15k molecular weight. (a-c) AFM phase images of BCP thin films with different morphologies in areas of varying initial film thickness (by varying polymer concentration) after annealing. White lines are contour lines. All the images are 2 × 2 μm^2. Adapted from reference 227 with permission of the American Physical Institute. 41

Figure 2.4. (a) The pre-annealed BCP film spin-coated onto silicon, locking in the initial film thickness. (b) Solvent vapor annealing (SVA) to a predetermined swelling degree (SD) using a feedback-controlled annealing system. Adapted from reference 158 with permission of the American Chemical Society... 42

Figure 2.5. Schematic representation of the chemoepitaxy DSA process used to study the kinetics of the defect annihilation. The schematic is from reference 242 with permission from the American Chemical Society. 43

Figure 2.6. Comparison between DOE vs. OFAT approaches for finding optimum parameters for two input parameter systems. (a,b) OFAT sampling of an uncorrelated system and (c,d) OFAT sampling of a correlated system. (e) DOE approach with orthogonal sampling of a correlated system. (f) Approximation of the true output parameter map produced by ML fitting methods applied to the six data points acquired by DOE in (e). Adapted from reference 256 with permission from the American Chemical Society. 45

Figure 2.7. Relationship between initial film thickness and concentration (% m/v) of PS-*b*-PDMS (43k-*b*-8.5k) solution in toluene. Film thickness determined by ellipsometry. The plot is reproduced from reference 158 with permission of the American Chemical Society. 47

Figure 2.8. (a) High magnification SEM micrographs of BCP dots at various swelling degrees and initial film thicknesses, as indicated. Dot positions taken from these micrographs were used to calculate the statistical values used in the value dot maps corresponding to figures in the main text and ensemble statistics in the paper. Scale bars are 1 μm. (b) Details of (a) showing individual dots. Scale bars are 250 nm. The images are from reference 158 with permission of the American Chemical Society. 49

Figure 2.9. BCP lattice pitch as a function of SVA conditions. (a) Dot value maps showing dot locations for all 28 combinations of initial thickness of the PS-*b*-PDMS films and swelling degrees, indicated by the labelled rows and columns, respectively, and showing color values for BCP lattice pitch in nm. Scale bars are 1 μm. (b) Details

of (a) showing individual dots. Scale bars are 250 nm. The images are from reference 158 with permission of the American Chemical Society... 51

Figure 2.10. Support vector machine fitting using a radial basis function kernel showing the relationship between initial film thickness, swelling degree and median BCP lattice pitch. The image is from reference 158 with permission of the American Chemical Society. 52

Figure 2.11. BCP lattice cell orientation as a function of SVA conditions. (a) Dot value maps showing dot locations for all 28 combinations of initial thickness of the PS-*b*-PDMS films and swelling degrees, indicated by the labelled rows and columns, respectively, and showing color values for BCP lattice cell orientation in degrees. Scale bars are 1 μm. (b) Details of (a) showing individual dots. Scale bars are 250 nm. The images are from reference 158 with permission of the American Chemical Society. 53

Figure 2.12. (a) Dot value maps showing dot locations for all 28 combinations of initial film thicknesses and swelling degrees, indicated by the labelled rows and columns respectively. Color represents the number of BCP lattice cell neighbors as determined by Delaunay triangulation. Scale bars are 1 μm. (b) Details of (a) showing individual dots. Scale bars are 250 nm. The images are from reference 158, with permission of the American Chemical Society. 55

Figure 2.13. Registration error as a function of SVA conditions. (a) Dot value maps showing dot locations for all 28 combinations of initial thickness of the PS-*b*-PDMS films and swelling degrees, indicated by the labelled rows and columns, respectively, and showing color values for registration error in percent dot pitch. Scale bars are 1 μm. (b) Details of (a) showing individual dots. Scale bars are 250 nm. The images are from reference 158 with permission of the American Chemical Society. 57

Figure 2.14. (a) Dot value maps showing dot locations for all 28 combinations of initial film thickness and swelling degrees, indicated by the labelled rows and columns, respectively, with color values of local orientational order parameters. Scale bars are 1

μm. (b) Details of (a) showing individual dots. Scale bars are 250 nm. (c) Support vector machine fitting using a radial basis function kernel of the average local orientational order parameter. The images are from reference 158 with permission of the American Chemical Society.. 58

Figure 2.15. Defect distance as a function of SVA conditions. (a) Dot maps where the color value is the distance to the nearest defect. A defect is defined as having a registration error less than 17% where all of the vacancies and grain boundaries are included. Scale bars are 1 μm. (b) Support vector machine fitting using a radial basis function kernel of the effective defect distance per SVA condition. The images are from reference 158 with permission of the American Chemical Society. 59

Figure 2.16. (a) Dot value maps showing dot locations for all 28 combinations of initial film thickness and swelling degrees, indicated by the labelled rows and columns respectively. Color represents the defect cutoff of 17% of registration error, where orange dots are defects corresponding to Figure 2.13. Scale bars are 1 μm. (b) Details of (a) showing individual dots. Scale bars are 250 nm. The images are from reference 158 with permission of the American Chemical Society.. 60

Figure 2.17. (a-b) Cross-sectional schematic (a) low-magnification micrograph (b) of terraced phases of wetting, single- and double-layer morphologies with dot forming PS-*b*-PDMS, after solvent annealing and removal of polymer by plasma cleaning. (c-e) High magnification SEM micrographs of the single layer (c), double layer (d) and wetting layer (e). This image is from reference 155 with permission of the American Chemical Society. 61

Figure 2.18. Number of hexagonal dot layers as a function of SVA conditions. (a) False color low magnification SEM micrographs showing wetting layers in dark blue, single layers in green, and double layers in yellow. Scale bars are 50 μm. (b) Support vector machine fitting using a radial basis function kernel of the area averaged number of dot layers, where "0" represents a wetting layer, "1" represents a single layer of dots, and "2" represents double layer areas. Scale bar is set to 0.4–1.4 to improve contrast. The images are from reference 158 with permission of the American Chemical Society. 63

Figure 2.19. Support vector machine fitting using a radial basis function kernel of the (a) defect distance of the 20th percentile (where a defect is defined as having a registration error above 17%), where the majority of the vacancies and grain boundaries are included, (b) fraction single layer, and (c) multiplication of fraction single layer by defect distance. The images are reproduced from reference 158 with permission of the American Chemical Society. 65

Figure 2.20. The fit of the predicted SVM models in Figure 2.19 versus the actual values. (a) 20th percentile of defect distance, (b) fraction of single layer, and (c) multiplication of fraction single layer by defect distance. The images are from reference 158 with permission from the American Chemical Society. 66

Figure 3.1. SEM micrographs of (a) planar view (b) 70° tilted view of a porous thin film of PS after removal of PMMA by exposure to UV, followed by an aqueous development in acetic acid at (c) low magnification and (d) high magnification of a 100 nm thick suspended porous silicon membrane. This image is from reference 285 with permission from the American Vacuum Society. 70

Figure 3.2. (a) Structure and molecular weight of poly(styrene-*b*-2-vinylpyridine) (PS-*b*-P2VP). (b) Schematic representation of spin coating a solution of PS-*b*-P2VP in toluene on a silicon substrate with a native oxide layer. Thermal annealing of the pseudohexagonal arrays leading to a fingerprint pattern with P2VP cylinders embedded within the PS matrix. P2VP swelling as a result of protonation by immersing thermal annealed samples in an acidic cation solution. Electrostatic interaction of anionic metal salts with the protonated P2VP layer to load with metal salts, followed by plasma treatment to remove polymer and form metal wires on the surface. (c) Electrostatic attraction between anionic metal complexes with the protonated P2VP block, in an acidic environment. This image is from reference 169 with permission from the American Chemical Society. 71

Figure 3.3. Bright-field TEM images of thin film cast using micellar solutions of PS-*b*-P2VP treated with 0.5 equivalents of $HAuCl_4$ per pyridine unit after reduction with anhydrous hydrazine for different time intervals. (a) After 1 min reduction, one gold particle per micelle with diameter of 9 nm. (b) After 30 min reduction, the initially formed gold particles paired up. The insets show high magnification images for one (a) and two (b) gold particles. (c) After 2 days reduction, coagulation of initially formed gold particles resulting in large crystallites and empty micelles. This image is from reference 298 with permission from John Wiley & Sons. 72

Figure 3.4. SEM micrographs of top and cross-sectional view of Pt nanopatterns by PS-*b*-P2VP (125k-*b*-58k) template. (a) Pt dot pattern, (b) Pt line pattern. This image is from reference 303 with permission from the American Chemical Society. 73

Figure 3.5. (A) A schematic representation of a parallel line pattern in a polymer film. Characteristic line spacing for areas with a single layer of lines was L after the metallization step was performed (B). Line spacing was halved to $L/2$ for areas with double layers of lines (C). The cross-section image (D) represents both layers of lines, with the top layer lines being slightly brighter and narrower than those of the underlying layer. (E-G) Similar pattern formation and density doubling for dot patterns. All scale bars are 100 nm. This image is from reference 304 with permission from the American Chemical Society. 74

Figure 3.6. (a) A schematic representation (up) and SEM micrographs (bottom) of a sequential self-assembly of PS-*b*-PDMS to generate silica honeycomb patterns. (b) A schematic representation of three different scenarios of dot-to-dot contact within a lattice with the geometrical values of interest within the perfect hexagonal lattice with dot overlap ($\beta > 1$), touching ($\beta = 1$) and no contact ($\beta < 1$). This image is adapted from reference 305 with permission of the American Chemical Society........................... 75

Figure 3.7. SEM micrographs of (a) low and (b) high magnification images of a single layer of Pt nanodot pattern generated from PS-*b*-P2VP (44k-*b*-8.5k) of the same sample. (c) Low (d) high magnification images of sequential nanopatterning of Pt–Pt

double layer dot patterns using the single layer of Pt nanodot pattern in (a). Brighter dots correspond to the second layer of Pt nanopattern, and dark dots represent the bottom layer of Pt nanodots. All the scale bars are 250 nm, and the insets show the corresponding FFT of the nanopattern. 81

Figure 3.8. SEM micrographs of (a) low and (b) high magnification images of a single layer of Pt nanodot pattern generated from PS-*b*-P2VP (44k-*b*-18.5k) blended with 30% PS (10k). (c) Low and (d) high magnification images of sequential nanopatterning of Pt–Pt double layer dot patterns using the single layer of Pt nanodot pattern in (a). Brighter dots correspond to the second layer of Pt nanopattern and dim dots represent the bottom layer of Pt nanodots. All the scale bars are 250 nm, and the insets show the corresponding FFT of the nanopattern. 82

Figure 3.9. SEM micrographs of (a) low and (b) high magnification images of a single layer of Pt nanodot pattern generated from PS-*b*-P2VP (88k-*b*-18k). (b) Low and (c) high magnification images of sequential nanopatterning of Pt–Pt double layer dot patterns using the single layer of Pt nanodot pattern in (a). Brighter dots correspond to the second layer of Pt nanopattern and dark dots represent the bottom layer of Pt nanodots. All the scale bars are 250 nm, and the insets show the corresponding FFT of the nanopattern. 83

Figure 3.10. SEM micrographs for (a) a single layer of hexagonal SiO_x dot pattern from self-assembly of B30 (b) sequential self-assembly of a second layer of hexagonal Pt nanodots on the bottom layer SiO_x dot pattern using B’30 with pitch ratio of 1.0, and (c) low and (d) high magnification images of triple layer formation of SiO_x–Pt–Pt on top of the double layer of SiO_x–Pt using identical self-assembly process to the second layer. All the scale bars are 250 nm, and the insets show the corresponding FFT of the double and triple layers. 85

Figure 3.11. A schematic illustration of four types of plasma mechanisms. (a) Sputter etching, (b) chemical etching, (c) ion-enhanced chemical etching, and (d) inhibitor ion-enhanced chemical etching. This image is from reference 310 with permission from Springer Nature. 86

Figure 3.12. SEM micrographs of a single layer of Pt nanopattern generated by self-assembly of PS-*b*-P2VP (56k-*b*-21k) pattern transfer with (a) chemical plasma etching using 0.6 torr O_2 plasma for 1 min and (b) RIE using 0.1 torr O_2 plasma for 20 s..... 87
Figure 3.13. SEM micrographs of a single layer of Au nanoparticles fabricated using PS-*b*-P2VP (88k-*b*-18k) (a) after a RIE step and (b) after spin coating a second layer using only toluene without the BCP on the same sample shown in (a). All the scale bars are 250 nm... 88

Figure 3.14. SEM and AFM micrographs of (a,b) a single layer of a hexagonal Pt dot nanopattern from PS-*b*-P2VP (88k-*b*-18k) after the first RIE step. (c,d) After the first RIE step the same sample of Pt dot nanopattern is subjected to a second RIE step as the first. All scale bars are 250 nm and insets represent the FFT of the corresponding nanopattern.. 89

Figure 3.15. A schematic representation of island and hole formation upon etching of a thin film of a PS-*b*-P2VP layer on silicon. (a) The PS-*b*-P2VP layer contains $HAuCl_4$ embedded within the P2VP block. (b) The PS-*b*-P2VP contains Au nanoparticles upon etching. The gold nanoparticles etch faster under these conditions than both the PS and P2VP blocks. Reprinted from reference 314 with permission of Wiley-VCH........... 90

Figure 3.16. Higher magnification SEM micrograph of a (a) Au and (b) Pt nanopattern prepared via self-assembly of PS-*b*-P2VP (88k-*b*-18k), followed by RIE................ 91

Figure 3.17. SEM micrographs of Pt nanopatterns by PS-*b*-P2VP (88k-*b*-18k) developed using (a) partial RIE of 100 mTorr, O_2 RIE (80 sccm) at RF power of 30 W for 5 s (b) partial RIE of 100 mTorr, O_2 RIE (80 sccm) at RF power of 30 W for 15 s, followed by thermal annealing at 250 $^{\circ}$C for 1 h, and (c) thermal annealing at 250 $^{\circ}$C for 1 h without using RIE. All scale bars are 250 nm... 92

Figure 3.18. SEM micrographs of Pt nanopatterns by PS-*b*-P2VP (88k-*b*-18k) developed using (a) partial RIE of 100 mTorr, O_2 RIE (80 sccm) at RF power of 30 W for 15 s, followed by (b) thermal annealing at 550 $^{\circ}$C for 10 min, (c) thermal annealing

at 550 °C for 15 min, and (d) thermal annealing at 550 °C for 30 min. All scale bars are 250 nm. 93

Figure 3.19. SEM micrographs of Pt nanopatterns by PS-*b*-P2VP (88k-*b*-18k) developed using (a) RIE of 100 mTorr, O_2 RIE (80 sccm) at RF power of 30 W for 30 s, followed by (b) thermal annealing at 350 °C for 15 min, and (c) thermal annealing at 350 °C for 30 min. All scale bars are 250 nm. 94

Figure 3.20. SEM and AFM micrographs of (a,b) a single layer of a hexagonal Pt dot nanopattern from PS-*b*-P2VP (88k-*b*-18k) after the first RIE step, (c,d) after the first RIE step the same sample of Pt dot nanopattern was subjected to a thermal annealing step, and (e,f) after the thermal annealing step the same sample of Pt dot nanopattern is subjected to a second RIE step as the first. 95

Figure 3.21. SEM micrographs of Au nanopatterns from PS-*b*-P2VP (88k-*b*-18k) after (a) the first RIE step and (b) subsequent thermal annealing at 350 °C for 15 min. All scale bars are 250 nm. 96

Figure 3.22. SEM micrographs for sequential nanopatterning of a Pt–Pt double layer dot pattern using PS-*b*-P2VP (88k-*b*-18k) (a) bottom layer is after RIE and thermal annealing steps and top layer is only after the RIE step. (b) Low and (c,d) high magnification SEM micrographs of the same pattern after thermal annealing of the second layer. All the scale bars are 250 nm, and the inset shows the FFT of the corresponding pattern. 97

Figure 3.23. (A) A schematic illustration of an Au@Ag core-shell nanopatterning process. (B) SEM micrographs of the Au nanopattern by the PS-*b*-P4VP self-assembly process and (C) Au@Ag core-shell nanopattern after 40 min of growth time. (D) Average diameter and Au composition variation of core-shell plotted against Ag shell growth time. Reprinted with permission from reference 306 by the American Chemical Society 99

Figure 3.24. SEM and AFM micrographs of (a,b) a single layer of a hexagonal Au dot nanopattern from PS-*b*-P2VP (88k-*b*-18k) after RIE and thermal annealing. (c-f) Au@Ag core-shell formation using (a) for time intervals of (c,d) 10 min (e,f) 20 min. All the scale bars are 250 nm. 100

Figure 3.25. Size distribution of (a) single layer of Au nanopattern generated by self-assembly of PS-*b*-P2VP (88k-*b*-18k) after RIE and thermal annealing process, (b) single layer of an Au@Ag core-shell nanopattern after 10 min deposition of Ag on Au from (a), and (c) single layer of an Au@Ag core-shell nanopattern after 20 min deposition of Ag on Au from (a). 101

Figure 4.1. Schematic representation of sequential self-assembly of BCP to generate non-native morphologies using diblock BCPs. This schematic is reproduced from reference 344 with permission of John Willey and Sons. 104

Figure 4.2. SEM micrographs of binary combinations of Au-TiO_2 nanoarrays with different periodicities. (a) TiO_2 nanowires with a periodicity of 55 nm deposited on an Au nanopattern with a periodicity of 71 nm. (b) TiO_2 nanoparticles with a periodicity of 46 nm deposited on an Au nanopattern with a periodicity of 96 nm. (c) Similar sample as (b) before coating TiO_2, Au nanoparticle size was increased from 8 nm to 25 nm in diameter by electroless deposition. This image is from reference 353 with permission from the American Chemical Society. 105

Figure 4.3. (a) One-step density doubling of metal lines via self-assembly of double layers of BCPs. SEM micrographs of a single Pt line pattern (b), a double Pt line pattern (c), a single Pt dot pattern (e), and a density doubled Pt dot pattern (f). Tilted SEM micrographs of density a doubled Pt line pattern (d) and dot pattern (g). The image is from reference 304 with permission of the American Chemical Society. (h) Density multiplication via sequential self-assembly of PS-*b*-PDMS to generate double and triple layers of silica dot patterns. This image is from reference 305 with permission from the American Chemical Society. 106

Figure 4.4. (a) SEM micrographs of non-native 3D two-layer nanostructures generated by a sequential self-assembly of PS-*b*-PMMA. All scale bars 100 nm. Adapted from reference 354 with permission from Springer Nature. (b) SEM micrographs of various double layer Pt nanomeshes, a soft shear-laser zone annealing method. Scale bars are 200 nm. The images are from reference 343 with permission from Springer Nature. (c) Hierarchical nanostructures including line-in-line, dots-on-line, and dots-in-holes fabricated from smaller periodicity PS-*b*-PDMS on topographical templates of larger periodicity PS-*b*-PDMS. The SEM micrographs are from reference 355 with permission from John Wiley and Sons. 107

Figure 4.5. Three Moiré configurations from line patterns. (a) Formation of a 1D moiré pattern by superimposing two-line patterns with different line spacing. (b) Formation of a 2D Moiré pattern by superimposing two identical line patterns with relative in-plane rotational angle. (c) Formation of a 2D moiré pattern by superimposing two identical mesh patterns with relative in-plane rotational angle. This image is from reference 369 with permission of John Wiley and Sons. 108

Figure 4.6. (a) SEM micrograph of flower-like Moiré superstructures formed from a sequential annealing of two incommensurate BCP combinations (left) and schematic representation of the bottom and top layer angle of rotation (right). This image is from reference 322 with permission of the American Chemical Society. (b) SEM micrograph of triangular-like Moiré superstructures formed by a self-assembly of BCP on EBL post arrays (left) and schematic showing the corresponding BCP lattice rotation and mass density waves (right). This image is reprinted from reference 368 with permission of the American Chemical Society... 110

Figure 4.7. (a) Schematic of annealing setup. (b) Schematic representation of an annealing process of an Au nanoparticle lattice. (c) SEM micrographs of an Au nanoparticle lattice before (upper) and after (bottom) thermal annealing process. (d) Transmission electron microscopic (TEM) image of thermally annealed Au nanoparticles. (e) Experimental transmission spectra of untreated (black), a thermally annealed Au nanoparticle lattice after 1 d (red) and 1 month (blue). This image is

reprinted from reference 394 with permission of the National Academy of Science. 112

Figure 4.8. Top-down (a) and side-view (b) of the solvent annealing chamber with five different solvent reservoirs to contain solvents with different surface areas (vapor pressures). The image is from reference 155 with permission of the American Chemical Society... 115

Figure 4.9. Photograph of the static solvent vapor annealing setup with in-situ thickness monitoring. Image is from reference 155 with permission of the American Chemical Society. 115

Figure 4.10. Schematic illustration of the methodology for forming mixed component-based honeycomb/Moiré superstructures using hexagonal BCP dot arrays. (a) Formation of a bottom layer dots via self-assembly of a BCP, followed by solvent annealing and/or metallization and reactive ion etching (RIE) to convert the BCP into either hexagonal lattice of Pt or silica dots. (b) Deposition of the top layer of PS-*b*-P2VP on a preformed nanopattern of Pt or SiO_x dots from (a). (c) Solvent vapor annealing, metallization, and RIE of the second layer to convert BCP to Au or Pt nano-dots to form honeycomb/Moiré superstructures. 119

Figure 4.11. SEM micrographs of (a) a single layer Au nanodot array (b) a double layer Au–Au nanodot arrays self-assembled using subsequent deposition of PS-*b*-P2VP (88k-*b*-18k). All scale bars are 250 nm. 120

Figure 4.12. Low magnification (left) and high magnification (right) SEM micrographs of single layer SiO_x nanodots derived from different molecular weights of PS-*b*-PDMS. (a,b) 43k-*b*-8.5k (**P43**) and (c,d) 31k-*b*-14.5k (**B30**). All scale bars are 250 nm. 121

Figure 4.13. SEM micrographs of single layers of Pt (left) and Au (right) nanodots produced using PS-*b*-P2VP BCPs of different molecular weights. (a,b) 44k-*b*-18.5k (**B30**), (c,d) 88k-*b*-18k (**P88**), and (e,f) 135k-*b*-53k (**B15**). All scale bars are 250 nm. 122

Figure 4.14. Low magnification (first row, a–d) and high magnification (second row, b+e) SEM micrographs and schematics illustrate the high magnification SEM (third row) of honeycomb patterns from (a–c) Pt–Au derived from P88, with the bottom layer being Pt and the top layer Au. (d–f) SiO_x–Pt derived from bottom layer **B30** and top layer **B30**, metalized with Pt. The insets represent the FFT of the resulting nanopatterns. First row scale bars are 250 nm; second and third row scale bars are 100 nm. 125

Figure 4.15. (a) Low (scale bar 250 nm) and (b) high (scale bar 100 nm) magnification SEM micrographs and (c) schematic illustration of the high magnification SEM of Pt–Au Moiré patterns with incommensurate pitch ratios of 0.91; bottom layer **P88** (Pt) and top layer **B30**. The inset represents the FFT of the resulting nanopatterns. Orange and gray dots represent Au and Pt nanodots, respectively. 126

Figure 4.16. (a) SEM micrograph and (b) corresponding BCP dot map illustrating the mass density waves for a pitch ratio of 1.1, generated using self-assembly of **B30**(Pt)+**P88**(Au). All scale bars are 250 nm. 127

Figure 4.17. Low (first row, a–d) and high (second row, b–e) magnification SEM micrographs and schematic illustration of the high magnification SEM (third row) of Pt–Au Moiré patterns with incommensurate pitch ratios of (a–c) 0.58; bottom layer **B15** (Pt) and top layer **B30** (Au) and (d–f) 0.63; bottom layer **B15** (Pt) and top layer **P88** (Au). The insets represent the FFT of the resulting nanopatterns. Orange and gray dots represent Au and Pt nanodots, respectively. First row scale bars are 250 nm; second and third row scale bars are 100 nm. 129

Figure 4.18. Low (first row) and high (second row) magnification SEM micrographs and high magnification schematic representation (third row) of Pt–Au Moiré patterns with incommensurate pitch ratios of (a–c) 1.6; bottom layer **P88** (Pt) and top layer **B15** (Au) and (d–f) 1.7; bottom layer **B30** (Pt) and top layer **B15** (Au). Orange and gray dots represent Au and Pt nanodots, respectively. Insets show the corresponding FFT. First row scale bars are 250 nm; second and third row scale bars are 100 nm. 131

Figure 4.19. SEM micrographs of SiO_x–Pt Moiré patterns with incommensurate pitch ratios of (a) 0.9; bottom layer P48 (SiO_x) and top layer **P44** (Pt) (b–d) 1.1; bottom layer **B30** (SiO_x) and top layer **P88** (Pt). The red area represents a grain boundary in the bottom **B30** (SiO_x). The insets represent the FFT of the resulting nanopatterns. Small brighter dots are Pt, and dark larger dots are SiO_x. All the scale bars are 250 nm. .. 132

Figure 4.20. Experimentally measured SPR spectra of ellipsometric parameters, amplitude φ and phase Δ, at an angle of 70° for an array of (a) Au nanoparticles and (b,c) Au–Pt bilayers. All scale bars are 100 nm. 134

Figure 4.21. The UV-vis absorption spectra for self-assembled single layers of Au nanoparticle arrays on fused silica substrates. All scale bars are 250 nm. 135

Figure 4.22. The UV-vis absorption spectra for self-assembled single layers of Pt nanoparticle arrays on fused silica substrates. All scale bars are 250 nm. 136

Figure 4.23. Number of Au nanoparticles per unit area vs BCP combination. Error bars represent the standard deviation from several samples and SEM micrographs........ 137

Figure 4.24. (a,b) UV-vis spectrum of the P88 (Pt)/**P88** (Au) metal bilayer combination showing the distinct feature at wavelengths longer than 600 nm that could correspond to an extended plasmon band (EPB). (c) High magnification SEM micrographs and (d) high magnification schematic representation of the Pt–Au bilayer. Orange and gray dots represent Au and Pt nanodots, respectively. All scale bars are 100 nm............ 140

Figure 4.25. (a,b) UV-vis spectrum of the **P88** (Pt)/**B15** (Au) metal bilayer combination showing almost no the distinct feature at wavelengths longer than 600 nm. (c) High magnification SEM micrographs and (d) high magnification schematic representation of the Pt–Au bilayer. Orange and gray dots represent Au and Pt nanodots respectively. All scale bars are 100 nm. 141

Figure 4.26. (a,b) UV-vis spectrum of the **P88** (Pt)/**B30** (Au) metal bilayer combination showing the distinct feature at wavelengths longer than 600 nm that could

correspond to a EPB (c) High magnification SEM micrographs and (d) high magnification schematic representation of the Pt–Au bilayer. Orange and gray dots represent Au and Pt nanodots respectively. All scale bars are 100 nm. 142

Figure 4.27. (a,b) UV-vis spectrum of the **P88** (Pt)/**B30** (Au) metal bilayer combination showing the distinct feature at wavelengths longer than 600 nm that could correspond to EPB. (c) High magnification SEM micrographs and (d) high magnification schematic representation of the Pt–Au bilayer. Orange and gray dots represent Au and Pt nanodots respectively. All scale bars are 100 nm. 143

Figure 4.28. (a,b) UV-vis spectrum of the **B30** (Pt)/**B15** (Au) metal bilayer combination showing the distinct feature at wavelengths longer than 600 nm that could correspond to EPB. (c) High magnification SEM micrographs and (d) high magnification schematic representation of the Pt–Au bilayer. Orange and gray dots represent Au and Pt nanodots respectively. All scale bars are 100 nm. 144

Figure 4.29. (a,b) UV-vis spectrum of the **B15** (Pt)/**P88** (Au) metal bilayer combination showing the distinct feature at wavelengths longer than 600 nm that could correspond to EPB. (c) High magnification SEM micrographs and (d) high magnification schematic representation of the Pt–Au bilayer. Orange and gray dots represent Au and Pt nanodots respectively. All scale bars are 100 nm. 145

Figure 4.30. (a,b) UV-vis spectrum of the **B15** (Pt)/**B30** (Au) metal bilayer combination showing the distinct feature at wavelengths longer than 600 nm that could correspond to EPB. (c) High magnification SEM micrographs and (d) high magnification schematic representation of the Pt–Au bilayer. Orange and gray dots represent Au and Pt nanodots respectively. All scale bars are 100 nm. 146

Figure 4.31. UV-vis absorption spectrum of strongly interacting Au nanoparticles giving rise to EPB at near-IR region. (a) Aggregates of gold nanoparticles with LSPR absorbances at 540 nm are termed here as TSP (transverse SPR). This image is from reference 409 with permission from the American Chemical Society. (b) Gold

nanoparticle aggregates that are interconnected by conjugated molecular linkers with thiocarbamate groups on both ends. UV-vis absorption spectra as a function of time. This image is from reference 410 with permission from Springer Nature. 149

Figure 5.1. SEM micrographs and their manually drawn schematic representations of Pt–Au bilayers by self-assembly of PS-*b*-P2VP for pitch ratios (a) 0.59, (b) 0.63, (c) 1.1, and (d) 1.6. Orange and gray dots represent Au and Pt nanodots, respectively. All scale bars are 100 nm. 156

Figure 5.2. SEM micrographs of (a) planar and (b) tilted view of single layer of Pt nanoparticles self-assembled using PS-*b*-P2VP (44k-*b*-8.5k) and (c) planar and (b) tilted view of double layer of Pt–Pt nanopatterns by sequential self-assembled of PS-*b*-P2VP (44k-*b*-8.5k). All scale bars are 100 nm. 157

Figure 5.3. UV-vis absorbance spectra for Ag (blue), Pt (black), Au (orange), and Cu (brown) with the same geometry (size 40 nm and height 30 nm). The inset shows the extremely broad and weak absorbance band throughout the visible region. This image is from reference 420 with permission of the Royal Society of Chemistry. 159

Figure 5.4. Morphology and SERS performance of Ag coated Au bowtie arrays. This image is from reference 424 with permission from the American Chemical Society. 160

Figure 5.5. (a,b) UV-vis spectrum of the **P88** (Pt)/**P88** (Au) metal bilayer combination showing the distinct feature at wavelengths longer than 600 nm that could correspond to an extended plasmon band (EPB). (c) High magnification SEM micrographs and (d) high magnification schematic representation of the Pt–Au bilayer. Orange and gray dots represent Au and Pt nanodots, respectively. All scale bars are 100 nm. 161

List of Abbreviations

193i	193 nm Immersion
AFM	Atomic Force Microscope
BCP	Block Copolymer
CD	Critical Dimension
CMOS	Complementary Metal-oxide Semiconductor
CPS	Closely Packed Spheres
CTAC	Cetyltrimethylammonium Chloride
Đ	Dispersity
DLW	Direct Laser Writing
DoE	Design of Experiments
DSA	Directed Self-assembly
E-Beam	Electron Beam
EBL	Electron-beam Lithography
EDX	Energy Dispersive X-ray
EPB	Extended Plasmon Band
EUV	Extreme Ultra-violet
FDTD	Finite-difference Time-domain
FFT	Fast Fourier Transform
FinFET	Fin Field-electric Transistors
FOM	Figure of Merit
HSQ	Hydrogen Silsesquioxane
iCVD	Initiated Chemical Vapor Deposition
IEEE	Institute of Electrical and Electronics Engineers
IR	Infrared
IRDS	International Roadmap for Devices and Systems
ITRS	International Technology Roadmap for Semiconductors
LER	Line Edge Roughness
LSPR	Localized Surface Plasmon Resonance
MDWs	Mass Density Waves

ML	Machine Learning
M_n	Number Average Molecular Weight
M_w	Weight Average Molecular Weight
NGL	Next Generation Lithography
NIL	Nanoimprint Lithography
ODT	Order–disorder Transition
OFAT	One Factor at a Time
OOT	Order-to-order Transition
OVAT	One Variable at a Time
PS-*b*-PB-*b*-PS	Poly(styrene-*b*-butadiene-*b*-styrene)
PS-*b*-PDMS	Poly(styrene-*b*-dimethylsiloxane)
PS-*b*-PI	Poly(styrene-*b*-isoprene)
PS-*b*-PI	Poly(styrene-*block*-isoprene)
PS-*b*-PMMA	Poly(styrene-block-methyl methacrylate)
PS-*b*-PTMSS-*b*-PS	Poly(styrene-*b*-trimethylsilylstyrene-*b*-styrene)
PS-*b*-PVP	Poly(styrene-*b*-vinyl-2-pyridine)
PVC	Polyvinyl Chloride
PVP	Polyvinylpyridine
RBF	Radial Basis Function
R_e	Registration Error
RF	Radio Frequency
R_g	Radius of Gyration
RIE	Reactive Ion Etching
SAMs	Self-Assembled Monolayers
SAQP	Self-Aligned Quadruple Patterning
SAXS	Small-angle X-ray Scattering
SBR	Styrene Butadiene Rubber
SCCM	Standard Cubic Centimeter Per Minute
SCFT	Self-consistent Field Theory
SD	Swelling Degree
SEM	Scanning Electron Microscope

SERS	Surface Enhanced Raman Spectroscopy
SLR	Surface Lattice Resonance
SPIE	Society of Photo-optical Instrumentation Engineers
SR	Swelling Ratios
SSL	Strong Segregation Limit
SVA	Solvent Vapor Annealing
R	Gas Constant
T	Temperature
Tb	Terabyte
TEM	Transmission Electron Microscopy
T_g	Glass Transition Temperature
THF	Tetrahydrofuran
T_m	Melt Transition Temperature
T_{ODT}	Order–disorder Transition Temperature
vdWHs	van der Waals Heteroepitaxy
V_m	Molar Volume
WSL	Weak Segregation Limit
β	Empty Space Between in the Interstitial Position
Δ	Phase Difference
ΔH_v	Enthalpy Change of Vaporization
Ψ	Amplitude
χ	Flory-Huggins Interaction Parameter
δ	Solubility Parameter

CHAPTER 1

Introduction

1.1 Moore's Law and Its Limitations

Intel's co-founder Gordon Moore noted, back in 1965, that the number of transistors on a chip was doubling about every two years. Now termed Moore's Law (Figure 1.1), this observation still holds, even as feature sizes decrease to the sub-20 nm regime.[1] Moore's Law has thus been the guiding principle for the semiconductor industry for over fifty years.

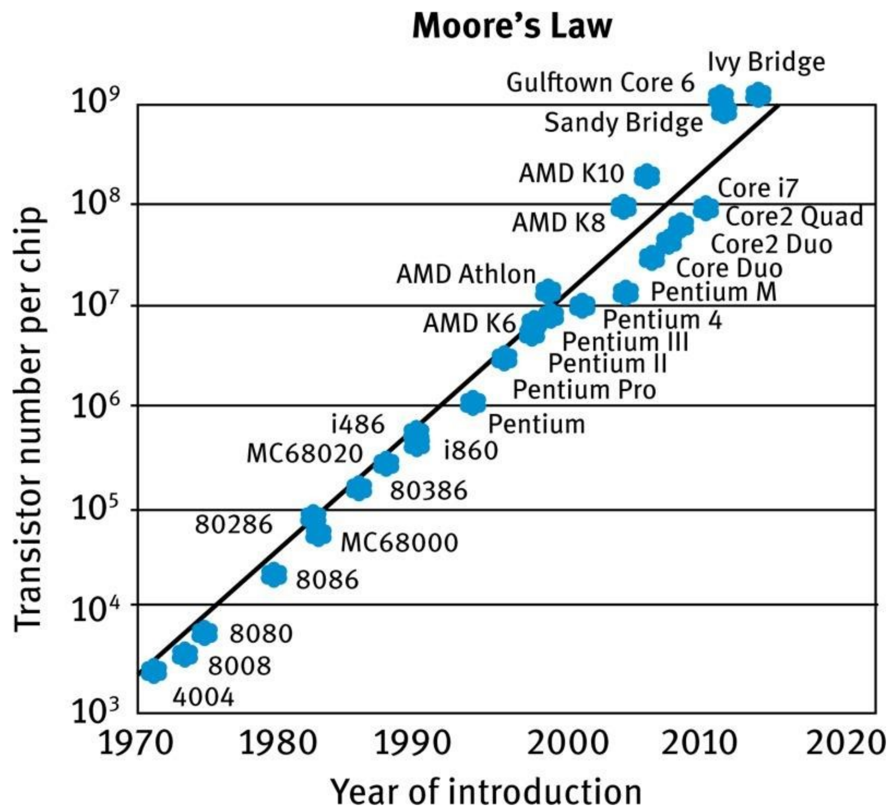

Figure 1.1. Moore's Law: The number of transistors on a chip doubles about every two years. Reprinted with permission from De Gruster, from reference 2.

In order to produce these ever-decreasing size transistors, lithography has had to make remarkable advances to enable production of >10^9 sub-20-nm features on each single chip.[3,4] The word "lithography" comes from Greek, where lithos means stones and graphia means to write, so 'writing on stones'.[5,6] Lithography can be divided up

into two main categories, serial and parallel patterning. Serial patterning is akin to writing, in which the patterning literally is written or drawn on the surface, one feature at a time, much like drawing with a pencil. Examples of serial lithographic techniques at the nanoscale include electron beam lithography[7–9] (e-beam), focused ion beam lithography,[10,11] and any scanning probe lithography technique.[12–15] Figure 1.2(a) shows a schematic representation of a serial lithographic technique by direct laser writing.[16–18] Parallel lithography, however, is like a printing press, in which multiple features are patterned simultaneously. The semiconductor industry is built upon the incredibly efficient and massively parallel method of photolithography, which uses light and masking/shadowing to enable highly complex nanoscale patterning on silicon surfaces, as shown in Figure 1.2(b).

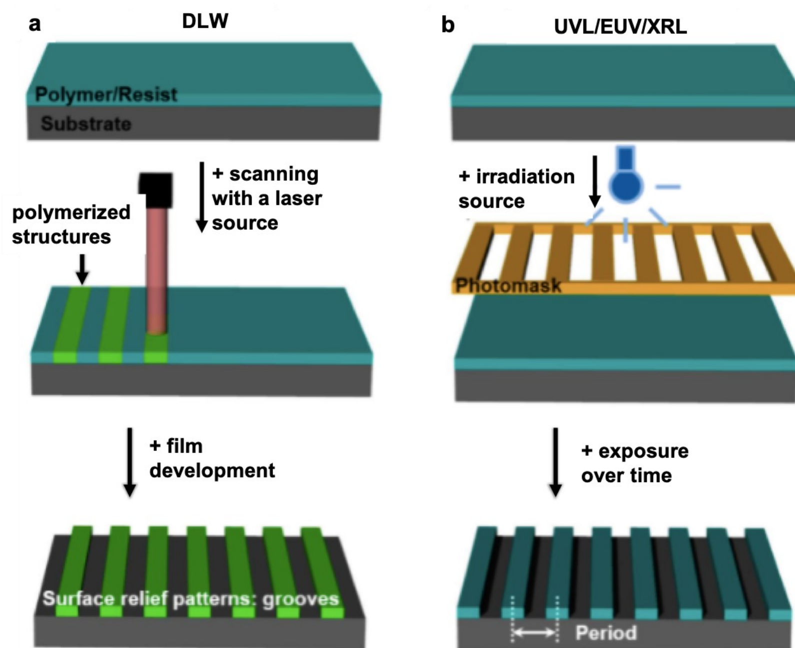

Figure 1.2. Schematic representation of the lithographic techniques. (a) Serial patterning using direct laser writing (DLW). (b) Parallel patterning using UV, extreme UV, and X-ray lithographies. Reprinted from reference 19.

Shrinking the size of transistors has enabled a dramatically increased density of devices in each generation of integrated circuits. The semiconductor industry has suggested that after the 14 nm node is reached, there is minimal to no reduction in cost before the next node is introduced.[20] Smaller transistors can enable a higher density of transistors per wafer, but the wafer costs at newer nodes could outweigh the benefits.[21]

Cost is not the only issue with respect to continuation of Moore's Law, as miniaturization of transistor size increases the complexity of the design of the integrated circuit and introduces various manufacturing challenges.[1,22] Thus, the main challenge using photolithography is a Venn diagram, where the sweet spot lies at the intersection of cost and the minimum achievable resolution. Hence, the requirement for low cost lithographic techniques to obtain minimum resolution is essential for the further development of the semiconductor industry in the way it has proceeded until today.

Advances in photolithography have played a very central role in driving Moore's Law over the decades, and continuous improvements in optics and 'tricks' such as immersion lithography and multiple patterning meant few deviations from the linear behavior shown in Figure 1.3. The general principle of photolithography is to expose a photoresist, which is a very thin film of a light sensitive polymer deposited on a substrate, typically silicon, to UV light, as shown in Figure 1.3. Depending on the type of photoresist (positive or negative) used, UV radiation facilitates the decomposition or crosslinking of the polymer film, rendering exposed regions either more soluble or less soluble to a selected solvent in the developer step of transferring the pattern to the substrate.

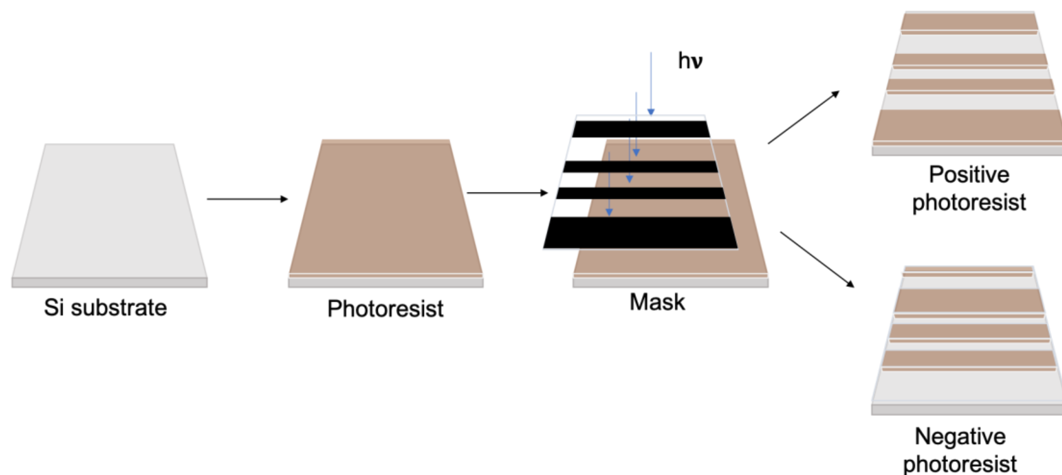

Figure 1.3. Schematic representation of a photolithographic process with an (upper) positive and (lower) negative photoresist, where the irradiated polymer molecules decompose to become either more soluble in a specific developer solution than the unexposed regions (positive photoresist) or less soluble due to crosslinking of the photoresist (negative photoresist) to render the exposed regions insoluble in the developer.

The nanometer scale resolution of the photolithography underpins the relentless decrease in size of the features on chips. The resolution of photolithography is expressed by the Rayleigh Equation:

$$CD = \frac{k\lambda}{NA} \quad \text{Eq. 1.1}$$

where *CD* is the critical dimension of a features, *k* is the Rayleigh coefficient of resolution, *NA* is the aperture of the lens, and λ is the wavelength of light used. The critical dimension of a feature printed by photolithography can be decreased by reducing the wavelength λ of the light source according to Equation 1.1. For the past two decades, feature sizes have decreased to the range of 22 nm[23] due to resolution enhancement techniques and immersion methods that push past the intrinsic resolution limit of photolithography as defined by Equation 1.1.

Modifying the light source from G-line mercury arc lamps (436 nm) to I-line (365 nm) to KrF (248 nm) to commercial argon fluoride laser (193 nm) sources have helped to increase the resolution successfully.[24] At the same time, improvements in the depth of focus (*NA*) have been enabled by placing a transparent fluid between the lens and the photoresist, in what is termed immersion lithography.[25] The state of the art of the semiconductor industry and predictions 10 years forward are summarized in what used to be termed the International Technology Roadmap for semiconductors (ITRS), now the International Roadmap for Devices and Systems (IRDS).[26,27] ITRS 2015 proposed new directions as an extension of Moore's Law, such as More Moore and More than Moore.[28] While More Moore focuses on the improvement of device structure, materials, and fabrication techniques, More than Moore concentrates on application-based strategies, such as sensors and actuators,[29] radio frequency,[30] and high voltage drivers.[31] These applications add value to computing and memory devices that are made from the technology that falls under the traditional Moore's Law umbrella. The continuous advancement of nanofabrication techniques is important for improving the performance of future computational devices and others, including those based on optoelectronics,[32,33] photonics,[34] sensors,[35] biomedicine,[36] and biology.[37] Hence, enormous efforts have been made to achieve this goal.

The various IRDS predict that logic metal levels will drive improvements in the resolution of lines and spaces. The 2020 roadmap in Figure 1.4 predicts the projected time frames for implementation of different product nodes, along with the possible patterning options.[38] It is important to keep in mind that logic nodes are just numerical values for each node and do not represent the feature size or minimum half pitch of those nodes. According to the 2020 prediction, 12 nm half pitch resolution will improve by 2022, which corresponds to the logic 3 nm node achieved using EUV and double patterning. There is also a delay in resolution improvement for the logic 2 nm node until 2028, and it will take the same time to decrease the half pitch to 8 nm by EUV double patterning. The next section of this chapter will discuss these next generation lithography (NGL) techniques and their role in the relentless decrease of device size.[38,39]

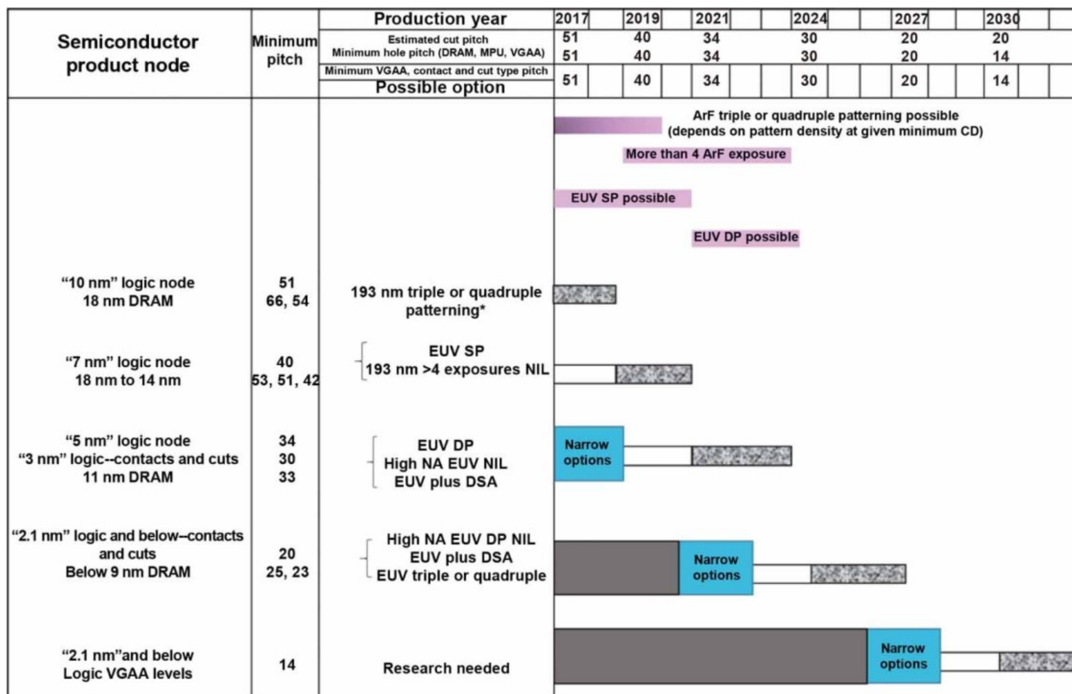

Figure 1.4. International Roadmap for Devices and Systems (IRDS) predictions for semiconductor product nodes and expected production timeline with respect to next generation lithography techniques. The image is from reference 40. Reprinted with permission from IOP Publishing.

1.2 Next Generation Nanolithography (NGL)

In this thesis, we focus upon lithography on the nanoscale and thus will use the term "nanolithography" to emphasize this length scale. Traditional photolithography has been the primary technique for nanolithography applications but is now reaching what appear to be limits that are both physical and economic. Various research laboratories and industries around the globe have devoted considerable efforts to next generation lithography (NGL) techniques to continue to decrease feature sizes and increase device density on the chip surface. These techniques include extreme UV (EUV), electron beam (e-beam) lithography, nanoimprint lithography (NIL), and directed self-assembly (DSA), and they have the potential to complement or, in some specific applications, replace the current photolithographic techniques.

1.2.1 Extreme UV (EUV)

As optical photolithography using 193 nm light reaches its physical limits, the obvious next step has been to decrease the wavelength of the light source. X-rays, termed in this application extreme UV with a very short wavelength of 13.5 nm, are produced using a tin plasma source.[6,41] Companies, including Intel and Motorola, began to contemplate EUV lithography as an NGL technique in the late 1980s and by the early 1990s,[42,43] and it has taken two decades to overcome the very considerable engineering challenges to attain the 7 nm node/generation and beyond.[44] Figure 1.5 shows a schematic representation of one of the 53 EUV systems in operation around the world and a comparison of cell patterns in 7 nm logic pattern by ArF immersion lithography and EUV, clearly showing that EUV has better pattern fidelity.[45,46]

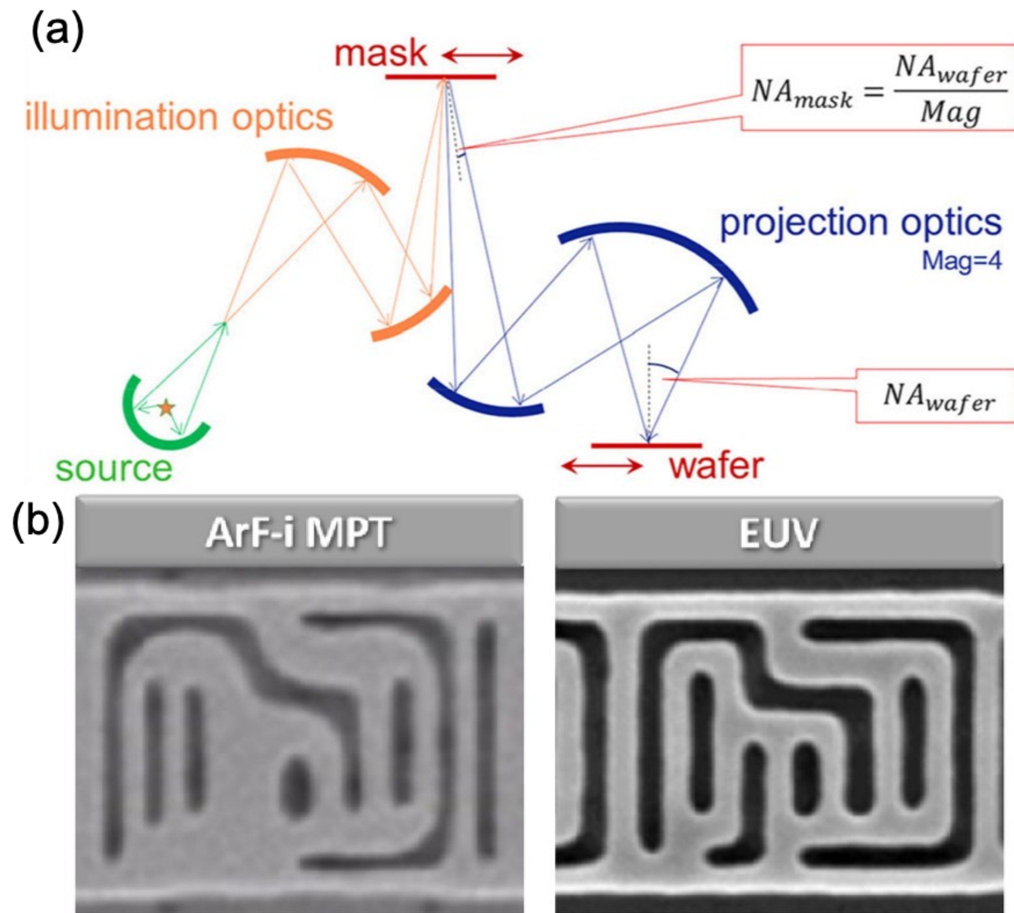

Figure 1.5. (a) Schematic illustration of the EUV system. The image is from reference 47 with permission from SPIE-The International Society for Optical Engineering. (b) Standard cell pattern of metal layer in 7 nm logic produced by ArF immersion multipatterning and single exposure EUV. Reprinted from reference 45 with permission from SPIE.

The industrial implementation and mass production of EUV had to overcome issues with the power source, masks, and resist materials.[48,49] The power source requires a stable high power exposure since it is converting plasma into light of 13.5 nm and due to the low transmissivity of materials to X-rays. Today, EUV has the capability to enable production at the 7 nm node,[50] but the power of the plasma source cannot generate power to allow an EUV scanner to move faster or make it economically feasible.[51,52] The available EUV power sources emit a great deal of heat when producing 13.5 nm photons, which makes it difficult to select optics with sufficient thermal stability. The detritus from the exposed regions can contaminate the mirrors and eventually decrease the power and lifetime of the power source.[51] However,

ASLM, a leading EUV instrumentation manufacturing company, states that their next generation EUV machine will be available by 2023.[53] This machine has several advancements compared to the currently available EUV instrumentations, such as increased productivity and improvement in overlay. The selling point of the instrument is its cost, which makes it highlighted since few companies can afford the currently available machines. Among them, the world's leading foundry, Taiwan based TSMC, as well as Samsung in South Korea and Intel, own the majority of these instruments.[53]

1.2.2 Electron Beam Lithography

Electron beam (e-beam) lithography is a versatile, maskless, and serial lithography technique widely used in research labs to generate two-dimensional nanometer scale patterning since the 1970s.[54] The major constraint of photolithography arises from the wavelength limitation of the photons. Electrons and ions, which have smaller wavelengths due to their mass, can be harnessed to generate smaller feature sizes. The wavelength of these particles is given by the de Broglie Equation:

$$\lambda = \frac{h}{\sqrt{2mE}} \qquad \text{Eq. 1.2}$$

where h is Planck's constant, m is the mass of the particle, and E is the energy of the beam.

E-beam lithography uses a focused electron beam to draw patterns on a surface in a dot by dot fashion, generally with a sub-10 nm resolution.[55] When used with a film of resist on a substrate, the resist is modified chemically by the electron beam, changing its solubility profile. One can use a positive or negative resist and, upon rinsing with solvent, the patterned resist can be transferred to the substrate via etching in a similar fashion to other lithographic techniques.

E-beam lithography has its own unique advantages, like high resolution (sub-10 nm), high sensitivity, high density, and high reliability (See Figure 1.6). The main issues associated with e-beam lithography for mass production and industrial processing is its serial nature, which results in low throughput as well as higher complexity (needs to be done in high vacuum) and expense compared to other lithographic techniques. However, multiple e-beam direct write lithography, in which

more than 10,000 e-beams write in parallel, has been shown as a possible route of increasing the system throughput.[57,58]

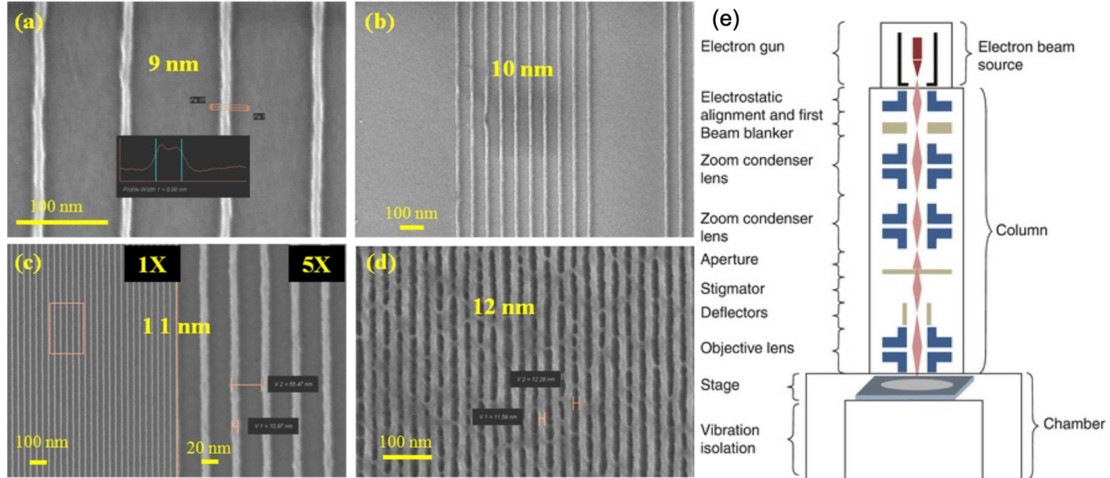

Figure 1.6. E-beam exposed resist for high resolution patterning (a) 9 nm CD isolated pattern. (b) 10 nm line to space ratio = 5 (*L*/5*S*). (c) 11 nm *L*/4*S*. (d) 12 nm dense *L*/*S* patterns. (a-d) Adapted from reference 55. Copyright © 2020 American Chemical Society. (e) Schematic representation of electron beam lithography setup: side view. The figure has been reprinted from reference 56 with permission from Springer Netherlands.

1.2.3 Nanoimprint Lithography

Nanoimprint lithography (NIL) is a parallel lithographic technique that is complementary to photolithography;[38] it is considered to be an NGL technique with high throughput and high resolution (sub-20 nm) and comparatively low cost. NIL is a well-studied and developed nanofabrication technology that utilizes a hard mold or stamp to imprint 2D or 3D nanopatterns into a soft polymer. The nanoimprint technology can be classified into four categories, depending on the fundamental mechanism used for the pattern transfer: thermal NIL, UV NIL, laser-assisted NIL, and electrochemical nanoimprinting. The basic steps of the different NIL processes are shown in Figure 1.7.

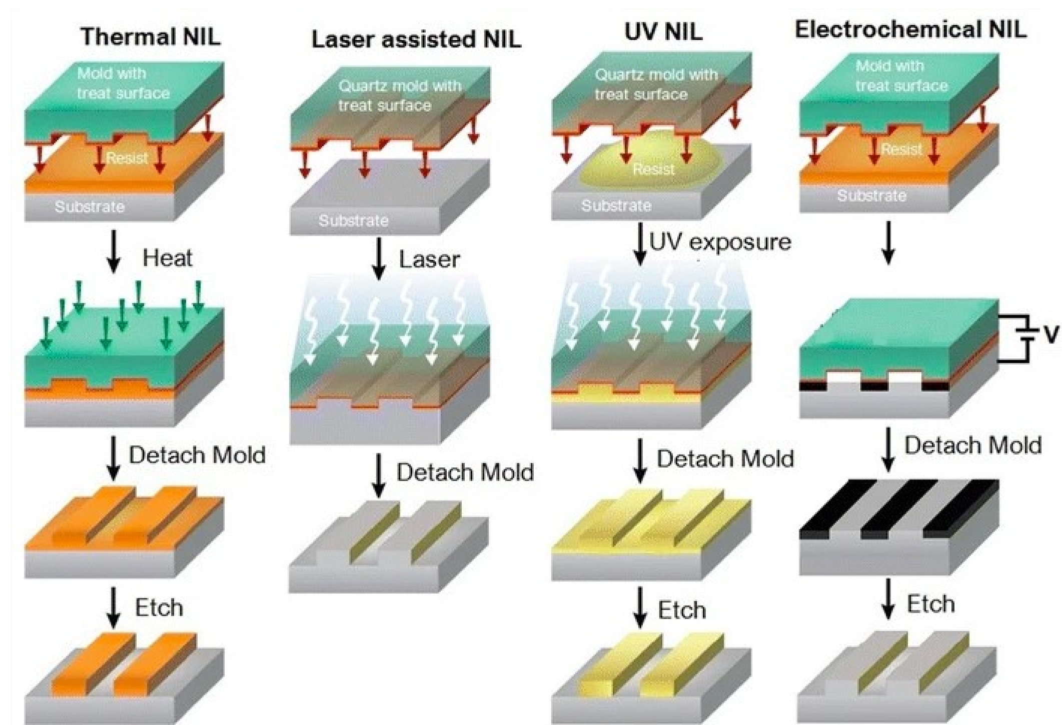

Figure 1.7. The basic process steps of all categories of nanoimprint lithography. Figure reproduced from reference 48 with permission from IEEE.

The resist materials, type of the mold, and the power sources are changed, depending on the type of NIL. For example, in thermal NIL, a thermoplastic polymer is used as a resist, and a prefabricated mold is pressed together with the resist-coated substrate under pressure. Subsequent heating of the polymer resist above its glass transition temperature softens the polymeric film. The resist is patterned by a cooling process of the substrate, followed by removal of the mold. Then, the resist pattern is transferred to the substrate by an etching process. UV NIL uses a UV-curable liquid resist to coat the substrate surface in a low-pressure environment. Next, the resist material is exposed to UV radiation to solidify, and the pattern is extracted by pressing an optically transparent mold into the resist coated substrate. A final etching process of the residual resist transfers the pattern into the substrate surface.

NIL is an extremely simple and fast process with high resolution patterning capabilities that offers a low cost alternative lithographic technique.[59,60] This processing approach can be a high throughput technique since it can fabricate nanopatterns on a larger scale in as short a time as 15 wafers per hour.[61,62] NIL has created a wide range of opportunities for future lithography owing to its flexibility and

ability to combine with other lithographic techniques.[38,63] However, there are a few disadvantages and drawbacks of NIL that include low overlay structure accuracy, the thermal expansion effect, and the flexibility of patterning.[48] For example, even when the designed pattern is changed slightly, the mold must be remanufactured; moreover, the fabrication of the mold relies on the other lithographic techniques, leading to additional required steps and processes.

1.2.4 Directed Self-assembly (DSA)

The term directed self-assembly, or DSA, emerged as a very promising next generation patterning techniques in the mid 1990's to achieve sub-10 nm resolution patterning via self-assembly.[64] The approach is based upon polymers that contain sufficient chemical information to undergo nanoscale phase segregation and form a nanopattern on a surface, which can be used as a template for further processing. In DSA, the use of either a chemically or topologically patterned substrate to direct block copolymer self-assembly in thin films is called chemoepitaxy and graphoepitaxy, respectively. DSA allows control of the orientation of domains as well as precise pattern registration on the substrate and minimizing defects in the resulting pattern. Figure 1.8(b) depicts a schematic of chemoepitaxy and graphoepitaxy applied to BCP self-assembly.

In chemoepitaxy, a neutral substrate surface is modified chemically to generate preferential wetting sites for one of the blocks.[65] The substrate surface can be modified by a variety of brushes, including self-assembled monolayers (SAMs),[65] end-grafting homopolymers,[66] or random copolymers,[67] and crosslinked polymer mats.[68] This interfacial layer at the substrate surface can promote pattern alignment and orientation. The chemical guides can anchor cylindrical BCP domains perpendicular to the substrate (hexagonal)[69] and lamellar forming BCPs parallel to the substrate (linear),[70] as shown in Figure 1.8(a).

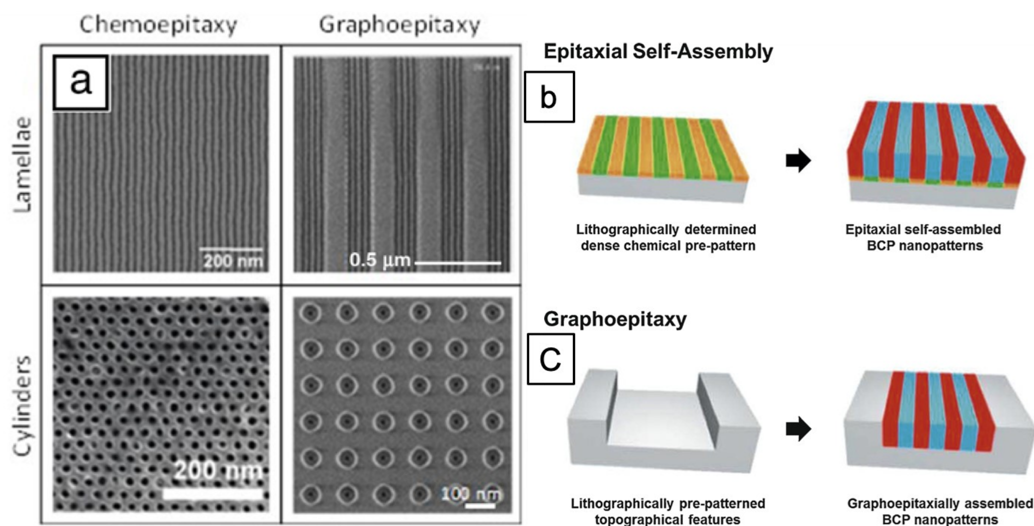

Figure 1.8. (a) SEM micrographs for patterns produced using DSA of BCPs that form cylindrical and lamellar structures using chemoepitaxy and graphoepitaxy. The images are adapted from references 69,71-73. Copyright © 2008 Wiley, 2016 SPIE, 2009 American Chemical Society and 2015 American Chemical Society. Schematic diagram of (b) chemoepitaxy and (c) graphoepitaxy. Figure has been reproduced from reference 74 with permission from Elsevier BV.

For graphoepitaxy, 3D features are fabricated on the substrate surface to guide the self-assembly process using standard lithographic processes of the semiconductor industry. These topographical features, like trenches and dots, can be used to guide the self-assembly process by confining the arrays of microdomains to areas that are a finite number of native domain spacing of the BCPs. The interactions of the blocks of the BCPs with the walls and base of the trenches are also important. The isolation of small clusters of cylinders and lamellae by topographical guides can break the natural periodicity of the BCP.[75] Similarly, the chemical affinity and lateral dimensions of the guide pattern are also critical to adjust the number of domains in the cluster.

Ross and co-workers used a surface patterned with periodic hydrogen silsesquioxane (HSQ) nanoposts as a guiding pattern to self-assemble a sphere, forming PS-*b*-PDMS where nanoposts preferentially interact with the spherical microdomains, as shown in Figure 1.9(c).[76] The preferential interaction is created by functionalizing the surfaces of the substrate and the nanoposts with either a PDMS brush layer, which corresponds to the schematic in Figure 1.9(a) or a PS brush, as in Figure 1.9(d). Similarly, by having commensurate spacing between the square lattice HSQ nanoposts template and the native pitch of the cylinder forming PS-*b*-PDMS, the orientation of

the BCP cylinders can be restricted to two orthogonal in plane directions, as shown in Figure 1.9(f).[77]

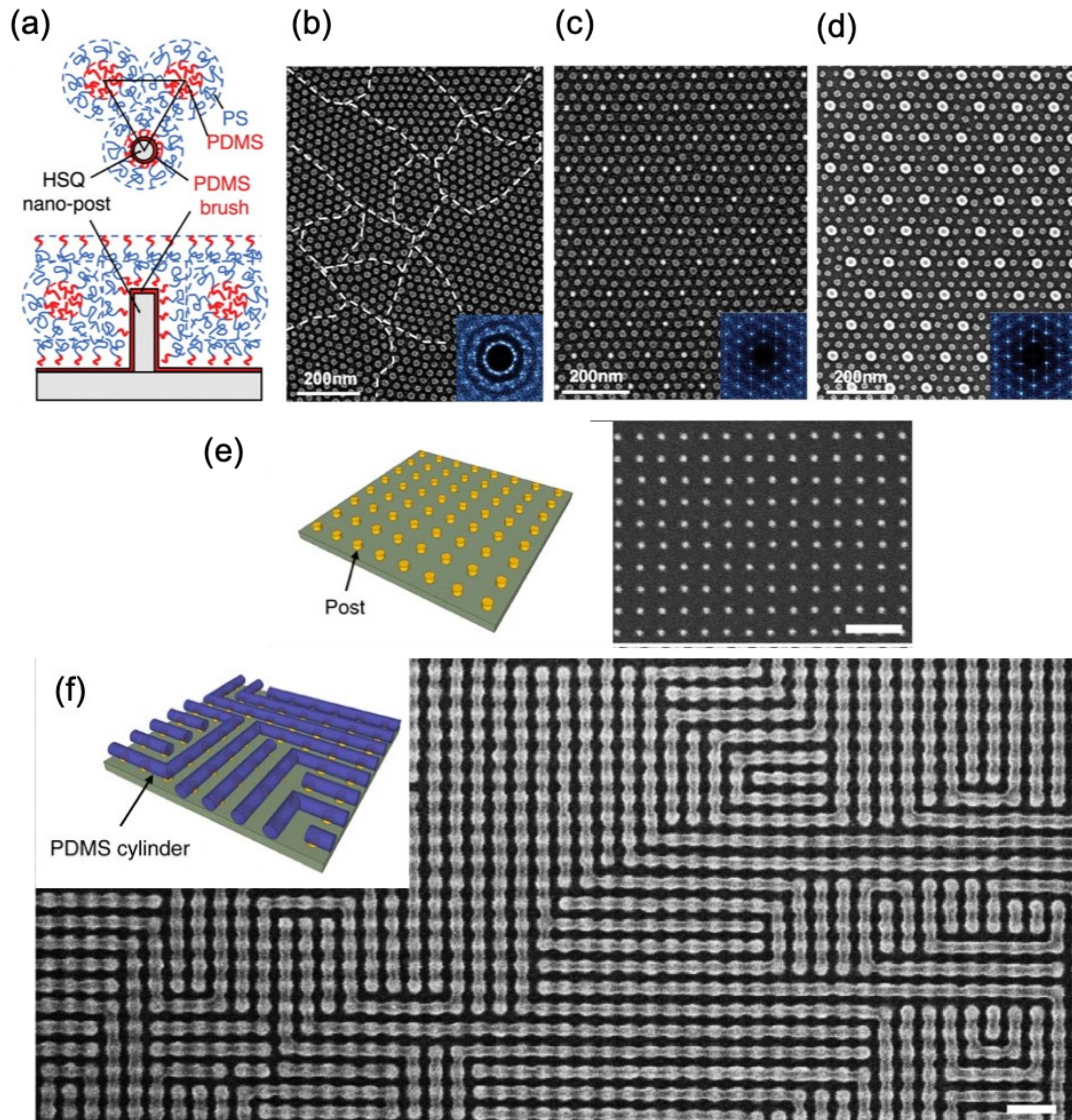

Figure 1.9. (a) Schematic representation of top and side view of the PS-*b*-PDMS arranged in the region surrounding a single HSQ nanopost chemically modified surface by a monolayer of short-chain PDMS brush. (b) SEM image of spherical microdomains without a guiding template. (c-d) SEM images of ordered spheres directed self-assembly within the sparse 2D lattice of HSQ nanopost (brighter dots). The substrate and nanopost surface functionalized with (c) PDMS brush and (d) PS brush. Images are from reference 76 with permission of the American Association for the Advancement of Science. (e) Schematic and SEM image of square arrays of nanopost template. (f) Commensurability of the spacing between nanoposts and native pitch of the BCP generated two equally probable orientations (parallel to the x- and y- axes). Bends and terminations appear when the orientation of the BCP changes. Scale bars, 100 nm for (e-f). Adopted from reference 77 with permission from the Nature Publishing Group.

The 2020 IRDS has listed DSA as one of the lithography techniques being considered by industry for the fabrication of 3–5 nm technology node devices with enhanced pattern resolution, when combined with other lithography techniques, such as EUV[78,79] and 193 nm immersion (193i).[40,40,80–82] DSA offers a variety of configurations for high density integration, with low cost manufacturing to fabricate nanoscale devices, such as fin field effect transistors[83–85] and bit patterned storage media.[86,87] Difficulty in controlling the defects during the self-assembly process is one of the patterning limitations of this patterning technique.[88–90] The defect densities must be <0.01 defects/cm^2 for DSA to be a viable option for next-generation lithography.[3,91–93] Achieving this defect density in devices fabricated from DSA has been a struggle, but the semiconductor industry, with the help of academic labs, has achieved an acceptable level of defectivity when using EUV or e-beam to define guiding features lithographically to help direct the self-assembly process and induce long-range order.[40,88,94] The next section will discuss the basic chemistry of polymers and BCPs as well as the thermodynamics of phase segregation of BCP self-assembly.

1.3 Block Copolymer Self-assembly

Continuous shrinking of feature sizes within the semiconductor industry is driven by the demand for computers with higher speed at lower energy consumption. The semiconductor industry has circled around photolithography. Several alternate technologies, including EUV lithography, nanoimprint lithography, interference lithography, and DSA of block copolymer (BCP), have gained attention as solutions for the challenges facing the semiconductor industry.[3] In contrast, DSA using BCPs is a combination of top-down and bottom-up techniques with high versatility, including tunable shapes and sizes to sub-20 nm nanoscopic elements in a cost-effective way.[40,74,95–97] The main focus of this thesis is about block copolymer self-assembly and process optimization related to the self-assembling process, such as solvent annealing, reactive ion etching, and fabrication of multicomponent patterns using block copolymer self-assembly.

1.3.1 Polymer Chemistry

Polymers are a class of natural or synthetic macromolecular materials or substances composed of repeating chemical units.[98] These repeating units are called monomers, and the process of covalently linking these monomers into a chain or network is termed polymerization. These polymers have their own unique physical, chemical, and mechanical properties, which make these categories of macromolecules essential and ubiquitous to everyday life. There are large numbers of polymers in nature: from natural biopolymers, such as DNA, carbohydrates, and proteins; plant based polymers, such as natural rubber, silk, and cellulose; synthetic polymers, such as polystyrene, polyethylene (synthetic plastic), and polyvinyl chloride (PVC). Synthetic polymerization can be divided into two methods, step-growth polymerization[99,100] and chain-growth polymerization, as shown in Figure 1.10.[101,102] In step-growth polymerization, an uncontrolled polymerization involves bifunctional or multifunctional monomers that are combined together to form first dimers, then trimers, oligomers and, eventually, long chain polymers. Chain-growth polymerization, on the other hand, is based upon polymerization, in which unsaturated monomers are added to the chain, one at a time. Based on the monomer type used for the polymerization, there are two types of polymers, homopolymers and copolymers.[103,104] Homopolymers are made of similar monomer units, and copolymers consist of two or more chemically different monomers linking together. For example, polystyrene is made of styrene monomer, which is a homopolymer, whereas styrene/butadiene rubber (SBR) is a copolymer.

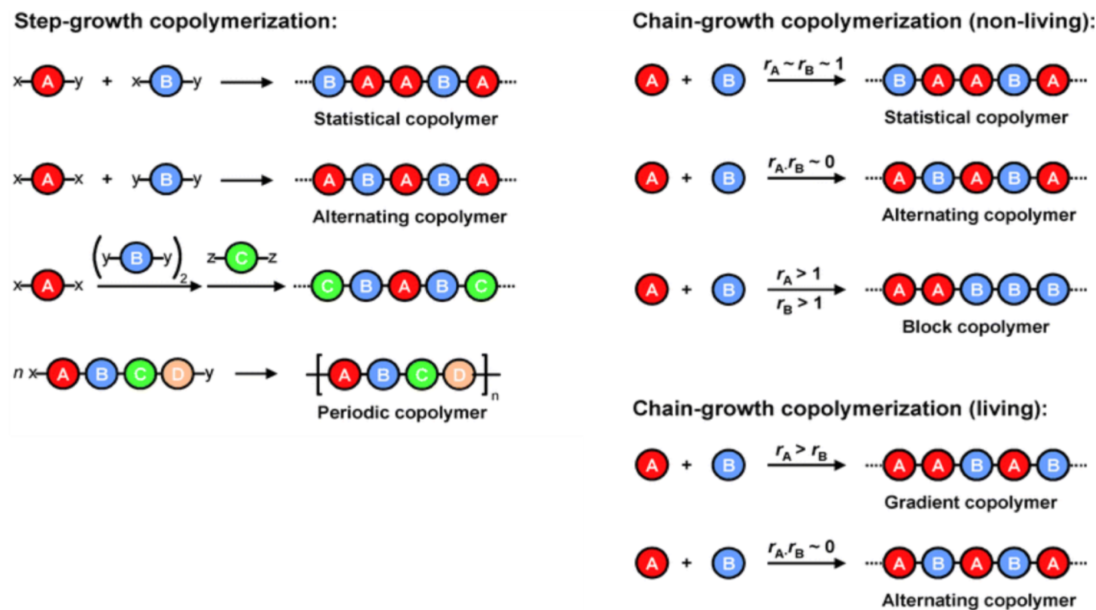

Figure 1.10. The schematic diagrams of synthetic polymerization processes, step-growth polymerization and chain-growth polymerization (non-living and living). The letters A, B, C, D, E represent different monomers. The symbols r_A and r_B represent the reactivity of the monomers A and B respectively. Diagram is from reference 105 with permission from the Royal Society of Chemistry.

There are a number of important parameters related to polymers that are used when describing a polymer, including the molar mass distribution (molecular weight distribution), dispersity ($Đ$) glass transition temperature (T_g), and melt transition temperature (T_m). The molar mass is defined as a distribution rather than a specific number since polymerization of monomers forms different chain lengths of polymers, unlike typical small molecule synthesis. The size (for linear polymers of different chain lengths) is different, even for the same type of polymer molecules, therefore, the average molar mass will depend on the method of averaging. Weight average molar mass (M_w) and number average molar mass (M_N) are the two different average values used to define the molar mass of a polymer, depending on the statistical method used to determine the molar mass. These average molar masses can be calculated as follows. Number average molecular weight (M_N):

$$M_N = \frac{\sum_{i=1}^{N} N_i M_i}{\sum_{i=1}^{N} N_i} \qquad \text{Eq. 1.3}$$

Weight average molecular weight (M_w):

$$M_w = \frac{\sum_{i=1}^{N} N_i M_i^2}{\sum_{i=1}^{N} N_i M_i} \qquad \text{Eq. 1.4}$$

In this equation, i is the number of polymer molecules and N_i is the number of polymer molecules with molecular mass M_i. The number average molar mass (M_N), is the average molecular mass of the individual polymer molecules, and this value is important for the colligative properties of the polymer, such as boiling point elevation, freezing point depression, vapor pressure depression, and osmotic pressure change. The weight average molar mass (M_w) underpins the mechanical properties of a given polymer since larger polymer molecules have a larger contribution than small polymer molecules. Both molecular weights can be determined using gel permeation chromatography or size exclusion chromatography. The ratio between weight average molecular mass (M_w) and number average molecular mass (M_N) is known as the dispersity ($Đ$) of a polymer given by:

$$Đ = \frac{M_w}{M_N} \qquad \text{Eq. 1.5}$$

For synthetic polymers, $M_N < M_w$, keeping $Đ$ higher than 1. $Đ$ measures the distribution of a polymer sample where $Đ$ is closer to 1, and the more closely M_N and M_w match one another, the more symmetric the distribution curve. A higher $Đ$ can be obtained for both step growth polymerization and chain growth polymerization, whereas living polymerization, a type of chain growth polymerization, yields polymers with $Đ$ closer to 1 and a uniform molecular weight distribution.[106]

The glass transition temperature (T_g) is a very important parameter when it comes to processing polymers for a specific end-use. Below T_g the elasticity of a polymer is low, and polymer molecules have poor relative mobility in a glassy or crystalline state. As the temperature increases to T_g, the polymer chains are able to move around the matrix, thus behaving like a rubbery material.[107] The polymers change drastically from hard and brittle to soft and pliable at T_g. T_g can be measured using several techniques, and the value depends on the strain rate and cooling or heating rate.

1.3.2 Block Copolymers

Block copolymers (BCPs) are made by covalently bonding two or more chemically distinct homopolymer chains. This type of copolymer has its own unique properties, which differ from random copolymers and homopolymers. The first synthetic BCP, in 1952, was poly(styrene-*block*-methyl methacrylate) (PS-*b*-PMMA),[108] which is a linear diblock copolymer (A-*b*-B). Since then, various BCPs have been produced owing to development of living-anionic polymerization,[109] living-cationic polymerization,[110] and living–radical polymerization.[111] BCPs have been applied as thermoplastic elastomers,[112–114] pressure sensitive hot-melt adhesives,[115,116] and drug delivery systems,[117] as well as nanopatterning applications,[118,119] and for development of porous membranes.[120–122]

Block copolymer architecture can be varied, depending on the number of blocks or homopolymers (diblock copolymer, triblock copolymer etc..) present and the way these blocks connect to each other, as shown in Figure 1.11. There can be hundreds of different BCPs commercially available, such as a simpler linear BCPs and star block copolymers.[123] A star block copolymer is formed by connecting a few linear BCPs to a common branch point, to cyclic BCPs. BCPs with precisely controlled molecular weights and defined architectures can be prepared owing to the advancement of polymer synthetic strategies and techniques.[124] In the following sections, discussions will focus mainly on simple linear diblock copolymers, and the term BCP will refer uniquely to linear diblock copolymers of the formula A-*b*-B.

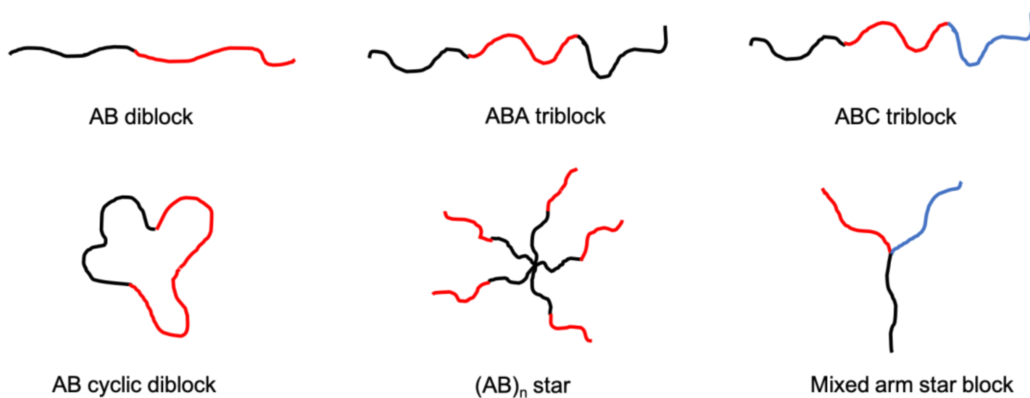

Figure 1.11. Common examples of block copolymer architectures.

1.3.2 Phase Behavior of BCPs - The Basis of Self-assembly

When the magnitude of the enthalpic contribution (generally positive and decreasing with temperature) to the free energy of mixing of the two species is greater than the magnitude of the entropic contribution (always negative and ideally independent of temperature), phase separation between two components occurs, thus minimizing unfavorable interactions between dissimilar species. For a mixture of two or more polymers, the entropy is reduced because of the covalent bonds between the monomers, which prevent the distribution of monomer units, leading to phase separation. However, in BCP, the covalent bonds between blocks prevent the macroscopic phase separation.

BCPs can undergo a microphase separation that leads to nano-scale ordered morphologies due to thermodynamic incompatibility between blocks. Even though microphase separation was identified in the 1960s by the observation of elastomeric properties of an ABA system,[113] the dimensions of these nanoscopic domains could not be identified by optical microscopy until the application of transmission electron microscopy (TEM) and small-angle X-ray scattering (SAXS) in the late 1960s.[126] A number of theories have been developed in order to explain the phase behavior of diblock copolymers in the bulk phase. The pioneering work on microdomain structure of ordered BCPs was developed by D.J. Meier, based on the competition between interfacial tension and chain stretching.[127] Later on, Helfand and co-workers used self-consistent field theory (SCFT) to study microphase separation.[128–131] Figure 1.12 shows the phase diagram of a diblock copolymer developed using SCFT.[125]

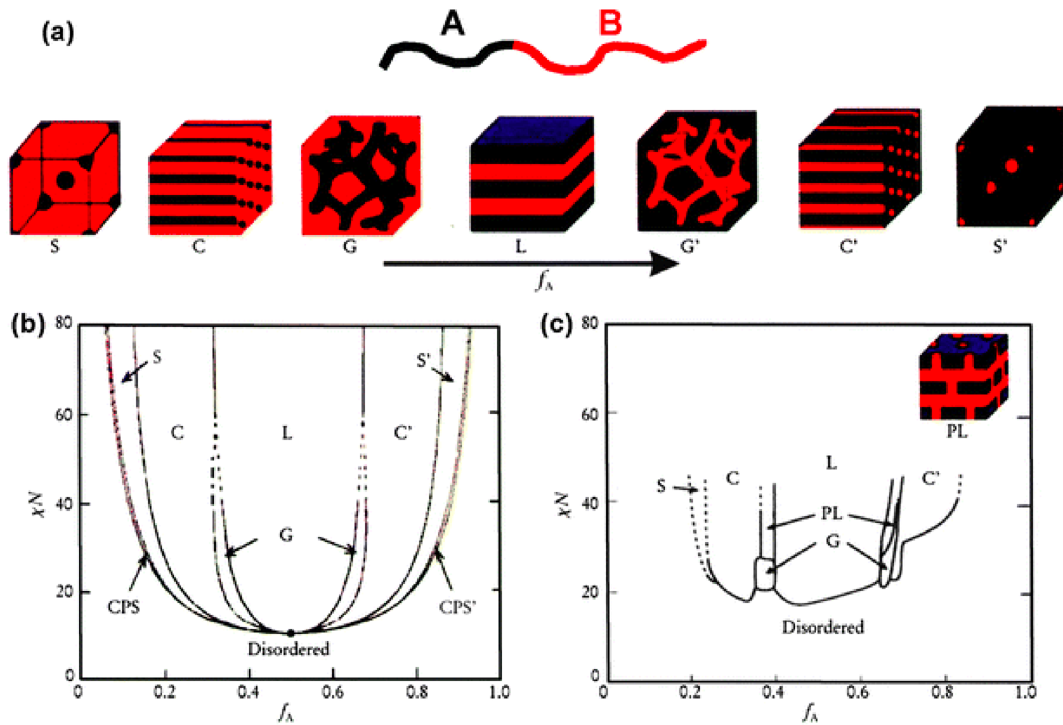

Figure 1.12. Diblock copolymer bulk phase behavior. (a) Schematic illustration of diblock copolymer equilibrium morphologies as a function of volume fraction of block A. (b) Theoretical phase diagram of diblock copolymer predicted by SCFT. (c) Experimental phase diagram of PS-*b*-PI. The phase diagram is from reference125 adapted with permission from the American Institute of Physics.

The microphase separation of the BCP in the bulk depends on the following three experimentally controlled parameters:

1. The total degree of polymerization,

$$N = N_A + N_B \quad \text{Eq. 1.6}$$

The degree of polymerization is the number of monomer units that make up a polymer chain, where N_A is the number of monomers (repeating units) in block A and N_B is the number of monomers (repeating units) in block B.

2. The volume fraction of the A and B blocks,

$$f_A + f_B = 1 \quad \text{Eq. 1.7}$$

$$f_A = \frac{N_A}{N} \quad \text{Eq. 1.8}$$

The volume fraction of a component can be controlled experimentally by changing the stoichiometry of the two blocks:

3. The Flory–Huggins interaction parameter, χ,[132,133]

$$\chi_{AB} = \left(\frac{z}{k_B T}\right)\left(\varepsilon_{AB} - \frac{1}{2}\left(\varepsilon_{AA} + \varepsilon_{BB}\right)\right) \qquad \text{Eq. 1.9}$$

The sign and the magnitude of the energy of mixing is approximated by the Flory–Huggins interaction parameter, where z is the number of nearest neighbors per repeating unit in the polymer, k_B is the Boltzmann constant, T is the temperature, and ε_{AA}, ε_{BB}, and ε_{AB} are the interaction energies per repeating units of A-A, B-B and A-B respectively.

The order–disorder transition (ODT) is a thermodynamic phase transition driven by an unfavorable mixing enthalpy coupled with a small mixing entropy. The segregation product, χN, determines the degree of microphase separation of diblocks. The incompatibility of the constituent blocks decreases with increasing temperature or decreasing χN. The y-axis of the theoretical phase diagram for a diblock copolymer is shown in Figure 1.12(b), and represents the χN as a function of the volume fraction of block A (f_A). When χN does not exceed 10, the entropic factor dominates, and the diblock copolymer is in a spatially homogeneous disordered state. There are two limiting regimes in the phase diagram: the weak segregation limit (WSL) and the strong segregation limit (SSL). In the WSL, where $\chi N = 10$, the interface becomes diffuse, and sharp phase boundaries between two phases are not visible since the segregation power is not strong enough. Increasing the χN further raises the ODT. When $\chi N > 100$ at the SSL, nearly pure domains can be observed with a narrow interface between them. The balance between minimization of interfacial free energy and the maximization of conformational entropy of the polymer chain under incompressible conditions determines the equilibrium domain spacing in the SSL and is given by:

$$d = a N^{\frac{2}{3}} \chi^{\frac{1}{6}} \qquad \text{Eq. 1.10}$$

where a is the statistical segment length of diblock copolymer. This equilibrium domain spacing at WSL is given by:[134]

$$d = N^{1/2} \chi^{0} \qquad \text{Eq. 1.11}$$

Above ODT for a fixed χN with increasing volume fraction of one block, the order-to-order transition (OOT) starts from closely packed spheres (CPS), which separates the disordered state and S phase, passing through body-centered cubic

spheres (S), hexagonally packed cylinders (C), and discontinuous gyroids (G), to lamellae (L), as shown in Figure 1.12(a). When the composition is inverted, a morphological inversion takes place (L→G'→C'→S'→CPS'→disordered), making the phase diagram have a mirror symmetry at $f_A = 0.5$. Figure 1.12(c) shows the experimental phase diagram developed for poly(styrene-*block*-isoprene) (PS-*b*-PI) by Khandpur and co-workers.[135] As shown in Figure 1.12(b) and (c), there is a qualitative similarity between the phase diagram calculated by SCFT and the experimental results. However, in the SCFT calculations, thermal concentration fluctuations were not included; thus, the ODT occurs at higher χN values than predicted, and the CPS phase was not observed experimentally. Hence, the experimental phase diagram is asymmetric in terms of volume fraction f.

Unlike in the bulk, the equilibrium morphologies of microphase separated block copolymers in thin films are influenced strongly by the film thickness, film air interface, substrate surface chemistry, and topography. The confinement and surface interactions in thin films are additional parameters for controlling the phase behavior of the BCPs and lead to a different and more complicated phase diagram compared to those of their bulk counterparts. There are numerous experimental and theoretical studies that have been carried out attempting to predict the phase diagram of BCPs in a thin film. The phase diagram of a diblock BCP confined between two identical preferential flat surfaces was investigated by Li and co-workers using SCFT, as shown in Figure 1.13.[136]

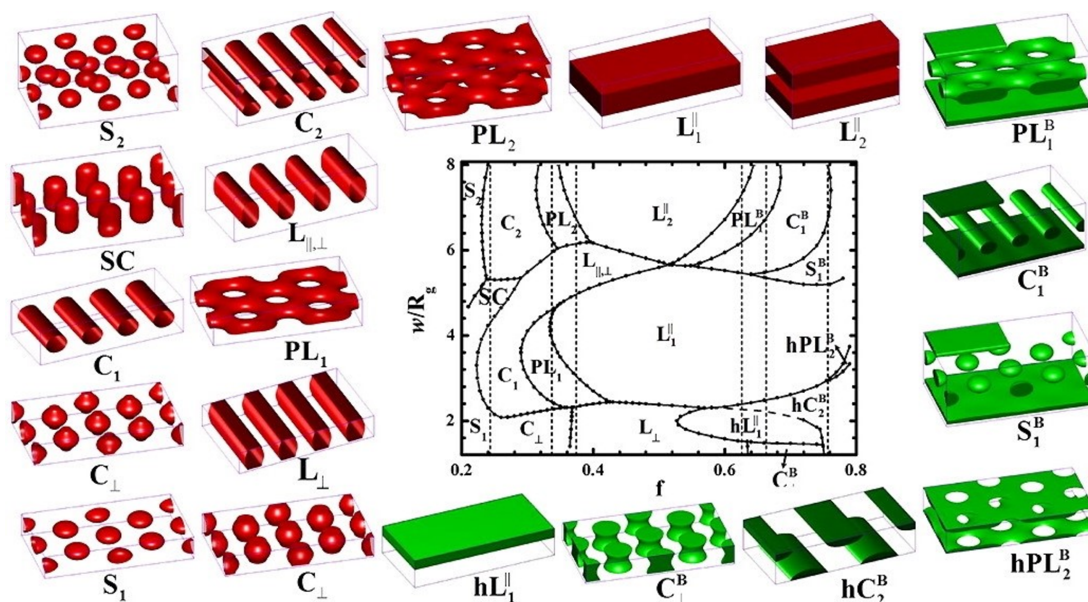

Figure 1.13. Theoretical phase diagram of AB diblock copolymer in a thin film, where χN is fixed at 20 as a function of volume fraction of A and film thickness w in the units of radius of gyration (R_g), and the resulting morphologies formed. Reprinted from reference 136 with permission from the American Chemical Society.

While keeping the interaction parameter (χN = 20) and the surface preference fixed, 20 different morphologies, including centrosymmetric and noncentrosymmetric morphologies, were observed by only changing the volume fraction and the film thickness. These morphologies can be categorized as sphere, cylinder, perforated lamellae (corresponding to the gyroid phase in bulk), and lamellae when the volume fraction varies from 0.2 to 0.8 and include even the bulk lamellae or bulk cylinder phase regions upon tuning the film thickness.

The affinity of each block to the different surfaces (air/substrate) can be different, leading to preferential wetting or neutral wetting of the blocks with the substrate and air interfaces. These wetting conditions can change the orientation of the domains on the substrate surface, as shown in Figure 1.14. In the symmetric wetting conditions, one of the blocks shows more affinity to both substrate and air interfaces, causing the lamellae to orient in-plane (horizontally) in the film. Likewise, when two blocks show opposite affinities to the substrate and air, asymmetric wetting conditions can be observed, leading to the same in-plane orientation to the substrate. Commensurability of the film thickness with the native domain spacing of the BCP is important in preferential wetting conditions. When both the blocks show similar

affinity to both air and substrate interfaces, the orientation of the lamellae domains is out-of-plane and there is no effect from the commensurability; thus, there is no limit to the film thickness.

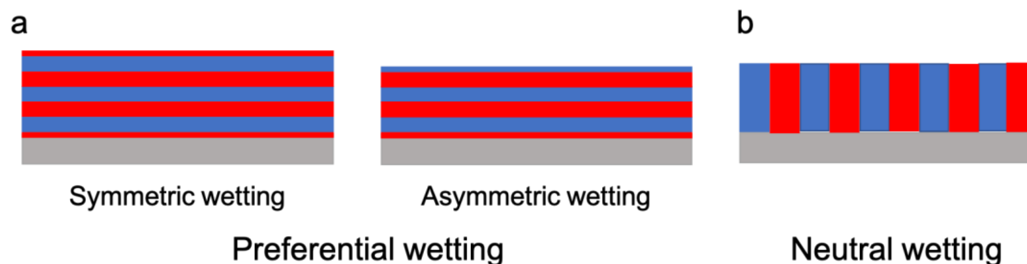

Figure 1.14. Schematic illustration of different surface affinities of lamellae forming AB diblock copolymers.

1.3.3 High χ BCPs

Feature sizes have reached the 20 nm and smaller length scale. In order to achieve these smaller feature sizes via self-assembly, one area of research is focused upon the development of high χ BCP materials, block copolymers with highly incompatible segments. The characteristic feature of these BCPs is that their polymer chains are relatively short (and thus their molecular weights are lower), and the two blocks are chemically very different, leading to the high χ parameter, consequently, a smaller pitch and higher density of features. This high χ value can compensate for a low N value so that χN still can be above 10.5 while annealing.

PS-*b*-PMMA is the most widely used BCP for patterning until these high χ BCPs were introduced due the availability, well-known properties, easy synthesis, and straightforward self-assembly by thermal annealing of PS-*b*-PMMA. The smallest achievable feature size from PS-*b*-PMMA is limited to about 18 nm[141] owing to a relatively low χ value. Furthermore, the absence of a definite interface between the features from PS-*b*-PMMA due to weak segregation of PS and PMMA domains can increase the line edge roughness, which can alter the morphology of nanopatterns after pattern transfer.[141] In fact, the pattern transfer process becomes more difficult since PMMA domains have to be removed by etching or chain scission in order to arrive at a lithographic mask. However, PS-*b*-PMMA still has been important in academic

research, such as fin field-electric transistors (FinFET) and random-access memory circuit patterns.[83,84,142]

Fully organic BCP in the absence of any metal or silicon also can achieve sub-10 nm features. Poly(styrene-*b*-vinylpyridine) (PS-*b*-PVP) is also a highly incompatible BCP owing to its hydrophobic PS block and hydrophilic PVP block, due to the strong polarization of the pyridine ring. PS and PVP monomers are structurally similar, except for the nitrogen in the aromatic ring structure of PVP. The properties of the two isomers, P2VP (ortho position) and P4VP (para position), where the position of the nitrogen in the pyridine changes, are significantly different from each other, including the χ values where P2VP is at least half of the χ of P4VP at 25 °C. This thesis will focus mainly on the use of PS-*b*-PDMS and PS-*b*-P2VP self-assembly process.

Silicone polymer-containing BCPs have intrinsically large χ values.[143] Flory–Huggins interaction parameters of some selected BCPs are given in Table 1.1. Polystyrene-*b*-polydimethylsiloxane (PS-*b*-PDMS) is one of the well-known, commercially available, and extensively used high χ BCPs, with a high degree of chemical incompatibility between the two blocks that is facilitated by the incorporation of both hydrocarbon and inorganic blocks.[144] This PDMS-containing block copolymer has the added advantage of higher contrast for pattern transfer to the substrate upon oxygen plasma etching.

Table 1.1. Flory-Huggins Interaction Parameters for Different Block Copolymers

Polymer	χ (25 °C)	Flory-Huggins χ (T)	Reference
PS-*b*-PMMA	0.043	$+0.028+3.9/T$	137
PS-*b*-PDMS	0.265	$+0.037+68/T$	138
PS-*b*-P2VP	0.178	$-0.33+63/T$	139
PS-*b*-P4VP	~0.300	_	140

1.4 Annealing

As-deposited thin films of a desired block copolymer are in a kinetically trapped non-equilibrium, disorganized state, as they are transferred from a solvent onto a substrate, coupled with fast solvent evaporation. Annealing is required to provide mobility to the entangled and trapped polymer chains to enable structural reorganization into an equilibrium pattern. Annealing not only enables plasticization so that the system may undergo self-assembly and nanoscale phase segregation, it also is also important for defect elimination.[145,146] Thermal annealing,[147–151] including microwave annealing[152–154] (with/without solvent), solvent vapor annealing,[155-158] and combinations of the two, called solvothermal annealing,[159,160] are the most widely used techniques to enable plasticization and nanoscale phase segregation towards an equilibrium structure. The main purpose of annealing is to facilitate chain mobility in order to speed up the structural organization into a reasonable time length. The other annealing techniques, such as laser annealing,[161-164] shear annealing,[165-166] and zone annealing, use basic principles of either or both of the thermal and solvent annealing techniques. The following sections will discuss the annealing techniques used in self-assembly of thin films of BCPs extensively.

1.4.1 Thermal Annealing

The basic mechanism of thermal annealing is to increase the polymer chain mobility significantly by simply heating the system above its glass transition temperature (T_g) and below the order–disorder transition temperature (T_{ODT}) for an extended period of time to enhance the polymer self-assembly.[65,66,167,168] It is important to heat a thin film of BCP uniformly in a controlled manner below its decomposition temperature in a vacuum or an inert gas atmosphere to avoid oxidation and decomposition and achieve the equilibrium morphology.[150,156] Thus, the conventional thermal annealing process can be carried out in a vacuum oven, a hot plate in an inert atmosphere glove box, or a tube furnace with either vacuum or an inert gas flow in the temperature range of 120 to 250 °C on the order of hours to days.[65,66,169,170] Furthermore, thermal annealing has the advantage of being compatible with the current semiconductor industry processes, such as spin casting, baking, and etching processes. The diffusivity ($D(T)$)

of a polymer above its T_g is inversely proportional to the time (t) and is given by the Arrhenius Equation where ΔE_a is the activation energy of the polymer, A is the Arrhenius constant, and R is the gas constant. At higher annealing temperatures, equilibrium morphologies can be achieved faster:

$$\frac{1}{t} \sim D(T) = A \exp\left(-\frac{\Delta E_a}{RT}\right) \qquad \text{Eq. 1.12}$$

From a practical perspective, an important resource for both commercial and research throughput is the time required for annealing. Microwave annealing is well-known for its rapid, non-classical heating, not only in domestic settings but also academic ones.[152-154,159,171] In 2010, Buriak and co-workers proposed that microwave annealing can be used to anneal a BCP thin film on Si wafers with or without a solvent.[152] The final morphology of the annealed BCP has fewer defects and reduces the annealing time considerably, to seconds/minutes. Similarly, Buriak and co-workers have investigated the mechanism of microwave annealing and determined that it is the silicon substrate responsible for the rapid heating and not the solvent or BCP,[153] as shown in Figure 1.15(a). The Morris group microwave annealed PS-*b*-PDMS and PS-*b*-PMMA without any use of solvent, and the annealing process was compatible with graphoepitaxy in the case of PS-*b*-PDMS to achieve long-range translational alignment along the topographic pattern.[171] Recently Kim and co-workers used a fast (~3 min) solvo-microwave annealing process to get highly ordered crystalline nanostructures from conjugated polymer based BCP.[172] The incompatibility between the ordered nanostructured and the conjugated polymer results in a comparatively longer annealing time (24 h) via conventional thermal annealing.

In contrast to uniformly heating BCP thin films as in conventional thermal annealing, zone annealing[173-176] uses a directional ordering (hot or cold zone annealing) or orientation dependent growth kinetics due to a thermal gradient, as shown in Figure 1.15(b). This zone annealing was applied first by Hashimoto and co-workers to a lamellae forming BCP polystyrene-*b*-polyisoprene (PS-*b*-PI), where heating and cooling across T_{ODT} was carried out.[173,174] Larger lamellae microdomains were produced parallel to the gradient direction, and their work into the mechanism revealed initial surface-induced ordering, which would propagate from ordered to disordered

regions on passage through the zone. Cold zone annealing was introduced by Karim and co-workers for high χ/high molecular weight BCPs, where T_{ODT} cannot be achieved without degrading the polymer.[175] In cold zone annealing, BCP is locally heated above its T_g and below T_{ODT}. Zone annealing can be performed with already available common equipment to control the temperature, and it is compatible with roll-to-roll printing allowing large area processing.

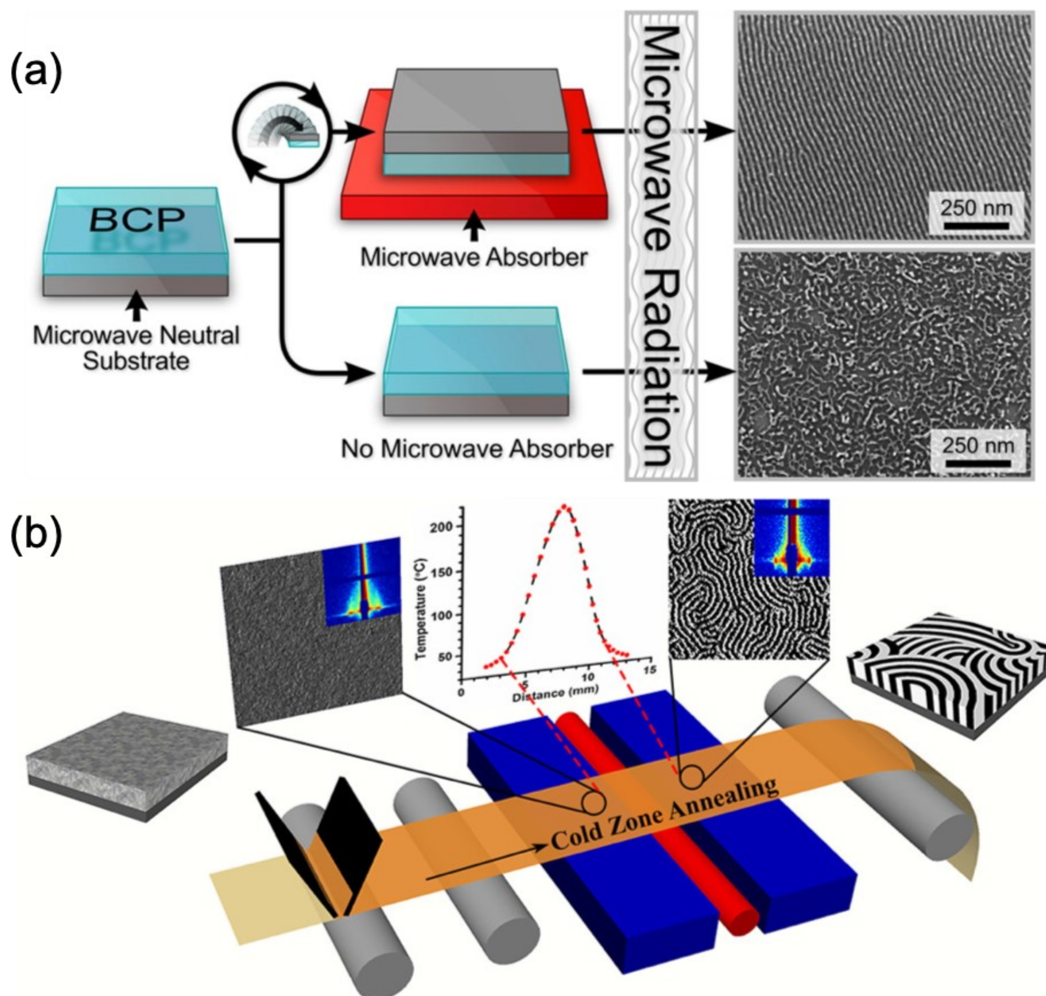

Figure 1.15. Thermal annealing methods of block copolymer thin films. (a) Scheme of the effect of a microwave absorber on self-assembly of PS-*b*-P2VP via microwave annealing. Image is from reference 153 and is reprinted with permission from the American Chemical Society. (b) Schematic representation of cold zone annealing with sharp thermal gradient of PS-*b*-PMMA as cast disordered thin film (left) and vertically ordered lamellae (right). The figure is from reference 176 and is reprinted with permission from the American Chemical Society.

Even though it is compatible with the existing integrated circuit manufacturing processes, it is sometimes problematic for high χ or high molecular weight block

copolymers, as higher annealing temperatures and longer times are required to increase chain mobility, which can result in thermal decomposition of the polymer[177-179] and a higher thermal budget.[156,178,180] Other approaches, including solvent vapor annealing, enables annealing either at room temperature or in conjunction with heating to arrive more rapidly at a range of morphologies in annealing times of a few minutes or less.[155,178,180]

1.4.2 Solvent Annealing

Solvent annealing was introduced to anneal BCP thin films by Thomas and co-workers in 1998.[181] They observed a significant improvement in the order of the cylindrical and lamellar morphologies of annealed polystyrene-*b*-polybutadiene-*b*-polystyrene (PS-*b*-PB-*b*-PS) triBCP solvent compared to the thermal annealed patterns. The general concept of solvent annealing involves exposing a thin film of BCP to a solvent, and polymer chain mobility is induced without degrading the polymer. The Hildebrand solubility parameter (δ) is a good way to measure the interaction between two species, such as polymer and a solvent; this is defined as the square root of the cohesive energy where, ΔH_v is enthalpy change through vaporization, R is gas constant, T is temperature and V_m is molar volume.

$$\delta = \sqrt{\frac{\Delta H_v - RT}{V_m}} \qquad \text{Eq. 1.13}$$

If the Hilderbrand solubility parameter of the solvent is closer to either one or both blocks in the BCP, it often is termed a ‘good solvent’, and it is expected that the solvent molecules will act as plasticizers when absorbed. The ‘good solvent’ thus swells the BCP film and leads to an increase in film thickness, depending upon how much solvent has been absorbed.

Solvent annealing is more complicated than thermal annealing due to the increased number of variables (See Figure 1.16). First, the solvent swells the BCP film, effectively reducing the T_g and significantly increasing the chain mobility. Second, the solvent absorbed within the film can shield either one or both blocks of the BCP, leading to a decrease of the interaction parameter ($\chi_{eff} = \chi(1-f)$, where f is the volume fraction of the solvent in the swollen film) and varying (increase, decrease or no

change) the effective volume fraction of the blocks in the swollen film. Third, the solvent incorporation in the film can alter the surface free energies of polymer–substrate and polymer–air to change the preferential wetting of the blocks with the free surfaces. Fourth, solvent interactions with the substrate can minimize the undesirable interaction between polymer–substrate, leading to film dewetting. Finally, due to changes in the interaction parameter χ, the previously established film thickness commensurability conditions are altered, resulting in a new pitch ($L_o \propto (\chi_{eff})^{1/6}$), which is different from the native pitch.

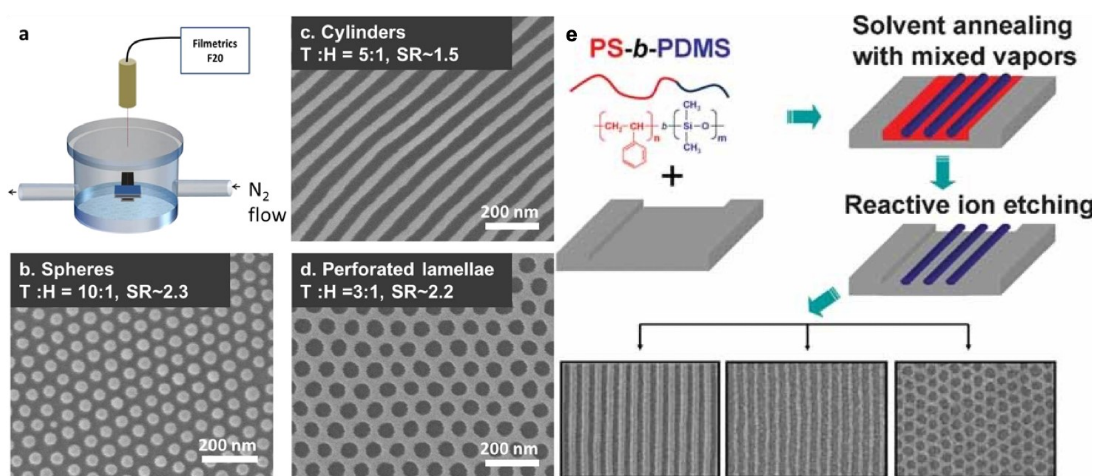

Figure 1.15. (a) Controlled solvent vapor annealing using nitrogen inlet and outlet. (b-d) SEM micrographs of silica nanostructures formed by PS-*b*-PDMS with different solvent annealing conditions with corresponding toluene:hexane (T:H) and swelling ratios (SR). Adopted from reference 182 with permission from IOP Publishing. (e) Schematic representation of processing steps for DSA of cylinder forming PS-*b*-PDMS on topographically patterned substrate annealed using mixed solvent vapors and SEM micrographs of resulting patterns. Image is from reference 183 and is reprinted with permission from Wiley-VCH.

Generally, a solvent annealing process occurs in three,[184] two,[185] or one[186,187] stage(s). First, a thin film of BCP absorbs the solvent, and the film swells in an atmosphere of solvent at temperatures typically well below the bulk T_g of both blocks. Secondly, the solvent concentration in the film reaches equilibrium. Finally, the thin film is dried by removing the solvent by a rapid and nonequilibrium process. There should be great control over each step in order to achieve the highest degree of structural order in a microphase-separated film. The lack of a standard annealing apparatus or set up is a major drawback for solvent vapor annealing to control the SVA process, which may affect the final microstructure and the defect density crucially.

Hence, poor reproducibility and difficulties in comparison of results become challenging. Various solvent vapor annealing apparati[157,188] have been developed for this purpose and this will be further discussed in Chapter 2.

1.4.3 New Trends in Annealing

In the early days of DSA using BCPs, there was much work in examining both the mechanism and design of systems to enhance lateral ordering with lower defects and faster annealing processes. The attention in the DSA research gained several new annealing techniques, such as laser,[162-164] shear,[165] electric field,[189-192] and magnetic field[193–195] annealing as alternative annealing techniques.

BCPs with high interaction parameters are used to decrease the feature size to as small as 10 nm. Thus, orientating and achieving long range order of such BCPs are challenging due to considerable dissimilarities of surface energies of the blocks. As solutions, synthesis of high χ BCPs with similar surface energy blocks[196-198] or an application of a top coat[199-201] to alter the surface energies of the block are being considered. Generally, a top coat is composed of a random copolymer of the constituent monomers of the BCP. However, it is difficult to spin-cast a random copolymer from a solvent on top of the BCP film without dissolving or swelling the underlying BCP film. Willson and co-workers reported a top coat soluble in water that can be deposited on a BCP film soluble in organic solvents; this is subsequently removed after DSA.[200] The resulting patterns are shown in Figure 1.17(a). Limitations of this process include the number of processing steps and the inability to use with water soluble BCPs containing huge difference in polarities of the blocks.[199] To overcome such difficulties, Nealy and co-workers proposed to deposit a topcoat from the vapor phase.[199] Initiated chemical vapor deposition (iCVD) was used to deposit a topcoat, which can be grafted to the as spun disordered BCP film as in the schematic shown in Figure 1.17(b). Since the grafted BCP topcoat has similar interfacial energy as the underlying BCP thin film, the pattern was transferred successfully to the Si substrate without removing the topcoat.

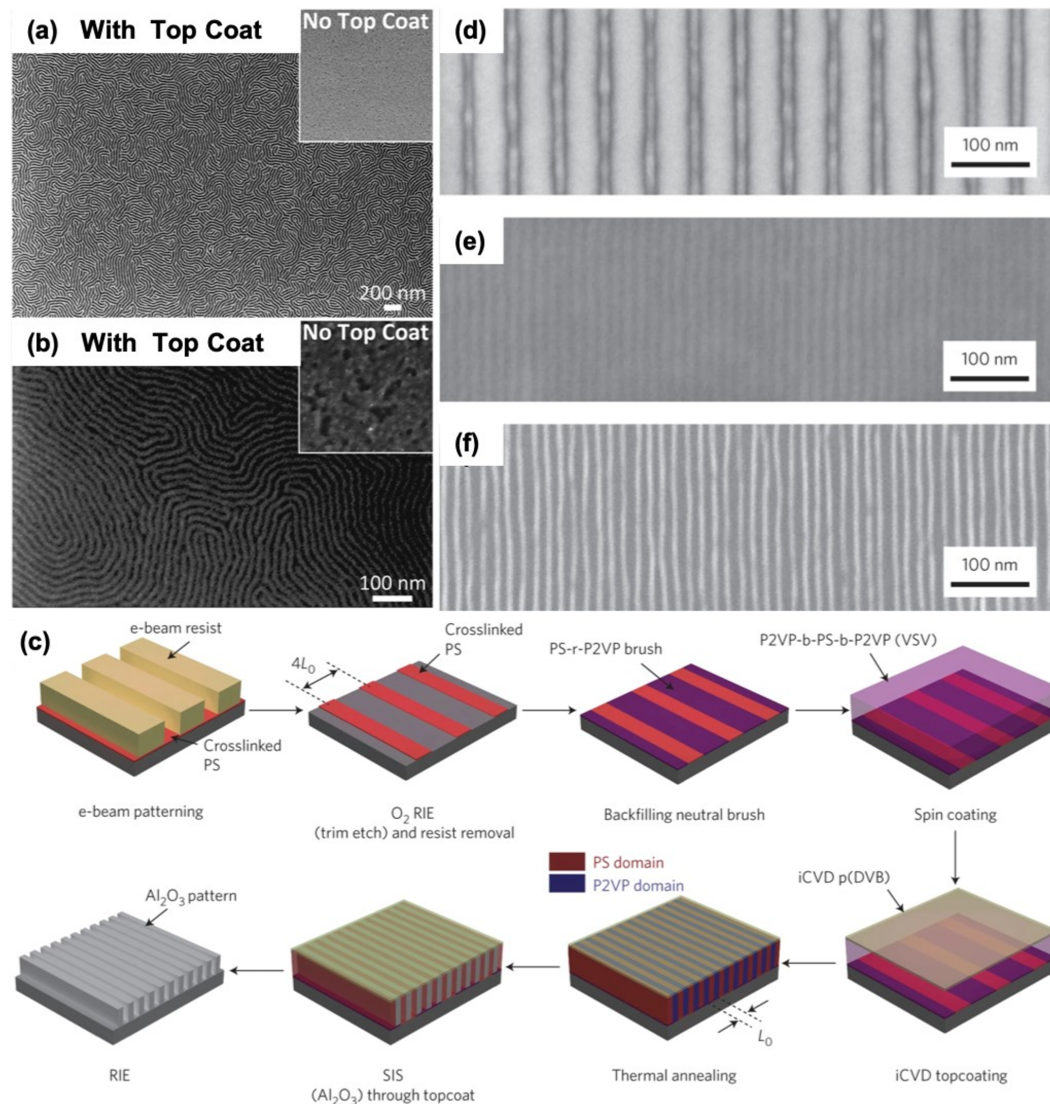

Figure 1.16. Scanning electron micrographs of (a) Poly(styrene-*b*-trimethylsilylstyrene-*b*-styrene) (PS-*b*-PTMSS-*b*-PS) with a water soluble topcoat after thermal annealing. Inset is without the topcoat. (b) Poly(trimethylsilylstyrene-*b*-d,l-lactide) (PTMSS-*b*-PLA) topcoat after thermal annealing. Inset is without topcoat. The images are from reference 200. Copyright American Association for Advancement of Science. (c) Process flow of DSA with BCP using chemoepitaxy and topcoat via iCVD. (d-f) SEM micrographs of (d) e-beam resist pattern after trim etch (e) DSA pattern after sequential infiltration and synthesis and removal of the topcoat with reactive ion etching (RIE). (f) Alumina line/space pattern after removal of organic components by RIE. Image is from reference 199 with permission of the Nature Publishing Group.

1.5 Applications of BCP Based Nanopatterning

There are many well-known applications of block copolymers in bulk phase, such as drug delivery[202-205] to structural materials,[206-208] and this section will focus on applications of block copolymer in thin films. As described earlier, DSA is a high-

resolution and cost-effective patterning technique that can produce feature sizes <10 nm, particularly when combined with other lithographic techniques. So far, DSA of BCPs has been used to fabricate numerous patterns that can be used for fin field effect transistors (FinFETs)[83,84,209] and memory devices.[210,211]

1.5.1 FinFET Fabrication

The first finFET was invented in 2001 to fulfill the requirement of device scaling and performance enhancement.[209] Arrays of high-density lines and spaces can be formed using DSA with BCP that are used in finFET patterns. These arrays of high density lines and spaces can be smaller than the resolution limit by the current patterning approaches used in photolithography.[84,85] Fin fabrication using DSA can utilize both chemoepitaxy[84] and graphoepitaxy[83] to improve the pattern quality by reducing the line edge roughness (LER). Corliss and co-workers have shown a complete process of chemoepitaxy based DSA for 7 nm fin fabrication, as shown in Figure 1.18(b). A comparison between finFET formation by DSA and self-aligned quadruple patterning (SAQP) was carried out using a fully integrated 'research 7 nm' finFET test vehicle in a 300 mm research lab. Even though there were minor structural dissimilarities between DSA and SAQP finFETs, the performance of the devices was associated statistically with the structural differences. Graphoepitaxy was used by Tsai et al. to form 29 nm pitch fins using PS-*b*-PMMA, Figure 1.18(a). A PS-*b*-PMMA thin film was deposited on a silica guiding pattern that had been fabricated using EBL and then thermally annealed. DSA has demonstrated its capabilities in dense line/space patterning, and DSA can achieve sub-10 nm patterning when combined with other nanopatterning techniques, such as EUV and EBL.

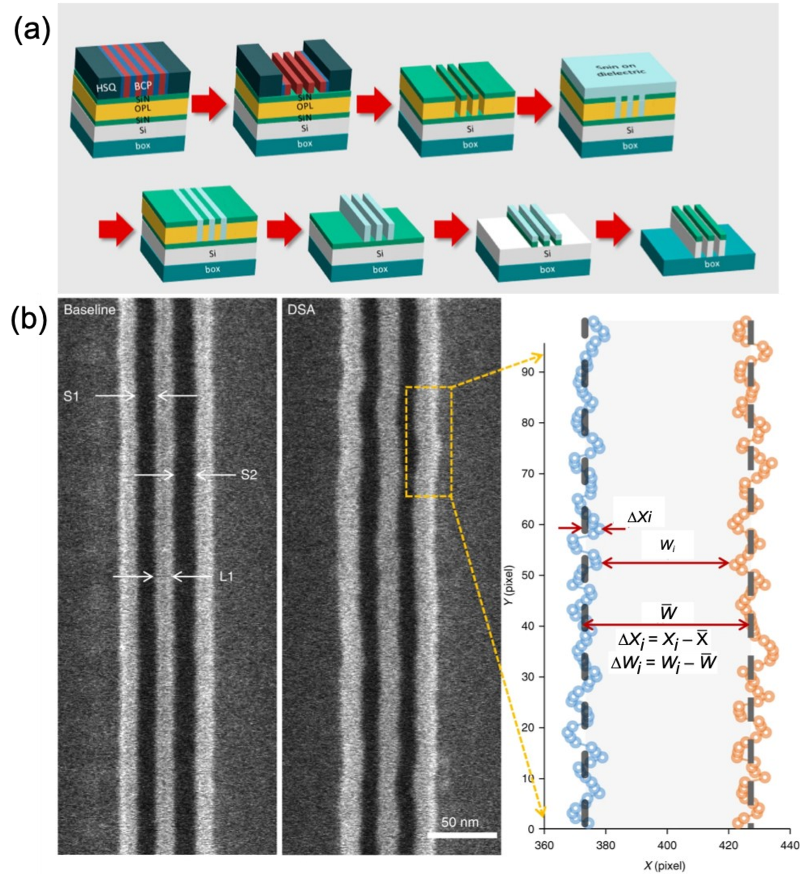

Figure 1.17. Fin formation by PS-*b*-PMMA. (a) Process flow diagram of graphoepitaxy based fiFET fabrication. Reprinted from reference 82. American Chemical Society. (b) Comparison of pattern quality between self-aligned quadruple patterning (SAQP-baseline) and DSA-based finFET fabrication. Reprinted from reference 83 Nature Publishing Group.

1.5.2 Bit-patterned Media Fabrication

Magnetic grains within the magnetic film are used to store data in conventional hard disk drives. The reality, however, is that the data storage is limited since dozens of magnetic grains are required to store a single bit of data. Hence, bit-patterned media (BPM) is proposed as a potential solution for increasing the storage capacity of future hard disk drives (300 Tb/in^2).[212] However, existing nanopatterning techniques, such as EBL, are either expensive or time consuming for fabrication of BPM.[213] In contrast, DSA of BCPs is an excellent technique for patterning sub-10 nm resolution in the manufacturing of high-density storage units; therefore, it has been the subject of research by industry leaders, such as Seagate,[86,214] Hitachi,[215,216] and IBM[210,211,217] in the early efforts of DSA for BPM patterning using cylinder or sphere forming BCPs to directly pattern the magnetic thin film.[218]

Integrated templates with both servo and data zone were fabricated by Kao's group using two different BCPs, cylinder forming PS-*b*-PMMA and sphere forming PS-*b*-PDMS, as shown in Figure 1.19(B-E).[86] Nanoimprint lithography was used to create the pre–pattern for DSA. Bit–patterned media with a theoretical capacity of 5 Tb/in^2 were fabricated. One challenge with densely packed arrays of nanodots for bit-patterned media pattern fabrication is that the read–write head should be smaller than the track width to ensure correct reading and writing. Rectangular shaped bit arrays elongated along the cross-track direction were proposed as a solution for the problem. Nealy and co-workers used a lamellae forming high χ triblock copolymer, P2VP-*b*-PS-*b*-P2VP, on an e-beam guiding pattern.[219] The complete rectangular bit pattern was obtained by overlapping two bit-patterned media templates, one with a circumferential pattern and the other with a radial pattern as shown in Figure 1.19(A).

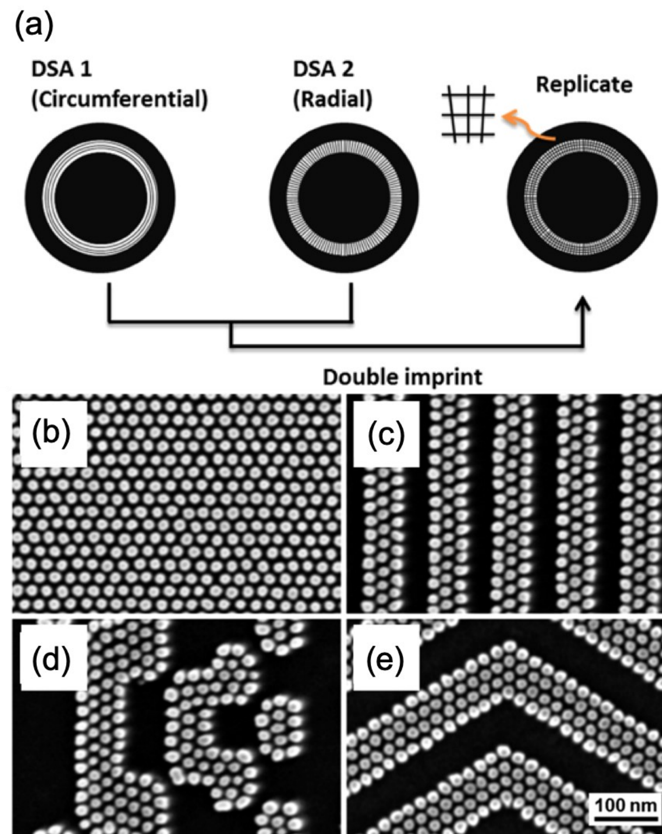

Figure 1.18. (a) Using double imprinting to create rectangular bits by intersecting circumferential and radial line space patterns. Reprinted from reference 219 with permission from IOP publishing. (b-e) SEM micrographs of bit media patterns from DSA of PS-*b*-PDMS on nanoimprint template. Images are from reference 86 with permission from the American Chemical Society.

1.6 Scope of the Thesis

Directed self-assembly, DSA, a combination of block copolymer self-assembly with top-down lithographic approaches, has been the focus of a great deal of research attention as a promising nanolithography that addresses the limitations of other lithographic techniques, from physical limits to cost. This chapter sets the background for the thesis in order to provide a broad overview of nanopatterning in general and to set the stage for block copolymer directed self-assembly-based nanolithography. This thesis contains altogether five chapters.

DSA achieves high resolution patterning via a self-assembly of polymers to yield a wide range of morphologies, including spheres, cylinders, lamellar structures, and gyroids. The development of high χ BCPs further increases the patterning resolution of DSA at a reduced level of defectivity. The defectivity of the patterns is a critical metric, thus, precisely controlling, and understanding the processing conditions, in particular the annealing step, is absolutely necessary. Chapter 2 discusses the optimization of the process parameters related to block copolymer self-assembly via solvent annealing using machine learning approaches and analyzes the defect densities related to the process.

In most lithography applications, thin films of self-assembled BCP serve as sacrificial masks or templates, and the resulting pattern is transferred to the underlying substrate for device fabrication. A widely used method for pattern transfer of block copolymer self-assembly is reactive ion etching or dry etching. In Chapter 3, the effect of reactive ion etching on thin films of PS-*b*-P2VP metalized with different metal ions to improve the etching contrast is discussed.

Density multiplication of BCP self-assembly via sequential annealing of incommensurate BCP films of PS-*b*-PDMS can form an enormous array of highly complex Moiré superstructures. While providing insights into commensurate and incommensurate boundary conditions for BCP self-assembly, the application of the resulting Moiré superstructures is not clear. In Chapter 4, incommensurate self-assembly of block copolymers with mixed metal nanopatterns and their tunable optical properties are investigated and discussed for possible photonic applications.

Finally, Chapter 5 provides a summary of the thesis as well as the conclusions and possible future research directions related to BCP self-assembly.

CHAPTER 2

Machine Learning Approaches for Solvent Vapor Annealing Process Control [a]

2.1 Introduction

In this chapter, a solvent vapor annealing (SVA) flow-controlled system combined with Design of Experiments (DOE) and machine learning (ML) approaches are used to characterize and quantify the defects, at various length scales, within the resulting patterns from block copolymer self-assembly.[158] The SVA flow-controlled system enables precise optimization of the conditions of self-assembly of the high Flory–Huggins interaction parameter (χ) hexagonal dot array-forming block copolymer (BCP), PS-*b*-PDMS.[155] The defectivity of the resulting nanopatterns remains too high for many applications in microelectronics and is exacerbated by small variations of processing parameters, such as film thickness and fluctuations of solvent vapor pressure and temperature, among others.[91,220–224] These parameters also significantly contribute to the quality of the resulting pattern with respect to grain coarsening as well as the formation of different macroscale phases (single and double layers and wetting layers).[155,225–229] Then, the results of qualitative and quantitative defect analyses are compiled into a single figure of merit (FOM) and are mapped across the experimental parameter space using ML approaches, which enable identification of the narrow region of optimum conditions for solvent vapor annealing (SVA) for a given BCP.

The ideal defect free line pattern generated from a cylinder or lamellar forming BCP should consist of straight lines extending across the entire substrate surface without any disruption, with the assumption that topological defects are not present. The defects seen in a two-dimensional line pattern can be simplified to junctions, terminational points, and dots, shown in Figure 2.1.[224]

[a] "The content of this chapter is adapted from the following publication Ginige, G.; Song, Y.; Olsen, B. C.; Luber, E. J.; Yavuz, C. T.; Buriak, J. M. Solvent Vapor Annealing, Defect Analysis, and Optimization of Self-Assembly of Block Copolymers Using Machine Learning Approaches. *ACS Appl. Mater. Interfaces* **2021**, *13* (24), 28639–28649. https://doi.org/10.1021/acsami.1c05056."

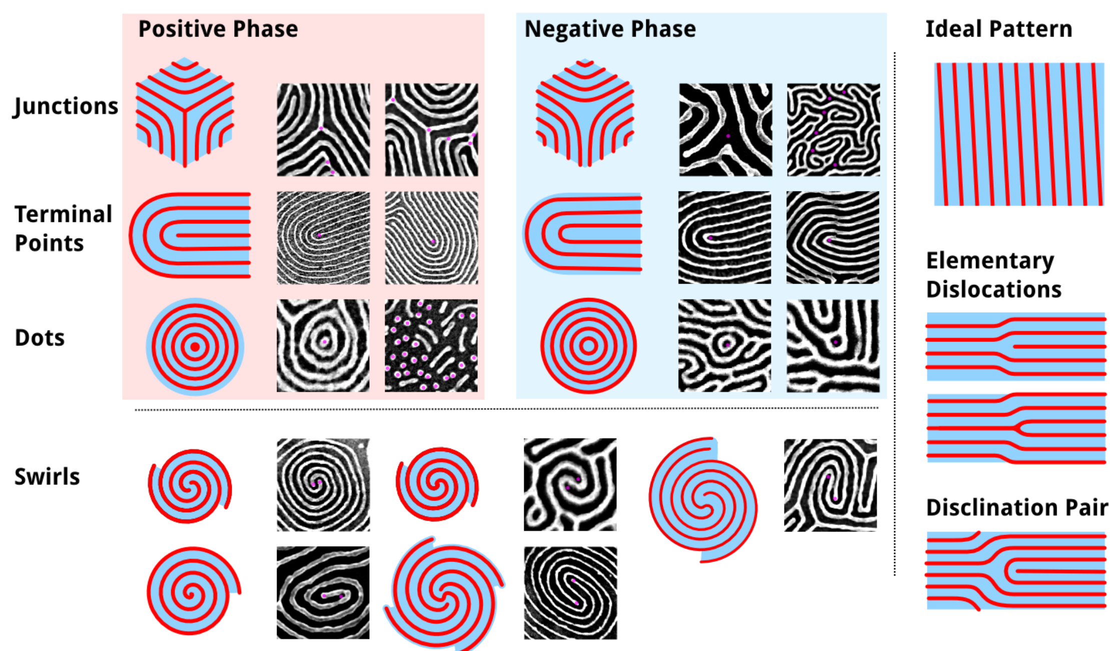

Figure 2.1. Topological defects found in line patterns generated from BCP PS-*b*-P2VP self-assembly. The positive phase is the P2VP block and the negative phase is the PS block. The image is from reference 224 with permission from the Public Library of Science.

2.2 Apparatus for Solvent Vapor Annealing

As discussed in Chapter 1, the majority of high χ BCP-based nanopatterning relies on solvent vapor annealing due to its fast processing times compared to thermal annealing and to not contributing to the thermal budget.[155,229,230] The SVA process is used widely and is capable of forming long-range order nanoscale morphologies, even though a broad understanding of the practice is not established completely. Much of the research on directed self-assembly (DSA) has been carried out in static, non-standardized annealing systems that lack in–situ monitoring of film thickness and dewetting, as shown in Figure 2.2.[155,231] The lack of a standard annealing apparatus or setup is a major drawback for solvent vapor annealing to control the SVA process, which plays a critical role in the self-assembly of the final microstructure, which includes defect formation and annihilation. Hence, comparison of results from one group to another is challenging due to lack of standardization.

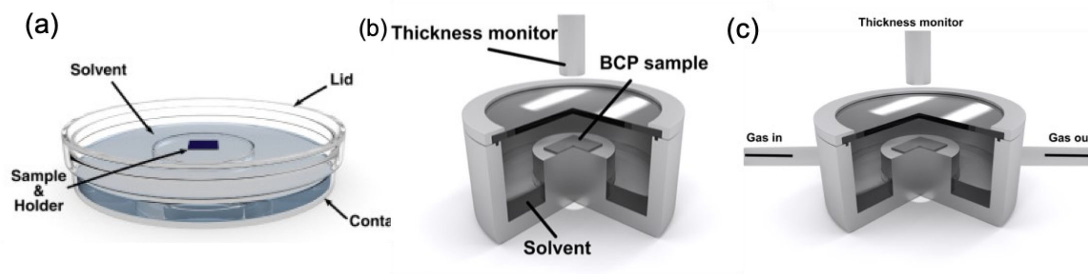

Figure 2.2. Examples of general solvent vapor annealing apparatus. (a) “Jar” annealing using a Petri box. Schematic is from reference 232 with permission of Elsevier. (b) Static solvent vapor apparatus, and (c) static solvent vapor apparatus with gas flow. Adapted from reference 155 with permission from the American Chemical Society.

The most basic setup used for solvent annealing is a sealed chamber with a solvent reservoir and the sample of a thin film of BCP on a substrate. The entire system is kept at room temperature and there are no additional controls over temperature. This is known as static or “jar” annealing, which can be used to produce self-assembled thin films of BCPs in an effective way. The early examples of static annealing used either a beaker or crystallization dish with flat glass cover or a desiccator with a sample exposed to a vial of solvent, as in Figure 2.2(a).[232] The next general family of static annealing apparatus used a custom-designed chamber with a transparent window. In–situ ellipsometry or reflectometry was used through the glass window to monitor the film thickness during the annealing process, as shown in Figure 2.2(b).[155] The swelling rate and final degree of swelling depend on the volume of the annealing chamber, surface area of the solvent reservoir, and possible leakage of solvent vapor from the annealing chamber. The major drawbacks of this type of annealing apparatus include difficulty in controling over the swelling rate during annealing and precise reproducibility, as the solvent vapor pressure depends on the humidity and the temperature of the room.

The next general family of annealing apparatus also consists of a static annealing chamber attached to an inert gas flow to control the solvent vapor pressure inside the chamber, as shown in Figure 2.2(c).[178] Hence, there is a great control over both the swelling and, in particular, the deswelling processes. The degree of swelling is defined as the film thickness ratio between the swollen and initial samples and is an important parameter with respect to the final morphology attained by the annealing. For general static annealing after reaching the desired swelling degree, deswelling is

carried out by simply opening the chamber lid and releasing the solvent vapor to trap the self-assembled structure kinetically. However, in this case, deswelling is controlled by purging inert gases at different flow rates in the second-general annealing apparatus.

A sophisticated family of solvent vapor annealing apparatus includes a flow control, a purge line, and in–situ film thickness monitoring. The swelling degree can be controlled greatly by managing the solvent flow, and highly reproducible results can be obtained.[155,231,233–236] Ellipsometry and reflectometry provide useful information when collected in–situ during the solvent annealing process, in addition to data regarding the swelling degree as a measure of swollen film thickness. The assumption of uniform film thickness over large areas (hundreds of micrometers) is important when using these techniques that measure thickness, as they analyze over large areas; thus, they represent an average over that area. However, dewetting and terrace formation during the annealing process of the film can occur, leading to regions of different microstructures with different thicknesses, as shown in Figure 2.3.[227] This formation of terrace phases and dewetting disturbs the long range order of the resulting pattern and increases the defect density, discussed further in this chapter.[155,227,237,238] Hence, an average or effective thickness over a large area is estimated by ellipsometry, reflectometry, or other non-mapping techniques, as these dewetted areas and terraces are averaged over the entire thickness of the film.

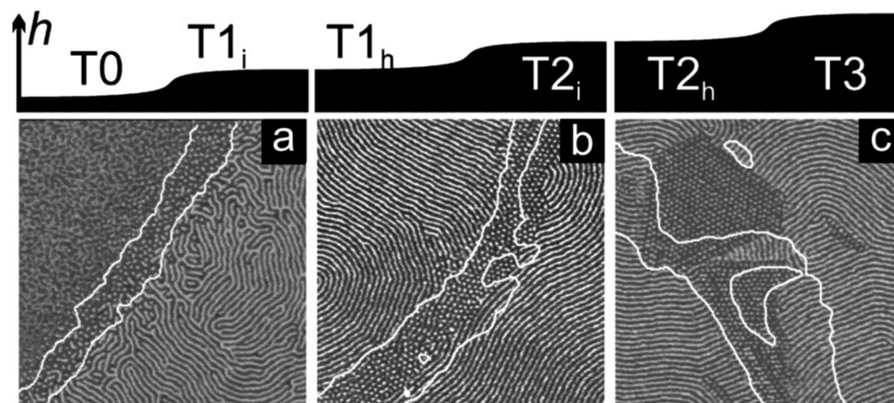

Figure 2.3. Profile and plan view of terraced phases of a thin film of PS-*b*-PB-*b*-PS with 14k-73k-15k molecular weight. (a-c) AFM phase images of BCP thin films with different morphologies in areas of varying initial film thickness (by varying polymer concentration) after annealing. White lines are contour lines. All the images are 2 × 2 μm^2. Adapted from reference 227 with permission of the American Physical Institute.

To enable a better degree of reproducibility, use of a feedback control linking the swelling degree to the solvent vapor flow has been developed. For instance, Buriak and co-workers developed a solvent vapor flow annealing apparatus with precise control over the swelling degree using a feedback control between in situ film thickness monitoring via laser reflectometry and solvent vapor flow, with external optical microscopy monitoring, as shown in Figure 2.4.[155] This combination of in–situ optical microscopy and laser reflectometry enables investigation of solvent vapor annealing of block copolymer thin films at both the millimeter scale (lateral) and nanometer-scale thickness. A similar apparatus has been developed by other groups, including the groups of Ross,[231] Ober,[233,235] Mokarian-Tabari,[236] and several others.[188,234,239]

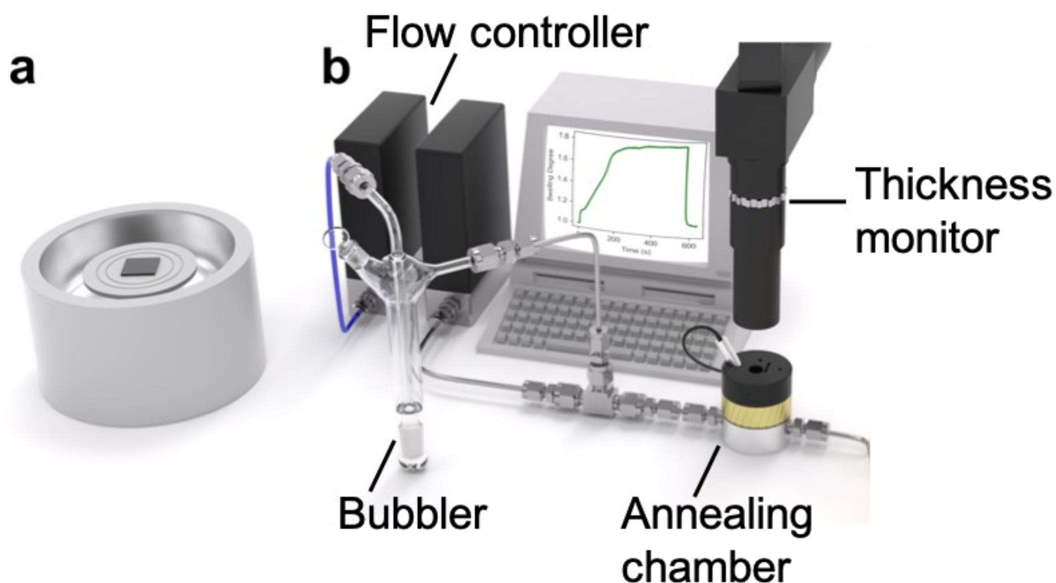

Figure 2.4. (a) The pre-annealed BCP film spin-coated onto silicon, locking in the initial film thickness. (b) Solvent vapor annealing (SVA) to a predetermined swelling degree (SD) using a feedback-controlled annealing system. Adapted from reference 158 with permission of the American Chemical Society.

Lithography multiplication via DSA reduces the defect density, as chemical and morphological features on the surface help to guide the BCP into the lowest energy equilibrium patterns.[220,240,241] For example, Nealy and co-workers investigated the complete defectivity information under various annealing conditions for a kinetic study of chemoepitaxy DSA in a 300 mm wafer fab, as shown in Figure 2.5.[242] Kim et al. used a photo-patterned surface to align BCP with low defectivity levels, where the

materials and techniques used can be adapted to a complex custom pattern for microelectronic devices.[241] Significant progress has been made in recent years, where the defectivity of DSA is now considered within tolerance when combined with using extreme UV (EUV) or e-beam lithography.[243] However, there is still a pressing need to reduce the defectivity of unguided BCP films, as this would allow for the fabrication of larger spacings between guiding patterns and greatly reduce the cost and demands of the lithographic step. Moreover, defects still remain a challenge, however, particularly with smaller molecular weight BCPs with a high Flory–Huggins interaction parameter (χ) that produce the sub-20 nm periodicities[199,241,244] and features.[245]

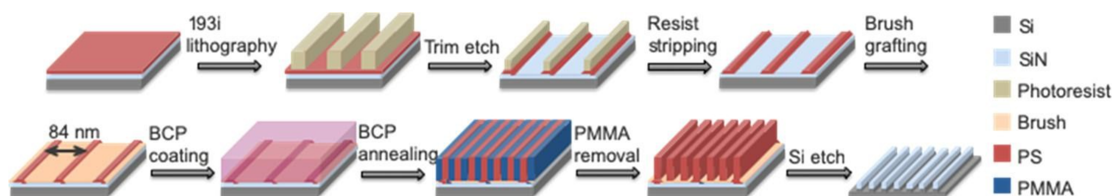

Figure 2.5. Schematic representation of the chemoepitaxy DSA process used to study the kinetics of the defect annihilation. The schematic is from reference 242 with permission from the American Chemical Society.

To achieve the desired nanopattern via self-assembly, not only are the annealing parameters critical, but the initial thickness of the applied BCP monolayer must be precise, typically within one or two nanometers.[246-251] The ideal thickness for a given BCP is unique and depends upon the composition of the BCP and factors such as surface functionalization and energy, the use of a topcoat, and other factors.[199,220,240,241,248,252] Both experimental and computational results strongly link the initial film thickness with the resulting self-assembled structure and persistent defects.[221,227,253] Small fluctuations of thickness within a monolayer film can lead to different self-assembled structures, as unfavorably thin domain thicknesses frustrate packing due to the buildup of strain.[91,227] Periodicity of structures formed from self-assembled BCP nanopatterns may be dependent upon film thickness and other processing parameters, as has been recently shown with bottlebrush BCPs.[247,254]

2.3 Design of Experiment and Machine Learning

Hexagonal dot-based nanopatterns are of interest for memory materials and devices, as these devices are more tolerant of hexagonal patterned defects than linear patterns for CMOS (e.g., vias), and thus the route towards commercialization appears more direct.[243] “Further improvement of process-friendly techniques”[243] is, however, still required, particularly over large areas. With the optimization of self-assembly of any new BCP, particularly high BCPs that may be challenging due to long-lived metastable defects or any change in processing conditions, annealing parameters will need to be re-evaluated. Empirical optimization of annealing of BCP films is time-consuming and, if not rationally devised, will sample variable space incompletely.[255,256] Hence, machine learning algorithms are a powerful tool for problem solving where large parameter spaces are involved.[257] Machine learning also has been applied in block copolymer self-assembly in order to determine the equilibrium phase behavior by simulations[258] or to optimize the chemical templates for DSA.[259,260] Ross and co-workers applied machine learning tools to investigate the interplay of solvent annealing parameters, such as initial thickness, swelling, time, solvent ratio, and to predict the effect on final morphology and defectivity.[261]

The typical way to confirm the roles of different factors that lead to the observed results is to change one variable at a time in academic laboratories. This method is called one factor/variable at a time (OFAT/OVAT). It is a slow process and has difficulty in finding the optima as the number of variable testing is increased in an experiment.[262] The experimentalist can sample a large multidimensional parameter space in a rational method using DOE and then combine it with ML to map the parameter space approximately.[256] Figure 2.6 depicts a comparison of the optimization process using DOE vs. OFAT for a two parameter system and the blue gradient maps out the output parameter of interest as a function of two input parameters. There is a possibility of not finding the optimum value of the output parameter for the correlated system, as shown in Figure 2.6(c,d).

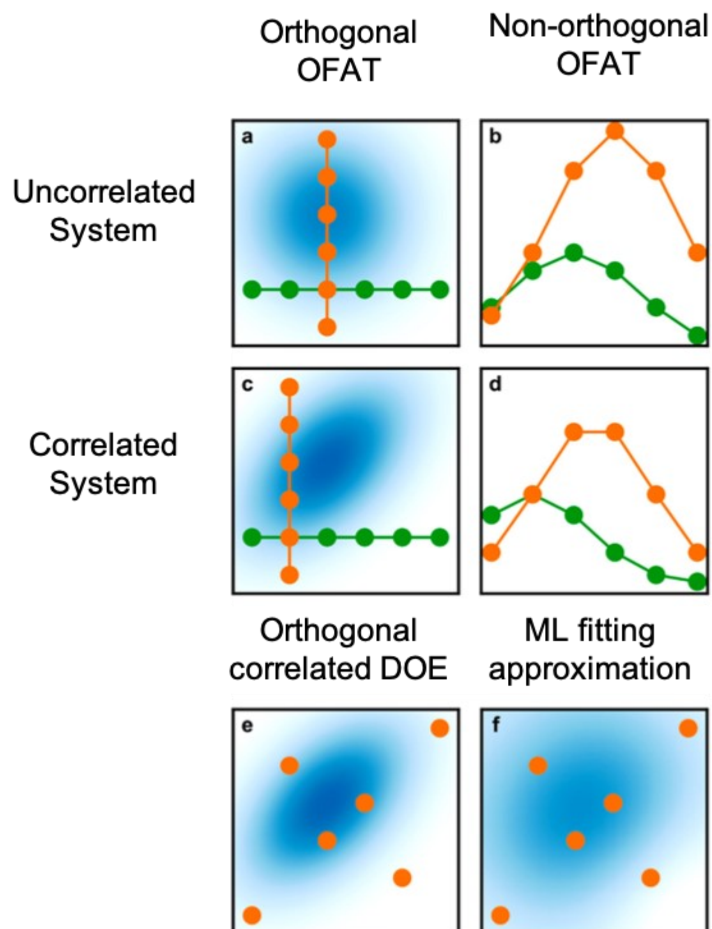

Figure 2.6. Comparison between DOE vs. OFAT approaches for finding optimum parameters for two input parameter systems. (a,b) OFAT sampling of an uncorrelated system and (c,d) OFAT sampling of a correlated system. (e) DOE approach with orthogonal sampling of a correlated system. (f) Approximation of the true output parameter map produced by ML fitting methods applied to the six data points acquired by DOE in (e). Green and orange dots represent two set of variables in the system. Adapted from reference 256 with permission from the American Chemical Society.

In an attempt to optimize these SVA parameters more efficiently with fewer laboratory resources (including time, one of the most precious resources), there a full factorial experimental design is used, complemented by machine learning (ML) approaches, to identify the optimized SVA parameters. However, the factors involved in solvent annealing are non-orthogonal and correlated, with one alteration affecting other parameters of the film during self-assembly, and the effects playing out over different length scales. Given the difficulties of optimizing correlated systems with numerous input parameters, we show how ML techniques may be applied to map out and minimize the defect densities of solvent-annealed hexagonal dot-forming BCP nanopatterns. While this work focuses exclusively upon solvent vapor annealing of

BCP films, the approach to optimization described here could be applied to other annealing methods.

In this chapter film morphology defects are analyzed and associated distributions observed in different thicknesses of PS-*b*-PDMS thin films that are solvent-annealed to a range of swelling degrees, plasma etched, and converted to silica nanopatterns. This analysis of defects runs through a wide range of magnifications, starting from defects in the lattice itself to grains of different macro-scale phases in the film (wetting, single, and double layers).

2.4 Experimental Methods

2.4.1 Materials

Poly(styrene-*b*-dimethylsiloxane) (43k-*b*-8.5k) diblock copolymer (PS-*b*-PDMS) with a dispersity of 1.04 was purchased from Polymer Source Inc. and used as-is. Toluene (>99%) and tetrahydrofuran (THF, >99%) were obtained from Fisher Scientific. Silicon wafers [<100>, 4 in. diameter, thickness 525 ± 25 mm, p-type (boron doped), resistivity <0.005 W cm] were purchased from WRS Materials. Sulfuric acid (96%) and hydrogen peroxide (30%) were purchased from Avantor Performance Materials.

2.4.2 Silicon Wafer Dicing and Cleaning

Silicon wafers were diced into 1 cm × 1 cm squares by a DSA 321 dicing saw and cleaned in freshly prepared piranha solution [3:1 v/v sulfuric acid (96%)/hydrogen peroxide (30%). **CAUTION**: Piranha solution violently reacts with organic matter] for 15 min, washed with deionized water, and dried in a nitrogen stream.

2.4.3 BCP Thin-film Self-assembly

A bulk BCP solution with a concentration of 2 wt% in toluene was used to prepare solutions with concentrations ranging from 0.6 to 1.4 wt%. BCP thin films with thicknesses between 20 to 33 nm were prepared by spin casting 25 μL of the desired polymer solution, as shown in Figure 2.7, on piranha solution-cleaned Si chips at 8500 rpm for 40 s with a WS WS-400BZ-6NPP/120 LITE spin-coater (Laurell Technologies Corporation). The initial film thickness was measured by ellipsometry and is the

average of ellipsometric measurements taken at five different points on the chip. The variation of thickness with the concentration of the BCP solution is shown in Figure 2.7.

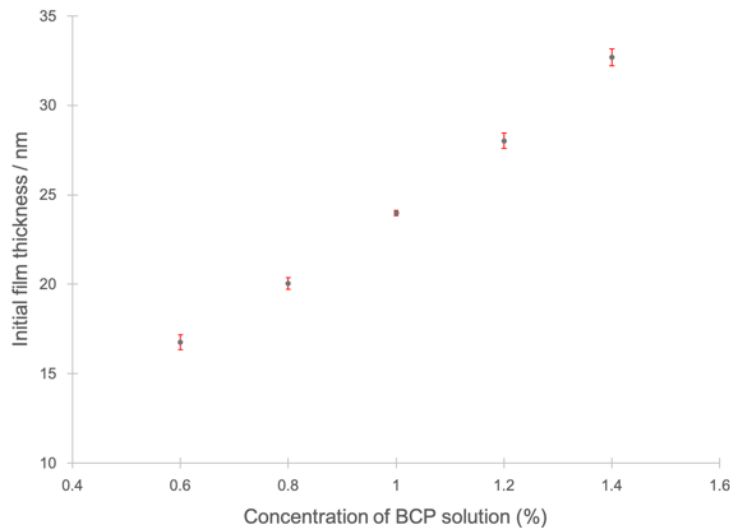

Figure 2.7. Relationship between initial film thickness and concentration (% m/v) of PS-*b*-PDMS (43k-*b*-8.5k) solution in toluene. Film thickness determined by ellipsometry. The plot is reproduced from reference 158 with permission of the American Chemical Society.

2.4.4 Controlled Solvent Vapor Flow Annealing System

A complete procedure for the annealing of a thin film of BCP on an oxide-capped Si chip using the controlled solvent vapor flow annealing system has been described previously.[155] The initial film thickness (in nm) and target swelling degree (SD = swollen film thickness/initial film thickness) were entered into the program controlling the solvent annealing system. The dwell time was 300 s, and the ramp speed was 0.3 SD/min, for all samples. It was ensured that the bubbler had enough solvent (THF) before commencing the annealing program, and 20 SCCM (standard cubic centimeter per minute) of Ar was bubbled into the solvent bubbler, along with another pure Ar mixer to adjust the value automatically. The program automatically stopped the solvent vapor flow at the end of the annealing, and the BCP film was deswelled by purging the annealing chamber with pure Ar. Briefly, the swelling degree is measured in situ and controlled via a feedback loop. As the volume of the annealing chamber is small, less than 1.5 cm^3, at a carrier gas flow rate of 20 sccm, full replacement of the

volume of the annealing chamber is complete within 4.5 s. This allows the films to be quenched to a swelling degree of less than 1.5 in under 2 s.

2.4.5 PS-*b*-PDMS Thin Film Reactive Ion Etching (RIE) Process

All PS-*b*-PDMS thin films were etched with a Plasmalab μEtch RIE using a two-step etch: The first step removed the surface wetting layer of PDMS on the BCP film by using a CF_4 plasma (100 sccm), 100 mTorr, 50 W for 8 s. In the second step, using an O_2 thicknesses between 20 to 33 nm, they were prepared by spin casting 25 μL of the desired polymer solution piranha solution-cleaned Si chips at 8500 rpm for 40 s with a WS WS-400BZ-6NPP/120 LITE spin-coater (Laurell Technologies Corporation). The initial film thickness was measured by ellipsometry and is the average of ellipsometric measurements taken at five different points on the chip.

2.4.6 Film Characterization

High magnification SEM micrographs were taken using a Hitachi S4800 scanning electron microscope (15 kV, 20 μA). Low resolution micrographs were taken using a Zeiss Sigma field emission scanning electron microscope (15 kV, 20 μA). The SEM micrographs for all the samples are shown in Figure 2.8.

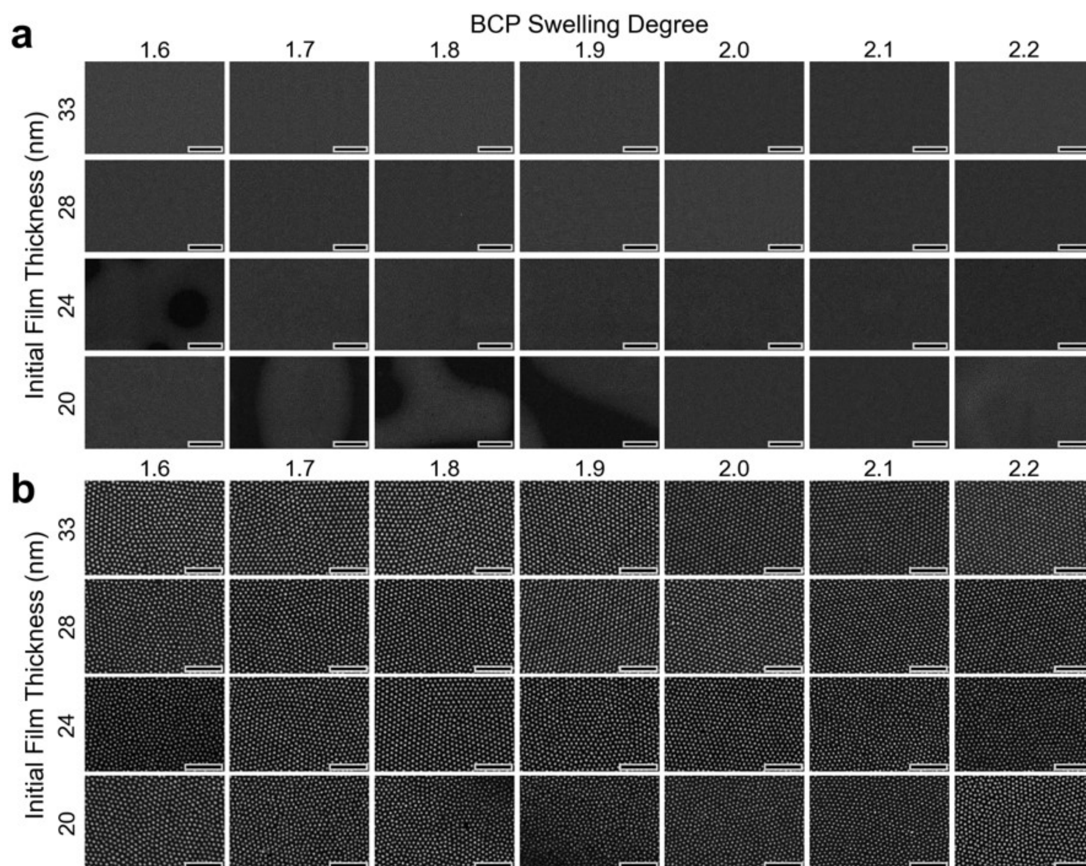

Figure 2.8. (a) High magnification SEM micrographs of BCP dots at various swelling degrees and initial film thicknesses, as indicated. Dot positions taken from these micrographs were used to calculate the statistical values used in the value dot maps corresponding to figures in the main text and ensemble statistics in the paper. Scale bars are 1 µm. (b) Details of (a) showing individual dots. Scale bars are 250 nm. The images are from reference 158 with permission of the American Chemical Society.

2.4.7 Data Processing

SEM micrographs were processed to extract dot positions and areas of single layer phase using Gwyddion image analysis software.[263] The background of the micrographs was removed using median scan line alignment, followed by polynomial background removal and revolve arc for the single layer and dot micrographs, respectively. Then a Gaussian filter was used to reduce high frequency noise. The layer and dots were marked by a brightness threshold found using Otzu's method.[264] Next, the ratio of a single layer area was averaged over eight SEM micrographs for each set of conditions studied to get the final area percent of the single layer phase. The dot positions were used to compute the various metrics of the BCP dot arrays. The raw SEM micrographs for all SVA conditions that were used to determine dot positions are shown in Figure

2.6. The size and resolution for silica dot arrays are 4.57 µm x 3.05 µm and 3070 x 2045 pixels, respectively. For the phase images, the size is 127 µm x 89 µm, and the resolution is 2560 × 1920 pixels.

The majority of the metrics used in this work are derived from the dot positions of the six nearest neighbors of each dot in relation to itself. The nearest neighbors are calculated using the ball tree algorithm in Scikit-learn.[265] The dot pitch of each dot is calculated from the mean distance of its six nearest neighbors to itself. The cell orientation angle of each dot is the circular mean of the angle of each nearest neighbor vector modulus with 60°. This gives a cell orientation angle from –30 to 30° for each dot. The registration error (R_e) is calculated from the six nearest neighbors, as explained in the chapter. The defect distance is defined as the shortest distance from each dot to a defect. For the ML fit maps, the ensemble averages are taken as the mean of all non-defective dots.

ML fit maps were made to visualize the changes in the relevant metrics across all conditions tested. The fitting is performed using a radial basis function (RBF) kernel support vector machine (SVM) from Scikit-learn.[265] After fitting, the function is remapped onto a grid to form an image for visualization.

2.5 BCP Pitch and Cell Orientation

The focus of this work is the quantification, prediction, and minimization of the defect density at all length scales of dot forming BCP films. However, other important metrics of the BCP dot array, such as pitch, can be determined easily, and the effects of the solvent vapor annealing (SVA) parameter space on pitch are analyzed. BCPs with ultra-small pitch (also known as period, domain spacing or d-spacing) have received the most attention in fulfilling Moore's law to decrease feature size. There are a few approaches to decrease the BCP pitch; one includes lowering the polymerization degree N of the polymer, however, a smaller N will weaken the segregation strength (χN) as a solution for high-χ BCP to achieve a high segregation strength. Even though the equilibrium domain spacing of a given block copolymer depends on the N and χ of the BCP ($d \approx aN^{2/3}\chi^{1/6}$) during the solvent vapor annealing, the χ parameter can be altered by incorporating the solvent vapor into the thin film, given by:

$$\chi_{eff} = \chi (1 - \varphi_s) \quad \text{Eq. 2.1}$$

where χ_{eff} is the effective Flory–Huggins interaction parameter, χ is the interaction parameter of the dry BCP, and $_{s}$ is the fraction of solvent molecules existing at the interface of the two blocks. This change in χ_{eff} can lead to a change in the equilibrium domain spacing of the BCP while solvent vapor annealing.

Shown in Figure 2.9 are the dot maps of the localized BCP dot pitch, where the pitch of each dot is determined by taking the mean distance of a dot and its six nearest neighbors. From both the low (Figure 2.9a) and high (Figure 2.9b) magnification maps, we can see that there is a clear trend of a small decrease in pitch with increasing swelling degree. These maps are color-coded, thus the shift in color from yellow-green to blue-green is showing a decrease of pitch as the degree of swelling increases.

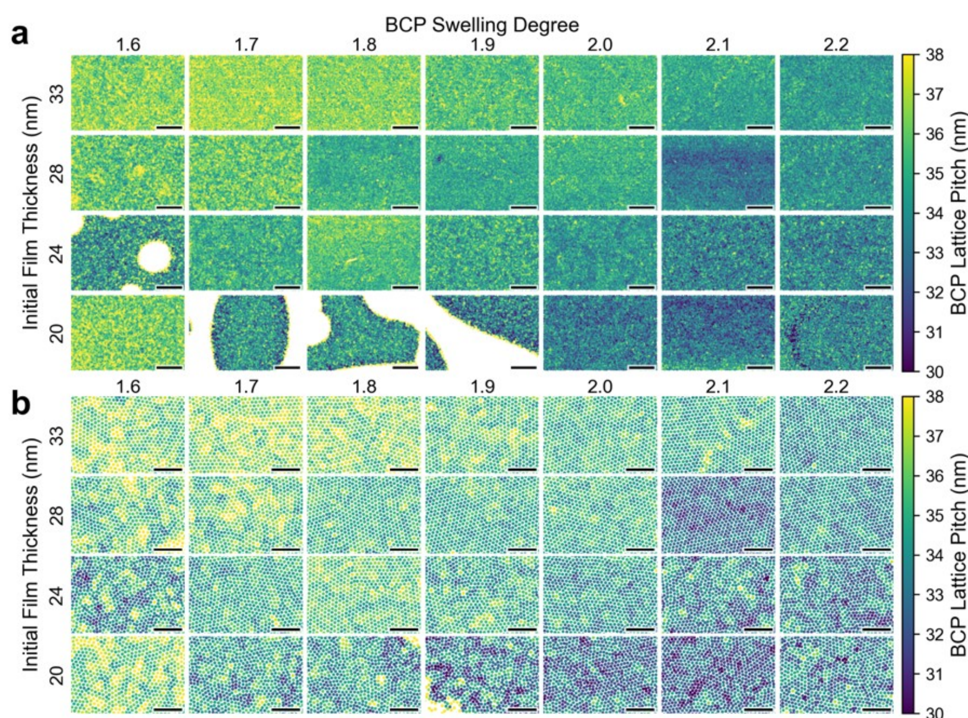

Figure 2.9. BCP lattice pitch as a function of SVA conditions. (a) Dot value maps showing dot locations for all 28 combinations of initial thickness of the PS-*b*-PDMS films and swelling degrees, indicated by the labelled rows and columns, respectively, and showing color values for BCP lattice pitch in nm. Scale bars are 1 µm. (b) Details of (a) showing individual dots. Scale bars are 250 nm. The images are from reference 158 with permission of the American Chemical Society.

As the degree of swelling is raised from 1.6 to 2.2, the average values of localized pitch range drop from 36.5 to 32.5 nm (displayed graphically in Figure 2.10).

Similar trends showing a decrease in pitch with increasing swelling degrees have been observed by Gu and co-workers as well as Ross and co-workers, for different initial film thicknesses.[230,266]

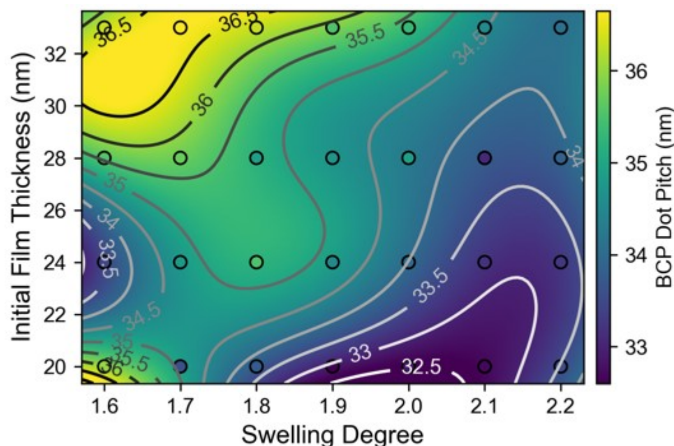

Figure 2.10. Support vector machine fitting using a radial basis function kernel showing the relationship between initial film thickness, swelling degree and median BCP lattice pitch. The image is from reference 158 with permission of the American Chemical Society.

At first glance, it may seem somewhat counterintuitive that the pitch decreases as the swelling degree increases, however, it is important to realize that the film can only swell in the vertical direction perpendicular to the substrate, which causes the microdomains to be become non-spherical, shrinking in size in the in-plane direction and stretching in the out-of-plane direction.[266] The decrease in pitch with increased swelling degree can be understood best by noting that the domain spacing, in the strong segregation limit is given by the equation $d \sim \chi^{1/6}$.[267,268] Given that the χ_{eff} decreases linearly with the amount of solvent incorporated into the film,[266,269] the domain spacing is expected to decrease as the swelling degree increases, as observed. Similarly, solvent molecules can incorporate fully into thinner films more easily compared to thicker films, leading to a decrease in pitch.[238] It is also worth noting that there are several blank/white patches in the films of thicknesses of 20.0 and 24.0 nm. These patches are wetting/lamellae phase layers that correspond to very thin regions of the BCP film.[155,227] These phases do not contain any dots/micelles and as such are left blank for all subsequent analyses.

Before quantitatively analyzing the defects in these BCP dot patterns, it is first useful to visualize the grain structures observed with different annealing conditions. The occurrence of a variety of grain boundaries generally disturbs the long-range order of the ordered phase during the self-assembly of BCP and separates ordered domains with different orientations and sizes, represented by Figure 2.11. The local cell orientation of each dot is mapped in Figure 2.11, which effectively maps out individual grains (regions where all the BCP dots have the same relative orientation).

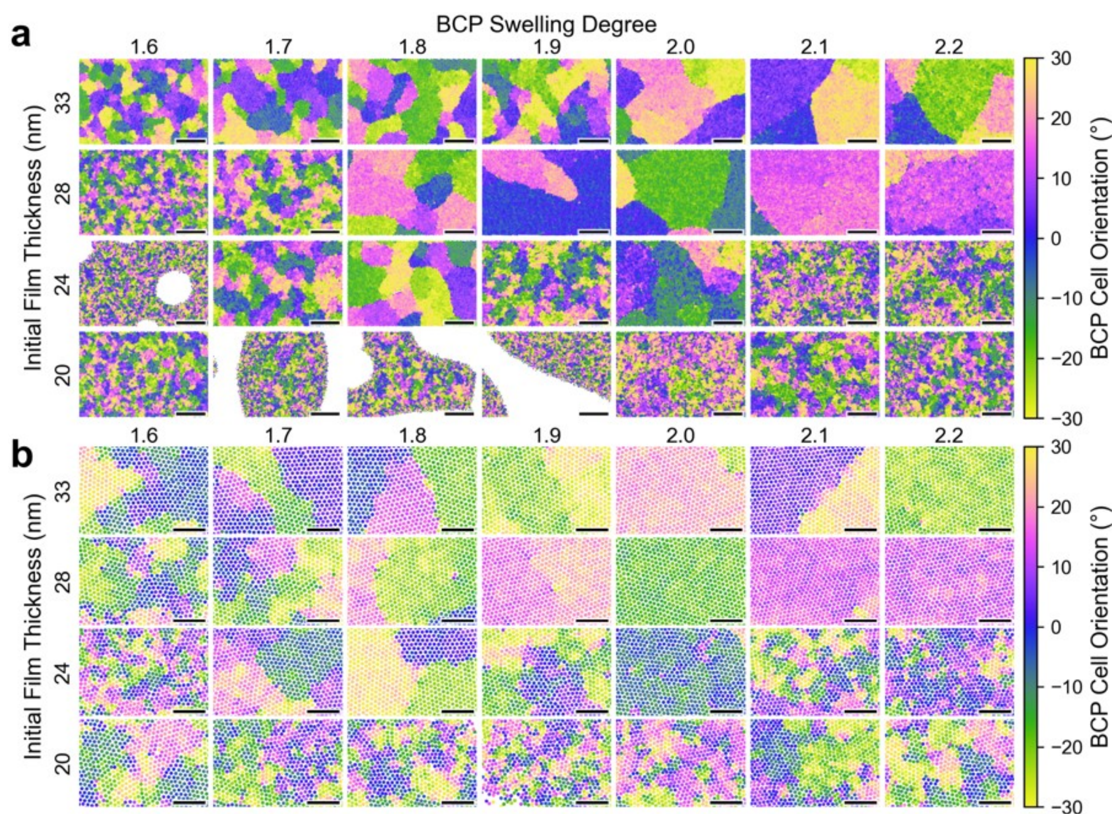

Figure 2.11. BCP lattice cell orientation as a function of SVA conditions. (a) Dot value maps showing dot locations for all 28 combinations of initial thickness of the PS-*b*-PDMS films and swelling degrees, indicated by the labelled rows and columns, respectively, and showing color values for BCP lattice cell orientation in degrees. Scale bars are 1 µm. (b) Details of (a) showing individual dots. Scale bars are 250 nm. The images are from reference 158 with permission of the American Chemical Society.

These results clearly demonstrate the large variability in long-range ordering as a function of the initial film thickness and swelling degree. Some films comprise many very small, sub-100 nm grains, and others are uniform over micron scales. The average grain size depends on various factors, including the swelling degree or the solvent vapor exposure of the film[270–273] and the initial film thickness.[274] At a film thickness of

20.0 nm, the annealed films have extremely small grains (on the order of a few lattice pitches), and the grains themselves have a low degree of local orientational ordering (vide infra). There also appear to be regions of optimal grain size and local orientational ordering. For example, at an initial film thickness of 24.0 nm, the grain size increases as the swelling degree increases, reaching a maximum size, but then decreases as the swelling degree is increased further; the local ordering also seems to decrease significantly. The initial increase in grain size with increased swelling degree is a result of the intended action of solvent annealing, where increased solvent vapor incorporated into the film increases chain mobility, allowing for the formation of ordered lattice structures with lower configurational energy.[230] However, this increase in chain mobility is accompanied always by a decrease in segregation strength; thus, as the segregation strength approaches the order–disorder transition (ODT), the local microdomain ordering begins to decrease.[230,274] These competing processes of chain mobility and segregation strength explain the trends observed in Figure 2.11, where there will be an optimal swelling degree for a given initial film thickness to maximize grain size and long-range ordering.

2.6 Point Defects

The defects observed in self-assembled monolayers of BCPs that form hexagonal dot patterns are dominated by disclinations and dislocations as well as point defects along grain boundaries between uncorrelated domains, multilayers, and the presence of lamellae.[155,225,227,275] Although these BCP cell orientation maps provide a useful qualitative sense of grain size and long-range ordering, it is necessary to define and measure defects quantitatively in order to apply ML methods to optimize the SVA processing. One of the most conventional methods for identifying defects is the determination of the coordination number, where any non-6-fold coordinated dots are marked as defects.[223,276] Maps of the local coordination number are shown in Figure 2.12, which very clearly identify topological point defects, like dislocations and disclinations having 5- and 7-fold coordinated sites. Although the coordination number very easily identifies point defects, it does not encode for fluctuations and deviations from perfect hexagonal coordination shells, which is a significant concern in these soft

BCP lattices during SVA. These deviations from perfect hexagonal lattice positions are important to consider when attempting to quantify the defectivity of these BCP lattices and their broader applications in devices requiring nanoscale positional accuracy. Specifically, it is easy to imagine a lattice with only 6-fold coordinated, but with sufficiently large local fluctuations in dot positioning to cause read/write errors. With this concept in mind, I define the metric of registration error (R_e) in order to identify fluctuational defects.

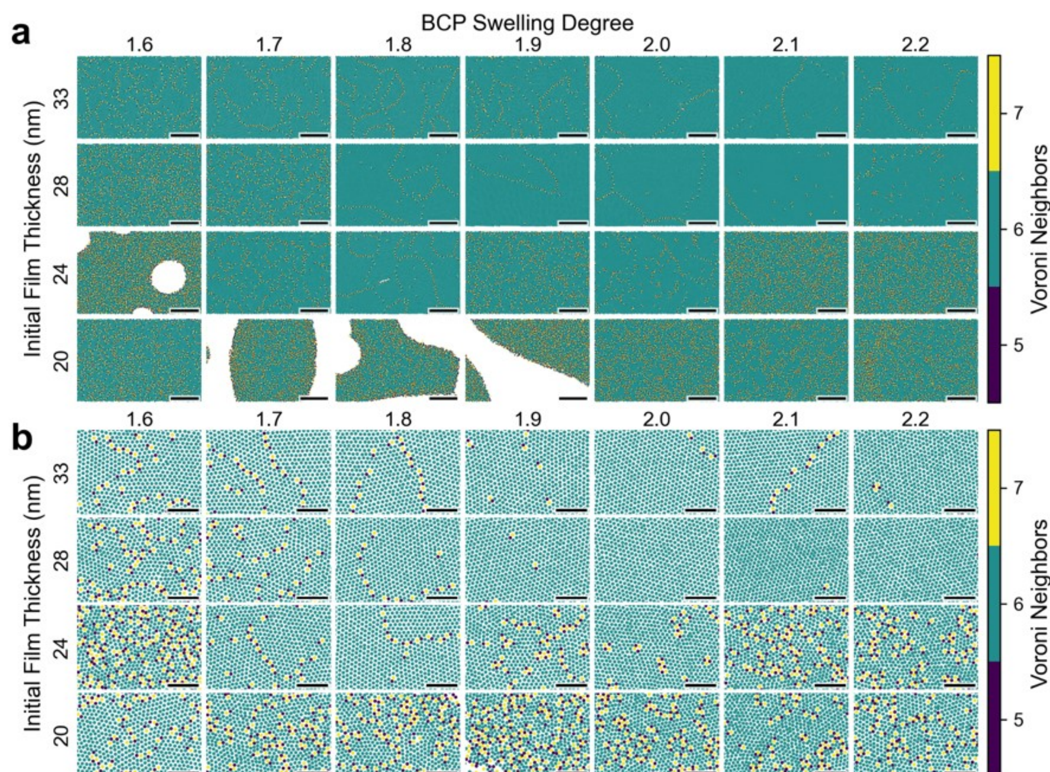

Figure 2.12. (a) Dot value maps showing dot locations for all 28 combinations of initial film thicknesses and swelling degrees, indicated by the labelled rows and columns respectively. Color represents the number of BCP lattice cell neighbors as determined by Delaunay triangulation. Scale bars are 1 μm. (b) Details of (a) showing individual dots. Scale bars are 250 nm. The images are from reference 158, with permission of the American Chemical Society.

2.6.1 Registration Error (R_e)

Simply put, the R_e of a given dot is a measure of the average distance of its six nearest neighbors from the corresponding perfect hexagonal coordination shell. Expressed mathematically, the R_e of any dot is given by:

$$R_e = \left(\frac{1}{6L_0}\sqrt{(x_n' - x_n^{NN})^2 - \left(y_n' - y_n^{NN}\right)^2}\right) \times 100\% \qquad \text{Eq. 2.2}$$

where L_o is the median pitch of the entire BCP dot array, x_n^{NN} and y_n^{NN} are the coordinates of the six nearest neighbors (sorted in a clockwise fashion) x_n' and y_n' are the coordinates of the regular hexagonal (with a pitch equal to L_0) that minimizes the value of R_e.

This effect of increased lattice deviations from perfect hexagonal coordination shells is illustrated in Figure 2.13 for an initial film thickness of 28.0 nm. At a low swelling degree of 1.6, the lattice has a very large number of point defects, but the number of defects sharply decreases as the swelling degree is increased to 1.8, at which point almost all of the point defects belong to the grain boundaries. However, as the swelling degree is increased further, a very subtle but important change can be observed in the maps, where the map appears to be darker purple (higher registration error) despite a similar number of point defects/grain boundaries. This increase of registration error is due to the average value increasing due to increased fluctuations in the local hexagonal coordination shell of BCP dots. This increase in the average for 6-fold coordinated sites is believed to be a result of the segregation strength decreasing as the swelling degree increases.

Using R_e as a measure of registration error, what constitutes a fluctuational defect can be defined in a physically meaningful way, as it relates to positional accuracy. Traditional measures of hexagonal lattice fluctuations, such as the local orientational order parameter, ψ_6,[277] also are very sensitive to fluctuations in hexagonal ordering, where mappings of ψ_6 are shown in Figure 2.14 and are very similar in appearance to the R_e mappings in Figure 2.13. However, there is no good way to relate values of ψ_6 to the possibility of a fluctuational defect, outside of choosing an arbitrary cut-off. Conversely, since R_e is a measure of actual distance, a fluctuational defect is defined when $R_e > r_o/L_o \times 100$, where r_o is the effective diameter of the BCP dots. From SEM data we estimate the average dot size to be ~8 nm, which is an overestimation due to charging effects and the non-zero spot size of the electron beam. To estimate the true/effective size of the dots more accurately, it is assumed that they are at least 2 nm smaller than measured by SEM, giving an effective dot radius of ~6 nm. Therefore, all

dots with a $R_e > 17\%$ are defined as a fluctuational (or point) defect. The physical interpretation of this defect definition is clear: if a read/write head is moved to the expected location of a nearest neighbor (based on a perfect hexagonal lattice) and the registration error is greater than 17%, the dot will not be detected. This definition of registration error is similar to the "jitter" model used in bit-patterned media, where a bit is considered to be written incorrectly if its effective jitter/excursion places it in its neighbor's write window.[278]

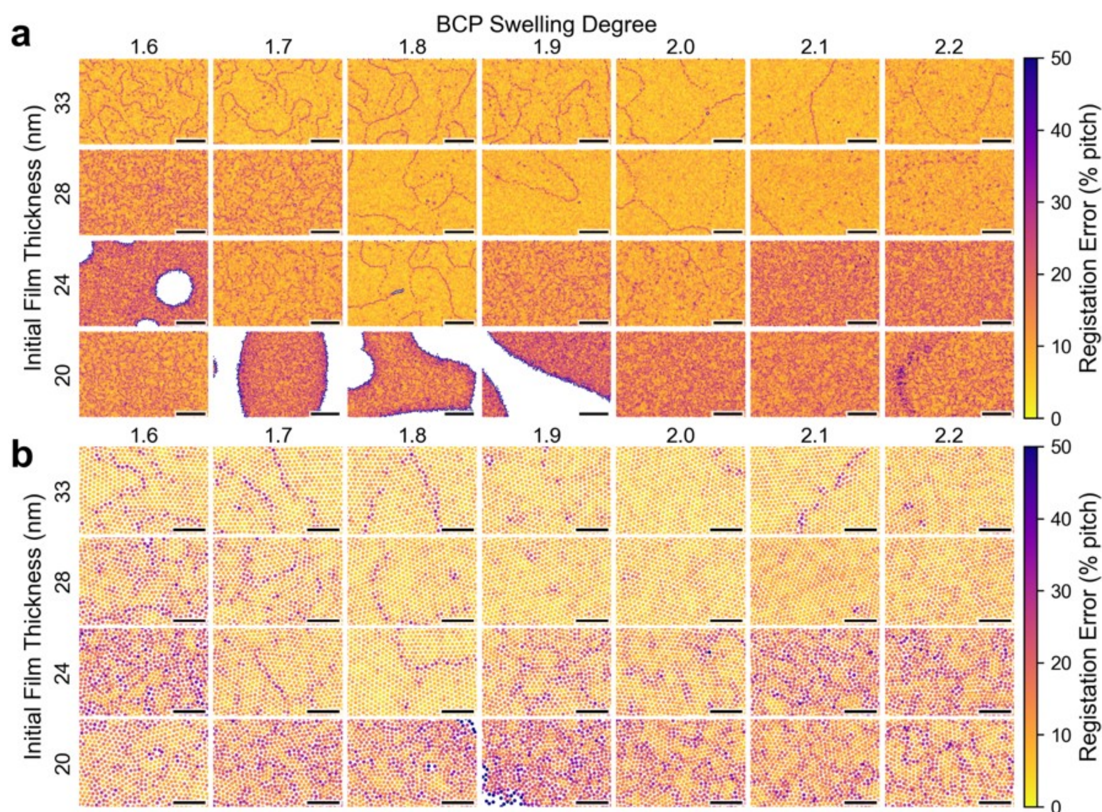

Figure 2.13. Registration error as a function of SVA conditions. (a) Dot value maps showing dot locations for all 28 combinations of initial thickness of the PS-*b*-PDMS films and swelling degrees, indicated by the labelled rows and columns, respectively, and showing color values for registration error in percent dot pitch. Scale bars are 1 µm. (b) Details of (a) showing individual dots. Scale bars are 250 nm. The images are from reference 158 with permission of the American Chemical Society.

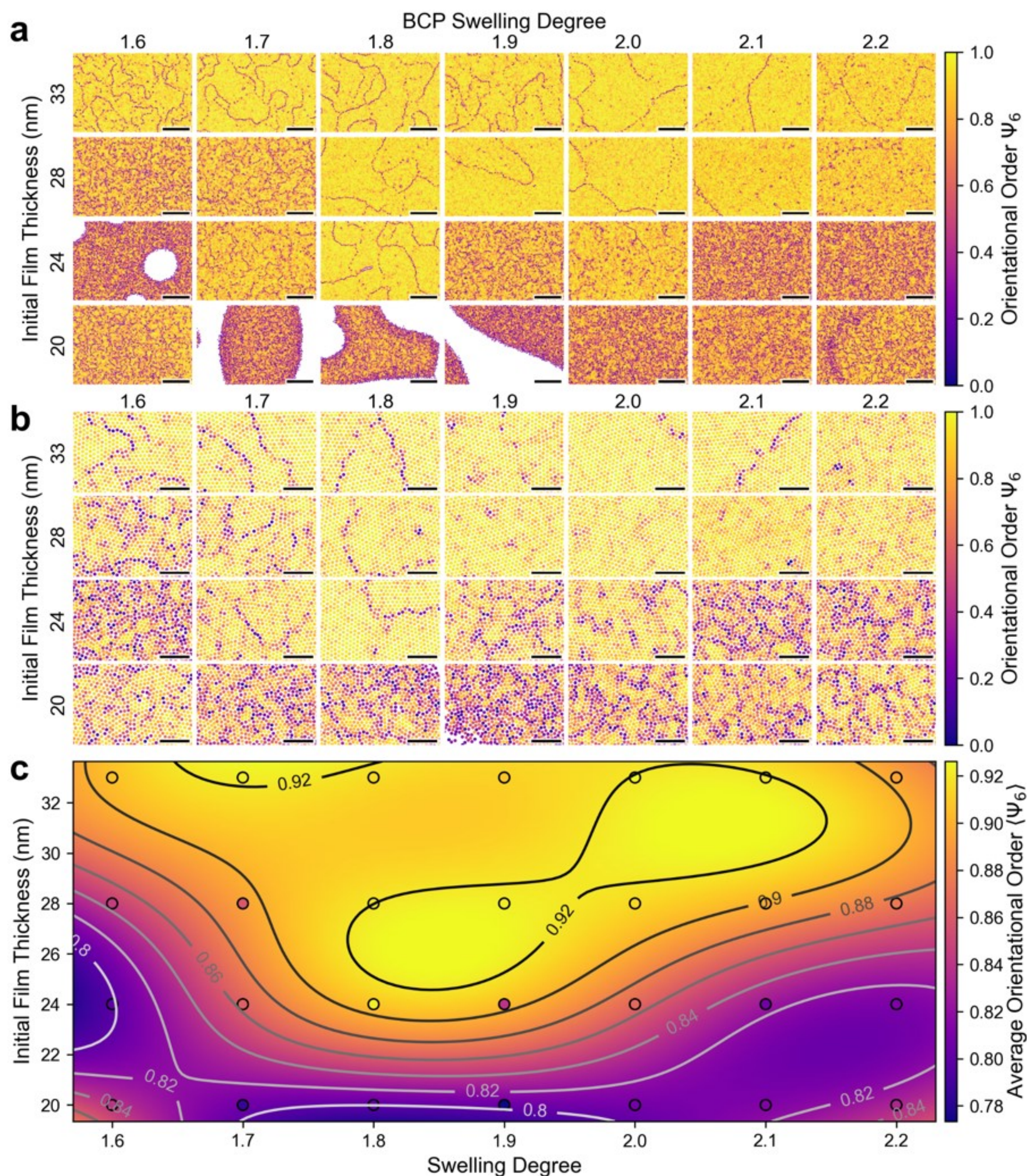

Figure 2.14. (a) Dot value maps showing dot locations for all 28 combinations of initial film thickness and swelling degrees, indicated by the labelled rows and columns, respectively, with color values of local orientational order parameters. Scale bars are 1 µm. (b) Details of (a) showing individual dots. Scale bars are 250 nm. (c) Support vector machine fitting using a radial basis function kernel of the average local orientational order parameter. The images are from reference 158 with permission of the American Chemical Society.

2.6.2 Defect Distance

Having defined defects as above (counting both point and fluctuational defects), we would like to compute an appropriate figure of merit (FOM) for a given BCP dot array,

which measures how desirable that BCP array would be if used for a DSA having a sparse lithographic definition. Although a raw average of the defect density is informative and simple to measure, it does not tell us how the defects are distributed in space. For instance, are they all located on grain boundaries, or are they uniformly distributed throughout? As such, a metric of local defect distance is defined, which is simply the minimum distance between a BCP dot and a defect (normalized by BCP pitch). Shown in Figure 2.15 are the local defect distance maps for each SVA condition tested. It is worth noting that these local defect distance maps are simply the Euclidean distance transform[279] of the defect maps (Figure 2.16). In contrast to the maps, the local defect distance maps show that, from a patterned device perspective, better BCP arrays can be made from films with initial thicknesses of 28 nm, compared to 33 nm (i.e., there are much larger regions that do not contain any defects).

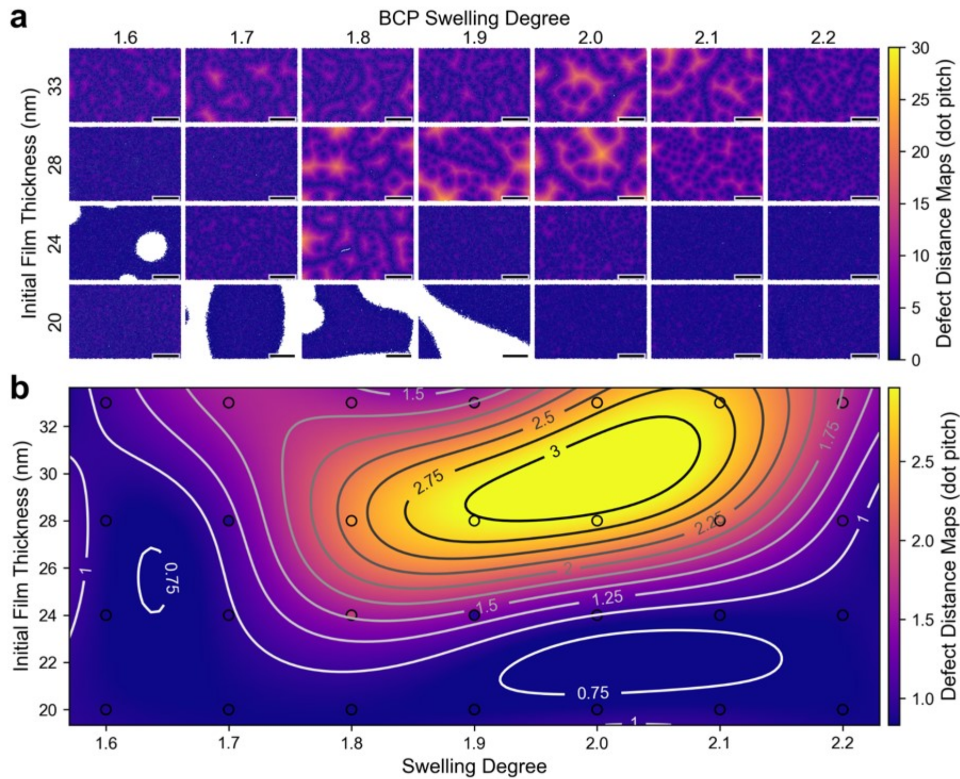

Figure 2.15. Defect distance as a function of SVA conditions. (a) Dot maps where the color value is the distance to the nearest defect. A defect is defined as having a registration error less than 17% where all of the vacancies and grain boundaries are included. Scale bars are 1 μm. (b) Support vector machine fitting using a radial basis function kernel of the effective defect distance per SVA condition. The images are from reference 158 with permission of the American Chemical Society.

The metric of defect distance can be used to provide a lower-bound estimate for the minimum spacing between DSA guiding features necessary to produce defect-free patterns. A map of the effective defect distance (as a function of SVA conditions) is shown in Figure 2.15b, which clearly identifies a narrow region of optimal annealing conditions centered around an initial thickness of ~30 nm and swelling degree of ~2.0.

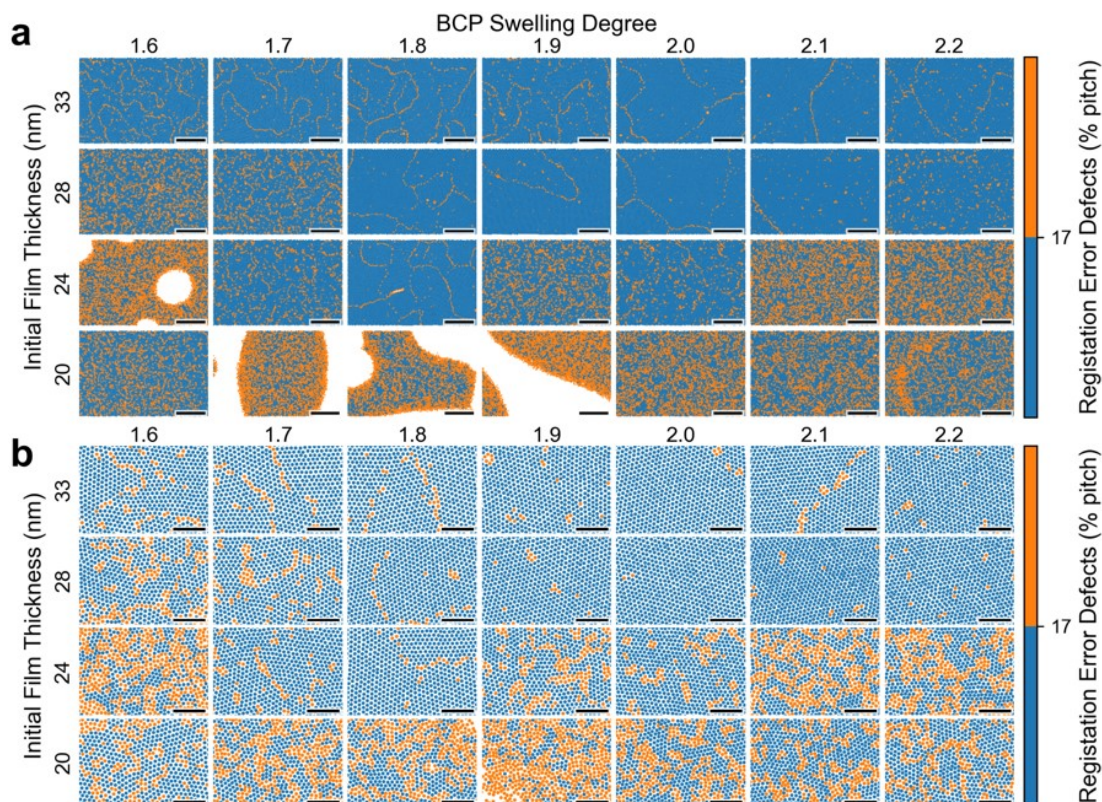

Figure 2.16. (a) Dot value maps showing dot locations for all 28 combinations of initial film thickness and swelling degrees, indicated by the labelled rows and columns respectively. Color represents the defect cutoff of 17% of registration error, where orange dots are defects corresponding to Figure 2.13. Scale bars are 1 μm. (b) Details of (a) showing individual dots. Scale bars are 250 nm. The images are from reference 158 with permission of the American Chemical Society.

2.6.3 Phase defects

The phase behavior of dot-forming BCP thin films (such as PS-*b*-PDMS used in this work) is quite complex, as lamellae/wetting layers, single layer hexagonal, or multiple stacked layers of hexagonal dots can be formed. Which phases form in a BCP thin film is dependent strongly on the initial thickness, which needs to be commensurate with the native BCP pitch.[249,250] Moreover, during SVA, the film swells in thickness, often resulting in the formation of multiple layers.[155,227] The non-uniformity of thickness of

the BCP films as well as the mass transport of the solvent vapor during the annealing play critical roles regarding the formation of single, double, or wetting layers, or bare exposed silicon, as shown in Figure 2.17.[155,226,227] The dot-forming BCP used here leads to a greater degree of single layers for thicker films at a lower degree of swelling; as the degree of swelling increases, however, more double layers are observed. Thinner films, on the other hand, have more single layers and wetting layers (or bare silicon) because there is insufficient BCP to form a continuous single layer of dots over the surface.[280] The final areal fraction of single layers (or desired phase) over the entire substrate is one of the most important (and often unreported) metrics of BCP thin film annealing. From the perspective of devices defined using DSA, any regions that are not the desired phase effectively would consist of 100% defects.

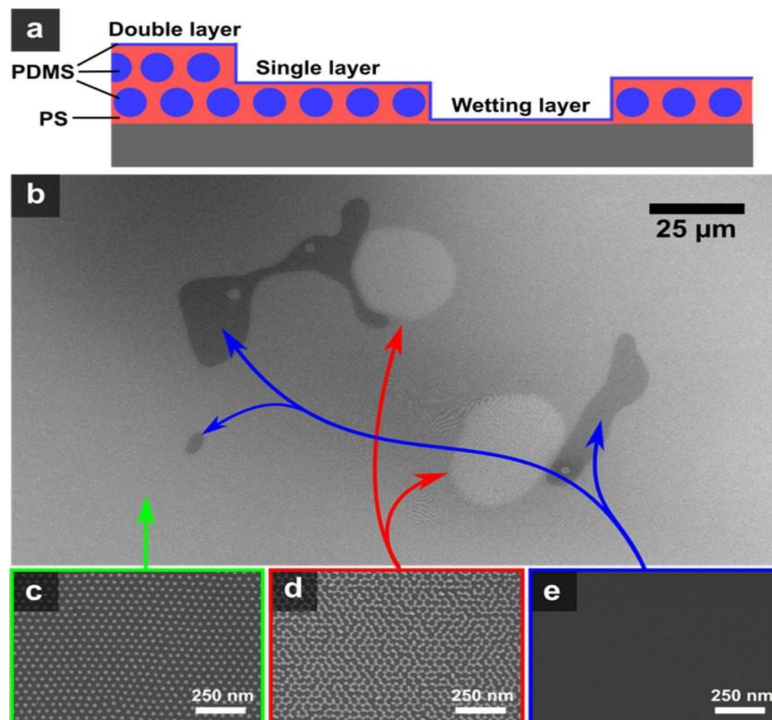

Figure 2.17. (a-b) Cross-sectional schematic (a) low-magnification micrograph (b) of terraced phases of wetting, single- and double-layer morphologies with dot forming PS-*b*-PDMS, after solvent annealing and removal of polymer by plasma cleaning. (c-e) High magnification SEM micrographs of the single layer (c), double layer (d) and wetting layer (e). This image is from reference 155 with permission of the American Chemical Society.

Shown in Figure 2.18a are false colored low magnification SEM images (100 μm × 100 μm), where purple shows lamellae/wetting layers, green a single layer,

and yellow a double layer. The first thing to note is that under almost all SVA conditions there are generally two phases present, either a combination of lamellae/wetting and single layer phases or single layer and double layer phases. To understand this phase behavior better, the average number of layers (per SVA condition) is measured as

$$N_{avg} = 0 \times f_l + 1 \times f_s + 2 \times f_d \qquad \text{Eq. 2.3}$$

where f_l is the area fraction of lamellae, f_s is the fraction of single layers, and f_d is the fraction of double layers. Shown in Figure 2.18b is an ML fit to the average number of layers, as a function of SVA conditions, which reveals several important features of the phase formation. As expected, we see that the average number of layers generally increases as the initial thickness and swelling degree increases. However, at swelling degrees less than ~1.8, the average number of layers is essentially insensitive to changes in the swelling degree, which is likely due to the very slow kinetics at these swelling degrees. One of the most useful features of this map is identifying the SVA conditions where the average layer number is close to 1.0 and is insensitive to fluctuations in SVA conditions. Specifically, from a practical device manufacturing perspective, there always will be non-uniformities in film thickness, mass transport, and solvent uptake over the entire substrate.[281] As such, it is important to consider these system sensitivities to inputs when selecting SVA conditions, where regions of a plateau with an average layer number of 1.0 are most desirable.

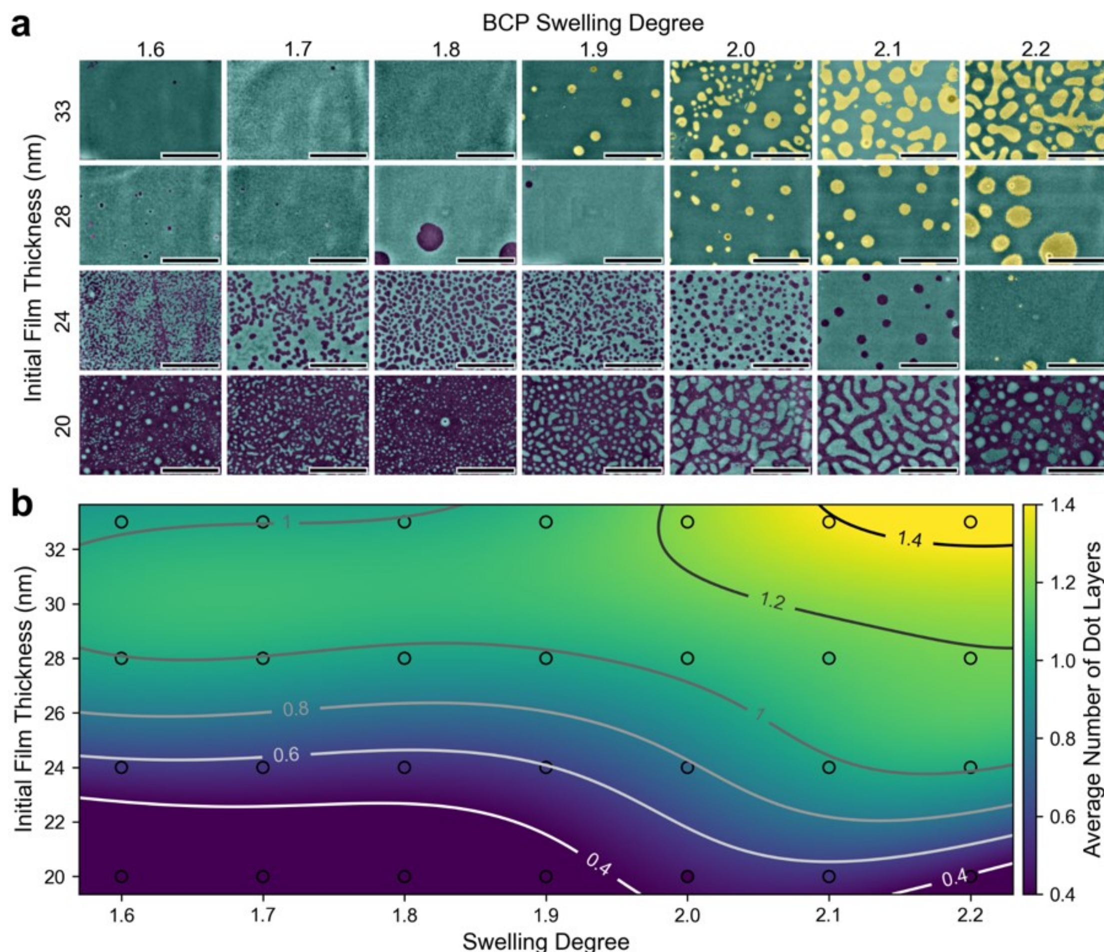

Figure 2.18. Number of hexagonal dot layers as a function of SVA conditions. (a) False color low magnification SEM micrographs showing wetting layers in dark blue, single layers in green, and double layers in yellow. Scale bars are 50 µm. (b) Support vector machine fitting using a radial basis function kernel of the area averaged number of dot layers, where "0" represents a wetting layer, "1" represents a single layer of dots, and "2" represents double layer areas. Scale bar is set to 0.4–1.4 to improve contrast. The images are from reference 158 with permission of the American Chemical Society.

2.7 Figure of Merit (FOM)

Making use of all of the above analysis, single FOM can be defined so that can be used to identify the optimal SVA conditions for producing BCP dot arrays for patterned media. The FOM chosen is simply the defect distance, modified by the fraction of single layers, to reduce proportionally the effective defect distance to account for the fact that non-single layer regions have a 100% defect density. A map of this FOM is shown in Figure 2.19, which is the product of the defect distance (Figure 2.19a) and fraction of the single layer (Figure 2.19b). It is noted that the optimal FOM does not correspond to either the optimal defect distance or the single layer fraction regions but

is rather the intersection of these two regions. This conclusion highlights the tradeoff between single layer fraction and defect distance: at lower swelling degrees, there is a large region of near 100% single layer, but the defectivity is much worse compared to that observed at higher swelling degrees. At higher swelling degrees, however, the decrease in defectivity is offset by a reduction in the number of single layers. This leads to a relatively narrow region of SVA conditions with the optimal FOM, which is located between a swelling degree of 1.9 to 2.0 and an initial film thickness of 28 to 30 nm. These conditions are clearly specific to this BCP with this molecular weight, but the methods presented here are completely general and can be utilized for different BCPs.

Shown in Figure 2.19 are the prediction fits of the ML algorithm to the measured values, including the FOM. Given the excellent prediction of the ML fit to the data, this figure suggests that the ground truth map of the FOM has a similar level of smoothness/bandwidth as that shown in Figure 2.20c. This is valuable information from an experimental optimization point-of-view, as it reveals that further experiments at different swelling degrees or initial thickness most likely will yield much higher FOMs. The knowledge gained from the ML fitting and visualization represents a significant time saving for the experimentalist, as further experiments are likely to produce only marginal increases in the desired FOM.

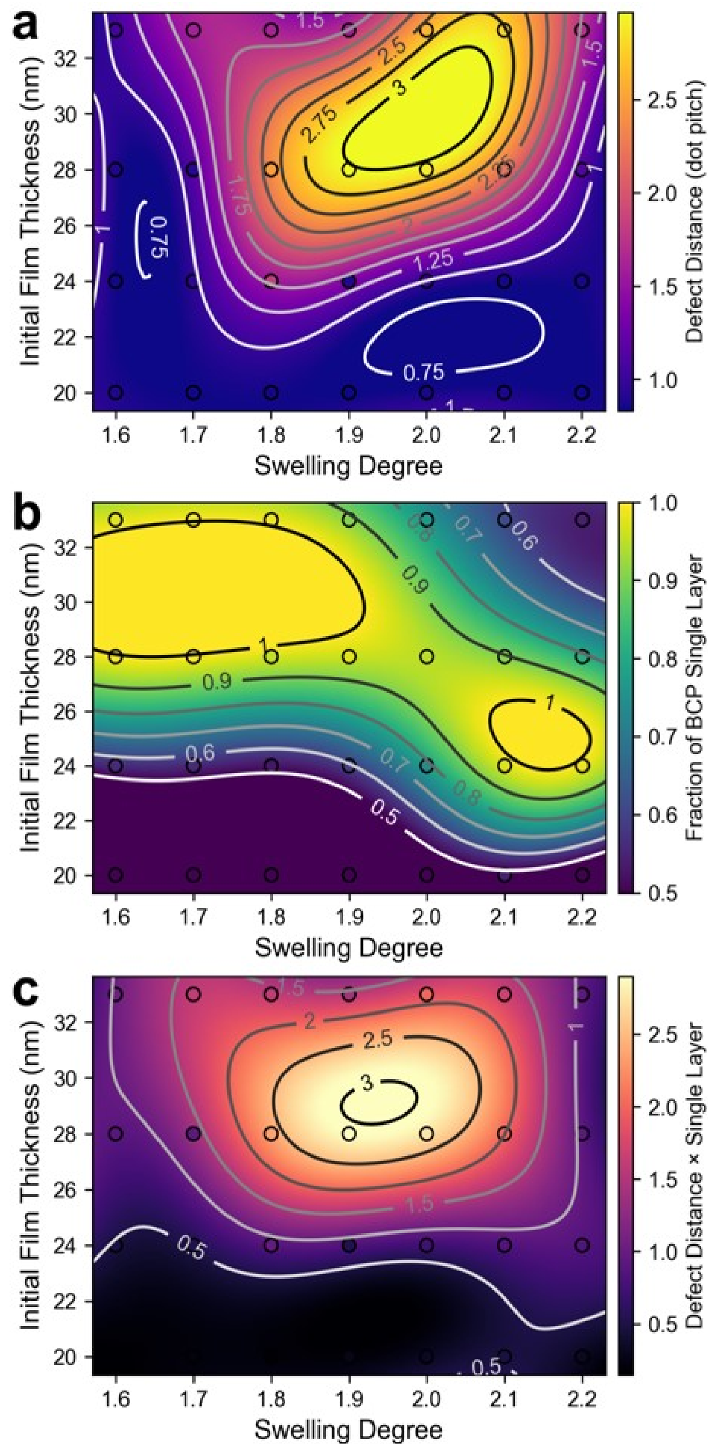

Figure 2.19. Support vector machine fitting using a radial basis function kernel of the (a) defect distance of the 20th percentile (where a defect is defined as having a registration error above 17%), where the majority of the vacancies and grain boundaries are included, (b) fraction single layer, and (c) multiplication of fraction single layer by defect distance. The images are reproduced from reference 158 with permission of the American Chemical Society.

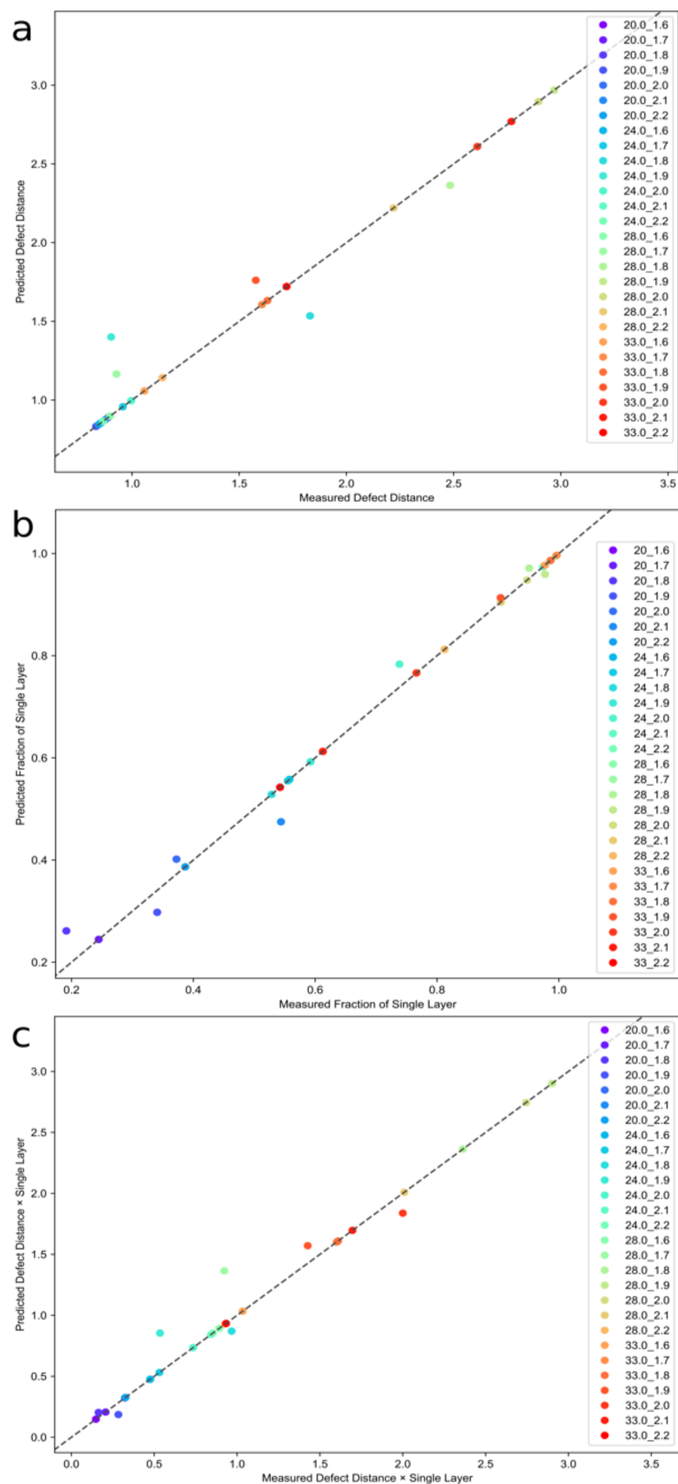

Figure 2.20. The fit of the predicted SVM models in Figure 2.19 versus the actual values. (a) 20th percentile of defect distance, (b) fraction of single layer, and (c) multiplication of fraction single layer by defect distance. The images are from reference 158 with permission from the American Chemical Society.

Although not presented in this work, several further refinements/modifications of this method can be applied for SVA optimization of nanopatterns derived from BCP films. As presented in previous work by the Buriak group on optimization of thin film organic photovoltaic cells,[255] the coupling of DOE with ML done in an iterative manner can be a very powerful tool for optimization. Specifically, in this work, what would be considered a full factorial design has been carried out, where the parameter space is sampled uniformly on a dense grid. The number of experiments could be reduced by applying a generalized subset design[282] and still performing the ML fitting to identify regions of interest with a high FOM. Then, these regions could be sampled further using DOE+ML in an iterative fashion. Furthermore, once the first-round optimization is done to identify these promising regions, even greater FOMs could be achieved if the annealing time was investigated in these regions, as longer annealing times likely will reduce defectivity in the films.

2.8 Conclusions

The application of block copolymer self-assembly for pattern generation with sub-lithographic resolution requires minimization of defect densities at both the nano- and macro-scales. Controlling and optimizing a large number of correlated and convoluted process parameters during processing and subsequent data analysis is time consuming if executed in an empirical fashion and may not arrive at the optimum conditions. The influence of the small thickness variations and swelling degrees on the final morphology of the BCP patterns was investigated and how to optimize these SVA parameters for fabrication of devices. A full factorial experimental design was used to probe the SVA parameter space, and a figure of merit was formulated to evaluate the quality of the resultant BCP nanopatterns, accounting for multiple length scales and the requirements of patterned devices. Then, machine learning was utilized to fit the SVA parameter space and identify the optimal annealing conditions with respect to the figure of merit. This approach is generalizable to optimize, analyze, and arrive at predictions of defect densities for different combinations of materials and processes for device fabrication. This combination of techniques may be applied to any combination of

materials and processes to optimize, analyze, predict, and minimize the defect densities in any given pattern.

CHAPTER 3

Reactive Ion Etching of Metal-loaded Self-assembled Block Copolymer Thin Films

3.1 Introduction

Patterns generated from any lithography techniques generally are transferred to the underlying material by a combination of etching and deposition processes. The template is transformed into a material with a specific functionality or functionalities integrated within a device. Similarly, pattern transfer is essential to convert a thin film of a self-assembled block copolymer (BCP) into functional elements. As is the case with any template, the transfer of the order and information should be selective and of high fidelity. Depending upon the desired application, a number of different protocols have been developed either to remove selectively one of the blocks within a self-assembled BCP film and/or transform it into a material of interest. Removal of one block would leave behind a polymer film with nanoscale ordered pores for use as an etching mask for further pattern transfer.[283,284] One of the earliest examples of applications of this approach was described by researchers from IBM, in which the PMMA block of thin films of poly(styrene-*b*-methyl methacrylate) (PS-*b*-PMMA) were removed selectively, leaving behind a nanopatterned array of polystyrene that was sufficiently robust to enable further processing (Figure 3.1).[285] In this example, the goal was the production of silicon nanoparticle-based patterns for flash memory. Other pattern transfer techniques, based upon self-assembled films of BCPs as templates for patterned etching of the underlying materials, include both dry and wet etching approaches.[286–290]

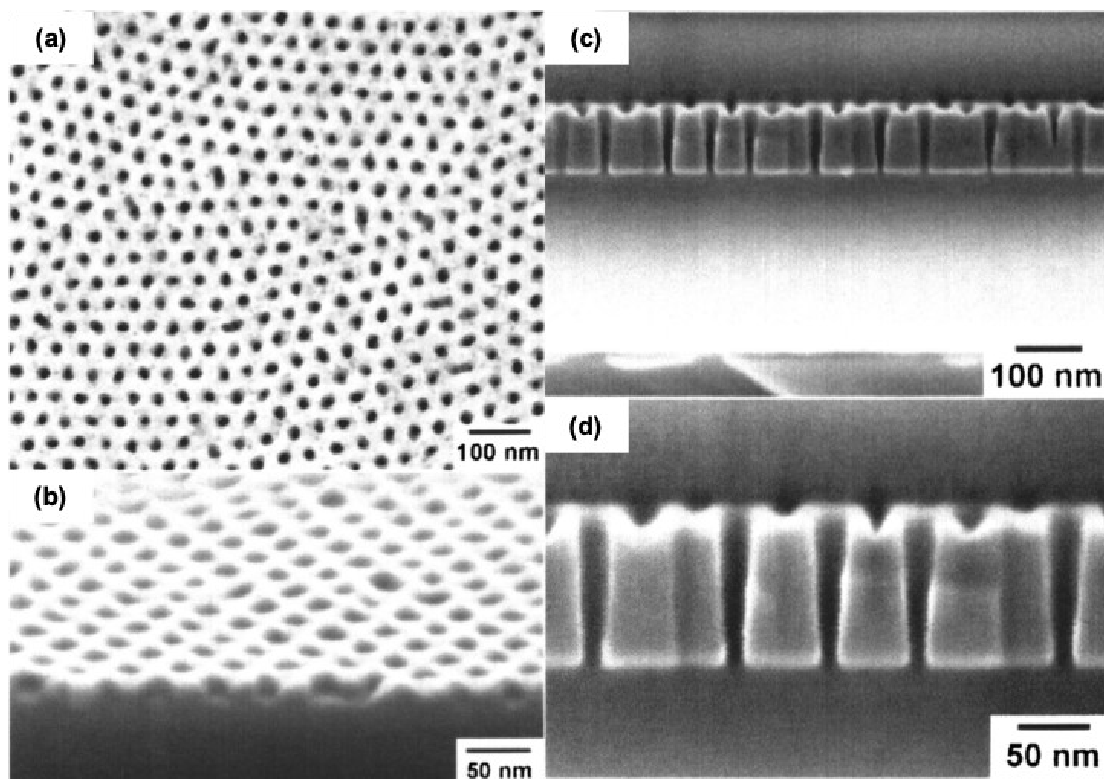

Figure 3.1. SEM micrographs of (a) planar view (b) 70° tilted view of a porous thin film of PS after removal of PMMA by exposure to UV, followed by an aqueous development in acetic acid at (c) low magnification and (d) high magnification of a 100 nm thick suspended porous silicon membrane. This image is from reference 285 with permission from the American Vacuum Society.

There has been much research into the development of procedures that harness the nanoscale chemical differences between the blocks in a thin film BCP assembly to direct the growth and deposition of metals, metal oxides, and other materials. As an example, the previous chapter relied upon the inclusion of silicon in the PDMS domains of self-assembled poly(styrene-*b*-dimethylsiloxane) (PS-*b*-PDMS) BCPs to be converted into nanopatterned SiO_x domains in a high-fidelity manner. Metals are of particular interest since they could form the basis of metal nanowires,[169,291,292] sensing elements,[293–295] and metal interconnects.[296] With self-assembled thin films of BCPs, chemical differences between the blocks can enable the selective loading of one block with a metal ion of interest, followed by a simple plasma treatment that renders a metal nanopattern on the surface that mirrors that of the parent BCP, as shown in Figure 3.2. In the case of the poly(styrene-*b*-2-vinylpyridine) (PS-*b*-P2VP) BCPs, the key is the use of protonation of the pyridine group of the polyvinylpyridine (PVP) block, which has a pK_b of ~6 upon immersion in an aqueous acid (HCl, HF).[287] The PVP block would

become at least partly protonated and positively charged and then can be loaded with an anionic metal complex via ion exchange of the chlorido or fluoride ligands at the metal. Treatment with a benchtop plasma reactor removes the organic block copolymer and reduces the metal ions to M(0), forming metallic dots or lines, depending upon the choice of BCP and annealing technique. A wide range of anionic metal complexes have been loaded into the protonated PVP blocks to yield metallic nanostructures comprising Au, Pd, Pt, Co, Ni, Fe, and others.[169,288]

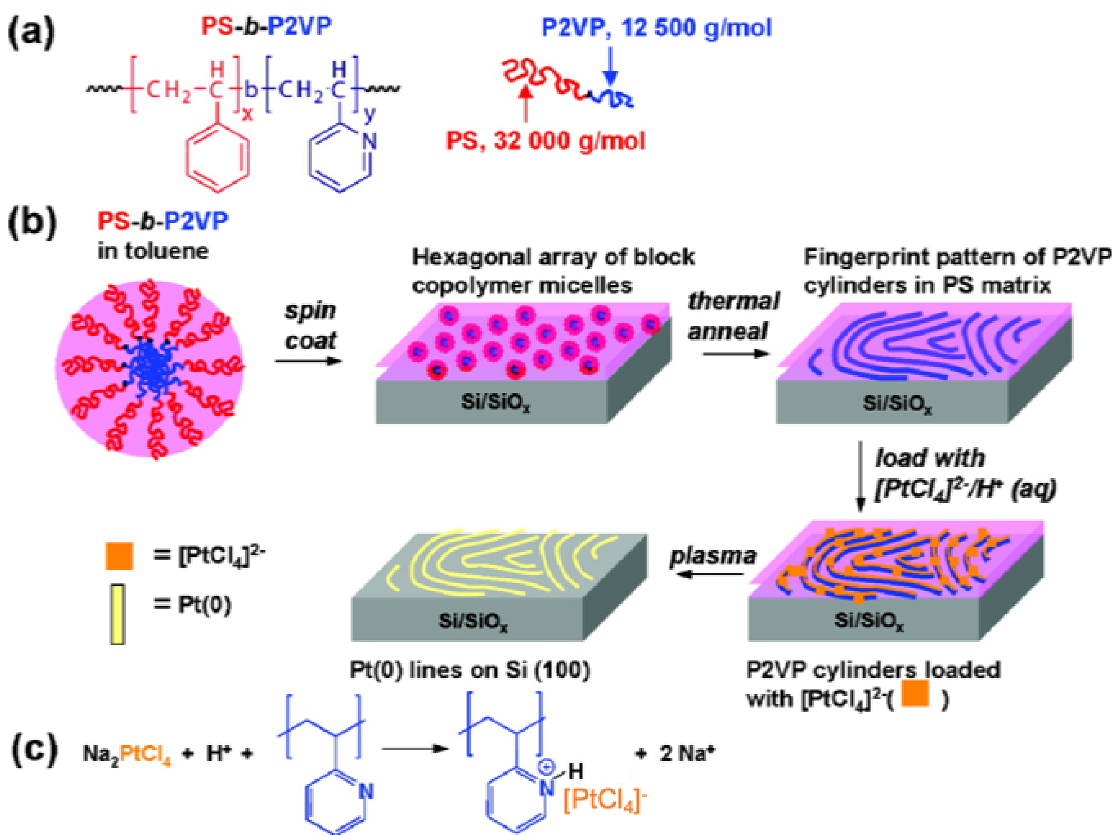

Figure 3.2. (a) Structure and molecular weight of poly(styrene-*b*-2-vinylpyridine) (PS-*b*-P2VP). (b) Schematic representation of spin coating a solution of PS-*b*-P2VP in toluene on a silicon substrate with a native oxide layer. Thermal annealing of the pseudohexagonal arrays leading to a fingerprint pattern with P2VP cylinders embedded within the PS matrix. P2VP swelling as a result of protonation by immersing thermal annealed samples in an acidic cation solution. Electrostatic interaction of anionic metal salts with the protonated P2VP layer to load with metal salts, followed by plasma treatment to remove polymer and form metal wires on the surface. (c) Electrostatic attraction between anionic metal complexes with the protonated P2VP block, in an acidic environment. This image is from reference 169 with permission from the American Chemical Society.

Almost three decades ago, the selective binding of metal complexes to specific blocks in self-assembled BCPs was demonstrated, starting with a paper by Schrock and

co-workers showing the binding of silver ions to phosphine-containing diblock copolymers formed via ring-opening metathesis polymorization.[297] The silver ions were reduced to Ag(0) clusters within the cores of the BCP self-assembled micellar assemblies. Another heavy late transition metal compound, OsO_4, was used to enable observation of the hexagonal micellar assemblies of PS-*b*-PB by transmission electron microscopy (TEM), where PB is polybutadiene, via binding of OsO_4 to the alkene functionalities in the PB domain. About the same time, Spatz et al. demonstrated the use of the PVP block as a chemical handle in self-assembled films of hexagonally packed micelles of PS-*b*-P2VP, with a large body of work starting in 1995.[298] The addition of $HAuCl_4$ resulted in protonation of the P2VP block, with $AuCl_4^-$ as the corresponding anion that was then reduced in-situ to Au(0) nanoparticles with hydrazine. The TEM imaging (Figure 3.3) revealed a hexagonal arrangement of gold nanoparticles in the cores of the PS-*b*-P2VP micelles.

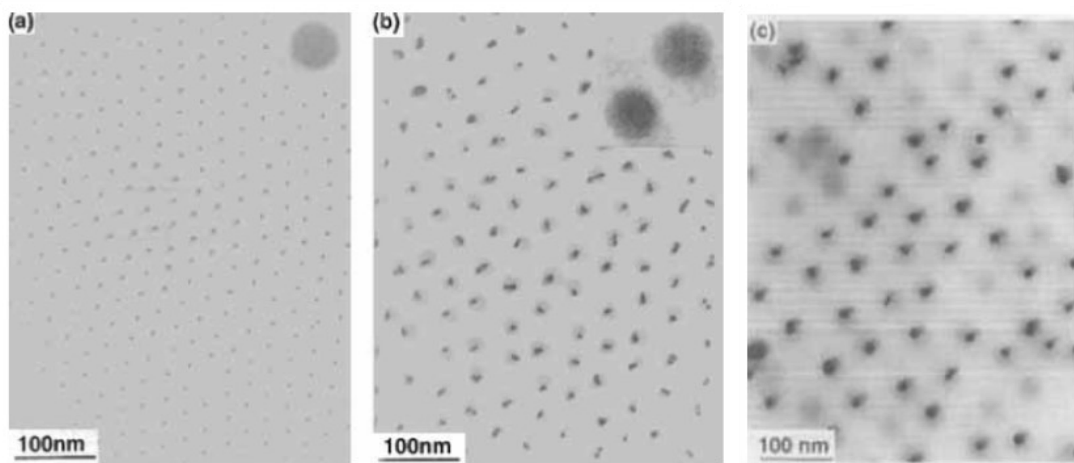

Figure 3.3. Bright-field TEM images of thin film cast using micellar solutions of PS-*b*-P2VP treated with 0.5 equivalents of $HAuCl_4$ per pyridine unit after reduction with anhydrous hydrazine for different time intervals. (a) After 1 min reduction, one gold particle per micelle with diameter of 9 nm. (b) After 30 min reduction, the initially formed gold particles paired up. The insets show high magnification images for one (a) and two (b) gold particles. (c) After 2 days reduction, coagulation of initially formed gold particles resulting in large crystallites and empty micelles. This image is from reference 298 with permission from John Wiley & Sons.

The application of the metallization procedure pioneered by Spatz and co-workers was extended by this group[299,300] and others to form nanopatterns of gold on surfaces.[169,301] Buriak and co-workers then showed that other metal ions could be used to prepare metal nanopatterns on silicon surfaces, expanding the repertoire from gold

to a variety of transition metal ions.[169,287,288] Figure 3.4 shows platinum dots and lines that were produced on silicon surfaces using the anionic metal complex, Na_2PtCl_4, which then, in this example, were incorporated into flexible PDMS to use as catalytic stamps.[118,302,303] The loading of PS-*b*-P2VP thin films with Na_2PtCl_4 in dilute acid also can be extended from monolayers on a surface to bilayers, which when treated with a plasma, collapses to form density doubled lines and dots, as seen in Figure 3.5.[304] This metal-loading approach to forming metallic nanopatterns is thus versatile and serves as the basis of the work described in this chapter.

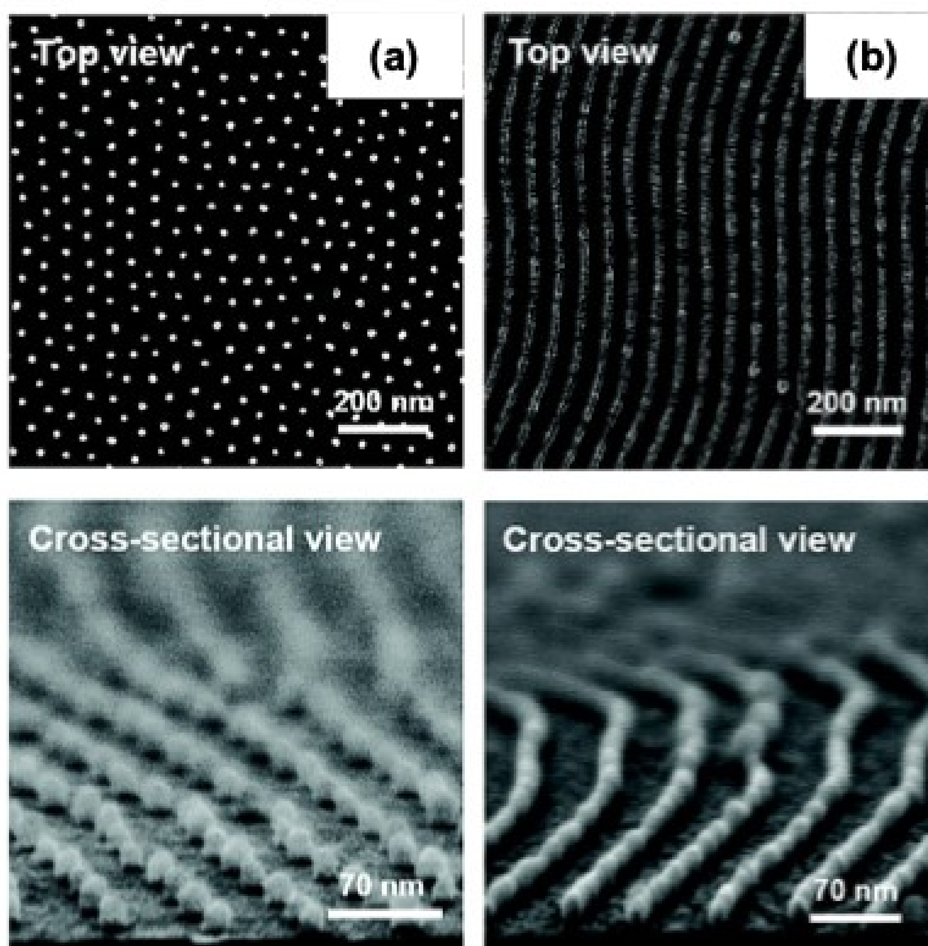

Figure 3.4. SEM micrographs of top and cross-sectional view of Pt nanopatterns by PS-*b*-P2VP (125k-*b*-58k) template. (a) Pt dot pattern, (b) Pt line pattern. This image is from reference 303 with permission from the American Chemical Society.

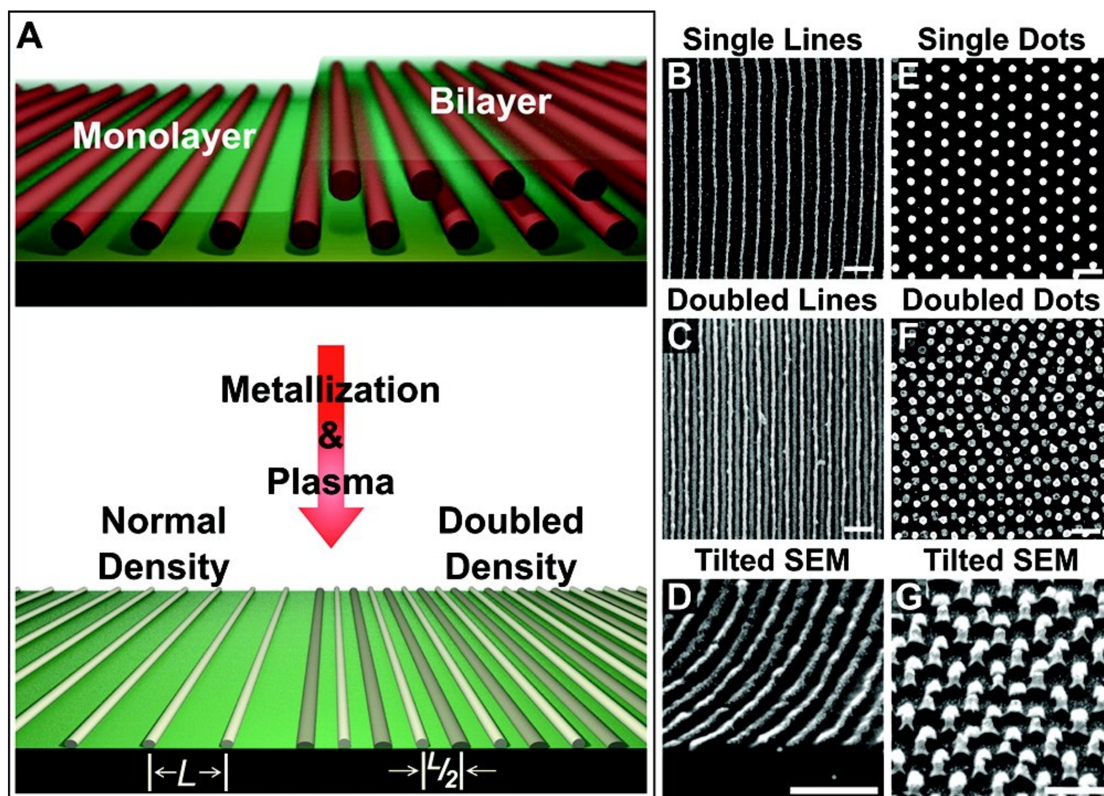

Figure 3.5. (A) A schematic representation of a parallel line pattern in a polymer film. Characteristic line spacing for areas with a single layer of lines was L after the metallization step was performed (B). Line spacing was halved to $L/2$ for areas with double layers of lines (C). The cross-section image (D) represents both layers of lines, with the top layer lines being slightly brighter and narrower than those of the underlying layer. (E-G) Similar pattern formation and density doubling for dot patterns. All scale bars are 100 nm. This image is from reference 304 with permission from the American Chemical Society.

Previous work by Buriak and co-workers involved the extension of BCP self-assembly towards sequential nanopatterning, in which two separate block copolymer patterning steps were carried out to form higher order, density-multiplied patterns.[305] Cong et al. used PS-*b*-PDMS BCPs that generate SiO_x dot patterns following annealing and plasma treatment. The first step resulted in the expected hexagonal dot pattern, which was then followed by a second step of spin-coating of the BCP solution, followed by annealing and plasma treatment. At the time, it was unclear as to whether the second self-assembly step would register with the first to form a hierarchical ordered structure, but the resulting patterns clearly indicated that the second layer of BCP indeed did register strongly with the initial SiO_x dots to form a commensurate honeycomb pattern [see Figure 3.6(a)].

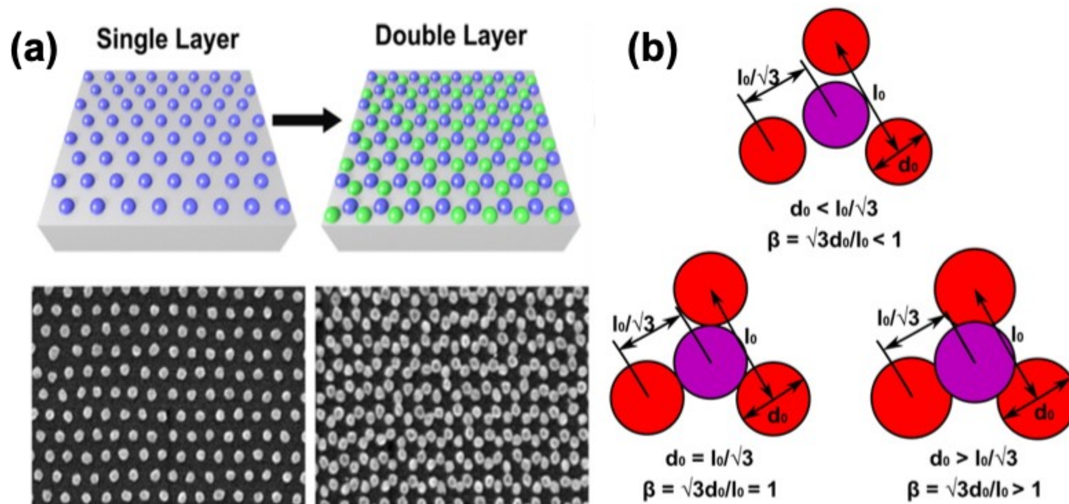

Figure 3.6. (a) A schematic representation (up) and SEM micrographs (bottom) of a sequential self-assembly of PS-*b*-PDMS to generate silica honeycomb patterns. (b) A schematic representation of three different scenarios of dot-to-dot contact within a lattice with the geometrical values of interest within the perfect hexagonal lattice with dot overlap ($\beta > 1$), touching ($\beta = 1$) and no contact ($\beta < 1$). This image is adapted from reference 305 with permission of the American Chemical Society.

This chapter discusses the optimization of the reactive ion etching process of metal ion-loaded BCP thin films to enable the generation of multiple layers of hexagonal metal nanopatterns using PS-*b*-P2VP, as opposed to SiO_x. Because mixed metal nanopatterns could have interesting plasmonic properties,[306–309] the goal is the preparation of highly registered ordered metal-based double layers using PS-*b*-P2VP as the BCP. As will be described here, however, the etching of the metal-loaded based BCP was fraught with challenges of over-etching when carrying out multiple self-assembly steps, including metal nanoparticle loss and loss of order due to damage by the plasma-based dry etching process. This issue needed to be examined in detail to proceed towards mixed-metal nanopatterns, and thus the goal of this chapter is the development of a general reactive ion etching (RIE) step that circumvents damage of the metal nanoparticles. The application of the RIE chemistry developed here to enable production of double layers of mixed metal nanopatterns then is applied in Chapter 4.

3.2 Experimental

3.2.1 Materials

PS-*b*-P2VP with different molecular weights of 88k-*b*-18k [dispersity (*Đ*) = 1.07], 44k-*b*-18.5k (*Đ* = 1.07), and 44k-*b*-8.5k (*Đ* = 1.07) diblock copolymers, PS-*b*-PDMS molecular weight of 31k-*b*-14.5k with *Đ* of 1.15, and polystyrene homopolymers [5k (*Đ* = 1.07) and 10k (*Đ* = 1.09)] were purchased from Polymer Source Inc. and used as-is. Toluene (>99%) and tetrahydrofuran (THF, >99%) were obtained from Fisher Scientific. Silicon wafers [<100>, 4 in. diameter, thickness 525 ± 25 mm, p-type (boron doped), resistivity <0.005 W cm] were purchased from WRS Materials. Hydrochloric acid (36.5–38%) was purchased from Fisher Scientific. Sulfuric acid (96%) and hydrogen peroxide (30%) were purchased from Avantor Performance Materials. Potassium tetrachloroaurate(iii) ($KAuCl_4$, >99%) and sodium tetrachloroplatinate(ii) (Na_2PtCl_4, 42.65%) were purchased from Strem Chemicals. Silver nitrate ($AgNO_3$), cetyltrimethylammonium chloride (CTAC, 25 wt% in water), and hydroquinone (99%) were purchased from Sigma Aldrich.

3.2.2 Substrate Preparation

Silicon wafers were diced into 1 cm × 1 cm squares by a DSA 321 dicing saw and cleaned in freshly prepared piranha solution [3:1 v/v sulfuric acid (96%)/hydrogen peroxide (30%). **CAUTION**: Piranha solution violently reacts with organic matter] for 15 min, washed with deionized water, and dried in a nitrogen stream.

3.2.3 BCP Thin-film Self-assembly

Individual solutions of 1% (w/v) BCP or homopolymer were prepared using toluene. The 30% blended PS-*b*-P2VP (44k-*b*-18.5k) and PS-*b*-PDMS (31k-*b*-14.5k) were prepared by mixing 1% (w/v) PS (5k) and 1% (w/v) PS-*b*-P2VP [B'30, (44k-*b*-18.5k)] and 1% (w/v) PS (10k) and 1% (w/v) PS-*b*-PDMS [**B30** (31k-*b*-14.5k)] together in a 3:7 volume ratio. A thin film of PS-*b*-P2VP with thicknesses of 35 ± 1 nm (88k-*b*-18k and 44k-*b*-8.5k), 31 ± 1 nm (B'30), and 30 ± 1 nm (**B30**), with a desired molecular weight was prepared by spin coating 17 μL from 1% (w/v) polymer solution on a piranha cleaned Si chip at 4200 rpm for PS-*b*-P2VP and 800 rpm for PS-*b*-PDMS (WS-

400BZ-6NPP/120 LITE spin-coater Laurell Technologies Corporation). The initial film thickness of the thin film was measured using ellipsometry. After that, a thin film containing Si chip was solvent annealed using THF vapor in a static solvent vapor apparatus with in situ thickness monitoring to achieve the desired swelling degree (SD = swollen film thickness/initial film thickness). The swelling degree for PS-*b*-P2VP with molecular weights 88k-*b*-18k and B'30 was 2.0, for 44k-*b*-8.5k was 1.6, and **B30** swelled to a swelling degree of 2.0. Then, all the PS-*b*-P2VP samples were subjected to the metallization process and corresponding RIE recipe, as explained in the next section.

In order to anneal a second layer of BCP sequentially on top of the bottom layer of hexagonal metal dot nanopatterns, samples were subjected to identical annealing, metallization, and RIE procedures, as described above. For SiO_x–Pt double layer and SiO_x–Pt–Pt triple layer patterns, a second layer of PS-*b*-P2VP from B'30 was annealed and a third layer from the same BCP were self-assembled using the corresponding annealing, metalizing, and etching procedure.

3.2.4 Metallization

For PS-*b*-P2VP, a metallization step was carried out prior to reactive ion etching. After annealing, thin films of PS-*b*-P2VP were immersed either in an aqueous platinum salt solution [10 mM Na_2PtCl_4, 2 mL and 1% (%v/v) HCl, 8 mL] for three h or a gold salt solution [10 mM $KAuCl_4$, 2 mL and 1% (%v/v) HCl , 8 mL] for 10 min. Then, the samples were removed from the metal salt solution, rinsed with ultra-pure water, and dried in a nitrogen stream.

3.2.5 Reactive Ion Etching and Thermal Annealing

For a sequential double layer self-assembly, a thin film of PS-*b*-P2VP with different molecular weights was etched using 100 mTorr O_2 plasma (Plasmalab μEtch RIE) at 80 sccm with a 30 W RF power for different time intervals, depending on the molecular weight of the BCP used to convert Pt^{2+} to Pt and remove the polymer. The etching time for PS-*b*-P2VP with molecular weights 88k-*b*-18k and 44k-*b*-18.5k was 30 s for Pt and 35 s for Au and with molecular weight 44k-*b*-8.5k was 20 s for Pt and 25 s for Au. Both

the layers were annealed identically, metalized with Pt, and used the same RIE recipe for sequential self-assembly. For all the RIE control experiments, a thin film of PS-*b*-P2VP with molecular weight 88k-*b*-18k was used after annealing with THF and metalizing with the Pt. Finally, its subsequent RIE recipe was used.

Thermal annealing of the samples was carried out after the RIE step for RIE control experiments and Au@Ag core-shell nanoparticle formation. A hot plate was preheated to 350 °C, and the Si chips containing Pt (for RIE control experiments) or Au (for Au@Ag core-shell nanoparticle formation) nanopatterns were placed at the center of the hot plate for 15 min in open air. The temperature of the hot plate and the thermal annealing time were optimized by using different temperatures and time intervals.

3.2.5 Formation of Au@Ag Core-shell Nanoparticle Arrays

Formation of Au@Ag core-shell nanoparticle arrays were carried out using a procedure developed by Cha et al.[306] A single layer of Au nanoparticles containing a Si chip was immersed in 1.0 L of beaker containing ultra-pure water at room temperature. Then, 10 mL of 10 mM $AgNO_3$, 10 mL of 20 mM hydroquinone, and 132.2 μL of CTAC were added simultaneously to the beaker while stirring with a magnetic bar. The immersion time varied in order to change the thickness of the Ag shell. After Ag deposition, the samples were taken out from the reaction mixture, washed with ultra-pure water, and dried with a nitrogen stream.

3.2.6 Film Characterization and Data Processing

All images were taken from a Hitachi S4800 scanning electron microscope (15 kV, 20 μA) or an atomic force microscope (AFM) (Digital Instrument /vecco, tapping mode under ambient conditions). All the SEM micrographs and AFM images were processed using ImageJ and Gwyddion softwares.

3.3 Sequential Self-assembly of BCPs

In this chapter, we wished to form mixed metal or mixed metal/metal oxide nanopatterns using the PS-*b*-P2VP BCP, utilizing its chemical handle to bind to anionic metal complexes in the presence of acid. As will be described, the biggest challenge

faced was the optimization of the RIE step, as it often resulted in damaged or missing metal patterns. To overcome this obstacle, substantial optimization and control experiments needed to be executed. To start with, the basic metric was one of establishing a route to patterns with no overlap, within a 'perfect' lattice, with a value of β less than 1, as shown in Figure 3.6(b); β represents the fraction of empty space between a dot residing in the interstitial position of the host hexagonal lattice. Table 3.1 shows the selected PS-*b*-P2VP BCPs with different molecular weights and their corresponding dot sizes, pitches, and β values. Hence, assuming that the β values are less than 1 for all the PS-*b*-P2VP BCPs tested here, honeycomb lattices were expected to be formed by sequential self-assembly of each PS-*b*-P2VP, assuming that the registration of the second layer would be driven by the topology of the resulting dot pattern and is not affected by the chemical inhomogeneity of the surface (native silica layer and Pt surfaces).

Table 3.1. Pitch, Dot Diameter and Calculated β of the Different BCPs Used in This Study

Molecular weight of PS-*b*-P2VP	Diameter of Pt dot (d_0) / nm	Pitch (l_0) / nm	Calculated β
88k-*b*-18k	19 ± 2	46 ± 1	0.72
B'30	20 ± 1	44 ± 1	0.79
44k-*b*-8.5k	17 ± 1	34 ± 1	0.85

Figures 3.7, 3.8, and 3.9 show attempts at formation of sequential nanopatterns of double layer of Pt–Pt dot patterns using different molecular weights of PS-*b*-P2VP, 44k-*b*-8.5k, B'30, and 88k-*b*-18k, respectively. Figures 3.7, 3.8, and 3.9 (a & b) show low and high magnification images of hexagonally ordered single layers of Pt nanodot arrays achieved by self-assembly of PS-*b*-P2VP with different molecular weights. Sequential deposition of a corresponding BCP with the same molecular weight of PS-*b*-P2VP on each single layer of Pt nanodot patterns did not, however, yield honeycomb lattices even though the expected β values were observed for all three molecular weights of PS-*b*-P2VP tested, as shown in Figures 3.7, 3.8, and 3.9 (c & d). The brighter dots appear to correspond to the top layer of Pt nanodots, and the dimmer/fainter dots

are what presumably remains of the bottom (first) Pt layer. The order also is affected as the process leads to rather randomly organized double layers of Pt–Pt nanodots. A major obstacle for the generation of double layers of Pt–Pt double layers from PS-*b*-P2VP BCPs was the disordering of the bottom layer of Pt nanoparticles upon self-assembly of the second layer of Pt nanoparticles [Figure 3.8 (c & d)] and [Figure 3.9 (c & d)]. It is clearly visible from Figures 3.7, 3.8, and 3.9 (a & b) that the corresponding bottom layers of Pt from the first double layer pattern have an ordered hexagonal nanodot pattern prior to self-assembly of the top layer of Pt dots, but that the this ordered initial layer undergoes deterioration upon assembly of the second layer. From Figure 3.8 (c & d) and Figure 3.9 (c & d), it can be seen that some of the bottom layer Pt dots appear to be missing from the double layer pattern. Hence, as a result of the second layer deposition, the order of the bottom layer Pt nanoparticles decreases and particles go missing, resulting in randomly organized nanodot patterns.

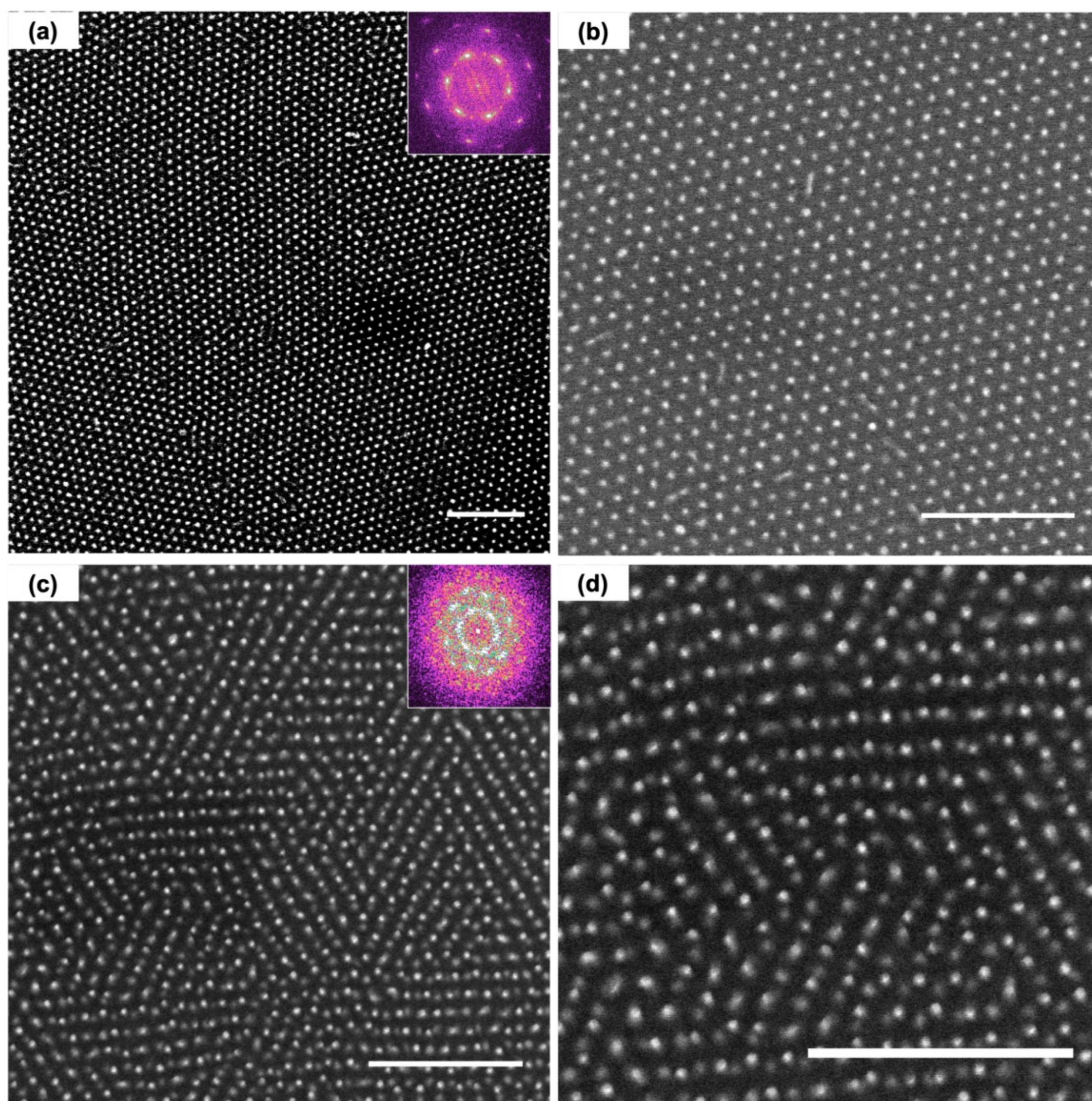

Figure 3.7. SEM micrographs of (a) low and (b) high magnification images of a single layer of Pt nanodot pattern generated from PS-*b*-P2VP (44k-*b*-8.5k) of the same sample. (c) Low (d) high magnification images of sequential nanopatterning of Pt–Pt double layer dot patterns using the single layer of Pt nanodot pattern in (a). Brighter dots correspond to the second layer of Pt nanopattern, and dark dots represent the bottom layer of Pt nanodots. All the scale bars are 250 nm, and the insets show the corresponding FFT of the nanopattern.

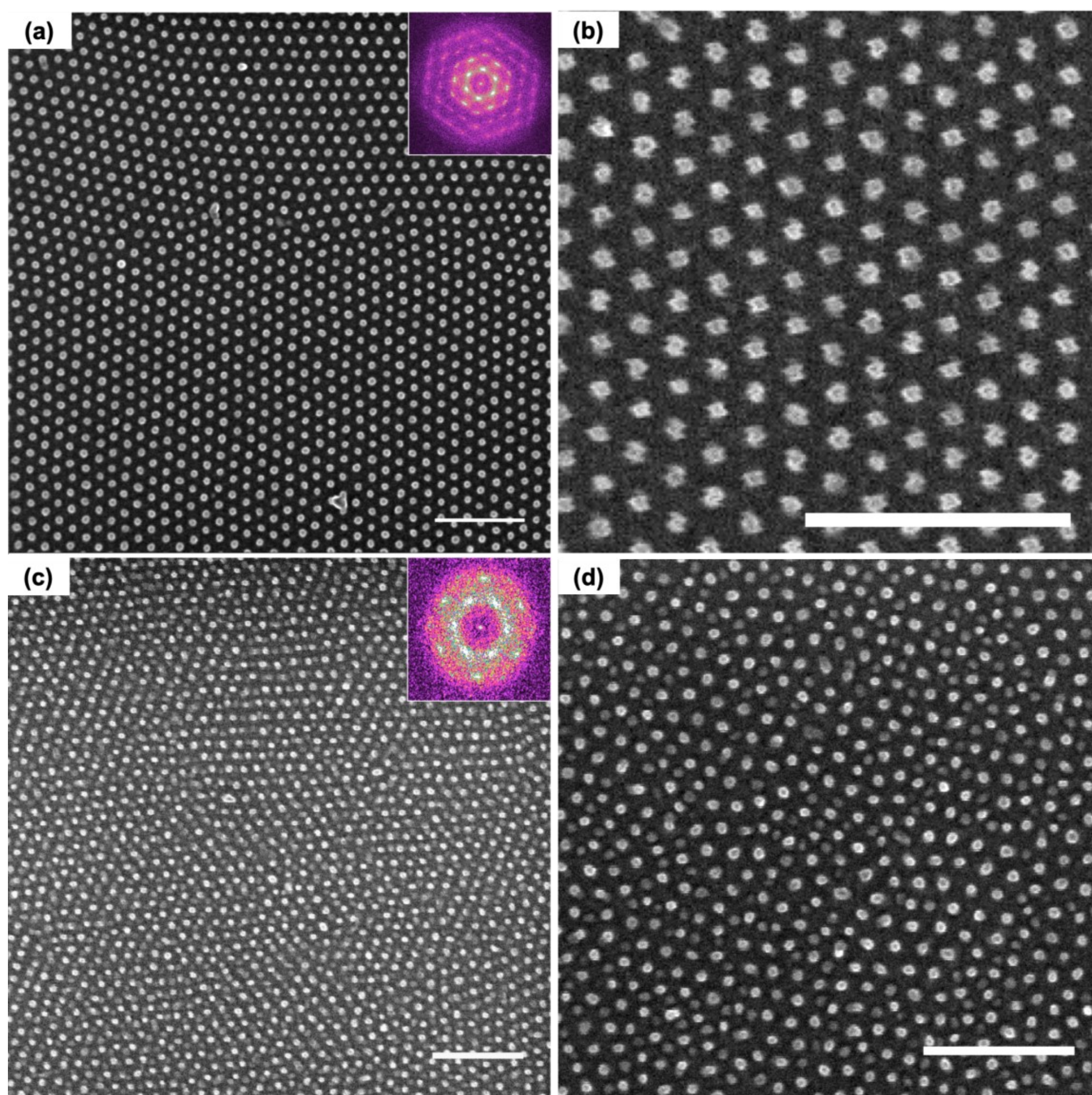

Figure 3.8. SEM micrographs of (a) low and (b) high magnification images of a single layer of Pt nanodot pattern generated from PS-*b*-P2VP (44k-*b*-18.5k) blended with 30% PS (10k). (c) Low and (d) high magnification images of sequential nanopatterning of Pt–Pt double layer dot patterns using the single layer of Pt nanodot pattern in (a). Brighter dots correspond to the second layer of Pt nanopattern and dim dots represent the bottom layer of Pt nanodots. All the scale bars are 250 nm, and the insets show the corresponding FFT of the nanopattern.

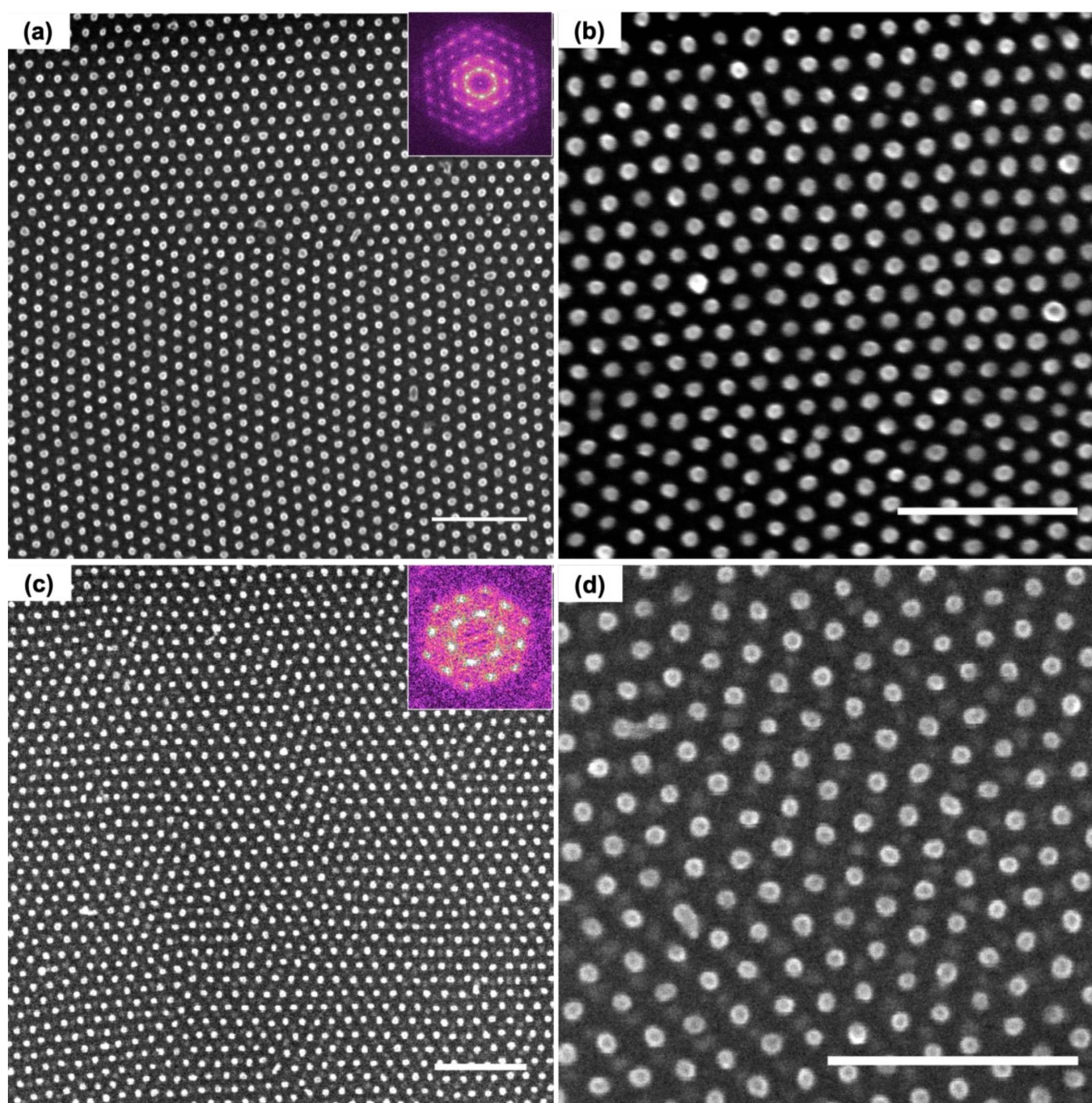

Figure 3.9. SEM micrographs of (a) low and (b) high magnification images of a single layer of Pt nanodot pattern generated from PS-*b*-P2VP (88k-*b*-18k). (b) Low and (c) high magnification images of sequential nanopatterning of Pt–Pt double layer dot patterns using the single layer of Pt nanodot pattern in (a). Brighter dots correspond to the second layer of Pt nanopattern and dark dots represent the bottom layer of Pt nanodots. All the scale bars are 250 nm, and the insets show the corresponding FFT of the nanopattern.

At this point, it is not possible to determine the origin of the disorder of the double Pt layers. Possibilities include damage resulting from contact with the BCP solution, the subsequent solvent annealing, the RIE treatment, or all three that could be damaging the initial Pt layer. Before this question was addressed, it was needed to determine whether PS-*b*-P2VP BCPs could form commensurate double layers with any hexagonal pattern since the Pt–Pt double layer project had too many issues to manage

simultaneously. To simplify the architecture, first prepared a pattern of SiO_x hexagonal dots from established PS-*b*-PDMS-based BCPs, followed by self-assembly of a second PS-*b*-P2VP BCP. Figure 3.10 shows the results of this density multiplication using PS-*b*-PDMS (**B30**) and PS-*b*-P2VP (**B'30**) sequential self-assembly where the pitch ratio is equal to 1.0. The PS-*b*-P2VP layer has been transformed into Pt. Figure 3.10(a) shows a single layer of hexagonal SiO_x nanodots, with the second layer of Pt nanoparticles derived from PS-*b*-P2VP (**B'30**); formation of a honeycomb lattice was observed, and the commensurate pitch ratio between SiO_x–Pt was as expected. The SEM image in Figure 3.10(b) shows the SiO_x–Pt honeycomb pattern, where the bigger dots are the SiO_x bottom layer, and the smaller brighter dots are derived from the Pt top layer. An attempt at depositing a third layer of Pt nanoparticles on the double layer of SiO_x-Pt nanopattern by self-assembly of PS-*b*-P2VP (**B'30**) is shown in Figure 3.10(c). The triple layer SiO_x–Pt–Pt pattern [Figure 3.10(c & d)] shows density multiplication in comparison to the double layer SiO_x–Pt pattern. Since polymers of different molecular weights [PS-*b*-PDMS (**B30**) and PS-*b*-P2VP (**B'30**)] were used to generate the triple layer SiO_x–Pt-–Pt pattern, the resulting pattern is expected to have two different size distributions (SiO_x and Pt). However, in the triple layer SiO_x–Pt–Pt pattern, a few different size distributions were observed, which made it difficult to distinguish the second layer and the third layer Pt nanoparticles separately [see Figure 3.10(c)]. In order to identify whether this observation is related to the self-assembly of the consecutive Pt layer, control experiments were carried out, as explained in the next section.

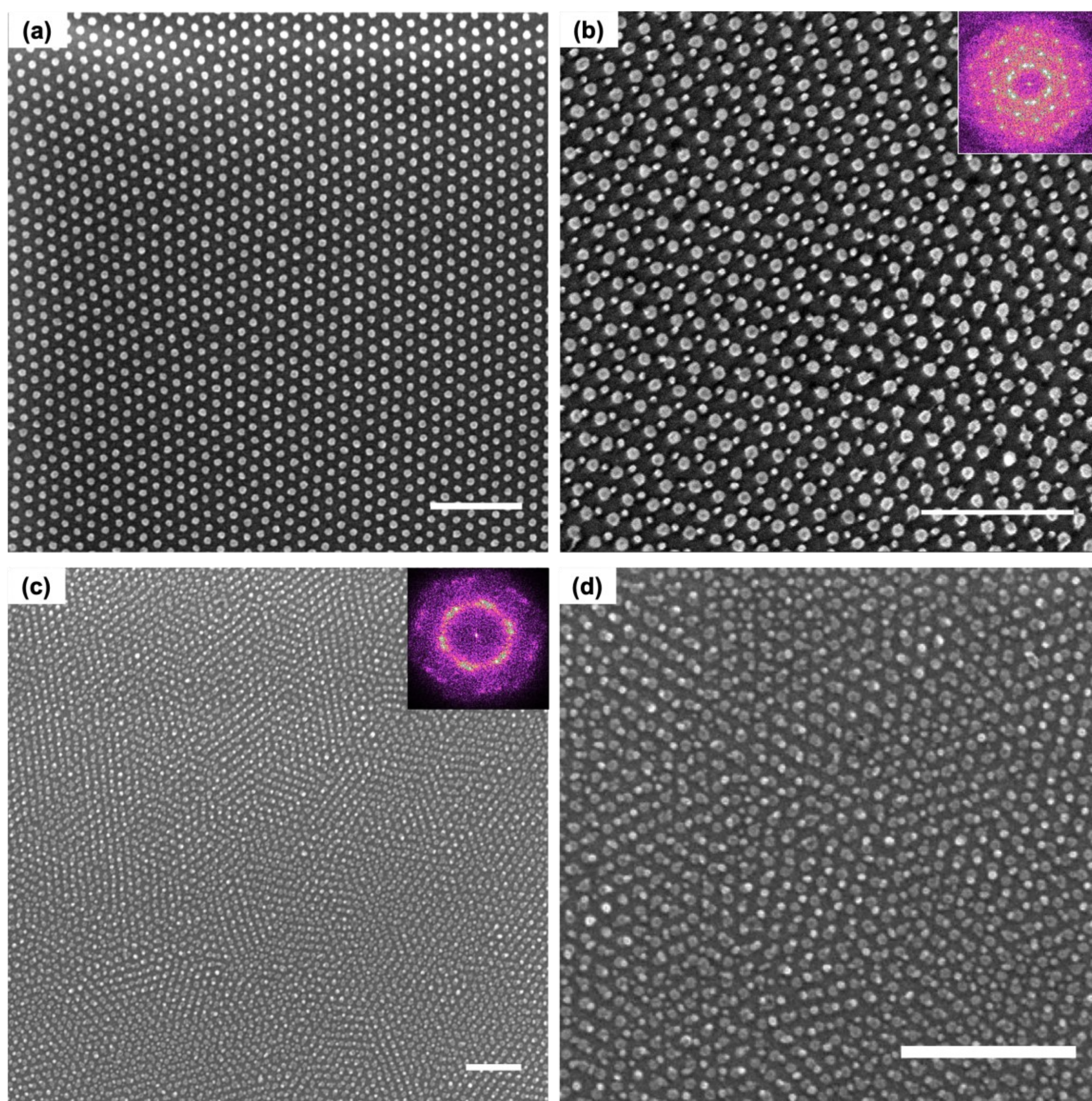

Figure 3.10. SEM micrographs for (a) a single layer of hexagonal SiO_x dot pattern from self-assembly of **B30** (b) sequential self-assembly of a second layer of hexagonal Pt nanodots on the bottom layer SiO_x dot pattern using **B'30** with pitch ratio of 1.0, and (c) low and (d) high magnification images of triple layer formation of SiO_x–Pt–Pt on top of the double layer of SiO_x–Pt using identical self-assembly process to the second layer. All the scale bars are 250 nm, and the insets show the corresponding FFT of the double and triple layers.

3.4 Optimization of the Reactive Ion Etching

A discharged gas containing reactive radicals, ions, and electrons is used in plasma etching to create ion sputtering or reactions with surfaces by reactive radical species with or without ion assistance to form volatile products.[310] The etching process proceeds by physically sputtering or evaporating chemically reacted volatile products. The etch directionality of the plasma etching can be controlled by energy input, a

suitable reactor, and plasma parameters. There are four types of reaction mechanisms involved in plasma etching, as illustrated in Figure 3.11.[311,312] 1) Sputter etching [Figure 3.11(a)] is a pure physical process, resulting from the surface bombardment of high-energy ions with anisotropic etching, poor selectivity, high surface damage, and low etching rates. 2) Neutral species generated in the plasma react with etched layers to form volatile compounds that can cause chemical etching (also known as chemical volatilization). This is typically an isotropic etching and can achieve high etch rates along with good etch selectivity and low damage to the substrate. 3) A combination of physical and chemical processes is called ion-enhanced chemical etching [Figure 3.11(c)], where ion bombardment enables the material selective etch anisotropy. 4) Inhibitor ion-enhanced chemical etching is another method, which utilizes both physical and chemical etching, where an inhibitor passivates the surfaces that are not exposed to ion bombardment [Figure 3.11(d)]. The last two types of etching are related to RIE.

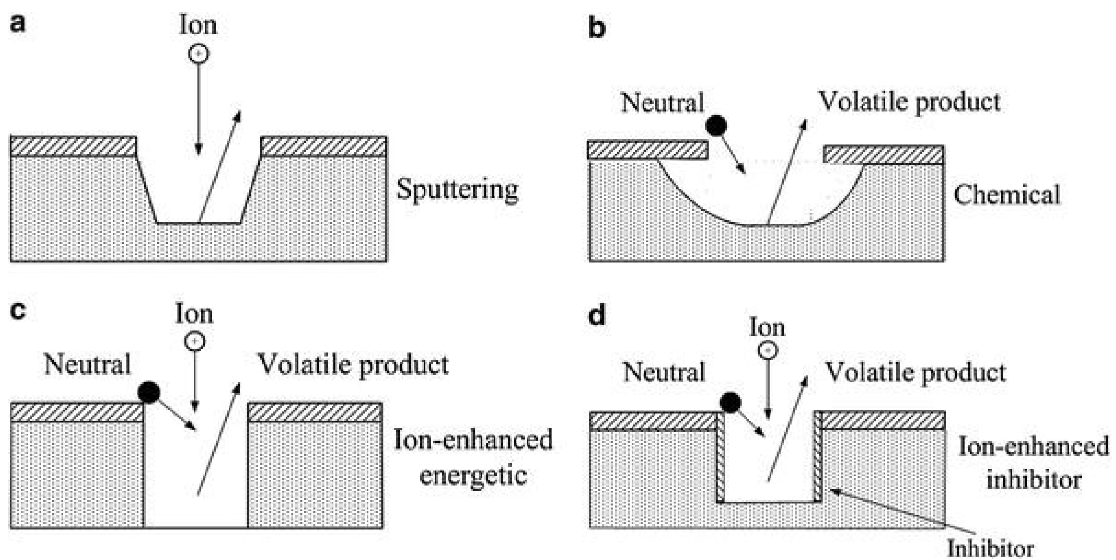

Figure 3.11. A schematic illustration of four types of plasma mechanisms. (a) Sputter etching, (b) chemical etching, (c) ion-enhanced chemical etching, and (d) inhibitor ion-enhanced chemical etching. This image is from reference 310 with permission from Springer Nature.

Chemical plasma etching generally is designed to have chemical reactions with plasma species, it minimizes physical effects involved with ion bombardment, and usually is an isotropic etching process. The pressure is relatively high in plasma chemical processes, between 0.2 torr to 1 torr.[311,312] For RIE, however, the pressure is

in the range of 0.01–0.2 torr. O_2 plasma is one of the most widely used methods for the preparation of various nanoparticle assemblies from PS-*b*-P2VP.[313] Figure 3.12(a) shows the SEM micrograph of a Pt nanodot array generated by self-assembly of PS-*b*-P2VP (56k-*b*-21k), followed by etching with 0.6 torr O_2 plasma for 1 min to remove the polymer and reduce the Pt^{2+} to Pt(0). Figure 3.12 (b) shows the Pt nanopattern generated using the same BCP with RIE of 0.1 torr O_2 plasma for 20 s. These results clearly show that RIE is superior to chemical plasma etching, and thus this method was used throughout this chapter.

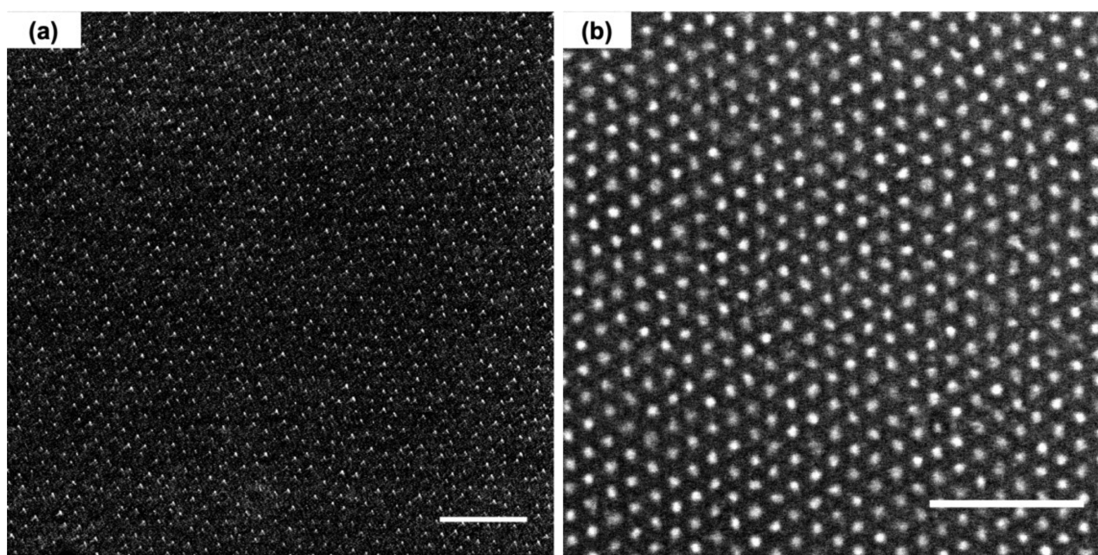

Figure 3.12. SEM micrographs of a single layer of Pt nanopattern generated by self-assembly of PS-*b*-P2VP (56k-*b*-21k) pattern transfer with (a) chemical plasma etching using 0.6 torr O_2 plasma for 1 min and (b) RIE using 0.1 torr O_2 plasma for 20 s.

In this chapter, PS-*b*-P2VP BCPs were going to generate metal nanodot patterns on native oxide-capped Si substrates using the chemistry described vide supra, in which anionic metal complexes interact with the protonated pyridine group in the P2VP block. Since it appears that the second block polymer assembly and the corresponding annealing and plasma treatment seems to be detrimental to the first patterned layer, examination of the individual components of the self-assembly process was carried out. First, the spin coating conditions were investigated to check whether the spin coating of a second layer of PS-*b*-P2VP using toluene can dissolve or rearrange the initial/bottom metal dot pattern layer. Figure 3.13(a) shows a single layer of Au nanopattern that had been prepared using PS-*b*-P2VP (88k-*b*-18k) after a 100 mTorr,

O_2 RIE (80 sccm) at an RF power of 30 W for 30 s. A hexagonal ordered Au nanopattern was observed by this self-assembly process. Figure 3.13(b) shows the same sample after spin coating a second layer using only toluene (no BCP). There was no significant difference to the hexagonal Au nanopattern observed before and after toluene spin coating. These results clearly show that contact of the metal dots with solvent upon deposition of a second layer of BCP did not affect the order of the hexagonal Au nanopattern; we would assume that the same is true for other metals, including Pt. Therefore, we focused our attention on the most energetic process of the second deposition step, the etching (in this case, RIE), which seems to be the most likely source of damage.

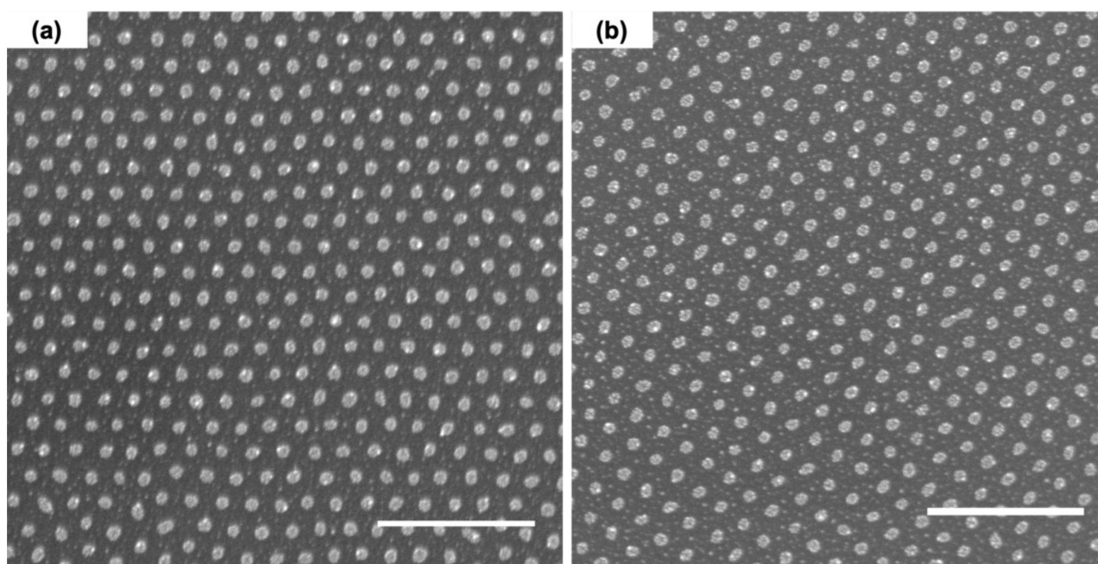

Figure 3.13. SEM micrographs of a single layer of Au nanoparticles fabricated using PS-*b*-P2VP (88k-*b*-18k) (a) after a RIE step and (b) after spin coating a second layer using only toluene without the BCP on the same sample shown in (a). All the scale bars are 250 nm.

We then analyzed the effect of exposing a single layer of self-assembled Pt nanoparticle array [Figure 3.14(a,b)] to an identical second RIE step (without self-assembling a second layer of Pt nanoparticles), as shown in Figure 3.14(c,d). After the second RIE exposure, the hexagonal Pt nanoparticle array was disordered, and the size and height of the Pt dots reduced significantly from 19 ± 2 nm and 24 ± 2 nm to a broader distribution of nanoparticle sizes [see Figure 3.14(d) inset]. Hence, these results show that the bottom layer of Pt nanopatterns cannot withstand a second RIE

step, and that it apparently can dislodge and enable mobility of the Pt nanoparticles on the substrate surface, while also reducing their size.

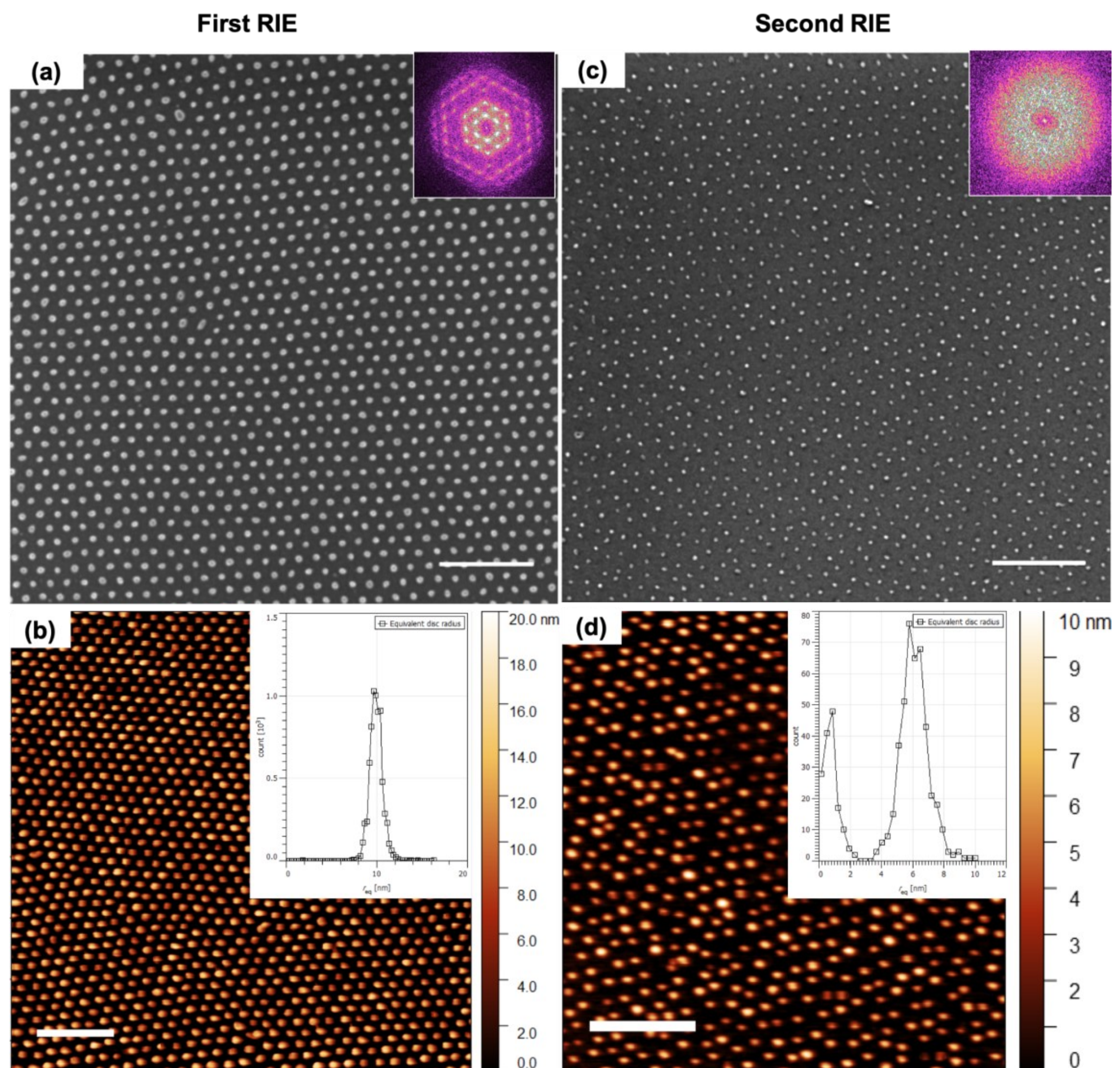

Figure 3.14. SEM and AFM micrographs of (a,b) a single layer of a hexagonal Pt dot nanopattern from PS-*b*-P2VP (88k-*b*-18k) after the first RIE step. (c,d) After the first RIE step the same sample of Pt dot nanopattern is subjected to a second RIE step as the first. All scale bars are 250 nm and insets represent the FFT of the corresponding nanopattern.

It is important to understand the reasons behind this observed phenomenon of disordering of a single layer of a metal dot pattern upon subsequent RIE to address the issue and come up with solutions. Research by the BCP self-assembly pioneers, Spatz and co-workers, noted that the presence of metal ions and/or metal nanoparticles can play a dramatic role with regard to the etching rates of self-assembled PS-*b*-P2VP

BCPs. They observed that thickness variations in the film and incorporation of inorganic complexes and nanoparticles, $HAuCl_4$ and gold nanoparticles, in the P2VP block alters the etching contrast between the blocks in the BCP.[314] They calculated the Ar^+ etching rates of different micellar domains with respect to the Ar^+ sputtering rate of a GaAs substrate (30 Å/min) using the height information gathered from SEM micrographs. There was no difference between etching rates of PS and P2VP. However, the P2VP blocks with incorporated $HAuCl_4$ etched twice as quickly as pure PS or P2VP blocks of the same thickness [see Figure 3.15(a)]. Most importantly, embedded gold particles with P2VP blocks were etched at a rate that was 10 times faster than P2VP blocks with $HAuCl_4$, with the results shown schematically in Figure 3.15(b). These observations can be explained by the fact that the sputtering probability is proportional to Z^2 where Z is the atomic weight. Due to the high energy interface of the gold nanoparticles, the gold nanoparticles ended up destroyed before the BCP itself.[315] Thus, these results by Spatz and co-workers are related closely to ours, that is, small metal nanoparticles will etch rapidly under these conditions, faster than the organic BCP, leading to the observed instability. A careful reconsideration of the goals of this work was required moving forward.

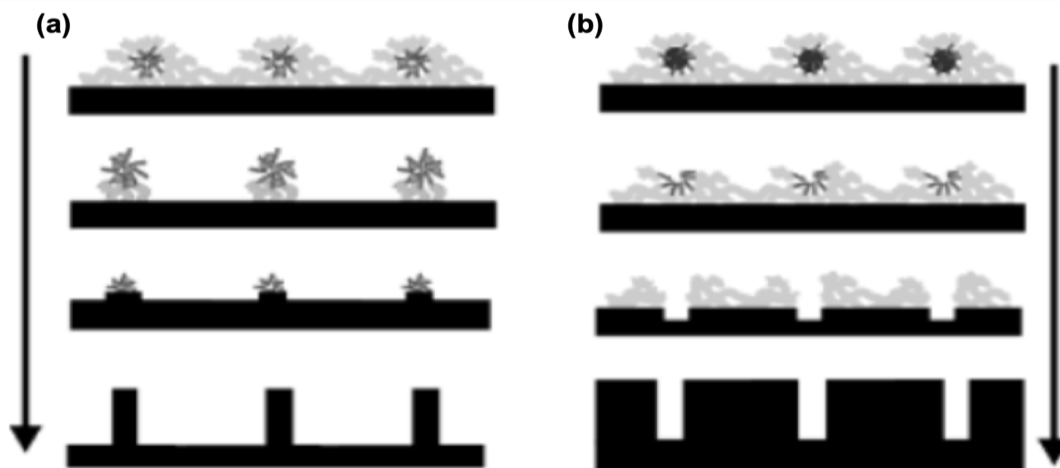

Figure 3.15. A schematic representation of island and hole formation upon etching of a thin film of a PS-*b*-P2VP layer on silicon. (a) The PS-*b*-P2VP layer contains $HAuCl_4$ embedded within the P2VP block. (b) The PS-*b*-P2VP contains Au nanoparticles upon etching. The gold nanoparticles etch faster under these conditions than both the PS and P2VP blocks. Reprinted from reference 314 with permission of Wiley-VCH.

3.5 Optimization of Thermal Annealing

In this section of the chapter, we regroup from the failure of the synthesis of metal double layers. The stability of the initial layer of Pt nanodots during the RIE etch is insufficient, but before abandoning, we considered one final attempt at generating more stable Pt nanodot arrays as a first layer. The source of the mobility of the Pt nanoparticles during the second RIE step could be due to residual polymer that, upon heating and decomposition within the RIE chamber, could lead to the observed nanoparticle mobility. In addition, close examination of SEM micrographs of the gold and platinum nanoparticles is suggestive of these dots being composed of several smaller particles lumped together (see Figure 3.16). Since the melting temperature of small gold and platinum nanoparticles is substantially lower than that of bulk gold and platinum,[316–318] a heating step to agglomerate these small gold or platinum nanoparticles was considered. Sufficiently high temperatures also could remove any remaining residual PS-*b*-P2VP that is providing mobility to the metal nanoparticles during the energetic RIE step.

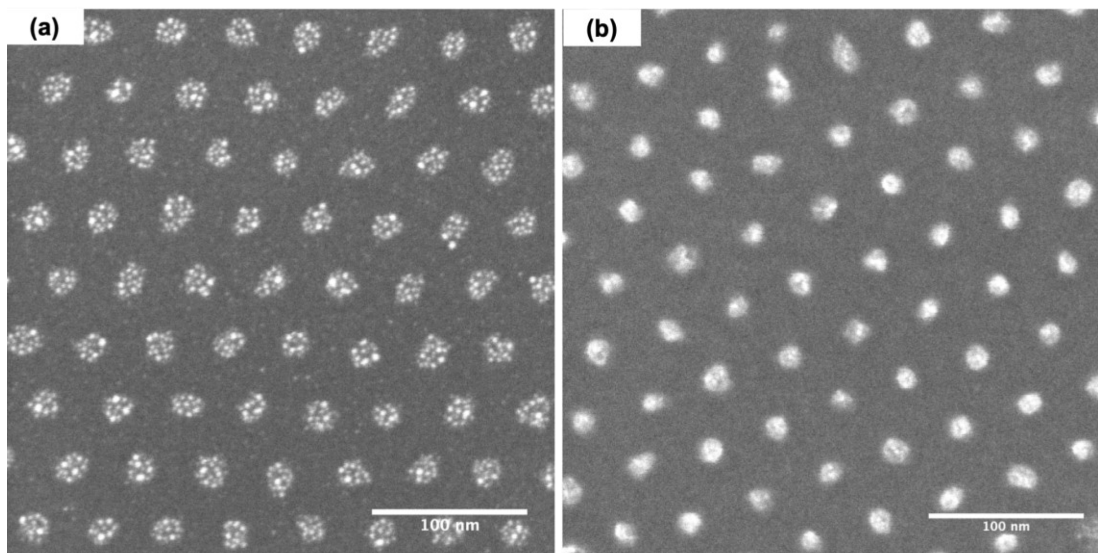

Figure 3.16. Higher magnification SEM micrograph of a (a) Au and (b) Pt nanopattern prepared via self-assembly of PS-*b*-P2VP (88k-*b*-18k), followed by RIE.

A simple hot plate thermal treatment in laboratory ambient was used, and the hotplate was preheated to different temperatures: 250 °C, 350 °C, and 550 °C. This optimization method is shown in detail only for Pt nanoparticle arrays and can be

generalized for Au nanopatterns. Pt nanoparticle arrays prepared from PS-*b*-P2VP (88k-*b*-18k) and subjected to one course of RIE were placed on the hot plate for different time intervals, as shown in Figures 3.17−3.18. Figure 3.17(a) shows the SEM micrograph of the Pt nanopattern after subjecting the sample to an O_2 RIE step for 5 s instead of 30 s of full RIE recipe. It is assumed that the Pt^{2+} would not be converted to Pt(0) completely with this short treatment and that the majority of the polymer would still be present.[319] Then, the sample was subjected to a thermal annealing process at 250 °C for 1 h, with the resulting pattern shown in Figure 3.17(b). Even though the thermal annealing seems to be converting all or some of the Pt^{2+} to Pt(0), even with partial RIE treatment, some dots are missing.[320] As a control experiment, Figure 3.17(c) shows a Pt pattern treated only with thermal annealing at 250 °C for 1 h without using RIE, which results in disordered Pt nanoparticles on the surface; clearly thermal annealing at 250 °C without RIE itself cannot generate a single layer of sufficiently ordered Pt nanoparticles.

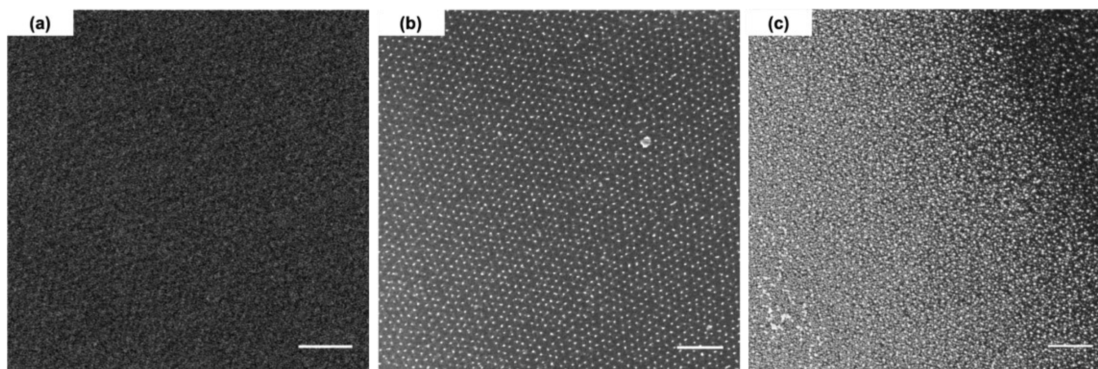

Figure 3.17. SEM micrographs of Pt nanopatterns by PS-*b*-P2VP (88k-*b*-18k) developed using (a) partial RIE of 100 mTorr, O_2 RIE (80 sccm) at RF power of 30 W for 5 s (b) partial RIE of 100 mTorr, O_2 RIE (80 sccm) at RF power of 30 W for 15 s, followed by thermal annealing at 250 °C for 1 h, and (c) thermal annealing at 250 °C for 1 h without using RIE. All scale bars are 250 nm.

In the next set of experiments, the highest temperature, 550 °C, was tested. Figure 3.18(a) shows the SEM micrograph of Pt nanopattern after subjecting the sample to an O_2 RIE step for 15 s, followed by thermal annealing at 550 °C for 10 min [see Figure 3.18(b)], 15 min [see Figure 3.18(c)], and 30 min [see Figure 3.18(d)]. As per the SEM micrographs, it is clear that longer times lead to more disordered patterns. The next set of experiments looked at the intermediate temperature of 350 °C, as shown in

Figure 3.19(a). This figure shows the SEM micrograph of a Pt nanopattern after subjecting the sample to an O_2 RIE step for 30 s, followed by thermal annealing at 350 °C for 15 min [Figure 3.19(b)] and 30 min [Figure 3.19(c)]. The apparent size of the Pt nanodots in the heated samples is 5 nm, and the patterns are nicely ordered with only a few dots missing. We then ended our work to optimization at this point with these successful conditions of a 350 °C thermal treatment post-RIE.

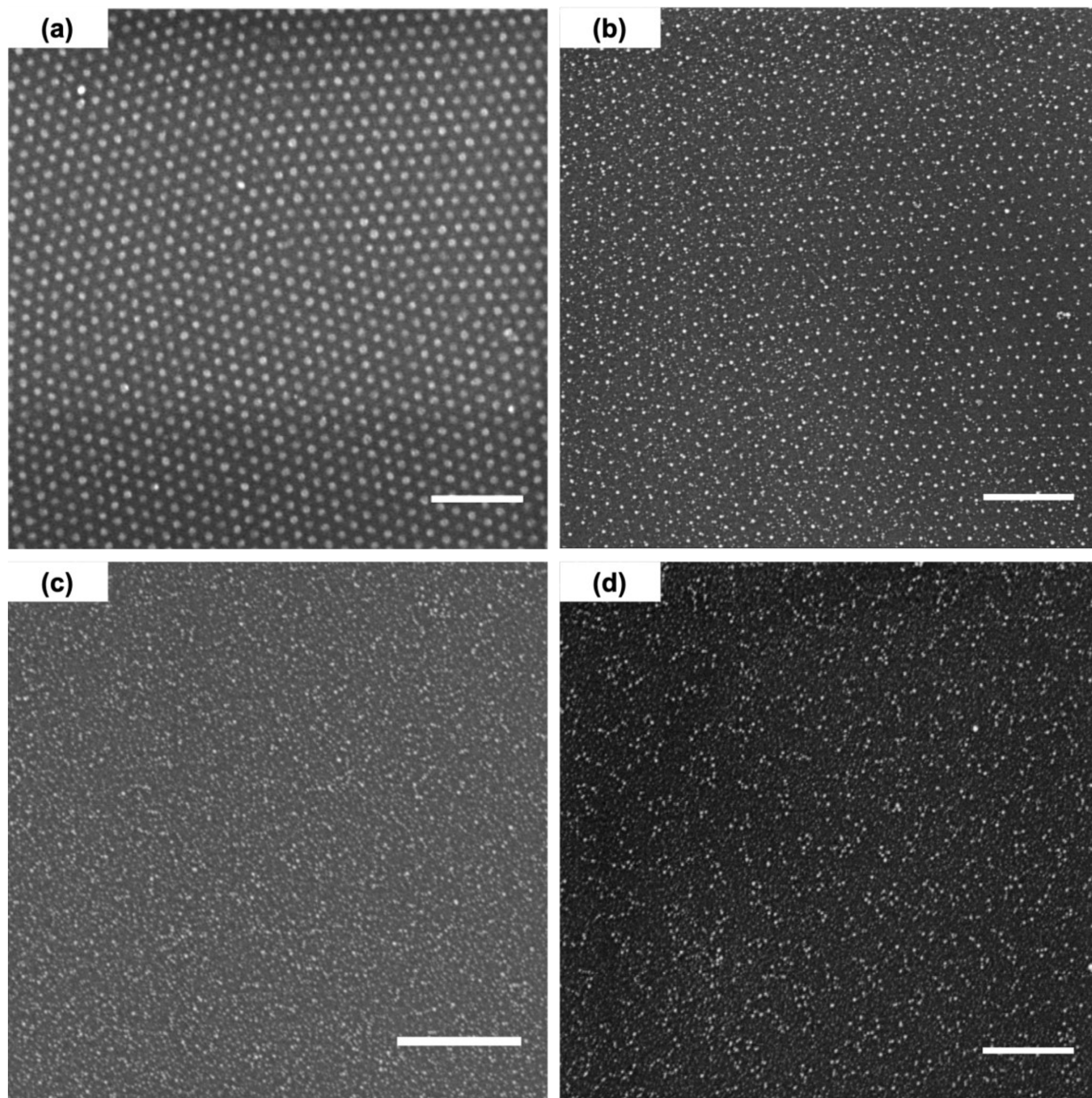

Figure 3.18. SEM micrographs of Pt nanopatterns by PS-*b*-P2VP (88k-*b*-18k) developed using (a) partial RIE of 100 mTorr, O_2 RIE (80 sccm) at RF power of 30 W for 15 s, followed by (b) thermal annealing at 550 °C for 10 min, (c) thermal annealing at 550 °C for 15 min, and (d) thermal annealing at 550 °C for 30 min. All scale bars are 250 nm.

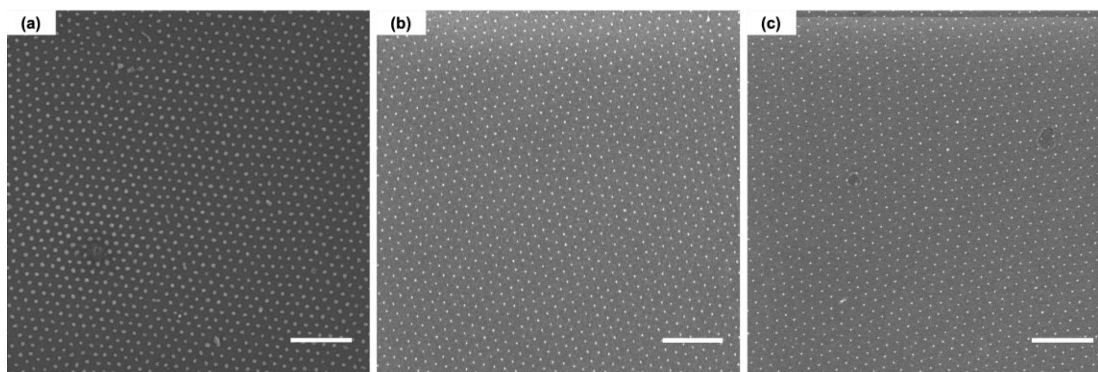

Figure 3.19. SEM micrographs of Pt nanopatterns by PS-*b*-P2VP (88k-*b*-18k) developed using (a) RIE of 100 mTorr, O_2 RIE (80 sccm) at RF power of 30 W for 30 s, followed by (b) thermal annealing at 350 ˚C for 15 min, and (c) thermal annealing at 350 ˚C for 30 min. All scale bars are 250 nm.

Even though the thermal annealing step was optimized, we had to ensure that these single layers of metal nanopatterns generated as a combination of RIE and thermal annealing steps are stable with respect to a subsequent RIE step in the second self-assembly process. For this purpose, a sample comprising a single layer of a Pt nanopattern generated by RIE and thermal annealing was exposed to an identical RIE treatment (without depositing a second layer of BCP). Figure 3.20(a,b) shows the Pt nanopatterns after plasma treatment, and Figure 3.20(c,d) shows the resulting Pt nanopatterns after the thermal annealing at 350 ˚C for 15 min of the same sample. The dot size and height were reduced from 19 ± 2 nm and 24 ± 2 nm to 7.0 ± 1 nm and 4.0 ± 1 nm, respectively, after the thermal annealing process. This decrease in size of the Pt nanodots substantiates the claim that the nanoparticles during RIE are not coalesced fully into single particles (they appear to be made up of multiple particles). After the second O_2 RIE exposure, the order of the Pt nanopatterns was not affected by the second RIE step, however, the size and the height of the nanoparticles was reduced further to 7.0 ± 1 nm and 3.0 ± 1 nm, respectively, as shown in Figures 3.20(e,f). These results confirm that a combination of RIE and thermal annealing can generate a single layer of stable Pt nanopatterns successfully as well as Au nanopatterns, without altering the order of the pattern, which then can be exposed to a second RIE step, potentially to generate double layers of Pt–Pt nanopatterns.

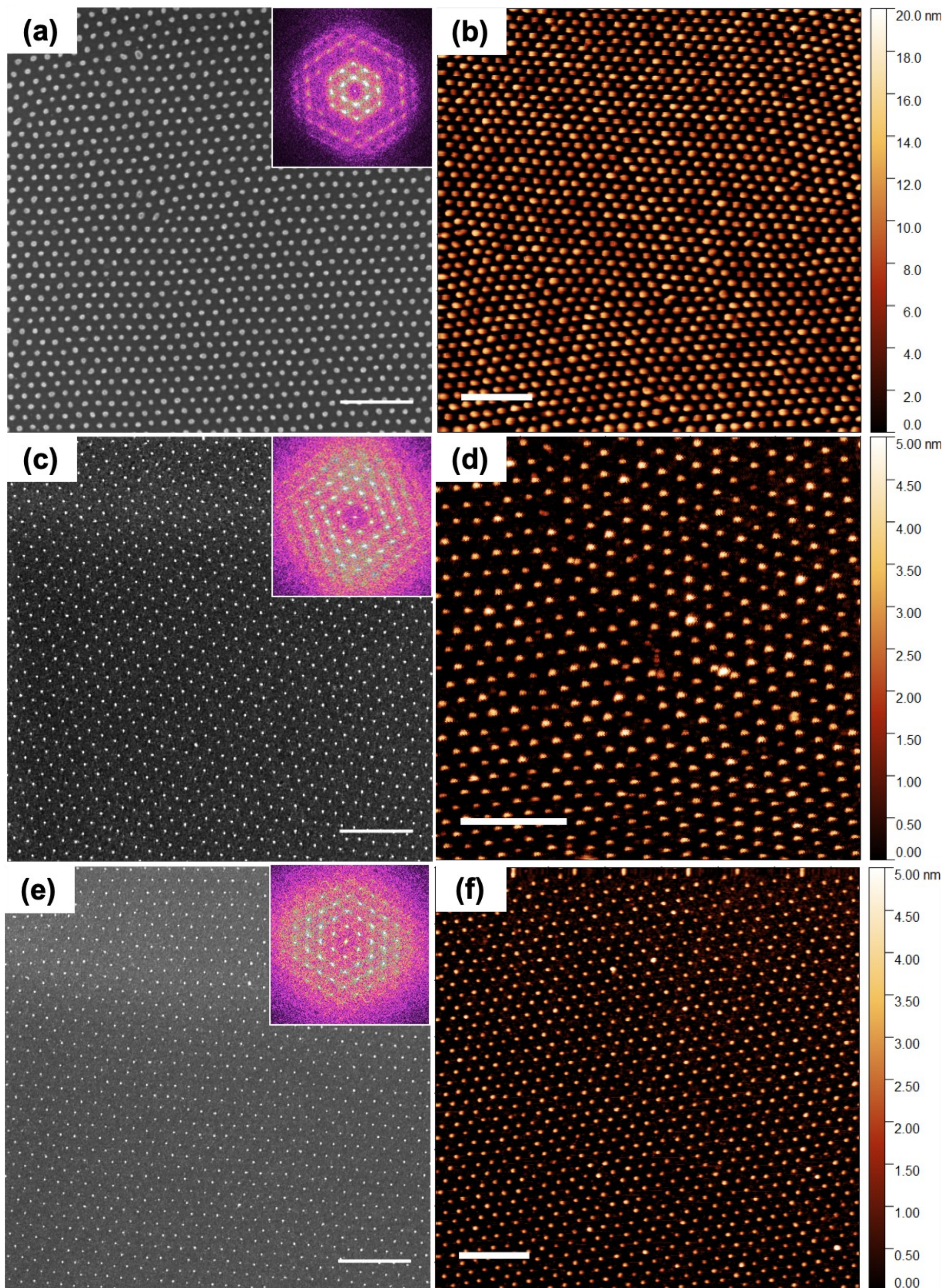

Figure 3.20. SEM and AFM micrographs of (a,b) a single layer of a hexagonal Pt dot nanopattern from PS-*b*-P2VP (88k-*b*-18k) after the first RIE step, (c,d) after the first RIE step the same sample of Pt dot nanopattern was subjected to a thermal annealing step, and (e,f) after the thermal annealing step the same sample of Pt dot nanopattern is subjected to a second RIE step as the first.

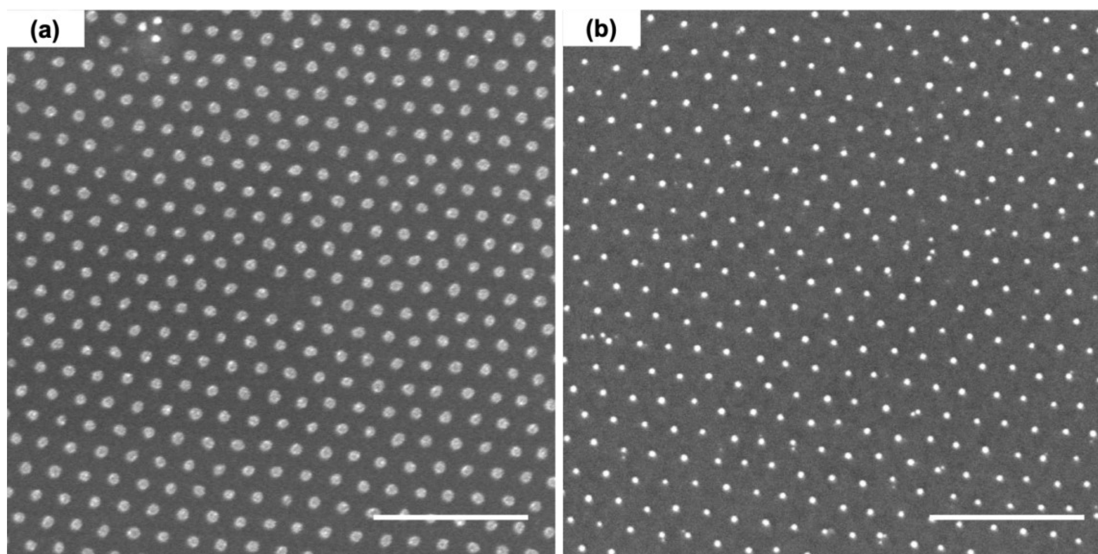

Figure 3.21. SEM micrographs of Au nanopatterns from PS-*b*-P2VP (88k-*b*-18k) after (a) the first RIE step and (b) subsequent thermal annealing at 350 ˚C for 15 min. All scale bars are 250 nm.

This optimized method of combining RIE with thermal annealing was used to generate self-assembled double layers of Pt nanopatterns on a native oxide-capped Si substrate, as shown in Figure 3.22. Figure 3.22 shows a double layer of Pt–Pt nanopattern formation using a combination of RIE and thermal annealing. Figure 3.22(a) is a double layer of Pt–Pt nanopattern, where the bottom layer is etched using RIE and then thermally annealed. The top layer is etched only using RIE and not thermally annealed. Hence, the size of the bottom layer is significantly smaller (seven times) compared to the top layer, even close to invisible in this high magnification SEM micrograph. Figure 3.22(b) is the same sample (low magnification) as that shown in Figure 3.22(a), after the thermal annealing step. Figure 3.22(c,d) shows the high magnification images of Figure 3.22(b). Unfortunately, the diameter and height of the metal nanoparticles decreased significantly from 19 ± 2 nm to 7.0 ± 1 nm for the bottom layer, with the top layer particle size around ~7.0 ± 1 nm in size. As can be seen in Figure 3.22(c,d), the density doubled patterns show no registration between the first and second layers, most likely due to the very small size of the bottom layer of Pt nanoparticles.[305,321,322]

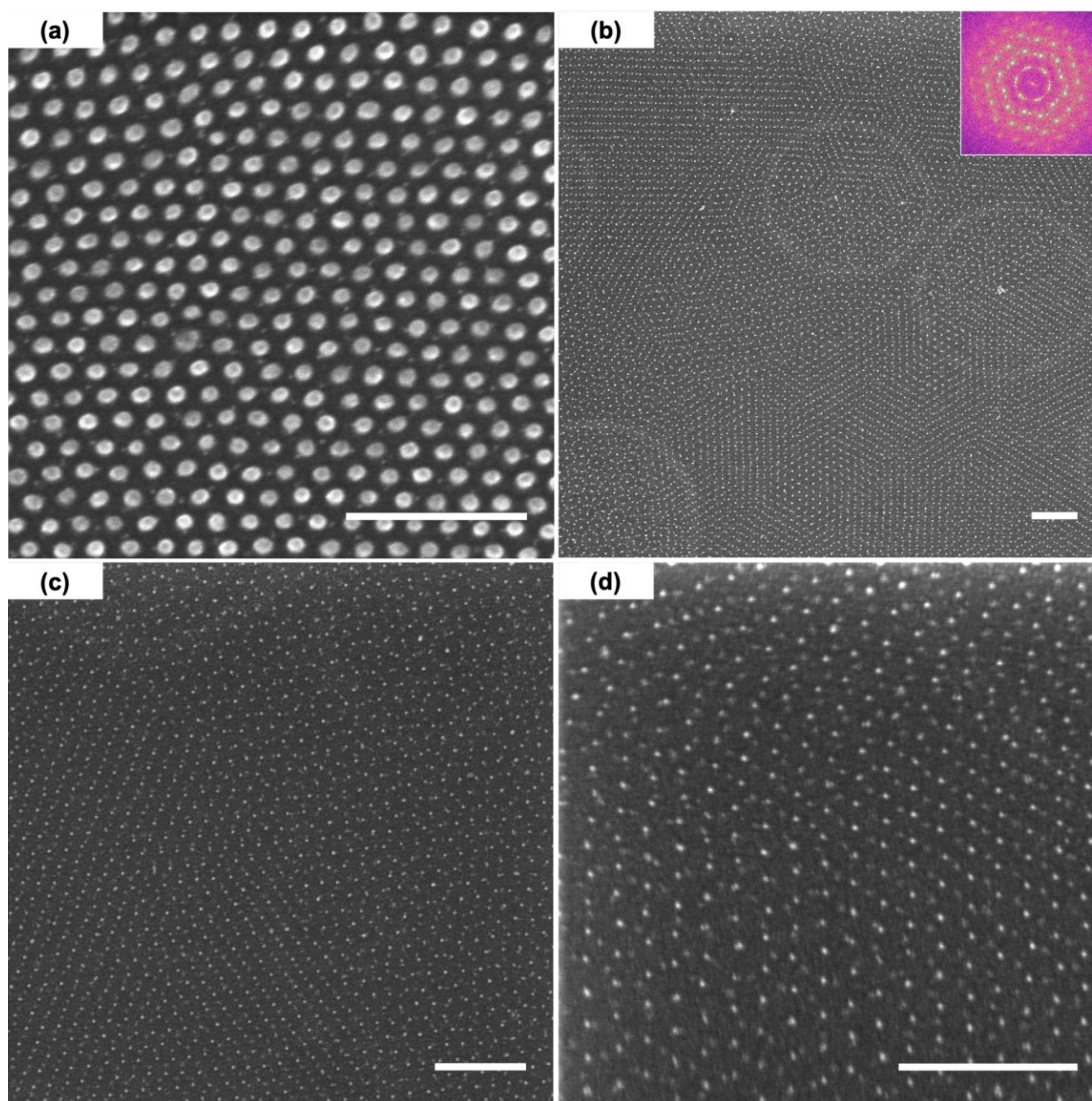

Figure 3.22. SEM micrographs for sequential nanopatterning of a Pt–Pt double layer dot pattern using PS-*b*-P2VP (88k-*b*-18k) (a) bottom layer is after RIE and thermal annealing steps and top layer is only after the RIE step. (b) Low and (c,d) high magnification SEM micrographs of the same pattern after thermal annealing of the second layer. All the scale bars are 250 nm, and the inset shows the FFT of the corresponding pattern.

Registration of the second BCP layer on the first depends upon the size and height of the first layer.[305,321,322] Cong et al. in their work of both commensurate and incommensurate self-assembly of BCPs to generate double layer patterns showed that subtle differences of size of the bottom layer dots can determine the final morphology.[305,322] In this study,[322] they compared an over etched bottom layer pattern (dot size = 18.2 nm, dot height = 5.2 nm) with a normally etched pattern (dot size = 21.8 nm, dot height = 7.3 nm) and observed a significant increase in the long range

ordering and decrease in point defects in the top layer for the pattern when using the over etched bottom layer pattern. Hence, the registration of the top layer is lowered if the size of the bottom layer dots decreases below a critical size. Similarly, for commensurate pitch ratios, they observed a substantial dot overlap instead of a honeycomb pattern formation when most of the dots are not isolated and distinct.[305] The fundamental requirement for density multiplication is that the dots form different layers and must be spatially separate and distinct from each other.[228] While we did not determine that critical size here for PS-*b*-P2VP, it is clear that the Pt nanoparticles are too small to enable registration with the top layer. The final attempt made to enable the use of the metal nanoparticle patterns as the bottom layer for density multiplication is to increase the size of the metal nanoparticles, which is the topic of the next section.

3.6 Au@Ag Core-shell Nanoparticle Arrays

Because the sizes of the metal nanoparticles comprising the bottom layer are too small for registration of the second BCP, we endeavored to increase the size of the metal nanoparticles. The method we chose was an electroless deposition method that results in greater control of the size of gold nanoparticles on a surface. Kim and co-workers combined BCP lithography and subsequent seeded-shell growth to produce highly ordered Au@Ag core-shell nanoparticle arrays with size tunability.[306] In this process, an Au nanopattern on an oxide-capped Si substrate is placed in a beaker containing an aqueous solution of $AgNO_3$, hydroquinone, and cetyltrimethylammonium chloride (CTAC), as shown in Figure 3.23(A). The Ag^+ ions are reduced by hydroquinone, catalyzed by the Au surface, leading to a selective deposition on the gold nanoparticles. This heterogeneous nucleation of Ag on Au nanoparticles is driven by the nanoscale curvature radii, which cause a higher energy interface and increase the reaction rate, as well as the similar crystal structures and lattice constants of Au and Ag 4.08 Å and 4.09 Å, respectively.[323] Figure 3.23(B) shows the Au nanopattern with a size of 11.5 nm, self-assembled using PS-*b*-P4VP, and Figure 3.23(C) shows them after 40 min of Ag deposition when the size increased to 24.6 nm. This method was applied to increase the size of the Au nanoparticle arrays generated by RIE and a thermal annealing process. However, this electroless deposition was not adapted for Pt and, by using an appropriate

electroless Pt deposition chemistry, this method might be generalizable to Pt nanopatterns as well.

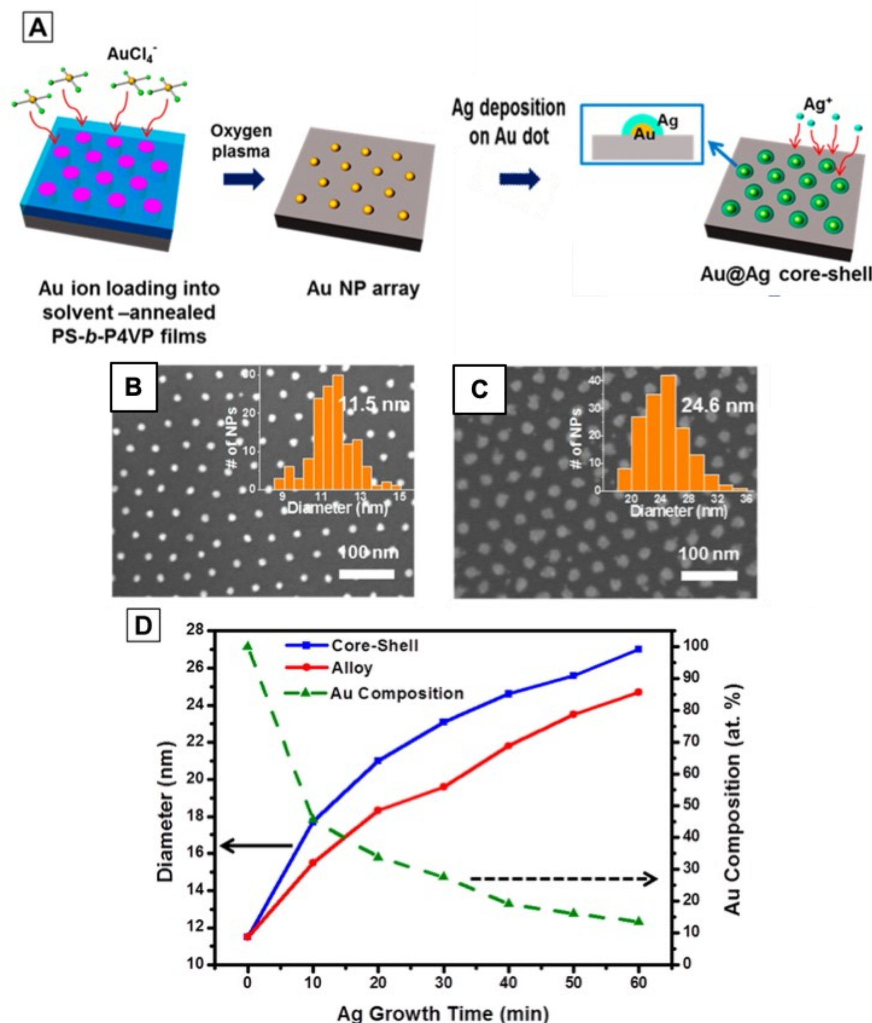

Figure 3.23. (A) A schematic illustration of an Au@Ag core-shell nanopatterning process. (B) SEM micrographs of the Au nanopattern by the PS-*b*-P4VP self-assembly process and (C) Au@Ag core-shell nanopattern after 40 min of growth time. (D) Average diameter and Au composition variation of core-shell plotted against Ag shell growth time. Reprinted with permission from reference 306 by the American Chemical Society.

A single layer of Au nanoparticles was prepared by RIE and the thermal annealing process described earlier. These Au nanoparticles have a diameter of 10 ± 1 nm, and a height of 4.0 ± 1 nm, as shown in Figure 3.24(a,b). After 10 min of Ag deposition on the Au nanoparticle arrays, the diameter and height of the nanoparticles increased to 13 ± 3 nm and 6.0 ± 2 nm, respectively, as shown in Figure 3.24(c,d). The average size of the Au@Ag nanoparticles can be increased further by extending the

deposition time. Further deposition of silver for another 10 min increased the dot diameter and height to 14 ± 2 nm and 7.0 ± 1 nm, respectively [Figure 3.24(e,f)].

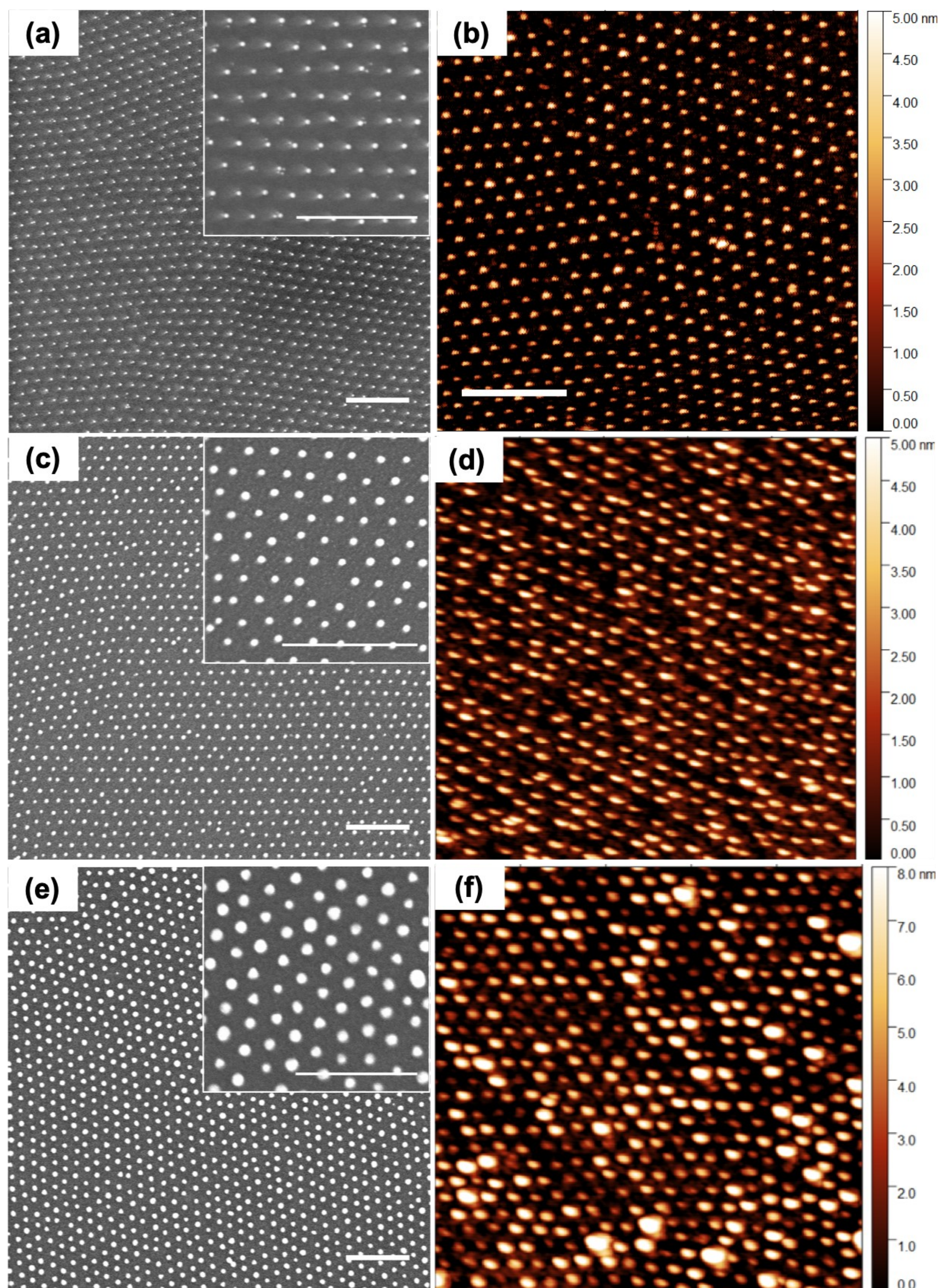

Figure 3.24. SEM and AFM micrographs of (a,b) a single layer of a hexagonal Au dot nanopattern from PS-*b*-P2VP (88k-*b*-18k) after RIE and thermal annealing. (c-f) Au@Ag core-shell formation using (a) for time intervals of (c,d) 10 min (e,f) 20 min. All the scale bars are 250 nm.

However, as mentioned in the previous section, the size and the height of the dots are important for the second layer self-assembly. It can be seen in Figure 3.24(c,e) that the deposition of Ag on Au is not uniform across the Au nanoparticles, leading to a broad size distribution of the resulting Au@Ag core-shell nanoparticle arrays [see Figure 3.25]. Moreover, the reproducibility of the method was not consistent, and we observed much variance in the size distribution across samples. This lack of reproducibility would be a problem when preparing metal-metal double layer patterns since a bottom layer with a broad distribution of size would lead to the formation of random or unpredictable morphologies on the substrate. Hence, this project was stopped at this point, and the RIE step was optimized again using a different etching instrument that enables for two consecutive RIE steps without subsequential nanodot degradation; this will be discussed in Chapter 4.

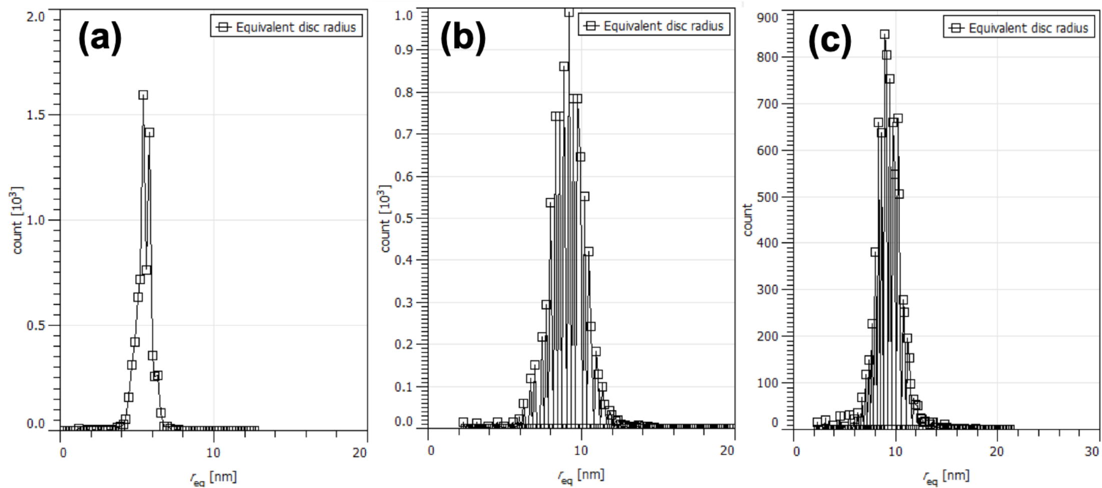

Figure 3.25. Size distribution of (a) single layer of Au nanopattern generated by self-assembly of PS-*b*-P2VP (88k-*b*-18k) after RIE and thermal annealing process, (b) single layer of an Au@Ag core-shell nanopattern after 10 min deposition of Ag on Au from (a), and (c) single layer of an Au@Ag core-shell nanopattern after 20 min deposition of Ag on Au from (a).

3.7 Conclusions

In this chapter, we attempted to optimize the RIE step of a single layer of metal nanopattern fabricated using block copolymer self-assembly in several ways. This optimization was important for the fabrication of double layers of metal-metal nanopatterns via block copolymer self-assembly, which will be the focus of Chapter 4.

Here, we discuss the problems we encountered during this optimization process and the scientific solutions we applied to troubleshoot these obstacles. Incomplete annealing of metal ion–loaded P2VP blocks during the RIE step tends to disorder the bottom layer metal nanoparticles on the silicon substrate upon further RIE treatment. As a result of this incomplete annealing and residual P2VP left in the pattern, this pattern cannot withstand a second RIE step that forms part of the subsequent deposition and processing sequence of the second array of metal nanoparticles. Close examination by SEM of the gold and platinum nanoparticles revealed that post-RIE, the particles actually are composed of multiple smaller particles, which could explain some of the instability to a subsequent RIE. Next, thermal annealing was applied to induce aggregation of these small nanoparticles into a single dot. This step, while successful in aggregating the metal particles into a single dot, resulted in a substantial decrease of the size of the resulting dots. These nanoparticle dots were too small to induce registration of the self-assembly of the second layer of BC properly, and instead, random unaligned morphologies were observed. The last approach taken was to increase the size of the resulting nanoparticles, following RIE and thermal annealing via electroless deposition. Chemical/wet electroless deposition of Ag(0) on self-assembled Au nanoparticles did increase particle sizes, but the variation in particle size distribution and poor reproducibility of the same particle size distribution can lead to random and unpredictable double layer metal-metal patterns. To summarize, a combination of RIE and thermal annealing steps can generate single layer metal nanopatterns via self-assembly of PS-*b*-P2VP successfully, but density multiplication using these single layer metal nanopatterns was not possible, as the resulting particles were too small to induce registration.

Chapter 4

Incommensurate Block Copolymer Self-assembly for Photonic Mixed Metal Nanopatterns

4.1 Introduction

Complex periodic structures on the nanoscale form the basis of many applications and their formation often requires sophisticated nanofabrication techniques. Block copolymer self-assembly is a versatile tool for generating patterns with periodicities in the range of a few nanometers to hundreds of nanometers; since the polymers themselves contain the chemical information necessary to undergo nanoscale phase segregation to form morphologies that include: spheres, cylinders, gyroids, and lamellae.[134,146,324,325] However, the geometric features attainable from diblock BCPs in thin films are limited due to a number of factors, including the thermodynamic driving force and boundary or commensurability effects.[325–329] Hence, strategies to attain non-native BCP structures via self-assembly are of great interest to researchers in the BCP community.[330–333] One strategy to form non-native BCP structures is to incorporate additional chemical blocks and build up complex BCP architectures, such as stars, brushed, H-shaped polymers, and structures based upon supramolecular interactions, to bring in novel functionalities.[334–339] Another strategy is the layer-by-layer stacking of BCP-derived features to arrive at new three-dimensional nanostructures from the self-assembly of BCP layers that could not be obtained via self-assembly of a single layer of BCP.[340,341] There are a variety of more complex and sophisticated processes to access non-equilibrium structures observed in the bulk, including the application of a protective layer,[342] direct self-assembly of a top BCP layer on an immobilized bottom layer,[343–345] crosslinking of consecutive layers,[346–348] and pattern transfer from a nanostructured film on top of an underlying layer,[349,350] as summarized in Figure 4.1.

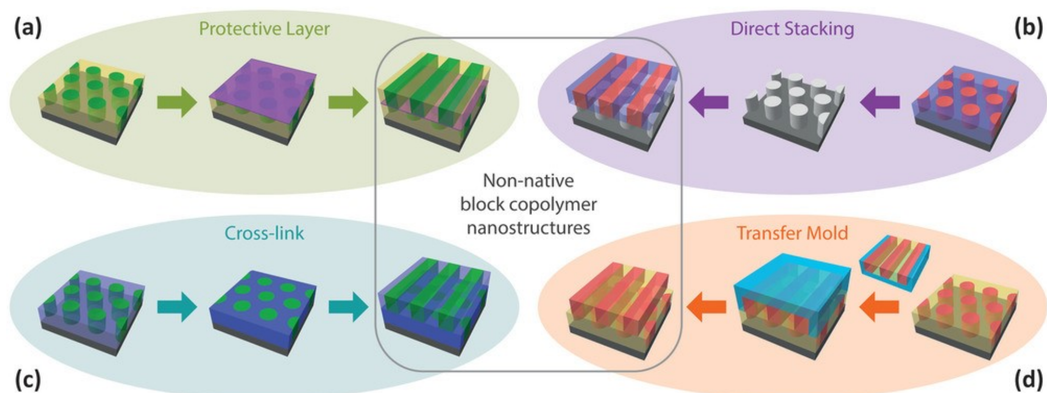

Figure 4.1. Schematic representation of sequential self-assembly of BCP to generate non-native morphologies using diblock BCPs. This schematic is reproduced from reference 344 with permission of John Willey and Sons.

The concept of density multiplication of BCP self-assembly has seen a great deal of attention for over a decade in order to surpass the intrinsic density achievable from a single nanopattern.[76,345,348,351,352] For instance, Nealey and co-workers demonstrated how BCP nanopatterns can result in density multiplication of chemically patterned surfaces.[167] Spatz and co-workers synthesized binary combinations of Au and TiO_2 dot-based nanoarrays using the self-assembly of PS-*b*-P2VP BCPs.[353] The resulting mixed metal–metal oxide patterns are shown in Figure 4.2. The gold–titania nanopattern was produced via a two-step dip-coating procedure, in which a layer of BCP micelles containing preformed titania cores was layered onto a surface coated by an array of gold nanoparticles. In some areas on the surface, a commensurate alignment of the two hexagonal lattices was observed, as shown in Figure 4.2. TiO_2-containing BCP micelles first and removal of BCP, followed by the second layer of BCP and gold-loading is considered as reverse ordering of the layers and it did not lead to reproducible graphoepitaxy; more particle-on-particle patterns were observed, which the authors state that they could not explain easily. These early results were intriguing and, possibly due to the synthetic challenges, the authors did not pursue this direction of research.

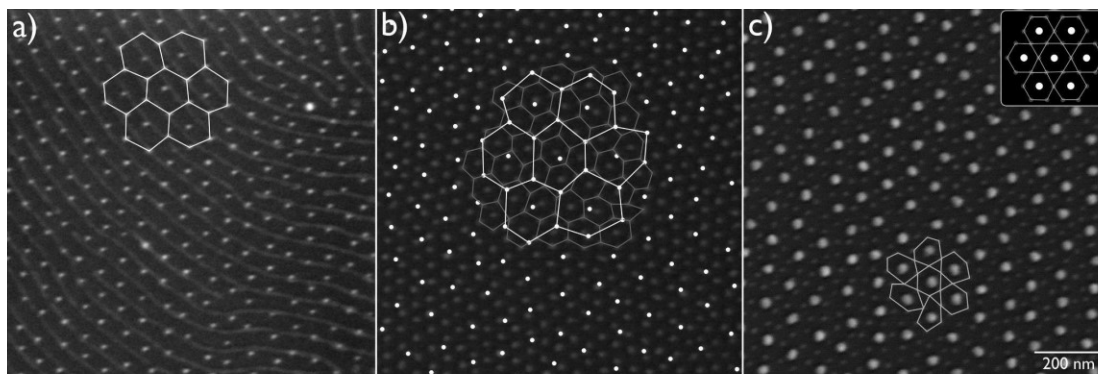

Figure 4.2. SEM micrographs of binary combinations of Au-TiO_2 nanoarrays with different periodicities. (a) TiO_2 nanowires with a periodicity of 55 nm deposited on an Au nanopattern with a periodicity of 71 nm. (b) TiO_2 nanoparticles with a periodicity of 46 nm deposited on an Au nanopattern with a periodicity of 96 nm. (c) Similar sample as (b) before coating TiO_2, Au nanoparticle size was increased from 8 nm to 25 nm in diameter by electroless deposition. This image is from reference 353 with permission from the American Chemical Society.

Buriak and co-workers showed density multiplication of all block copolymer nanopatterns using a one-step approach for density doubling of metal line or dot patterns templated by double layers of BCP-based cylinders.[304] Careful control over the initial film thickness and the solvent annealing conditions is essential for uniform features across the sample, as shown in Figure 4.3(a–g).[304] Furthermore, the same group showed sequential nanopatterning using BCP self-assembly to generate density doubled or tripled silica dot patterns with PS-*b*-PDMS, as shown in Figure 4.3(h).[305] In a honeycomb lattice pattern, the second layer of SiO_x dots can register in a commensurate manner with the triangular interstitial spaces of the first layer hexagonal pattern. In this example, an array of silica dots was generated from the PS-*b*-PDMS template and then was followed by a self-assembly of another layer of the same PS-*b*-PDMS BCP on top of the dot pattern, resulting in density doubling honeycomb lattice structures. The quality of the resulting patterns was dependent on the lattice parameters of the hexagonal dot pattern and the diameter and circularity of the dots.

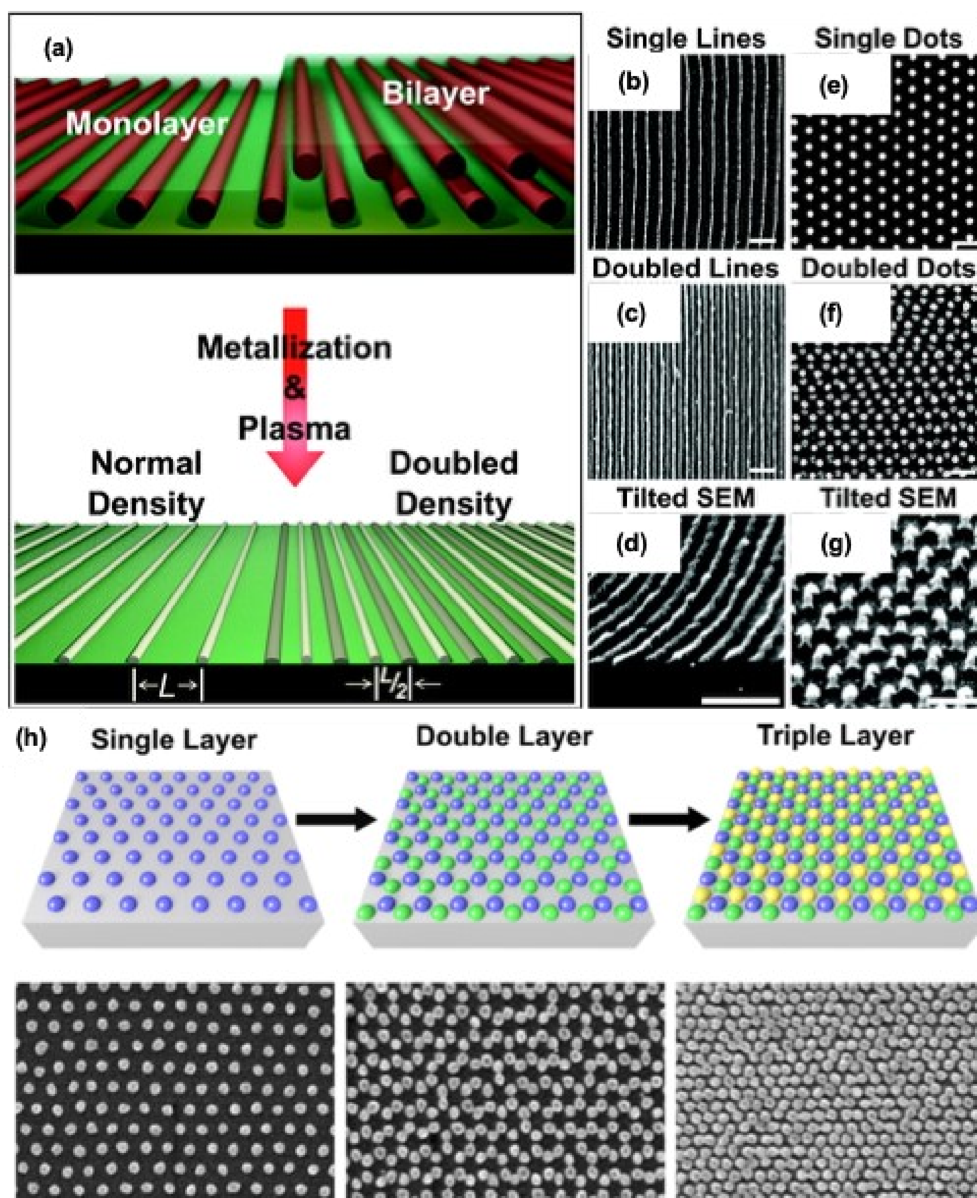

Figure 4.3. (a) One-step density doubling of metal lines via self-assembly of double layers of BCPs. SEM micrographs of a single Pt line pattern (b), a double Pt line pattern (c), a single Pt dot pattern (e), and a density doubled Pt dot pattern (f). Tilted SEM micrographs of density a doubled Pt line pattern (d) and dot pattern (g). The image is from reference 304 with permission of the American Chemical Society. (h) Density multiplication via sequential self-assembly of PS-*b*-PDMS to generate double and triple layers of silica dot patterns. This image is from reference 305 with permission from the American Chemical Society.

In this chapter we discuss the sequential layer deposition of BCPs and self-assembly to form highly ordered mixed metal or oxide nanopatterns and an investigation of their tunable optical properties as photonic metasurfaces. The selective conversion of one block into an oxide or metal and the concomitant removal of the

organic polymer by dry chemistries, as discussed in Chapter 3, leads to the formation of these non-native morphologies via BCP self-assembly and also enables density multiplication using only bottom-up methods. Other non-native morphologies prepared via multi-layer patterning approaches include the work by Yager and co-workers, who layered PS-*b*-P2VP to generate metal meshes using photothermal annealing, along with a soft-shear technique to access arbitrary lattice symmetries.[343] The resulting mesh patterns are shown in Figure 4.4(a). Similarly, several non-native 3D morphologies of BCP were fabricated by exploiting a responsive layering approach, in which subsequent layers were ordered as a function of the underlying layer, as shown in Figure 4.4(b).[354] Ross and co-workers used self-assembled BCP templates with larger periodicities as topographical guiding patterns to direct a second BCP self-assembly process, in which they successfully demonstrated line-in-line, dots-on-line, and dots-in-hole nanostructures using PS-*b*-PDMS with different periodicities and volume fractions.[355] Figure 4.4(c) shows the hierarchical nanostructures obtained from a sequential self-assembly process.

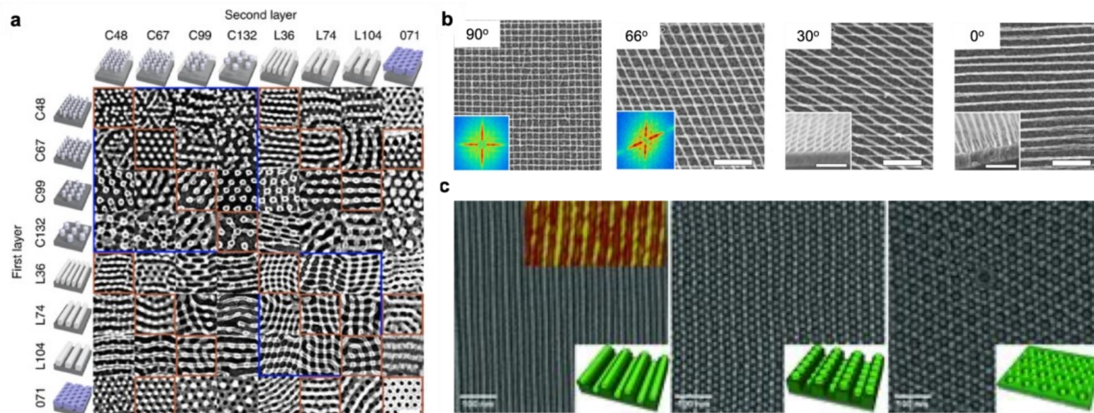

Figure 4.4. (a) SEM micrographs of non-native 3D two-layer nanostructures generated by a sequential self-assembly of PS-*b*-PMMA. All scale bars 100 nm. Adapted from reference 354 with permission from Springer Nature. (b) SEM micrographs of various double layer Pt nanomeshes, a soft shear-laser zone annealing method. Scale bars are 200 nm. The images are from reference 343 with permission from Springer Nature. (c) Hierarchical nanostructures including line-in-line, dots-on-line, and dots-in-holes fabricated from smaller periodicity PS-*b*-PDMS on topographical templates of larger periodicity PS-*b*-PDMS. The SEM micrographs are from reference 355 with permission from John Wiley and Sons.

4.2 Introduction to Moiré Patterns

Moiré patterns arise by superimposing two or more periodic lattice patterns with different lattice constants or relative spatial differences, such as sizes, periodicities, or angles.[356] Figure 4.5 illustrates three typical forms of Moiré patterns formed by either superimposing two 1D gratings of different periodicities or by overlapping two 2D periodic arrays with a relative in-plane rotation angle. The relative spatial displacement between the overlapping layers modifies the rotational symmetry and the periodicity of the resulting pattern. Because of these mechanical distortions, rotations, and displacements, Moiré patterns can be useful in various applications, including strain analysis,[357,358] optical alignment,[23,359] image processing,[360] and detection of document counterfeiting.[361,362] There are several fabrication techniques to make Moiré patterns, including colloidal nanosphere self-assembly,[363,364] interference photolithography,[365,366] imprint lithography combined with layer by layer stacking,[367] and self-assembly or DSA of BCPs.[322,368]

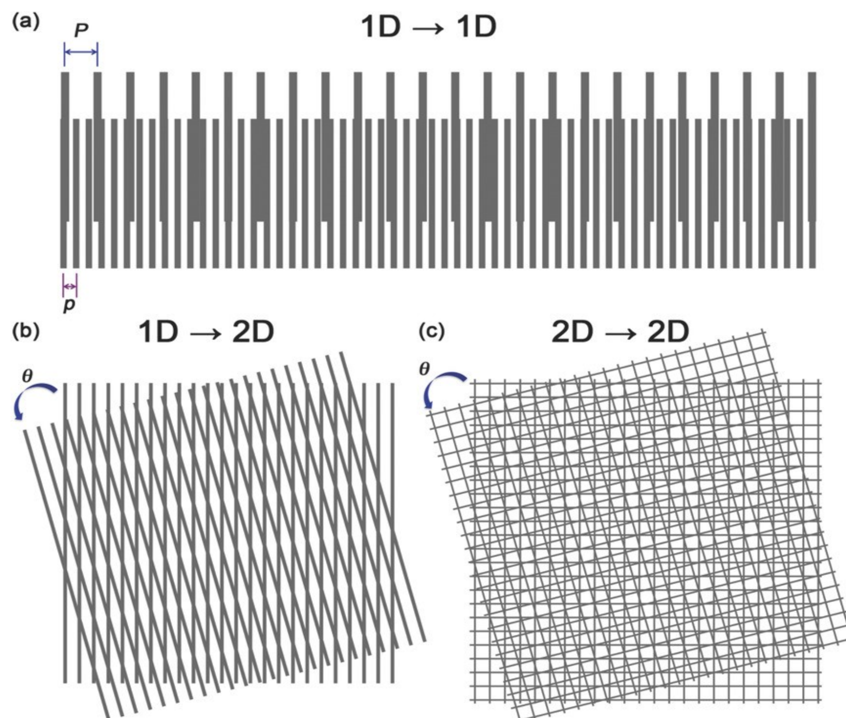

Figure 4.5. Three Moiré configurations from line patterns. (a) Formation of a 1D Moiré pattern by superimposing two-line patterns with different line spacing. (b) Formation of a 2D Moiré pattern by superimposing two identical line patterns with relative in-plane rotational angle. (c) Formation of a 2D Moiré pattern by superimposing two identical mesh patterns with relative in-plane rotational angle. This image is from reference 369 with permission of John Wiley and Sons.

Figure 4.6(a) shows a Moiré superstructure formed by a sequential self-assembly of PS-*b*-PDMS by Cong et al., where they demonstrated a preferential orientation of two incommensurate BCP dot arrays, which resulted in formation of this Moiré superstructure.[322] The difference in the periodicity of the bottom and top hexagonal dot pattern resulted in a predictable Moiré superstructure. A combination of different BCPs and annealing sequences were utilized to generate four distinct Moiré superstructures. The registration of the bottom layer was sufficient to direct the registration of the top layer to adopt a preferential relative angle of rotation. In a different study, the Buriak group demonstrated the growth of soft BCPs on hard hexagonal lattice patterns that lead to fundamental insights regarding van der Waals heteroepitaxy (vdWHs), as shown in Figure 4.6(b).[368] As per their experimental and simulation results, moderate registration forces for BCP-hard lattice vdWHs can have local structural relaxations, known as mass density waves (MDWs), in addition to a Moiré superstructure formation. These MDWs complement the energy minimization of the van der Waals bilayers, leading to the preferential rotational angle between lattices and, finally, Moiré superstructures. Since these structures, as synthesized to result in SiO_x patterns, have no obvious optical absorption that could lead to interesting plasmonic and optical effects, we decided to embark upon metal-based Moiré superstructures.[370–372]

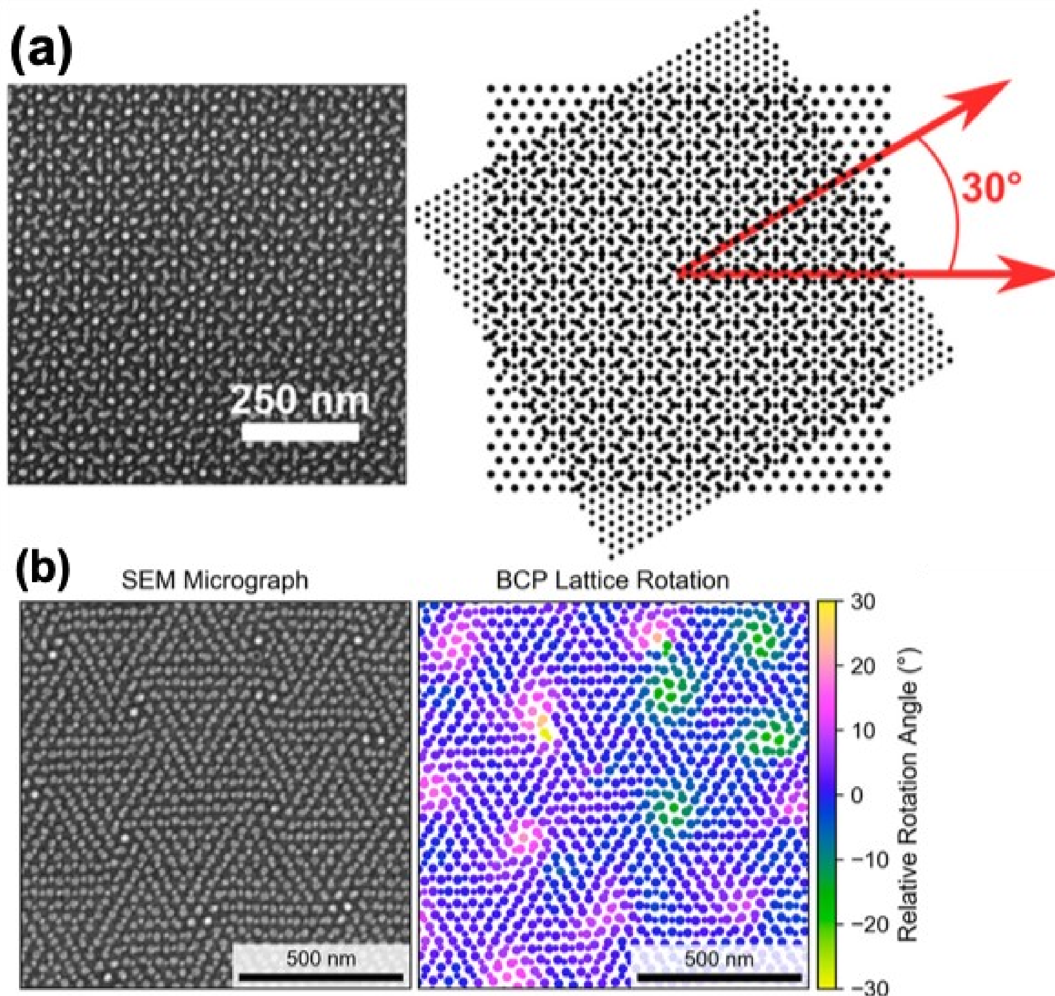

Figure 4.6. (a) SEM micrograph of flower-like Moiré superstructures formed from a sequential annealing of two incommensurate BCP combinations (left) and schematic representation of the bottom and top layer angle of rotation (right). This image is from reference 322 with permission of the American Chemical Society. (b) SEM micrograph of triangular-like Moiré superstructures formed by a self-assembly of BCP on EBL post arrays (left) and schematic showing the corresponding BCP lattice rotation and mass density waves (right). This image is reprinted from reference 368 with permission of the American Chemical Society.

4.3 Optical Metasurfaces

Optical metamaterials are a class of fabricated composites that show distinct optical properties that are not found in Nature; the term 'meta' comes from the Greek and means "go beyond".[369,373,374] As an interesting example, 2D arrays of nanoparticles that are aggregated to form spheres or raspberry-like structures show negative or zero refractive indices, a phenomenon that is not known in naturally occurring materials.[375–377] Metasurfaces are the 2D version of metamaterials, and, because of the reduced

dimensionality of the system, fabrication costs and better scalability may be achievable compared to bulk 3D metamaterials.[373] One characteristic of materials that is harnessed extensively in this area is plasmonics and, in particular, localized surface plasmon resonance (LSPR). Excitation of surface plasmons is capable of interacting with light beyond diffraction limits and represents the triple point of nanoscience, electronics, and photonics.[378] While fascinating from a fundamental science perspective, the coupling of light with the coherent oscillation of electron clouds in metals opens up many avenues to applications that include use as sensors,[379,380] antennas,[381,382] super absorbers,[383,384] and catalysts,[385,386] among many others. Fundamental material properties, such as a change of the refractive index or the plasmonic response of the material form, are the basis of many of these applications.

The core to these applications is the plasmonically active material, which is most commonly metals such as gold, silver, and aluminum, among others, that can display LSPRs in the visible region.[387–389] While single metal nanoparticles can exhibit an optical absorption arising from an LSP in resonance with the wavelength of illumination, it is when two or more metal nanoparticles are brought into close proximity (proximity will be defined shortly) that things, to put it in layman's terms, get interesting. The metal nanoparticles can interact and couple via a number of different mechanisms, resulting in highly unusual properties, as summarized in many reviews.[378,390–392] A recent example, shown in Figure 4.7, is of a very large field of plasmonic metamaterials called a surface lattice resonance, or SLR.[393,394] The fundamentals of SLRs first started to be developed back in the 1960's but were demonstrated experimentally only for 2D lattices in 2008. A very recent example from the Odom group demonstrates the remarkable property of a 2D SLR, as shown in Figure 4.7: an array of exquisitely prepared gold nanoparticles synthesized via e-beam lithography produces a single remarkably sharp absorption peak, with a fwhm of only 4 nm. The actual fwhm of a typical LSPR feature of a gold nanoparticle is on the order of many tens of nanometers,[395] but extensive research by groups from around the world since 2008 has led to this remarkable level of control over light.[378,390,392]

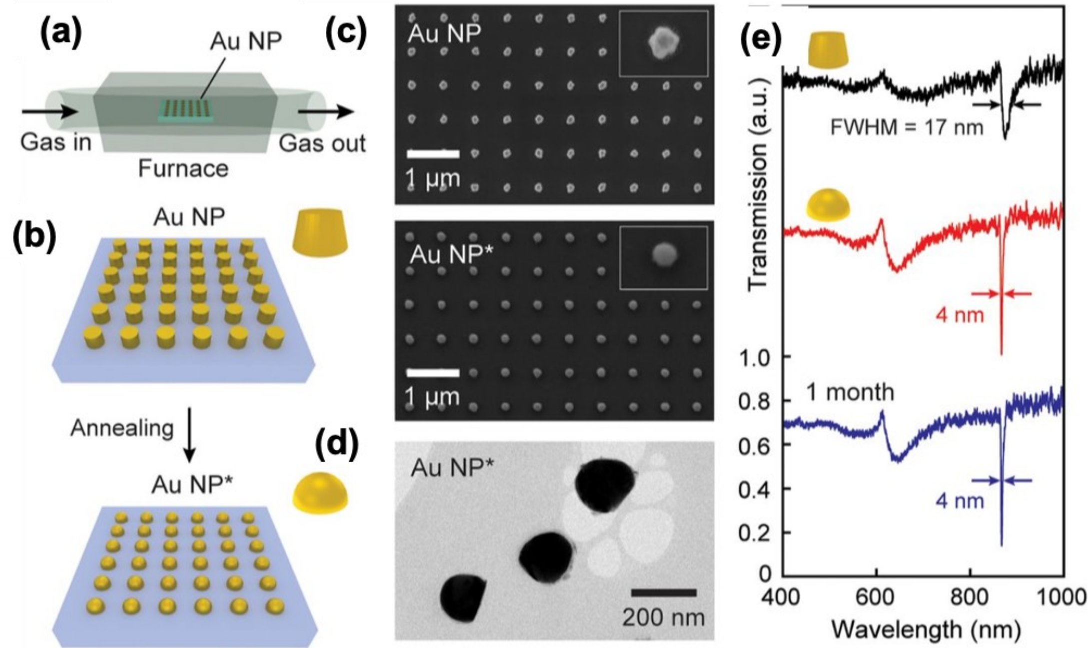

Figure 4.7. (a) Schematic of annealing setup. (b) Schematic representation of an annealing process of an Au nanoparticle lattice. (c) SEM micrographs of an Au nanoparticle lattice before (upper) and after (bottom) thermal annealing process. (d) Transmission electron microscopic (TEM) image of thermally annealed Au nanoparticles. (e) Experimental transmission spectra of untreated (black), a thermally annealed Au nanoparticle lattice after 1 d (red) and 1 month (blue). This image is reprinted from reference 394 with permission of the National Academy of Science.

The example in Figure 4.7 was prepared via exceedingly well-executed e-beam lithography, which is a serial nanopatterning approach that, while remarkably precise, is slow and very expensive, rendering it less useful for patterning large areas. Patterning large areas over many square centimeters to generate plasmonically active metal nanoparticle arrays for plasmonic applications, including SLRs, in a cost effective manner, is needed for both fundamental studies and applications.[396] It remains a challenge to fabricate highly ordered multicomponent nanostructures in a highly parallel manner over large areas. There have been many synthetic approaches pursued to address this immense challenge, which parallels the rapid growth and emergence of new and efficient synthetic approaches in nanoscience.[378] Techniques such as colloidal nanoparticle assembly,[397,398] nanoimprint lithography,[399] e-beam lithographic patterning,[400] and metal nanoparticle sorting in PDMS stamps,[401] among others, have seen extensive attention, and there are now reviews that summarize this vast area of nanoscience.

The length scales enabled by BCP self-assembly are ideal for much of the range required for the patterning of plasmonically active nanomaterials. In this chapter, we extend the previous research of our group on SiO_x-based Moiré patterns on surfaces to metals-based patterns. Double layers, both commensurate and incommensurate, of periodic hexagonal metal/oxide nanopatterns using PS-*b*-P2VP and PS-*b*-PDMS were fabricated. Multicomponent metal nanopatterns generated by sequential self-assembly could have interesting synergistic plasmonic properties due to modified structural morphology (size and shape) and composition of the resulting patterns. This approach enables the production of a new family of nanopatterns from mixed metal nanodots.

4.4 Experimental Methods

4.4.1 Materials

PS-*b*-P2VP [88k-*b*-18k, dispersity (*Đ*) = 1.07], PS-*b*-P2VP (44k-*b*-18.5k, *Đ* = 1.07), PS-*b*-P2VP (135k-*b*-53k, *Đ* = 1.18), PS-*b*-PDMS (43k-*b*-8.5k, *Đ* = 1.04), PS-*b*-PDMS (31k-*b*-14.5k, *Đ* = 1.15), and polystyrene (PS; 10k with *Đ* = 1.09 and 5k with *Đ* = 1.07) were purchased from Polymer Source Inc. Potassium tetrachloroaurate(III) ($KAuCl_4$, >99%) and sodium tetrachloroplatinate(II) (Na_2PtCl_4, 42.65%) were purchased from Strem Chemicals. Toluene (>99%) and THF (>99%) were purchased from Fisher Scientific. Hydrochloric acid (36.5–38%), sulfuric acid (96%), and hydrogen peroxide (30%) were purchased from Avantor Performance Materials. Silicon wafers [<100>, 4 in. diameter, thickness 525 ± 25 mm, p-type (boron doped), resistivity <0.005 Ω cm] were purchased from WRS Materials. A fused silica wafer [<100>, 100 mm diameter, thickness 525 ± 25 mm, p-type, resistivity 10–20 Ω cm] was purchased from the University of Alberta Centre for Nanofabrication (the nanoFab).

4.4.2 Substrate Preparation

Silicon and fused silica wafers were diced into 1 cm × 1 cm squares using Disco DAD 321 and Disco 3240 dicing saws, respectively. Prior to the self-assembly processing, the silicon and fused silica chips were cleaned with a fresh piranha solution by immersing chips in a 3:1 v/v sulfuric acid and hydrogen peroxide solution for 15 min. Then, they were rinsed with deionized water and dried with a nitrogen stream.

4.4.3 BCP Thin Film Self-assembly by Solvent Annealing

Individual solutions with a 1% (%w/v) concentration of PS-*b*-P2VP (88k-*b*-18k), PS-*b*-P2VP (44k-*b*-18.5k), PS-*b*-P2VP (135k-*b*-53k), PS-*b*-PDMS (43k-*b*-8.5k), PS-*b*-PDMS (31k-*b*-14.5k), and PS (10k and 5k) were prepared by dissolving the BCP in toluene. The polymer mixtures were prepared by mixing PS-*b*-P2VP (44k-*b*-18.5k) with PS (5k) to make a 30% (%v/v) solution, PS-*b*-P2VP (135k-*b*-53k) with PS (5k) 15% (%v/v) solution, and PS-*b*-PDMS (31k-*b*-14.5k) with PS (10k) 30% (%v/v) solution. From the PS-*b*-P2VP (135k-*b*-53k) blended with 15% PS solution, 20 μL were spin cast on piranha cleaned silica/fused silica substrates at 4200 rpm (WS-400BZ-6NPP/120 LITE spin-coater Laurell Technologies Corporation), and for all the other BCP solutions 17 μL were used at 8500 rpm for 40 s for all the samples. The film thickness for PS-*b*-P2VP (88k-*b*-18k), PS-*b*-P2VP (44k-*b*-8.5k) blended with 30% PS, PS-*b*-P2VP (135k-*b*-53k) blended with 15% PS, PS-*b*-PDMS (43k-*b*-8.5k), and PS-*b*-PDMS (31k-*b*-14.5k) blended with 30% PS were 36 ± 1 nm, 33 ± 1 nm, 37 ± 1 nm, 30 ± 1 nm and 30 ± 1 nm, respectively.

The BCP or BCP blended with PS thin films were solvent annealed in a custom-designed annealing chamber with THF as the annealing solvent, as shown in Figure 4.8. The film thickness was measured by using an in-situ ellipsometer (λ = 632.8 nm, θ = 70°) during the annealing process. The apparatus for solvent vapor annealing is shown in Figure 4.9. The final swelling degree was optimized for all the different samples of BCP or BCP blended with PS by controlling the steady-state solvent vapor pressure inside the chamber. The THF vapor pressure was varied by filling THF with different solvent reservoirs in the annealing chamber to change the THF solvent surface area exposed inside the chamber. The reservoir number iv (total surface area 2.71 cm^2) filled with 1 mL of THF was used for thin films of PS-*b*-P2VP (88k-*b*-18k), PS-*b*-P2VP (44k-*b*-18.5k) blended 30% with PS, and PS-*b*-PDMS (31k-*b*-14.5k) blended 30% with PS to obtain optimized swelling degree of ~2.0. The reservoir number iii and iv filled with 0.5 mL and 2 mL of THF, respectively, were used for thin films of PS-*b*-P2VP (135k-*b*-53k) blended with 15% PS to achieve a swelling degree of ~2.3. The closed annealing chamber was allowed to reach the equilibrium vapor pressure of THF

influenced by the surface area of the solvent exposed. The in-situ thickness monitoring was used to optimize the swelling degree for each sample by allowing the thin film to saturate with the solvent and deciding the annealing time required.

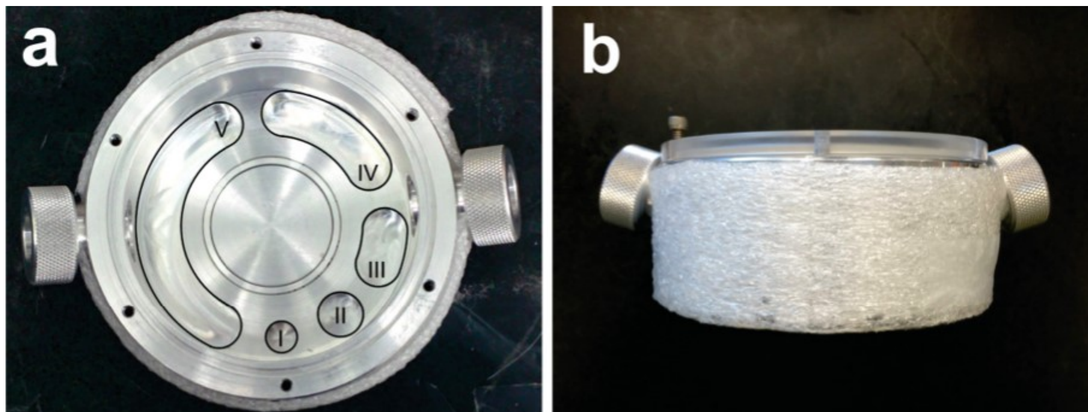

Figure 4.8. Top-down (a) and side-view (b) of the solvent annealing chamber with five different solvent reservoirs to contain solvents with different surface areas (vapor pressures). The image is from reference 155 with permission of the American Chemical Society.

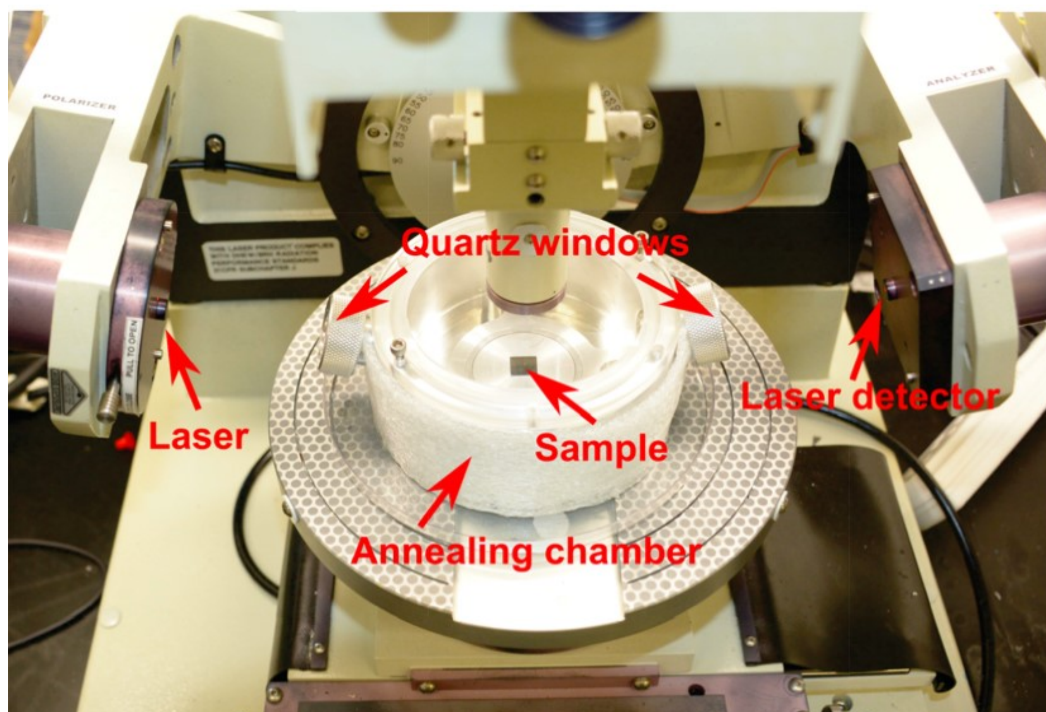

Figure 4.9. Photograph of the static solvent vapor annealing setup with in-situ thickness monitoring. Image is from reference 155 with permission of the American Chemical Society.

4.4.4 Metallization and Reactive Ion Etching

For PS-*b*-P2VP, a metallization step was carried out prior to reactive ion etching (RIE) to improve the contrast for visualization using scanning electron microscopy (SEM).[87,88] After annealing, thin films of PS-*b*-P2VP were immersed either in an aqueous platinum salt solution [10 mM Na_2PtCl_4, 2 mL, and 1% (%v/v) HCl, 8 mL] for 3 h or a gold salt solution [10 mM $KAuCl_4$, 2 mL, and 1% (%v/v) HCl, 8 mL] for 10 min. Then, the samples were removed from the metal salt solution, rinsed with ultra-pure water, and dried in a nitrogen stream.

The metalized samples of PS-*b*-P2VP (and blended PS-*b*-P2VP) were treated with 100 mTorr oxygen plasma (80 sccm) either in a Trion Phantom RIE (20 W RF power) or Plasmalab μEtch RIE (30 W RF power) for different time intervals, depending upon the molecular weight of the BCP, to convert either the Pt^{2+} to Pt or Au^{3+} to Au and remove the polymer. The details of the optimization of the etching recipe for each PS-*b*-P2VP are discussed in Chapter 3. All the thin film samples of PS-*b*-PDMS were subjected to CF_4/O_2 RIE directly after the solvent annealing process in Plasmalab μEtch RIE. During RIE etching, the PDMS domains are oxidized to SiO_x and the PS domains are etched away. RIE recipes for all the samples are given in Table 4.1.

After preparation of a single layer of hexagonal Pt or SiO_x nano-dots, a second layer was deposited using the same procedure. The second layer was always deposited using PS-*b*-P2VP and metalized to arrive at either Au or Pt nano-dots. Prior to the subsequent second layer deposition, the first layer was analyzed using SEM for all the samples on Si substrates, and all the first layers that had SiO_x nano-dots were cleaned with piranha solution.

Table 4.1. Experimental Parameters for Preparation of SiO_x, Pt and Au Nanopatterns from BCP with Different Molecular Weights

BCP sample	Spin coating conditions	Film thickness /nm	Annealing condition	Swelling degree	Etching recipe
PS-*b*-P2VP (88k–18k)	8500 rpm 40 s	36 ± 1	Reservoir iv 1 mL THF	~2.0	µEtch RIE 100 mTorr O_2 (80 sccm), 30 W, 30 s Trion RIE 100 mTorr O_2 (80 sccm), 20 W, 35 s
PS-*b*-P2VP (44k–18.5k) with 30% PS	8500 rpm 40 s	33 ± 1	Reservoir iv 1 mL THF	~2.0	µEtch RIE 100 mTorr O_2 (80 sccm) 30 W, 30 s Trion RIE 100 mTorr O_2 (80 sccm), 20 W, 30 s
PS-*b*-P2VP (135k–53k) with 15% PS	4200 rpm 40 s	37 ± 1	Reservoir iv 1 mL and iii 0.5 mL THF	~2.3	Trion RIE 100 mTorr O_2 (80 sccm), 20 W, 40 s
PS-*b*-PDMS (43k–8.5k)	8500 rpm 40 s	30 ± 1	Reservoir iv 1 mL THF	~2.0	µEtch RIE 1. 100 mTorr CF_4, 50 W, 10 s 2. 145 mTorr CF_4/O_2 (20%:80%) 30 W, 40 s
PS-*b*-PDMS (31k–14.5k) with 30% PS	8500 rpm 40 s	30 ± 1	Reservoir iv 1 mL THF	~2.0	µEtch RIE 1. 100 mTorr CF_4 50 W, 10 s 2. 145 mTorr CF_4/O_2 (20%:80%) 30 W, 40 s

After preparation of a single layer of hexagonal Pt or SiO_x nano-dots, a second layer was deposited using the same procedure. The second layer always was deposited

using PS-*b*-P2VP and was metalized to arrive at either Au or Pt nano-dots. Prior to the subsequent second layer deposition, the first layer was analyzed using SEM for all the samples on Si substrates, and all the first layers that had SiO_x nano-dots were cleaned with piranha solution.

4.4.4 Characterization

All SEM micrographs were taken using a Hitachi S4800 scanning electron microscope. The samples on Si substrates were used as-prepared for imaging (15 kV, 20 μA). The samples on fused silica substrates were coated first with a conducting metal layer, Au and Pd, to improve the conductivity for imaging (3 kV, 5 μA).

4.4.5 Ellipsometry and UV-vis Spectroscopy Analysis

UV-vis spectroscopy and spectroscopic ellipsometry have been employed to investigate the optical properties of single layer and double layer Au and Pt nanoparticle arrays. Optical measurements have been performed with a J. A. Woollam M-2000V, and samples were prepared on native oxide-capped Si substrates. The ellipsometric parameters, a ratio of amplitude (φ) and phase difference (Δ), were measured in the 350 nm–1000 nm spectral range at an angle of incidence from 55° to 80°. The UV-vis absorption spectra were measured using the Perkin-Elmer NIR-UV spectrophotometer in the 350–800 nm wavelength range on fused silica. For each sample five transmission measurements were performed with a normal incident angle.

4.4.5 Data processing

All the SEM micrographs were processed, and nanoparticle sizes and pitch calculations were carried out using ImageJ and Gwyddion software. All the schematic illustrations of the dot patterns were drawn manually using the high magnification SEM micrographs. The UV-vis spectra were processed using the origin lab.

4.3 Multicomponent Block Copolymer Self-assembly

In this work, two different BCPs, PS-*b*-PDMS and PS-*b*-P2VP, were used to form mixed metal/oxide nanopatterns. The general schematic for formation of mixed component honeycomb/Moiré superstructures is shown in Figure 4.10. The bottom

layer of hexagonal dots was formed by self-assembly of either PS-*b*-PDMS or PS-*b*-P2VP, followed by solvent annealing and reactive ion etching (RIE) to convert BCPs into SiO_x or Pt dots, shown in Figure 4.10(a). For PS-*b*-P2VP prior to RIE, an additional step of metallization was carried out using an acidic solution comprising a Pt^{2+} salt. A second layer of PS-*b*-P2VP BCP was spin-cast onto the initial hexagonal SiO_x or Pt dot array, annealed, and then metalized with one of two different acidic solutions of Na_2PtCl_4 or $KAuCl_4$, followed by an RIE step to convert the BCP into either Pt or Au hexagonal dots. The resulting nanopatterns are either honeycomb or Moiré superstructures, depending on the lattice parameter of the resulting hexagonal lattice. If the bottom layer is SiO_x, the top layer is Pt; when the bottom layer is Pt, the top layer is Au.

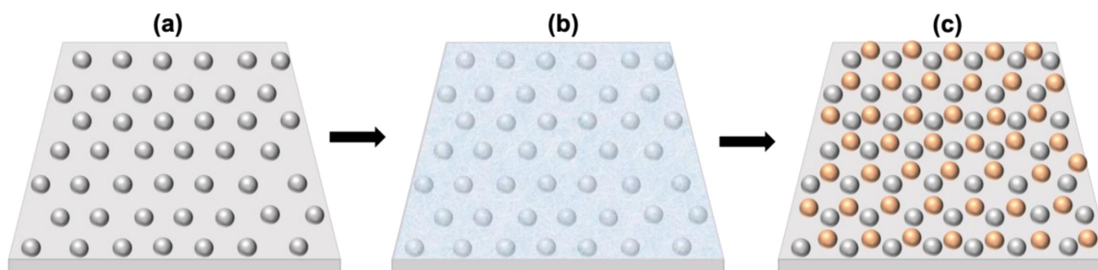

Figure 4.10. Schematic illustration of the methodology for forming mixed component-based honeycomb/Moiré superstructures using hexagonal BCP dot arrays. (a) Formation of a bottom layer dots via self-assembly of a BCP, followed by solvent annealing and/or metallization and reactive ion etching (RIE) to convert the BCP into either hexagonal lattice of Pt or silica dots. (b) Deposition of the top layer of PS-*b*-P2VP on a preformed nanopattern of Pt or SiO_x dots from (a). (c) Solvent vapor annealing, metallization, and RIE of the second layer to convert BCP to Au or Pt nano-dots to form honeycomb/Moiré superstructures.

Attempts to prepare double layers with a gold bottom layer failed due to the instability of this layer to subsequent RIE steps and, unfortunately, could not be explored *vide infra* (see Figure 4.11). Figure 4.11 shows a single layer of Au nanopattern fabricated via self-assembly of PS-*b*-P2VP (88k-*b*-18k) and a double layer Au–Au nanopattern using identical self-assembly of the same BCP. The double layer Au–Au nanopattern did not lead to a honeycomb pattern, and the bottom layer Au nanodots started to form randomly ordered smaller Au nanodots all over the surface after the subsequent RIE step.

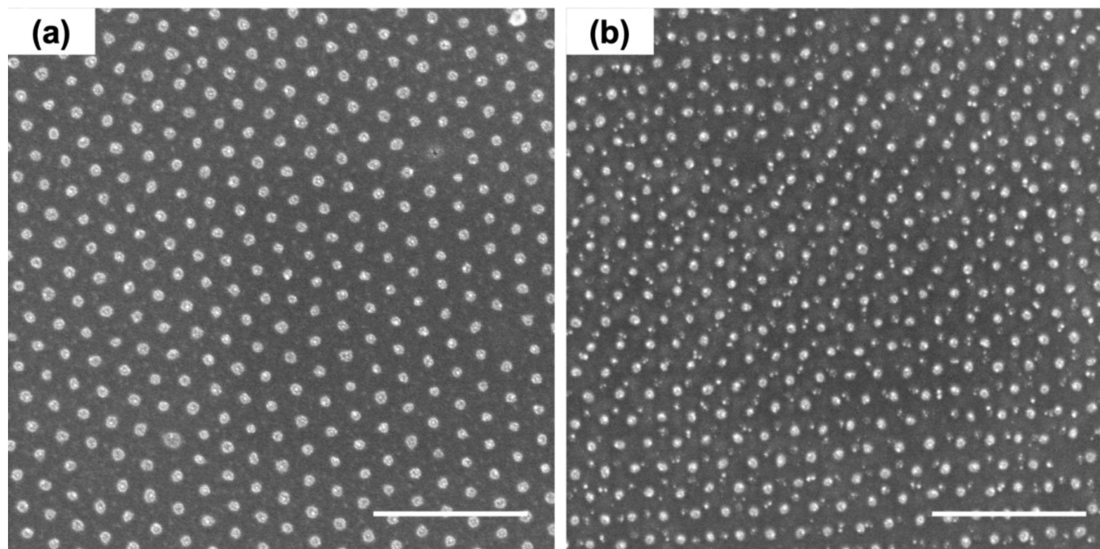

Figure 4.11. SEM micrographs of (a) a single layer Au nanodot array (b) a double layer Au–Au nanodot arrays self-assembled using subsequent deposition of PS-*b*-P2VP (88k-*b*-18k). All scale bars are 250 nm.

The different molecular weights of BCPs and BCP blends used for this work are listed in Table 4.2 with their corresponding abbreviations, pitch, and dot diameter.

Table 4.2. Pitch and Dot Diameter of the Different BCP Used in This Study

Abbreviation	Composition	L = Pitch /nm	Pt or SiO_x Dot Diameter /nm	Au Dot Diameter /nm
P43	PS-*b*-PDMS (43k-*b*-8.5k)	34 ± 1	16 ± 1 (SiO_x)	NA
B30	PS-*b*-PDMS (31.5k- *b* -14.5k) + 30% PS (10k)	42 ± 1	22 ± 1 (SiO_x)	NA
B30	PS-*b*-P2VP (44k- *b* -18.5k) + 30% PS (5k)	41 ± 1	17 ± 1 (Pt)	16 ± 1
P88	PS-*b*-P2VP (88k- *b* -18k)	44 ± 1	16 ± 1 (Pt)	19 ± 1
B15	PS-*b*-P2VP (135k- *b* -53k) + 15% PS (5k)	70 ± 1	26 ± 1 (Pt)	26 ± 1

Figure 4.12 shows SEM micrographs of the single layers of hexagonal SiO_x nanodots generated by the self-assembly PS-*b*-PDMS, and Figure 4.13 represents the

Pt and Au nanodots generated by the self-assembly of PS-*b*-P2VP. The layered structures are denoted by their deposition sequence and the corresponding composition of the dots. For example, **P88**(Pt)+**B15**

(Au) refers to the sample where the bottom layer comprises Pt dots using **P88**, and the top layer is composed of Au dots using **B15**. Different nanopatterns with commensurate and incommensurate pitch ratios of either SiO_x–Pt or Pt–Au were generated and the optical properties of the Pt–Au were studied in this work.

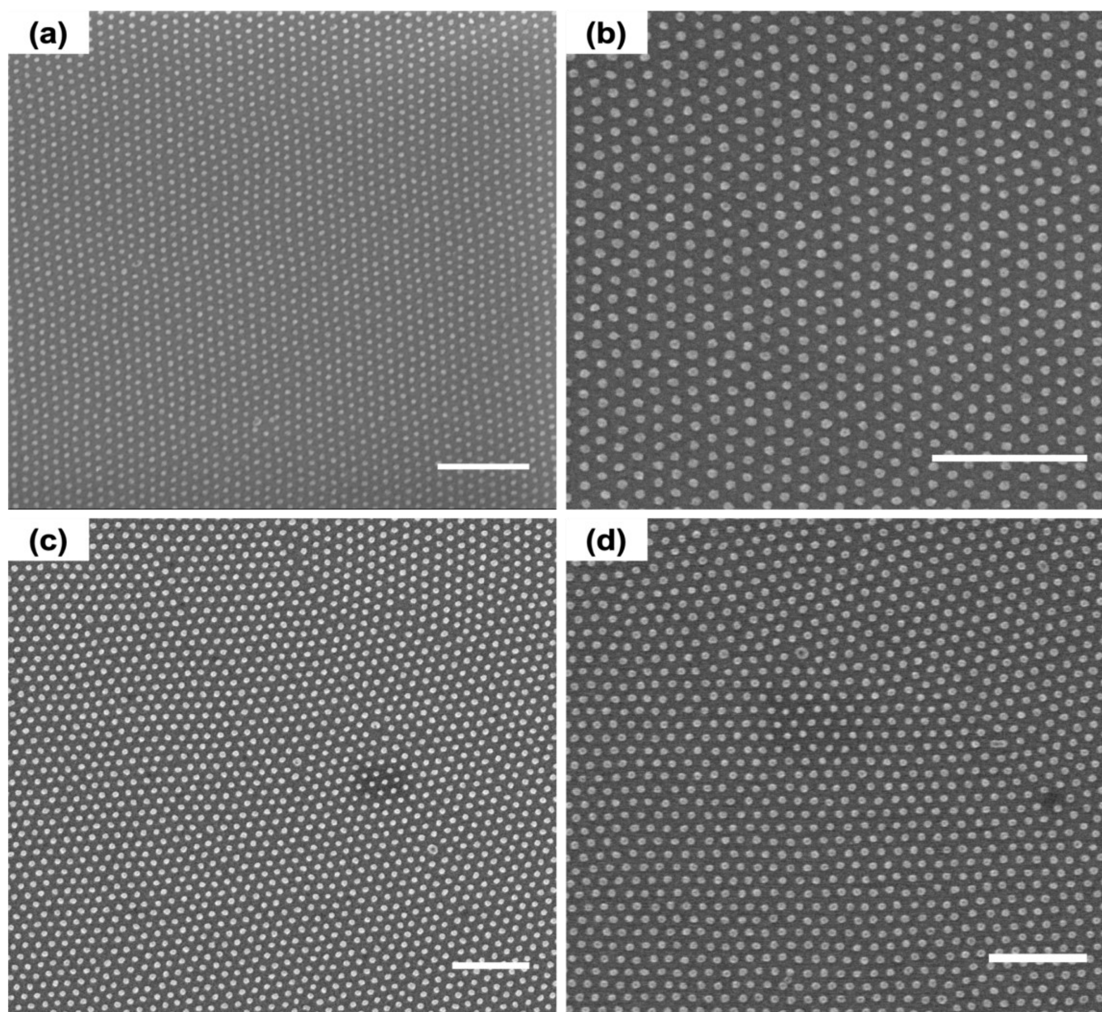

Figure 4.12. Low magnification (left) and high magnification (right) SEM micrographs of single layer SiO_x nanodots derived from different molecular weights of PS-*b*-PDMS. (a,b) 43k-*b*-8.5k (**P43**) and (c,d) 31k-*b*-14.5k (**B30**). All scale bars are 250 nm.

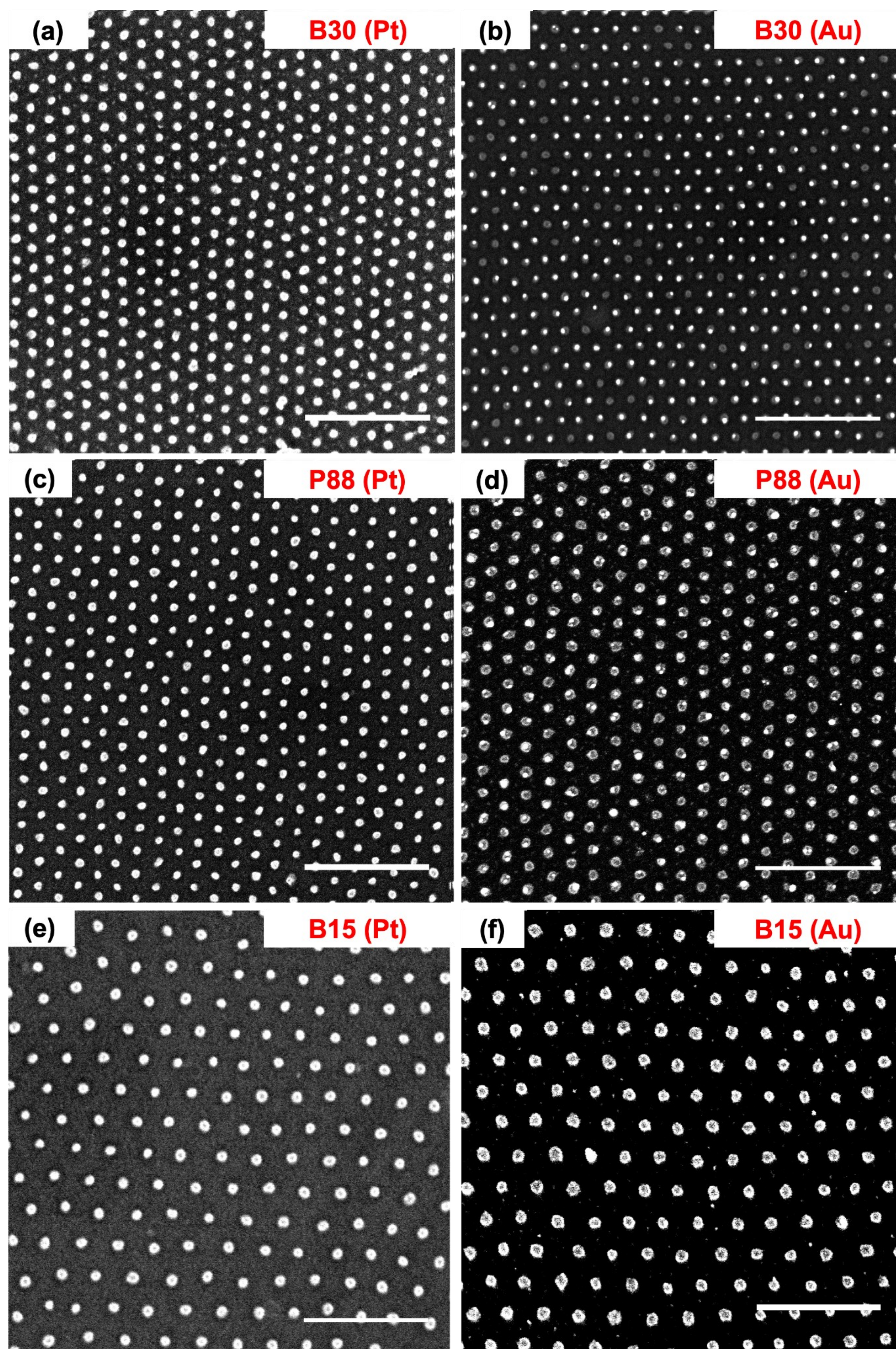

Figure 4.13. SEM micrographs of single layers of Pt (left) and Au (right) nanodots produced using PS-*b*-P2VP BCPs of different molecular weights. (a,b) 44k-*b*-18.5k (**B30**), (c,d) 88k-*b*-18k (**P88**), and (e,f) 135k-*b*-53k (**B15**). All scale bars are 250 nm.

The native pitch for all the polymers used in this chapter for double layer patterning and the corresponding pitch ratio for six different configurations of sequentially deposited BCP bilayers are summarized in Table 4.3. The native pitch ratio is calculated as a ratio of dot spacing of the top and bottom layer dots found in the single layer patterns.

Table 4.3. Native Pitch of the Bottom and Top Layer BCPs and the Corresponding Pitch Ratios for Six Different Configurations of Sequentially Deposited BCP Bilayers

BCP Layers (bottom layer+top layer)	L1 (Pt pattern in single layer)/nm	L2 (Pitch of Au pattern in single layer)/nm	Theoretical L2/L1 (Calculated using L1 and L2 of single layers)/nm[a]
B15+**B30**	70 ± 1	41 ± 1	0.58
B15+**P88**	70 ± 1	44 ± 1	0.63
P88+**B30**	44 ± 1	41 ± 1	0.91
P88+**P88**	44 ± 1	44 ± 1	1.0
B30+**P88**	41 ± 1	44 ± 1	1.1
P88+**B15**	44 ± 1	70 ± 1	1.6
B30+**B15**	41 ± 1	70 ± 1	1.7

[a] Theoretical pitch ratio of the double layers is calculated using the single layer pitches as determined experimentally for single layer samples.

In this chapter, we are going to start with commensurate ratios of top- and bottom-layer pitches. The deposition of a second layer on top of the first layer using different compositions of BCPs with a commensurate pitch ratio of 1.0 results in the formation of a combined dot pattern possessing a honeycomb lattice, as illustrated in Figure 4.14. There are two different compositions of honeycomb patterns formed using a sequential self-assembly of BCP. The first combination comprises PS-*b*-P2VP with the same BCP with molecular weight (**P88**) but with the bottom layer metalized with Pt and the top layer with Au, shown in Figure 4.14(a–c). The second combination is assembled from a sequential deposition of PS-*b*-PDMS (**B30**) as the bottom layer and PS-*b*-P2VP (**B30**) metalized with Pt, yielding a SiO_x–Pt honeycomb pattern, shown in

Figure 4.14(d–f). The dots from the second layer are registered in the triangular interstitial positions of the first layer to generate the honeycomb lattice.[36] The sizes of the dots in the two layers of each honeycomb pattern are significantly different. The SiO_x–Pt honeycomb, shown in see Figure 4.14(d–f), has larger silica dots (22 ± 1 nm) compared to the Pt dots (11 ± 1 nm; size is from the etching recipe used in μEtch), as the PDMS block is converted completely into the silica dots. The difference in the sizes of the Pt and SiO_x is due to the two different RIE steps used for PS-*b*-PDMS and PS-*b*-P2VP (see Table 4.1). The Pt–Au honeycombs, shown in Figure 4.14(a–c), are generated by sequential self-assembly of the same PS-*b*-P2VP. Even though both layers are from an identical self-assembly of PS-*b*-P2VP, the bottom layer Pt dots are considerably smaller (9.0 ± 1 nm) than the top layer Au dots (12 ± 1 nm) (see Table 4.4 for Au and Pt sizes). The reason behind these size differences is that the bottom layer Pt nanoparticles are annealed in the second RIE step used for the Au nanopattern. Chemically homogeneous surface (uniformly SiO_x) and inhomogeneous surface (SiO_x and Pt) are used for the second layer self-assembly, and both resulted in a honeycomb pattern, indicating that double layer formation is directed by the topology of the bottom layer and that it is independent of the chemical composition of the bottom layer for a pitch ratio of 1.0.

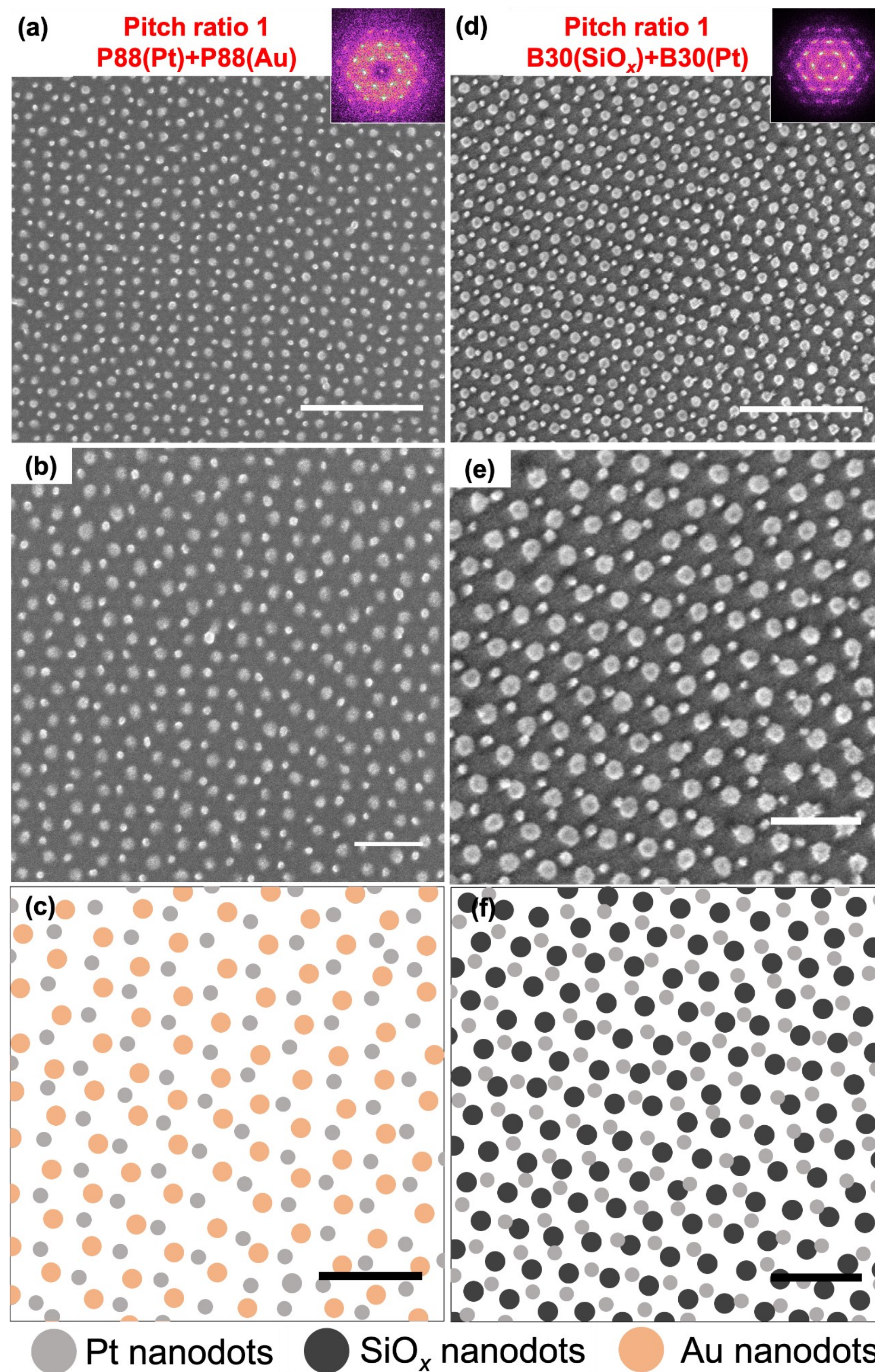

Figure 4.14. Low magnification (first row, a–d) and high magnification (second row, b–e) SEM micrographs and schematics illustrate the high magnification SEM (third row) of honeycomb patterns from (a–c) Pt–Au derived from **P88**, with the bottom layer being Pt and the top layer Au. (d–f) SiO_x–Pt derived from bottom layer **B30** and top layer **B30**, metalized with Pt. The insets represent the FFT of the resulting nanopatterns. First row scale bars are 250 nm; second and third row scale bars are 100 nm.

Figure 4.15 shows the double layer Pt–Au pattern by self-assembling two different PS-*b*-P2VP with a slight variation of pitches, where the bottom layer is **P88** (Pt) with a pitch of 44 ± 1 nm and the top layer is **B30** (Au) with a pitch of 41 ± 1 nm, leading to a pitch ratio of 0.91. When the pitch ratio is slightly reduced to 0.91 by self-assembling **P88**(Pt)+**B30**(Au), a similar honeycomb pattern was observed. However, these honeycomb patterns are surrounded by lines of alternate Pt and Au nanoparticles throughout the sample, as shown in Figure 4.15; it is displayed in a separate panel to make it easier to arrange the text with the remaining figures, and there is no specialty of the pattern.

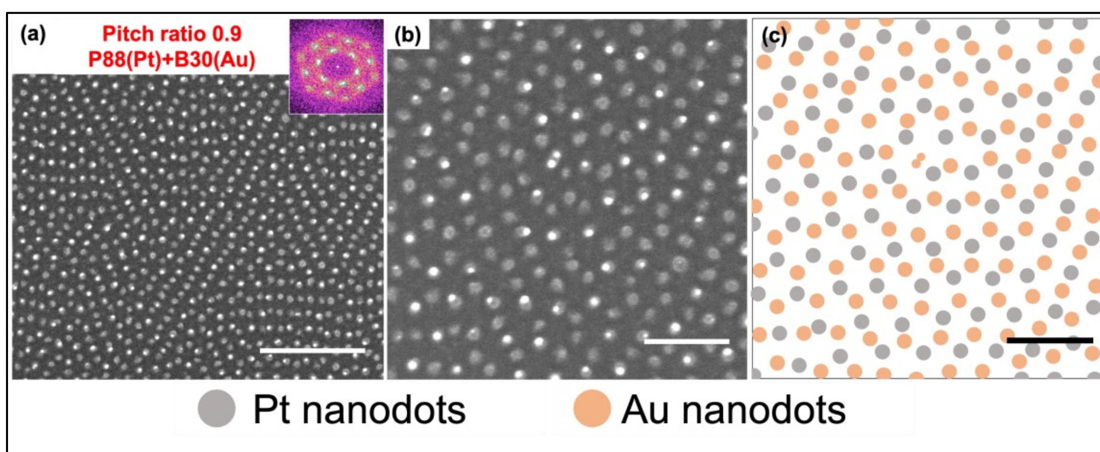

Figure 4.15. (a) Low (scale bar 250 nm) and (b) high (scale bar 100 nm) magnification SEM micrographs and (c) schematic illustration of the high magnification SEM of Pt–Au Moiré patterns with incommensurate pitch ratios of 0.91; bottom layer **P88** (Pt) and top layer **B30**. The inset represents the FFT of the resulting nanopatterns. Orange and gray dots represent Au and Pt nanodots, respectively.

Previous work from our group showed that the top layer BCP lattice would adopt a preferential twist angle to the bottom layer when BCPs with incommensurate pitch ratios self-assembled to form Moiré superstructures.[322,368] The twist angle for a given pitch ratio was determined by first measuring the local relative rotation (relative to the [10] direction of the bottom layer lattice) of each BCP dot in the top layer, which is the average angular rotation of its six nearest neighbors. As expected, the twist angle is near zero when the pitch ratio approaches 1.0, as shown Figure 4.14.[305,368] In addition to these global relative rotational angles, Cong et al. also observed the presence of localized lattice rotations near pitch ratios of 0.87 and 1.13, which they termed mass density waves (MDWs).[368] The observation of MDWs was clustered at pitch ratios

approaching 1, as opposed to combinations with highly incommensurate pitch ratios. Molecular dynamics simulations using the open source LAMMPS interface were performed to estimate the interaction between soft melted epilayers and the rigid silica-based bottom layer patterns for incommensurate pitch ratios.[402] The interlayer potential was assumed to be repulsive, with an energetic penalty for overlap between the bottom and top layers for the size regimes modelled; this overlap and energetic penalty decreases as the separation distance of the dots increases. These simulations indicated that the formation of MDWs in the soft epilayer (top layer) enables a further minimization of the configuration energy, in addition to that achieved with the adoption of global twist angles of the lattice formed by the soft epilayer of block copolymer micelles.[402] Similar localized rotational nodes were observed for a pitch ratio of 1.1 for Pt–Au nanopatterns, as shown in Figure 4.16, where the patterns consist of pseudocommensurate triangular domains connected via nodes as the BCP lattice strained compressively or extension towards a commensurate pitch ratio of 1.0 outside these nodal regions.

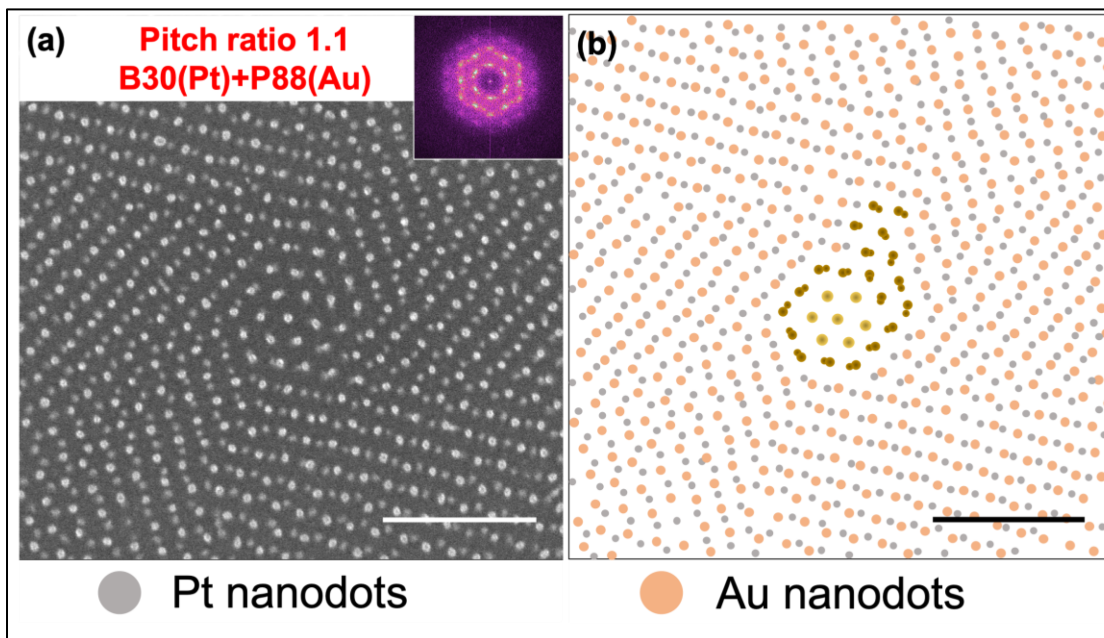

Figure 4.16. (a) SEM micrograph and (b) corresponding BCP dot map illustrating the mass density waves for a pitch ratio of 1.1, generated using self-assembly of **B30**(Pt)+**P88**(Au). All scale bars are 250 nm.

A further decrease from the commensurate pitch ratio of 1.0 to 0.58 and 0.63 resulted in a pattern that can be summarized as two Au dots located between two Pt dots, with a majority of the bottom Pt dots capped by an overlapping top Au dot, as shown in Figure 4.17. Thus, this nanopattern also can be described as every Pt dot being overlapped by an Au dot and surrounded by six Au dots as the nearest neighbors. From Figure 4.17(d–f), the pattern appears to be commensurate, which means that the pitch ratio would need to be $\sqrt{3} = 1.71$, therefore, the pitch of the Au layer would need to be $L2(Au) = L1(Pt)/\sqrt{3} = 70.0/\sqrt{3} = 40.4$ nm. As explained by Ross, Buriak, and their co-workers, there is an energetic penalty for overlapping dots, which is why the top layer adopts an angle of rotation, maximizing the infill of the interstitial positions of the bottom layer and reducing the number of overlapping dots to minimize the configurational energy.[76,340,368] However, for lower the pitch ratios of 0.58 and 0.63, a higher overlap between dots can be observed; this seems to contradict the behavior resulting from the energetic penalty of dot overlap. The observation of overlap between top and bottom Au–Pt dots in these two pairs of incommensurate lattices is presumably due to the low height of the bottom layer Pt dots. While not determined by AFM, the plan-view SEM micrographs suggest that the Pt dots are low and flat, therefore, the energetic cost of the overlapping PS-*b*-P2VP micelle is relatively low. In the global energy accounting spreadsheet, the gain from the commensurate arrangement must outweigh the cost of the dot overlap.[322,403]

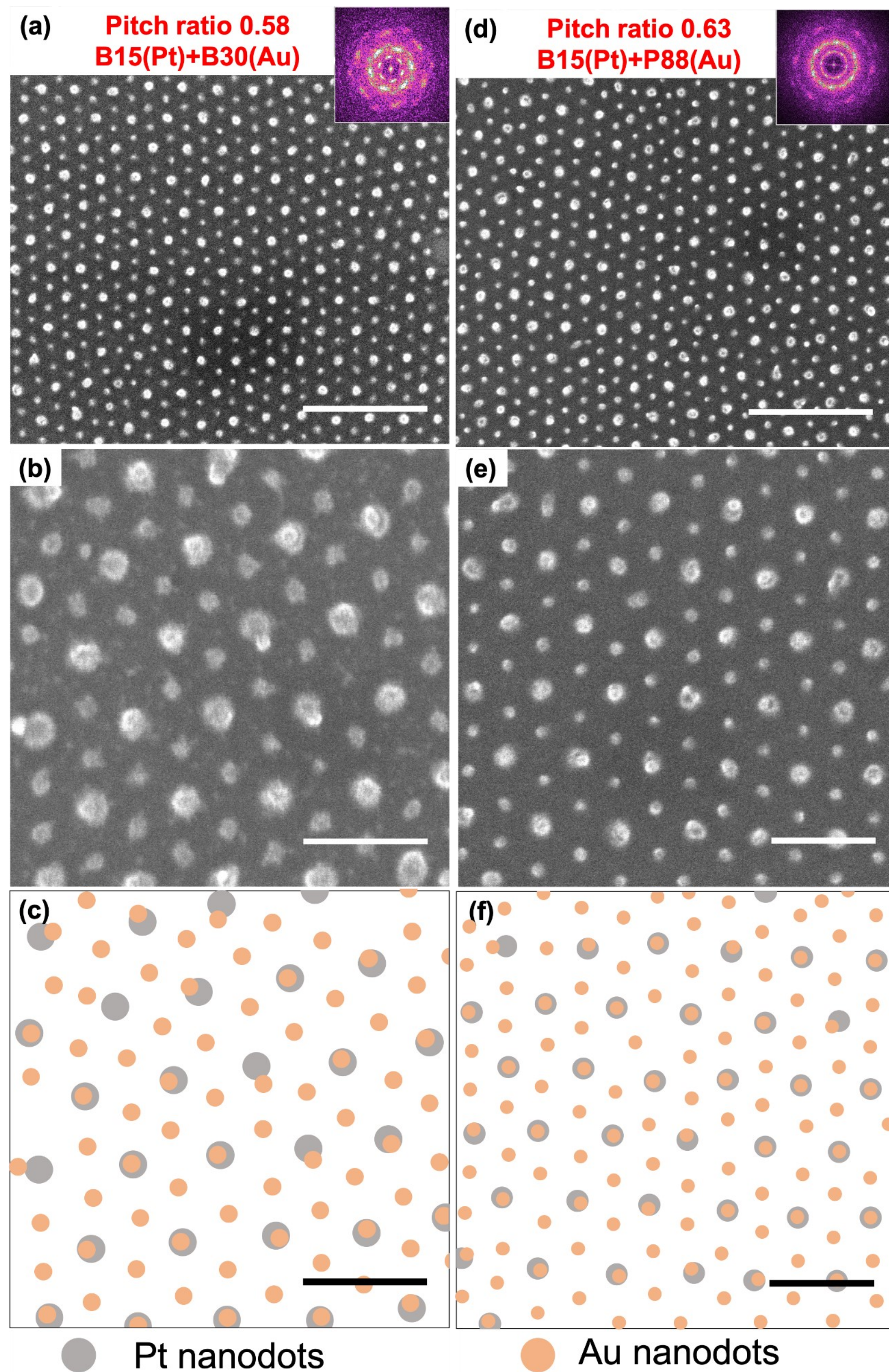

Figure 4.17. Low (first row, a+d) and high (second row, b+e) magnification SEM micrographs and schematic illustration of the high magnification SEM (third row) of Pt–Au Moiré patterns with incommensurate pitch ratios of (a–c) 0.58; bottom layer **B15** (Pt) and top layer **B30** (Au) and (d–f) 0.63; bottom layer **B15** (Pt) and top layer **P88** (Au). The insets represent the FFT of the resulting nanopatterns. Orange and gray dots represent Au and Pt nanodots, respectively. First row scale bars are 250 nm; second and third row scale bars are 100 nm.

Figure 4.18 shows Pt–Au nanopatterns derived from high pitch ratios of 1.6 and 1.7, where the bigger dots (19 ± 1 nm diameter, top layer) represent Au and the smaller dots (11 ± 1 nm diameter, bottom layer) are Pt. For a pitch ratio of 1.6, shown in Figure 4.18(a–c), the majority of the larger Au nanodots are in contact with the smaller Pt nanodots, creating new structures of random and isolated Pt–Au dimers. When the pitch ratio is √3 = 1.7, shown in Figure 4.18(d–f), the Au nanodots from the top layer register within the triangular interstitial positions of the bottom Pt nanodot pattern with a 30° angle of lattice rotation, which is a configurational low energy conformation, as observed previously with PS-*b*-PDMS and SiO_x dots by Cong et al.[368]

Similar Moiré patterns were generated using two different pitch ratios of PS-*b*-PDMS and PS-*b*-P2VP metalized with Pt; the corresponding SEM images are shown in Figure 4.19. These Moiré patterns of SiO_x and Pt were fabricated to confirm that by using two different BCPs as top and bottom layers, similar relative angles of rotations can be observed when using the different BCPs. Figure 4.19(a) shows the Moiré pattern of SiO_x–Pt with a pitch ratio of 0.9. The large area displayed in Figure 4.19(d) is from a measured pitch ratio of 1.1 to show the influence of grain boundaries in the underlying SiO_x layer; the outlined red area in the image represents a grain boundary in the bottom SiO_x layer.[322] The majority phase comprises the triangular Moiré patterns, as shown in Figure 4.19(c), and the flower-like pattern in Figure 4.19(b) is associated with these grain boundaries. A similar misalignment caused by these grain boundaries was observed by Cong at al. for incommensurate pitch ratios of SiO_x Moiré superstructures derived from PS-*b*-PDMS.[322]

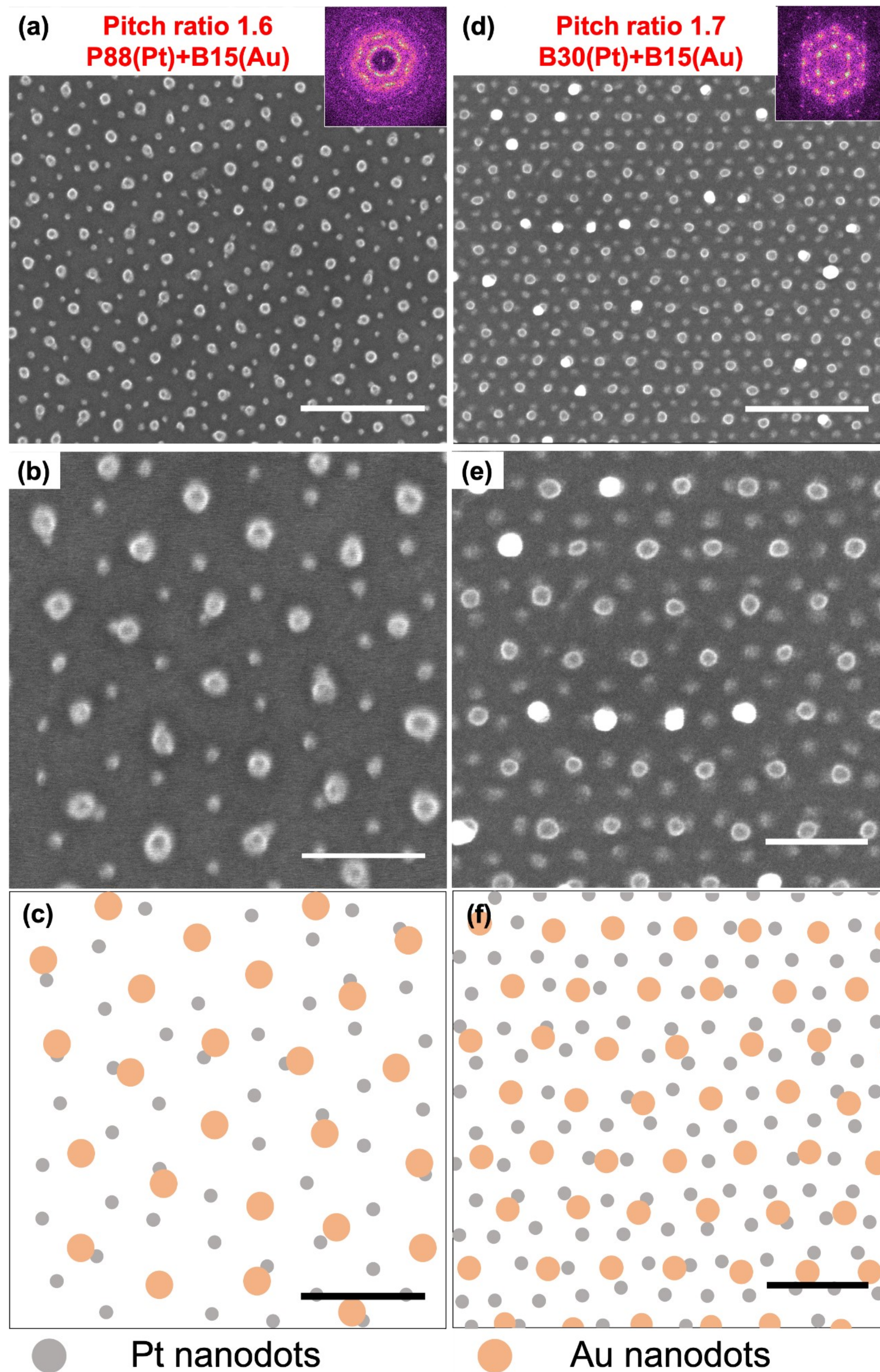

Figure 4.18. Low (first row) and high (second row) magnification SEM micrographs and high magnification schematic representation (third row) of Pt–Au Moiré patterns with incommensurate pitch ratios of (a–c) 1.6; bottom layer **P88** (Pt) and top layer **B15** (Au) and (d–f) 1.7; bottom layer **B30** (Pt) and top layer **B15** (Au). Orange and gray dots represent Au and Pt nanodots, respectively. Insets show the corresponding FFT. First row scale bars are 250 nm; second and third row scale bars are 100 nm.

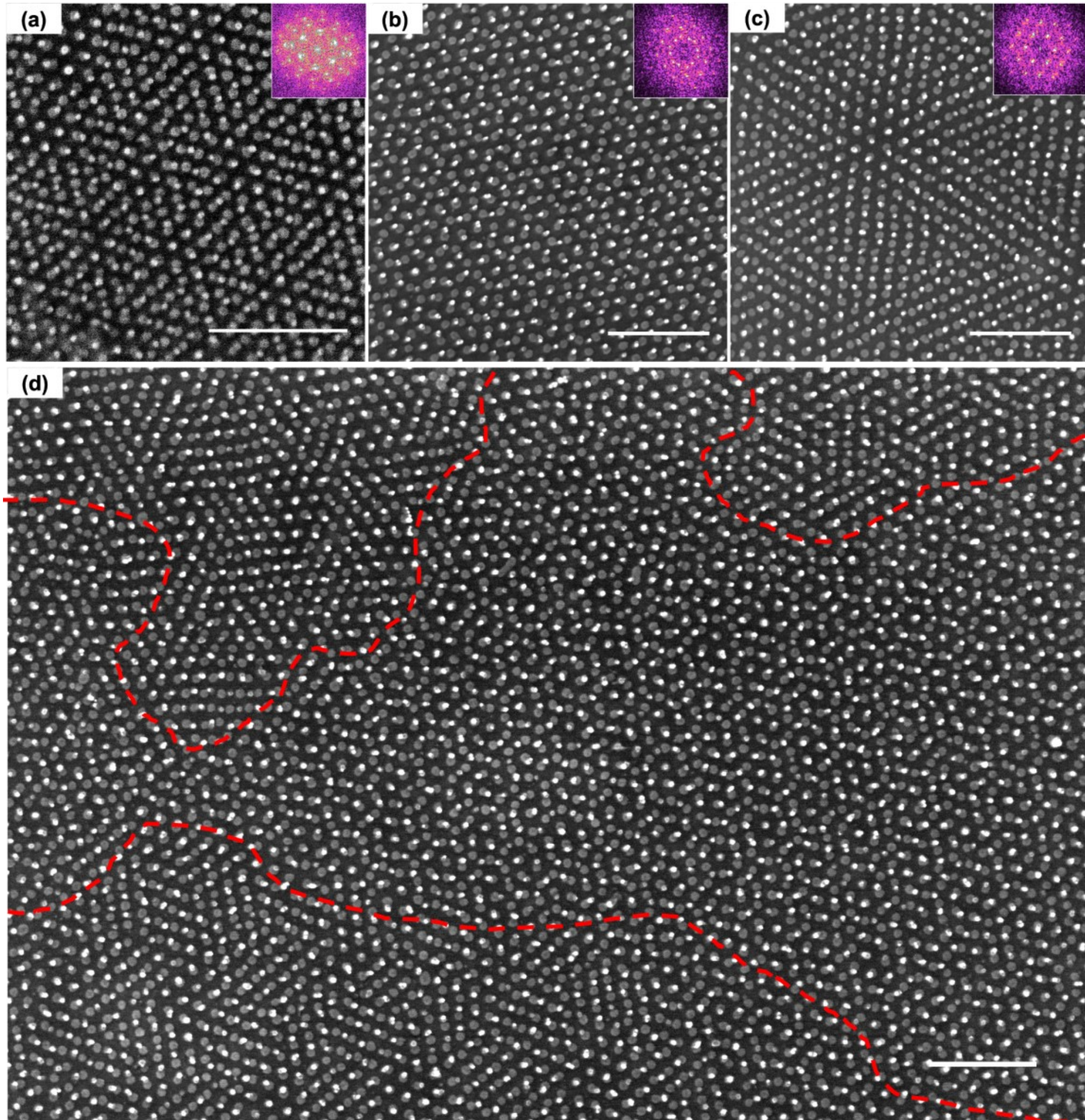

Figure 4.19. SEM micrographs of SiO_x–Pt Moiré patterns with incommensurate pitch ratios of (a) 0.9; bottom layer **P48** (SiO_x) and top layer **P44** (Pt) (b–d) 1.1; bottom layer **B30** (SiO_x) and top layer **P88** (Pt). The red area represents a grain boundary in the bottom **B30** (SiO_x). The insets represent the FFT of the resulting nanopatterns. Small brighter dots are Pt, and dark larger dots are SiO_x. All the scale bars are 250 nm.

4.4 UV-vis Spectroscopic Analysis of the Localized Surface Plasmon Resonance of the Metal Nanoparticle Arrays

The collective oscillations of the electrons at the metallic nanoparticle-dielectric interface in a confined volume results in the effects associated with the localized surface plasmon. Metals have this resonant response at the specific wavelength of

absorption, and the spectral features of the LSPR depend on several parameters, such as morphology (size and shape), chemical composition, and dielectric environment of the nanoparticles. It is well known that isotropic spherical Au nanoparticles demonstrate only one LSPR band that is dependent upon the diameter of the nanoparticle. For a 10 nm particle, the peak of the absorption is around 520 nm, it increase to 520–530 nm when the size is ~10-40 nm, and to ~530–540 nm when the size is ~40-80 nm, and is accompanied by an increase in the LSPR peak intensity.[404] One of the main aims of this chapter is to explore how the formation of non-native morphologies from a self-assembly of mixed metal components double layer arrays alters the optical behavior of native morphologies of a single layer metal nanopattern.

Ellipsometric measurements of the single and double layers of Pt–Au samples self-assembled on native oxide-capped Si substrates were acquired first to capture the absorption profile of the metal nanopatterns, with the goal of observing the features associated with the LSPR. Shown in Figure 4.20 are the spectroscopic analyses at angles varying from 55° to 85°. Ellipsometry measures a change in the polarization as the light (HeNe laser source) is reflected from the surface of the sample, which in this case comprises a metal nanopattern. This change in the polarization is measured as a ratio of amplitude (φ) and phase difference (Δ) in the incident and the reflected light. As can be seen in Figure 4.20, the feature corresponding to the LSPR absorbance was observable at 520 nm, but the low signal-to-noise ratio made it challenging to determine any possible blue or red shifts, shape changes, and other subtle changes. We then decided to prepare the metal nanopatterns on quartz substrates and perform UV-vis spectroscopy in direct transmission mode (with the beam normal to the quartz surface).

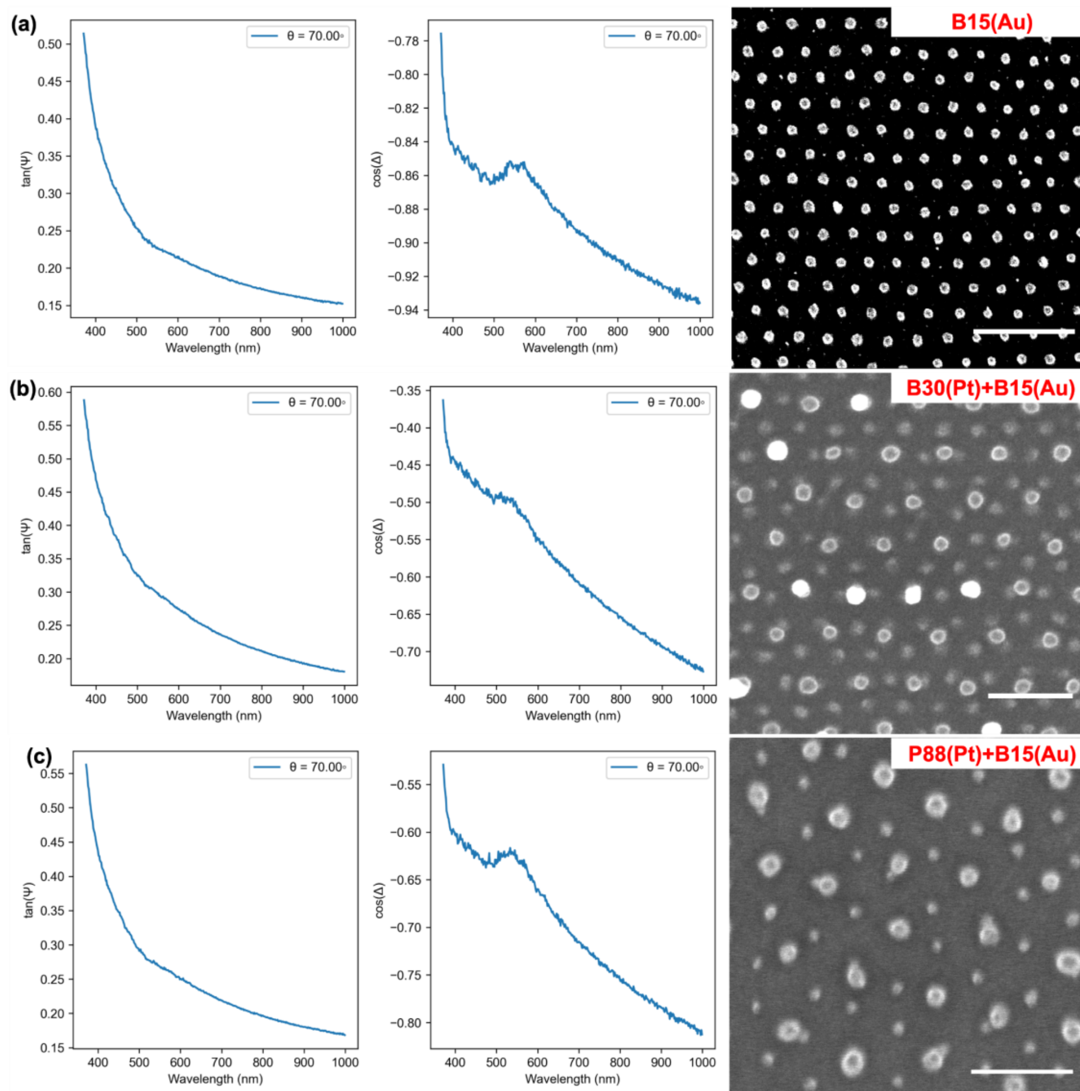

Figure 4.20. Experimentally measured SPR spectra of ellipsometric parameters, amplitude φ and phase Δ, at an angle of 70° for an array of (a) Au nanoparticles and (b,c) Au–Pt bilayers. All scale bars are 100 nm.

The UV-vis spectroscopic data were collected by self-assembling all seven bimetallic double layer samples on quartz substrates in the same manner as was carried out on the Si substrates. The LSPR peak around 520 nm is observed for the single layers of gold nanoparticle arrays self-assembled using **B30**, **P88**, and **B15**, as shown in Figure 4.21. The diameters of the nanoparticles are between 16 and 26 nm. The LSPR absorption of **B15** is slightly red shifted and is the most intense of the series, as it has the largest particle size (26 ± 1 nm). The number of particles per unit area was calculated to determine if there is a relationship to the intensity of the ~520 nm feature,

but no obvious connection was noted (Figure 4.23).[405,406] Single layers of Pt nanoparticle arrays exhibit a broad featureless absorption in the 350–800 nm range, with an increase in intensity at lower wavelengths due to interband excitation, as shown in Figure 4.22.[407] The intensity of the absorption spectra of **B30** and **B15** is comparatively high due to an angle in the sample positioning in spectrophotometer during the data collection. Hence, quantification is not possible for this analysis.

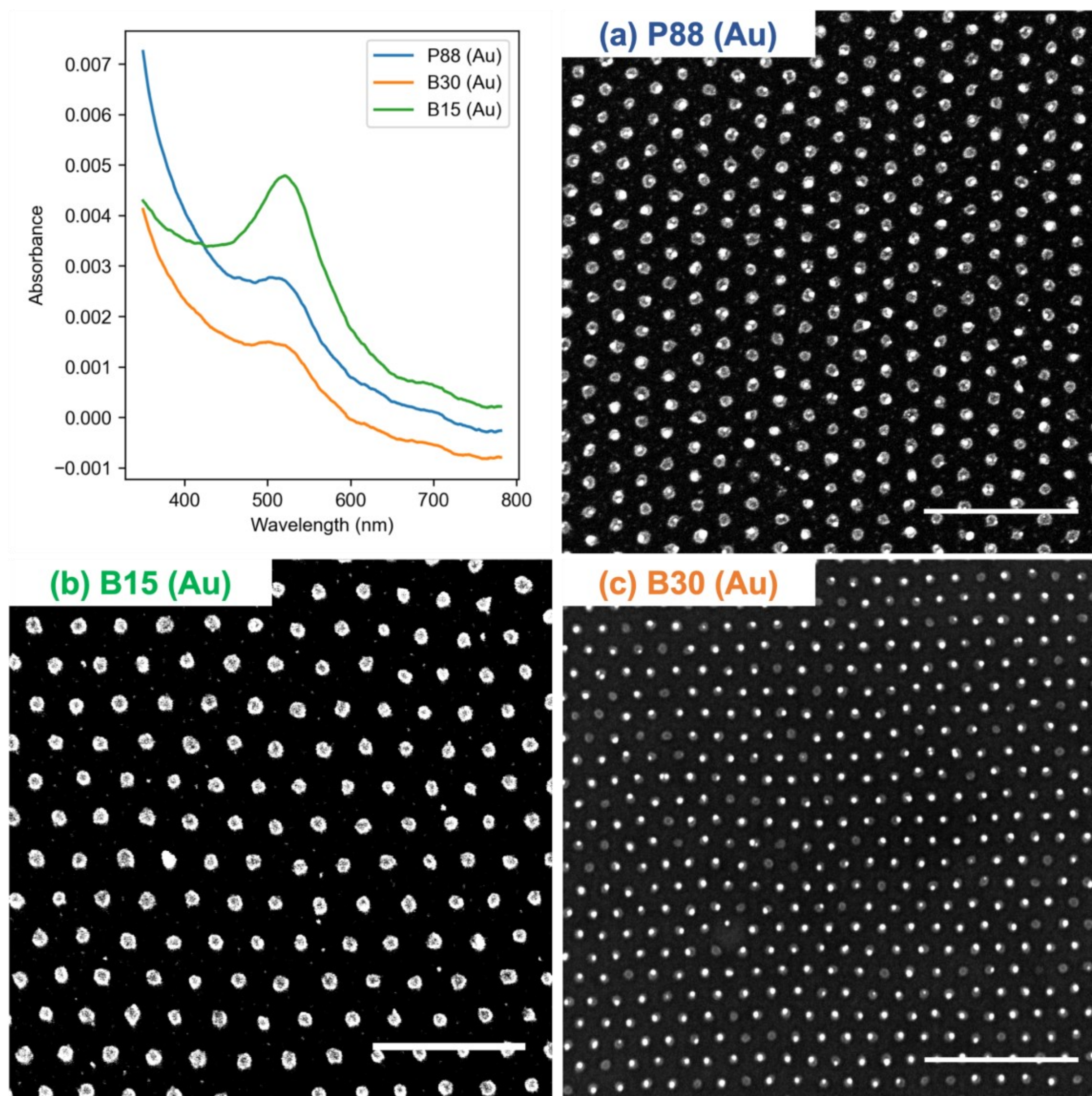

Figure 4.21. The UV-vis absorption spectra for self-assembled single layers of Au nanoparticle arrays on fused silica substrates. All scale bars are 250 nm.

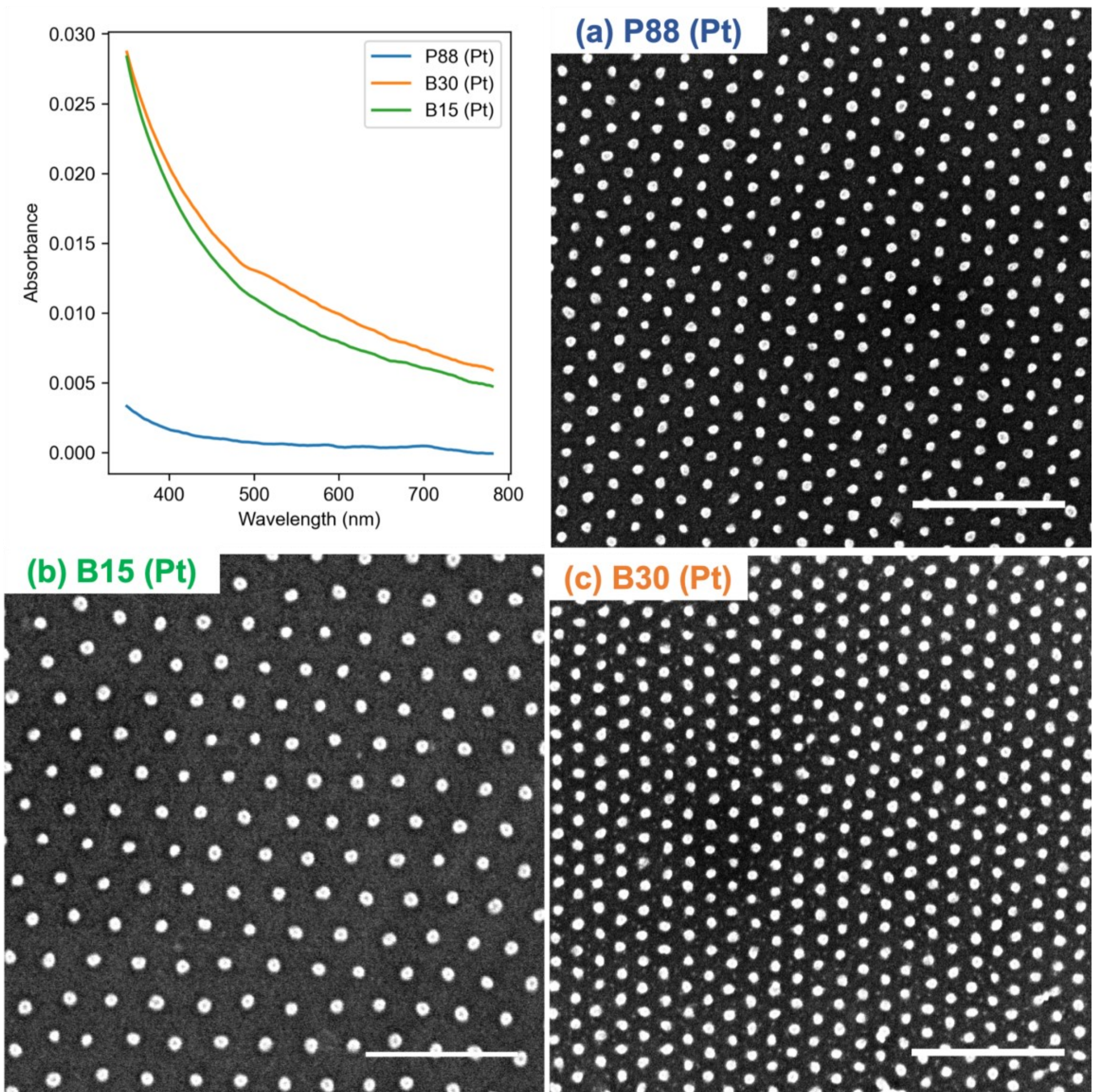

Figure 4.22. The UV-vis absorption spectra for self-assembled single layers of Pt nanoparticle arrays on fused silica substrates. All scale bars are 250 nm.

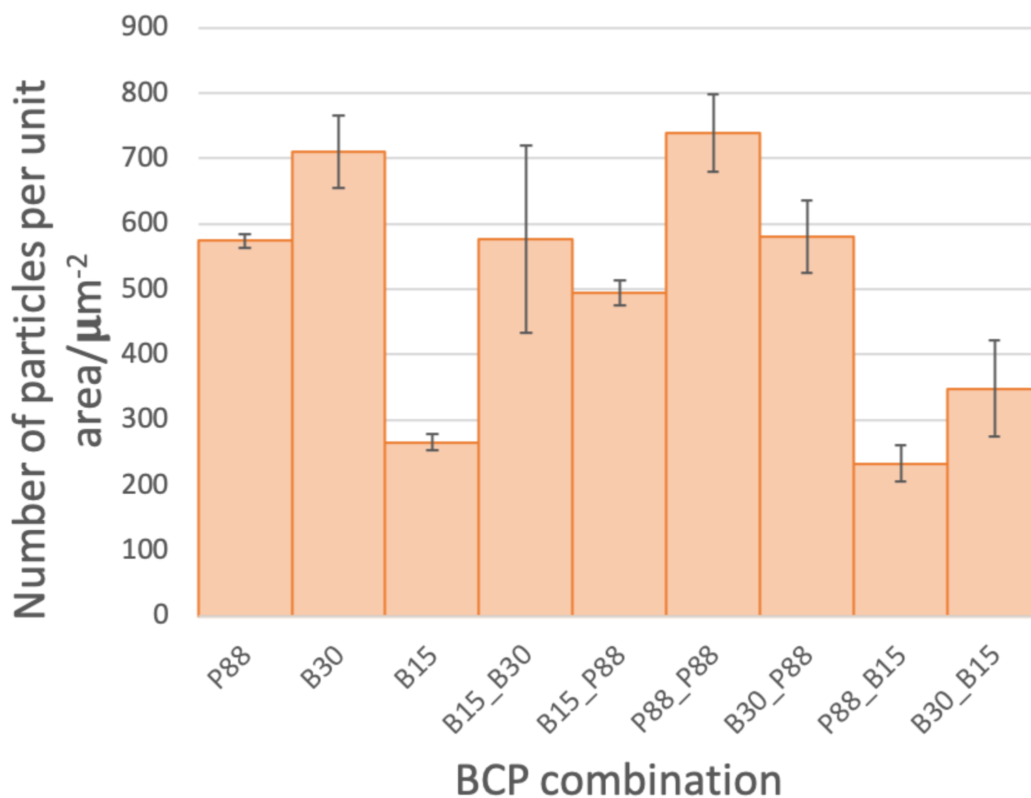

Figure 4.23. Number of Au nanoparticles per unit area vs BCP combination. Error bars represent the standard deviation from several samples and SEM micrographs.

Due to the aggressive nature of the RIE etching step, the diameters of the Au and Pt dot show a significant decrease from their corresponding sizes in a single layer (see Table 4.4). The etching contrast between the PS and $KAuCl_4$ metalized P2VP blocks varies in the second RIE step compared to a single layer of Au etching due to the presence of embedded Pt nanoparticles in the P2VP block, as discussed in Chapter 3. As stated earlier in this section, the LSPR peak of the Au nanoparticles depends on the size and morphology of the nanoparticles; when arranged in close proximity, additional LSPR-based features may arise, such as the SLR mentioned in the introduction of this chapter. These features depend on the periodicity of the metal nanoparticles, the plasmonic material, the local ordering of the metal nanoparticle array or lines, and the dielectric environment of the surroundings. The following section will use the UV-vis spectra to determine if any of these parameters affect the resulting spectroscopic characteristics of these metallic patterns.

Table 4.4. Native Pitch Ratios Calculated from a Single Layer of Pt and Au Nanopatterns and Diameters of Pt and Au Nanodots in Single Layers and in Their Corresponding Double Layer Patterns for Each Combination of BCP Patterns

BCP Layers (bottom+top)	Theoretical L2/L1 based upon single layers	Diameter of Pt nanodots in single layer / nm	Diameter of Pt nanodots in double layer / nm	Diameter of Au nanodots in single layer / nm	Diameter of Au nanodots in double layer / nm
B15+**B30**	0.58	26 ± 1	18 ± 2	16 ± 1	11 ± 2
B15+**P88**	0.63	26 ± 1	18 ± 1	19 ± 1	12 ± 1
P88+**P88**	1.0	16 ± 1	9.0 ± 1	19 ± 1	12 ± 1
B30+**P88**	1.1	17 ± 1	9.0 ± 1	19 ± 1	11 ± 1
P88+**B15**	1.6	16 ± 1	11 ± 1	26 ± 1	19 ± 1
B30+**B15**	1.7	17 ± 1	4.0 ± 1	26 ± 1	22 ± 1

The Pt–Au double layers all exhibit a plasmon peak at visible wavelengths that are dominated by the Au-based LSPR mode around 515–525 nm.[408] Due to the breadth of this gold-based LSPR mode, slight red or blue shifts cannot be discerned easily, but we can conclude that there are no significant shifts or broadening upon incorporation into the double layers with Pt, as shown in Figures 4.24–4.30. A slight blue shift might be expected as the average Au nanoparticle size decreases in the double layer, (see Table 4.4).

Note that in most spectra of the bimetallic Au–Pt double layers, interestingly, there is a very broad feature at lower energies that is not present in any of the single layer Au and Pt spectra. Using Figures 4.24(a,b) as an example, one can see an obvious change in the shape of the spectrum at 640 cm^{-1}; the same spectrum from Figure 4.24(a) is reproduced in Figure 4.24(b) with a narrower y-axis to reveal the low energy feature above 640 cm^{-1} better. Three possible explanations for this feature include: (i) an extended plasmon band (EPB) due to interparticle coupling of the LSPRs of the gold nanoparticles via the platinum nanoparticles,[395,409–411] (ii) resulting from either the obvious linear arrangements of Pt–Au–Pt dots and/or extended 2D arrays,[393,394,412] or (iii) anisotropic morphologies of overlapping Au–Pt nanoparticles that could have a

longitudinal LSPR mode, in addition to the transverse mode, which would be longer than the isotropic mode of the circular particles.[407,408] The third option, that of anisotropic plasmonic Au-Pt nanoparticles seems the least likely because the feature above 600 nm appears strongest in one sample with very few overlapping Au–Pt nanoparticles; this is seen, for example, by comparing Figure 4.24 (no overlap but a strong feature at >600 nm) and Figure 4.25 (a high degree of overlap and almost no apparent feature at 600 nm). In addition, the LSP of a Pt nanoparticle of this size is at a much higher energy than that of Au and requires illumination with light on the order of ~200–250 nm in order to be in resonance,[413–415] therefore, the Pt itself does not bring any additional features to the visible region due to its LSPR . It is, however, known that the growth of Pt on Au nanorods results in dephasing (broadening) of the LSPR of gold, with only a subtle red shift that is significantly smaller than the difference between the parent LSPR peak at 520 cm^{-1} from the isotropic gold nanoparticles and the broad feature above 640 cm^{-1} that we observe here in the double layers.[416] Therefore, for these reasons, it seems less likely that anisotropic Pt–Au nanoparticles are the cause of the lower energy feature. We will now discuss options (i) and (ii).

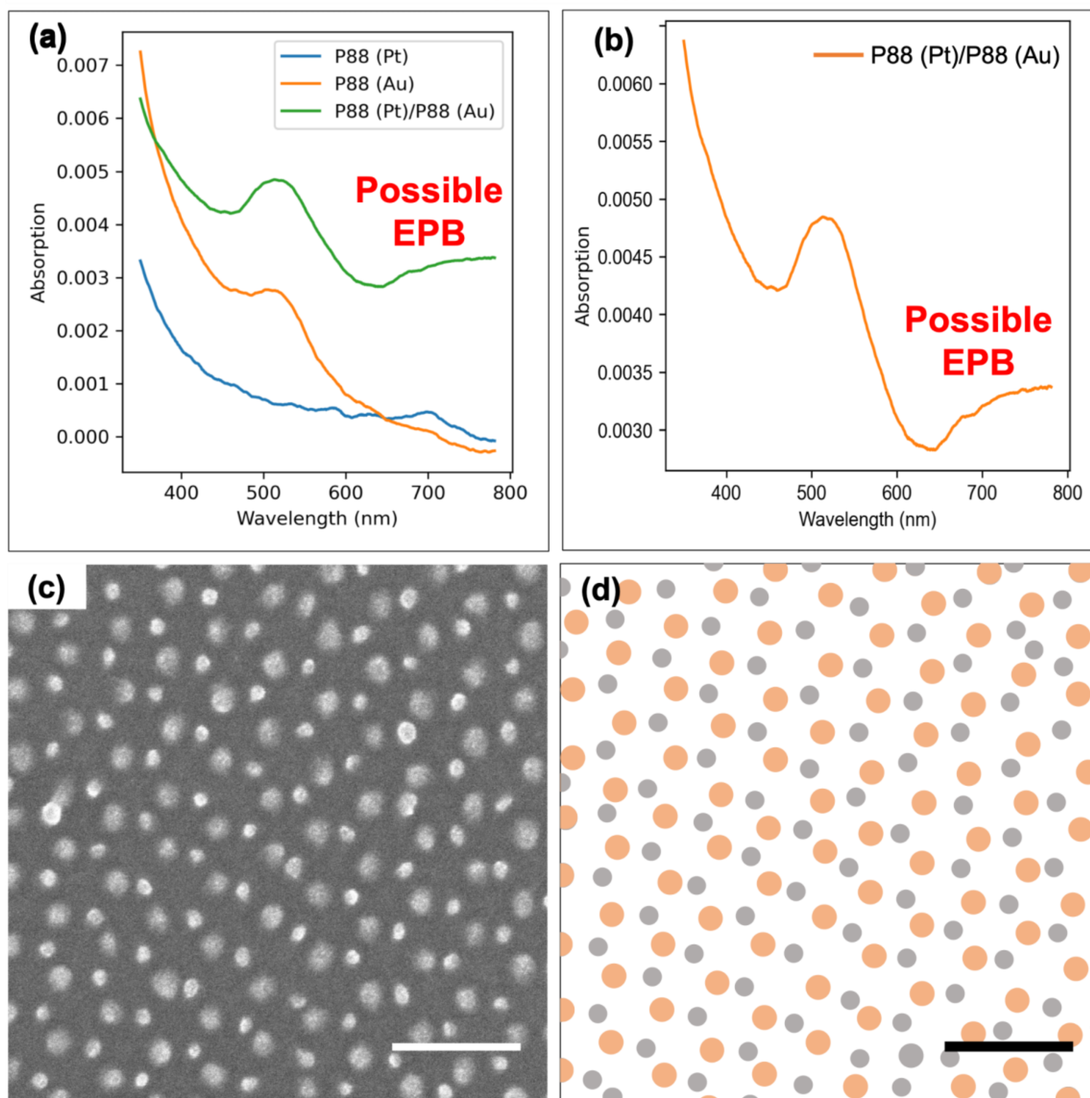

Figure 4.24. (a,b) UV-vis spectrum of the **P88** (Pt)/**P88** (Au) metal bilayer combination showing the distinct feature at wavelengths longer than 600 nm that could correspond to an extended plasmon band (EPB). (c) High magnification SEM micrographs and (d) high magnification schematic representation of the Pt–Au bilayer. Orange and gray dots represent Au and Pt nanodots, respectively. All scale bars are 100 nm.

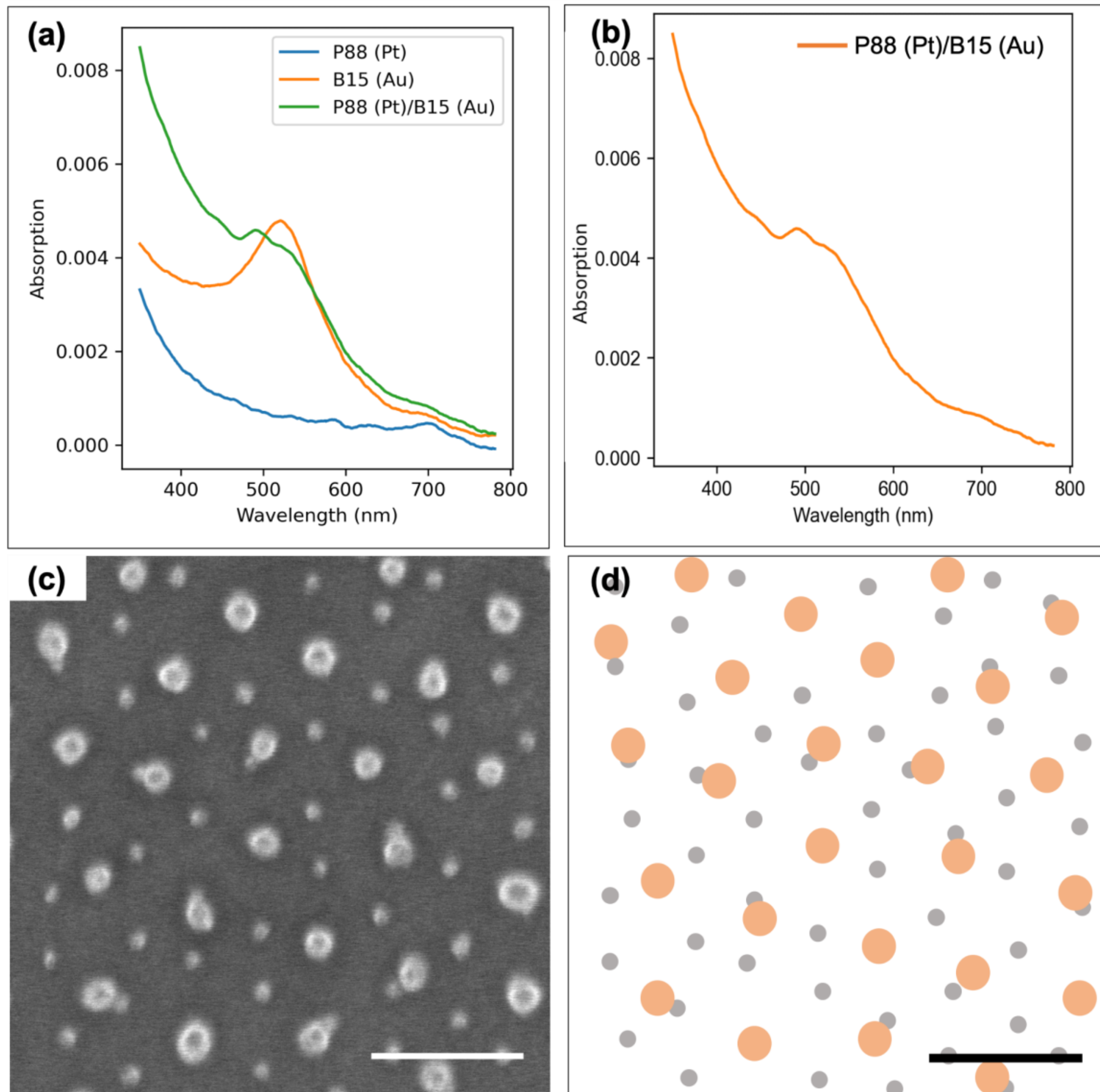

Figure 4.25. (a,b) UV-vis spectrum of the **P88** (Pt)/**B15** (Au) metal bilayer combination showing almost no the distinct feature at wavelengths longer than 600 nm. (c) High magnification SEM micrographs and (d) high magnification schematic representation of the Pt–Au bilayer. Orange and gray dots represent Au and Pt nanodots respectively. All scale bars are 100 nm.

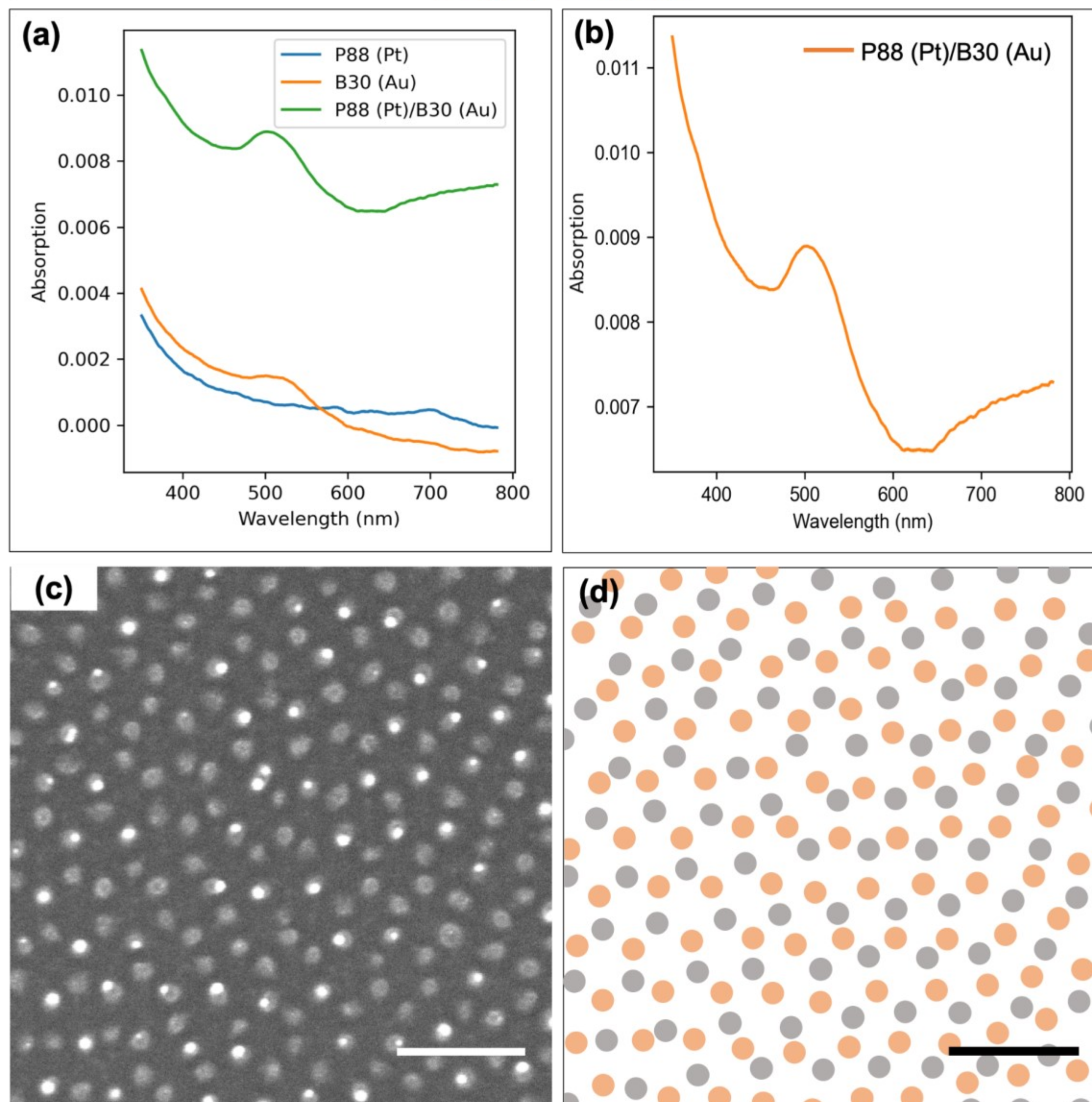

Figure 4.26. (a,b) UV-vis spectrum of the **P88** (Pt)/**B30** (Au) metal bilayer combination showing the distinct feature at wavelengths longer than 600 nm that could correspond to a EPB (c) High magnification SEM micrographs and (d) high magnification schematic representation of the Pt–Au bilayer. Orange and gray dots represent Au and Pt nanodots respectively. All scale bars are 100 nm.

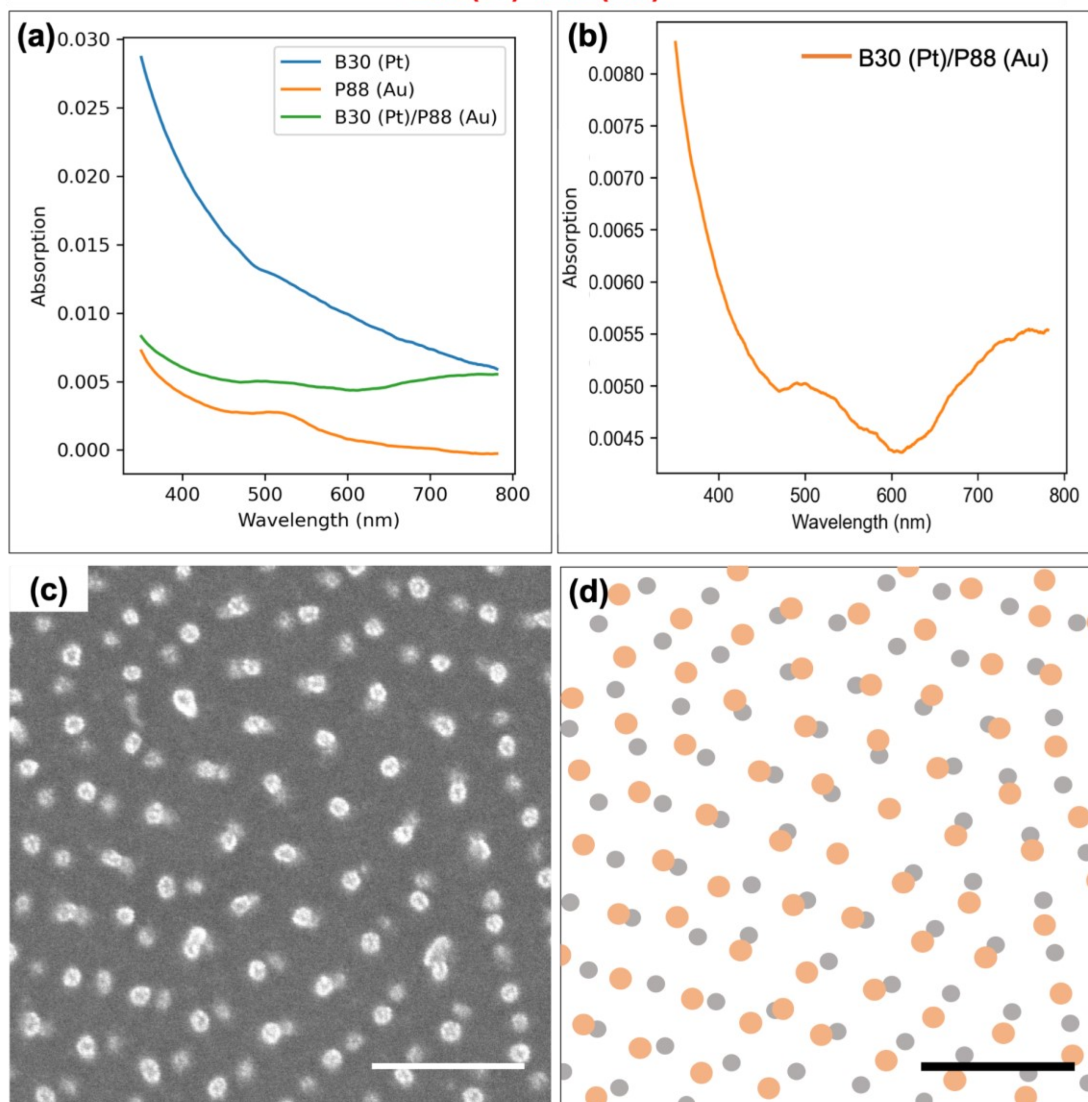

Figure 4.27. (a,b) UV-vis spectrum of the **P88** (Pt)/**B30** (Au) metal bilayer combination showing the distinct feature at wavelengths longer than 600 nm that could correspond to EPB. (c) High magnification SEM micrographs and (d) high magnification schematic representation of the Pt–Au bilayer. Orange and gray dots represent Au and Pt nanodots respectively. All scale bars are 100 nm.

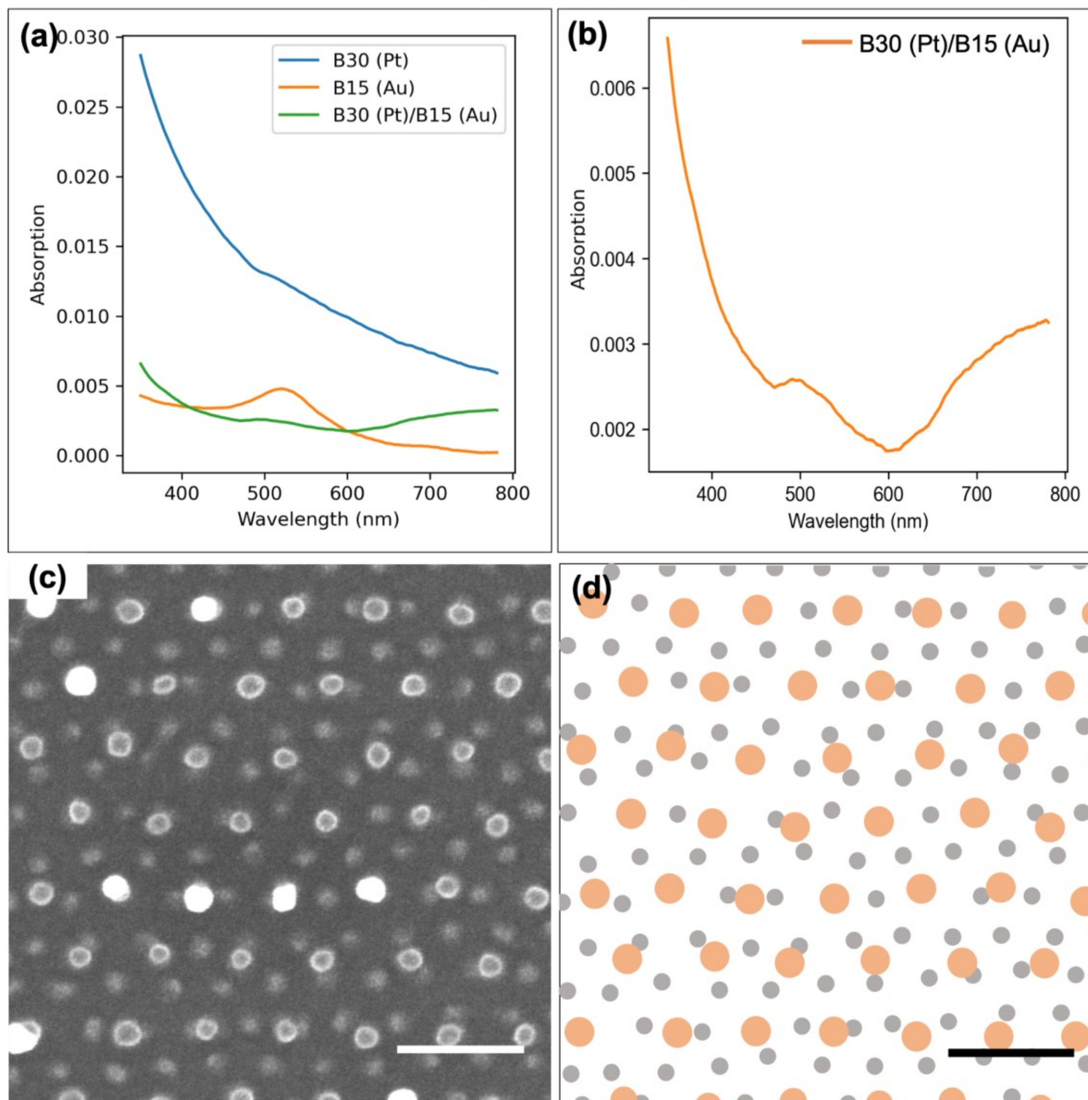

Figure 4.28. (a,b) UV-vis spectrum of the **B30** (Pt)/**B15** (Au) metal bilayer combination showing the distinct feature at wavelengths longer than 600 nm that could correspond to EPB. (c) High magnification SEM micrographs and (d) high magnification schematic representation of the Pt–Au bilayer. Orange and gray dots represent Au and Pt nanodots respectively. All scale bars are 100 nm.

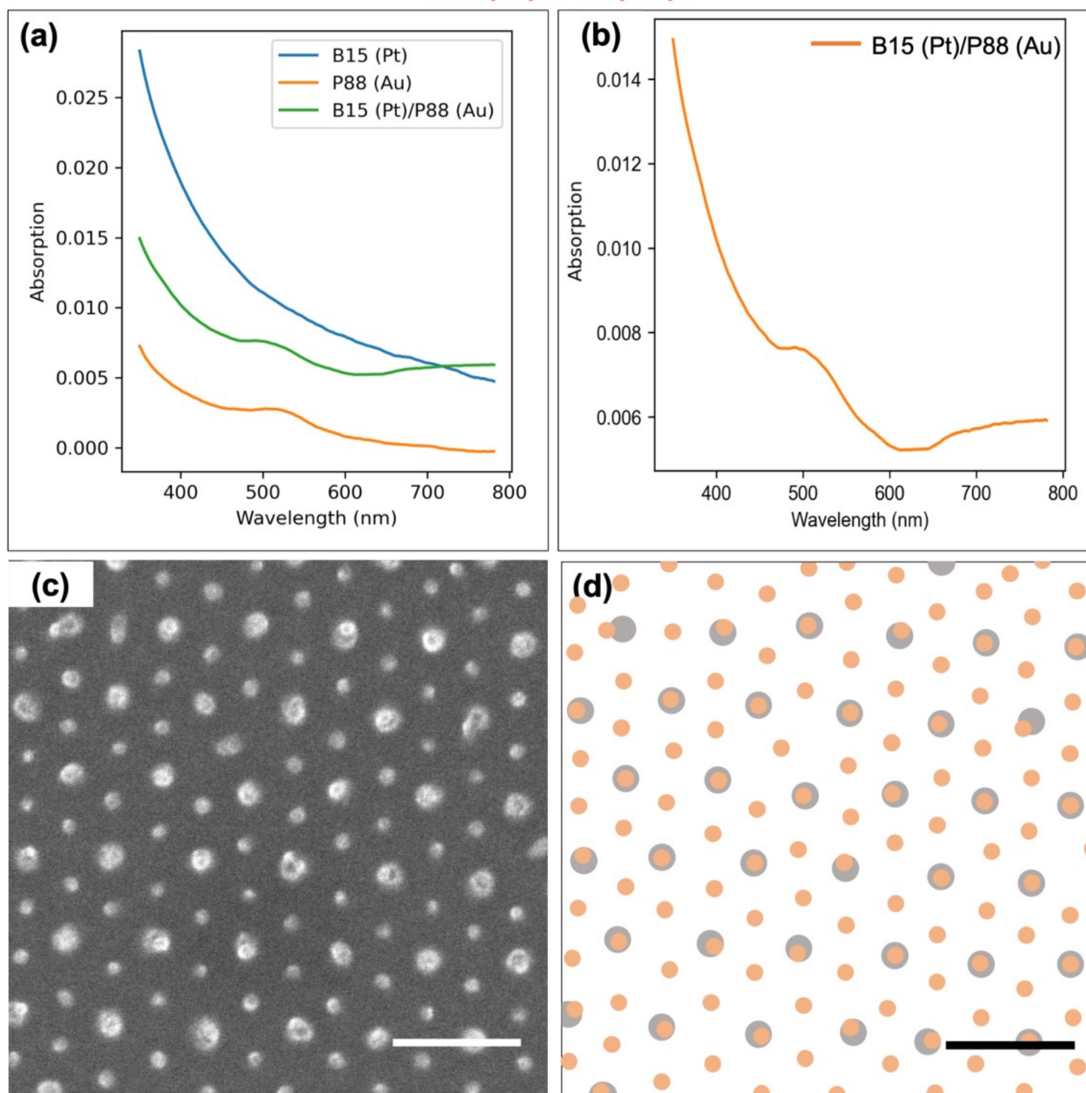

Figure 4.29. (a,b) UV-vis spectrum of the **B15** (Pt)/**P88** (Au) metal bilayer combination showing the distinct feature at wavelengths longer than 600 nm that could correspond to EPB. (c) High magnification SEM micrographs and (d) high magnification schematic representation of the Pt–Au bilayer. Orange and gray dots represent Au and Pt nanodots respectively. All scale bars are 100 nm.

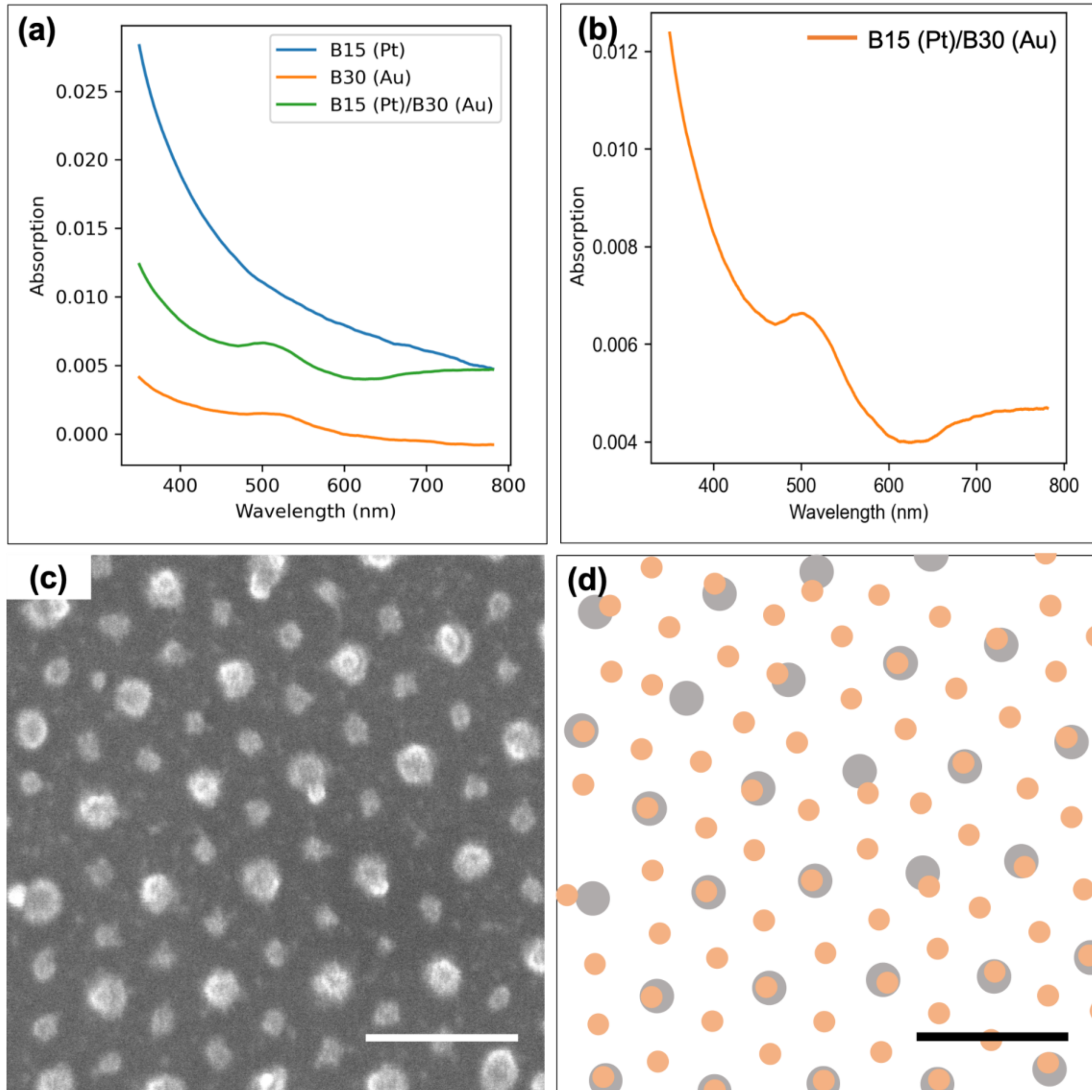

Figure 4.30. (a,b) UV-vis spectrum of the **B15** (Pt)/**B30** (Au) metal bilayer combination sho wing the distinct feature at wavelengths longer than 600 nm that could correspond to EPB. (c) High magnification SEM micrographs and (d) high magnification schematic representation of the Pt–Au bilayer. Orange and gray dots represent Au and Pt nanodots respectively. All scale bars are 100 nm.

When plasmonic nanoparticles, usually Au, are arranged into an ordered lattice with wavelength scale periodicities and are exposed to electromagnetic waves (EMs), the LSPRs of individual particles can couple with the light diffracted from the ordered array and give rise to SLR.[393,394,412,417] The position and the coupling strength are dictated by the LSPR of the individual plasmonic nanoparticles, in addition to the position of the Bragg diffractive modes. Hence, while the size and shape of the nanoparticles control the LSPR of the individual collection of nanoparticles, the lattice

periodicity is the critical feature underpinning the strength and the position of the SLR. The interesting fact about this low energy feature in the work presented here is that it is visible only in double layer patterns and does not appear in any of the single layer Au nanopatterns shown in Figure 4.21, where the variation of the periodicity of the pattern is less (more ordered) compared to the double layer patterns; if SLR was operating, it would be observed in the spectra of the single and more highly ordered gold nanopatterns. In addition, to cast further doubt on the possibility of this lower energy feature resulting from an SLR, the spacing and sizes of the metallic nanoparticles do not fall into the typical regime in which SLRs are observed; the reported spacings for SLRs are on the order of several hundreds of nanometers, while in the metallic nanopatterns here, the spacings are at least an order of magnitude smaller.[378,392,418] Therefore, SLRs are discounted as being the origin of this new feature above 640 cm^{-1}.

The last and, perhaps a more likely explanation for the observed absorption band above 640 cm^{-1} is that it is a result of the formation of ordered and periodic arrays of closely spaced Au and Pt nanoparticles that enable plasmonic coupling. The close proximity of these metallic nanoparticles enables strong interparticle coupling between the gold nanoparticles, leading to an extended plasmon band (EPB). Since interparticle coupling is responsible for EPB, the observed feature could be due to the proximity of gold and platinum nanoparticles in the ordered bimetallic arrays and not due to isolated nanoparticles. The fact that the feature above 640 cm^{-1} is not observed in any of the single layer gold patterns indicates that the nanoparticles are too widely spaced for their size to enable plasmonic coupling upon illumination[395] (see Table 4.5) in the metal nanoparticle arrays; the spacings of the nanoparticles in these bimetallic nanoparticle arrays decrease considerably in several of the combinations. The EPB is attributed to the coherent vibration of the LSPRs of the proximal array of metal nanoparticles. The breadth of the EPB is certainly due to the wide distribution of spacings in these hexagonal lattices, resulting from the range of distances between particles (see Table 4.5), disorder of the lattices, particle overlap, and inhomogeneities of size, polycrystallinity, and shape of the metal nanoparticles themselves.

Table 4.5. Native Pitch Ratios Calculated from a Single Layer of Pt and Au Nanopatterns and Diameters of Pt and Au Nanodots in Single Layers and the Estimated Edge to Edge Distance Between Two Nanoparticles for Each Combination of BCP Patterns and Single Layers of Nanoparticles

BCP Layers (bottom layer+top layer)	Theoretical L2/L1 (Calculated using L1 and L2 of single layers)/nm	Estimated edge-to-edge distance between two nanoparticles in the single and double layers/nm
B30	N/A	24
P88	N/A	26
B15	N/A	40
B15+**B30**	0.58	Range from 0–21
B15+**P88**	0.63	Range from 0–21
P88+**B30**	0.91	Range from 0–38
P88+**P88**	1.0	7
B30+**P88**	1.1	Range from 0–27
P88+**B15**	1.6	Range from 0–25
B30+**B15**	1.7	Range from 0–33

The first direct observation of the ultrafast electronic relaxation and coherent oscillation mode of strongly coupling Au nanoparticle aggregates using femtosecond laser spectroscopy was reported by Zhang and co-workers.[409] The Au aggregates were synthesized using Na_2S and chloroauric acid solution, and polyvinyl pyrrolidone was used to halt the reaction at the appropriate aggregation state. Aggregates of gold nanoparticles with very short interparticle separation (1–3 nm) fall under the category of a strong interacting regime,[395] and give rise to a new absorption in the near-IR, the EPB, in addition to the native LSPR of the gold nanoparticles at 520–540 nm, as shown in Figure 4.31(a). Similarly, Reeler et al. demonstrated the appearance of a new red shifted band for molecularly linked [two π-conjugated oligo(phenylene ethynylene) molecules (OPE) with dithiocarbamate anchoring groups] Au nanoparticles, depending on the degree of aggregation and the distance between the linked Au nanoparticles (corresponding to the EPB, as shown in Figure 4.31(b).[410] For individual Au

nanoparticles, the native LSPR was observed at 535 nm, and as the distance between Au nanoparticle decreased, a red shifted plasmon band appeared. The smaller the gap, the larger the red shifts.

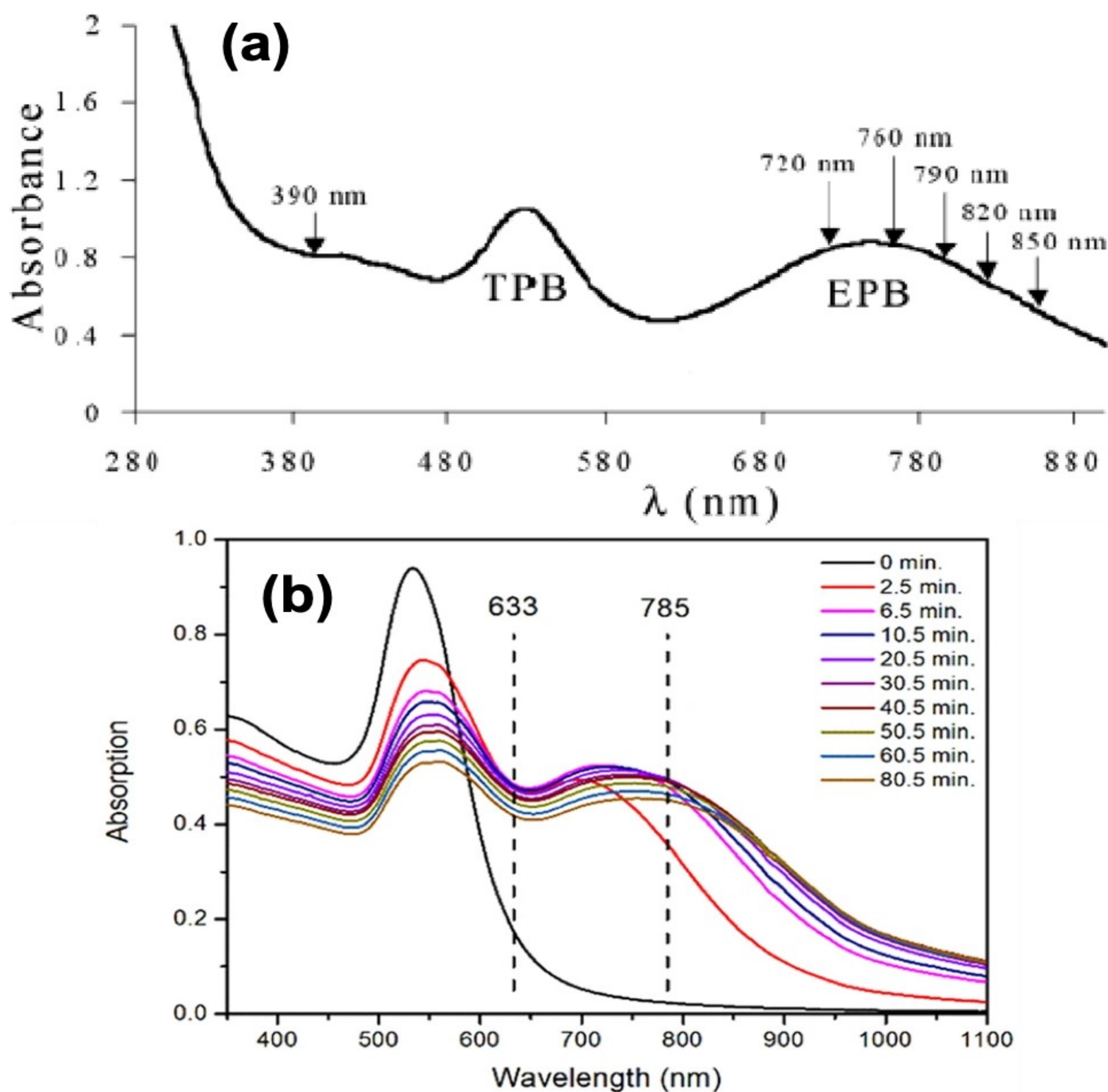

Figure 4.31. UV-vis absorption spectrum of strongly interacting Au nanoparticles giving rise to EPB at near-IR region. (a) Aggregates of gold nanoparticles with LSPR absorbances at 540 nm are termed here as TSP (transverse SPR). This image is from reference 409 with permission from the American Chemical Society. (b) Gold nanoparticle aggregates that are interconnected by conjugated molecular linkers with thiocarbamate groups on both ends. UV-vis absorption spectra as a function of time. This image is from reference 410 with permission from Springer Nature.

It is known that finite arrays or chains of metal nanoparticles can propagate electromagnetic waves upon excitation of their LSPR.[419-422] However, it is important to have an estimation of the interparticle coupling to identify the mechanism of energy

propagation along linear chains or assembly. Link and coworkers used generalized Mie theory to calculate the interparticle separation (σ) between Ag nanoparticles in an array to determine the interparticle coupling of Ag nanoparticle chains which is measured as

$$\sigma = \frac{d}{r} \qquad \text{Eq. 4.1}$$

where d is the center-to-center distance and r is the radius of a nanoparticle.[420,423] According to their study to observe interparticle coupling between the nanoparticles and to energy propagation along the linear chains or assembly, interparticle separation of $\sigma < 2.4$ lead to coupling. Therefore, σ was calculated for all 7 of our patterns to determine if they fall within this range, <2.4, as summarized in Table 4.6. Please note that the original calculations by link and co-workers assumed all-silver arrays, whereas ours comprise gold and platinum. Due to the 'wiggliness' of the patterns and the resulting broad range of values of σ, some of the patterned surface falls outside of this predicted upper limit of 2.4. Therefore, it would be assumed that only those areas in which the values of σ falls below 2.4 would be responsible for the observed feature that appears at a wavelength of >700 nm. Except for pitch ratio of 1.6 in which rather randomly ordered Pt–Au bilayers are observed instead of Au–Pt–Au chains all the other combinations of pitch ratios showed an extended plasmon band at lower energies of the UV-vis spectra. This confirms that to observe interparticle coupling which leads to extended plasmon band, Au–Pt–Au nanoparticles should be in a linear arrangement and at least a fraction of nanoparticles should have interparticle separation less than 2.4.

Table 4.6 Native Pitch Ratios Calculated from a Single Layer of Pt and Au Nanopatterns, the Estimated Center to Center Distance Between Two Nanoparticles, Radius of Au Nanodots in Single/Double Layers and Calculated Interparticle Separation for Each Combination of BCP Patterns and Single Layers of Nanoparticles

BCP Layers (bottom layer+top layer)	Theoretical L2/L1 (Calculated using L1 and L2 of single layers)/nm	Estimated center-to-center distance between two nanoparticles in the single (Au–Au) and double layers (Au–Pt) (d)/nm	Radius of Au nanoparticles (r)/nm	Calculated interparticle separation (σ = d/r)
B30	N/A	41	8.0	5.1
P88	N/A	44	9.5	4.6
B15	N/A	70	13	5.4
B15+**B30**	0.58	Range from 0–43	5.5	0–7.8
B15+**P88**	0.63	Range from 0–42	6.0	0–7.0
P88+**B30**	0.91	Range from 0–32	7.9	0–4.0
P88+**P88**	1.0	Range from 0–32	6.2	0–5.2
B30+**P88**	1.1	Range from 0–30	5.5	0–5.4
P88+**B15**	1.6	Range from 0–52	9.5	0–5.5
B30+**B15**	1.7	Range from 0–47	11	0–4.3

4.5 Conclusion

Sequential self-assembly of incommensurate BCP dot arrays of mixed metal/oxide components lead to preferential orientation over large areas. Interestingly, these bimetallic double layers show significant amounts of overlap and/or contact between Au and Pt nanoparticles from subsequent layers that is not observed prominently from the Moiré patterns fabricated using PS-*b*-PDMS. As a result, the bimetallic double layers of Pt–Au nanopatterns have interesting optical properties that differ from those of the single layers; a new plasmon band appears in the near-IR region, which is attributed to interparticle coupling of Au and Pt nanoparticles, due to their close proximity and propagation of the electromagnetic wave through the chains/arrays of Au–Pt–Au. The estimated interparticle separation (σ) for single layer Au nanoparticles shows a deviation from minimum requirement of $\sigma < 2.4$, which seems to correspond with the absence of extended plasmon band (EPB) at lower energies of the UV-vis spectra. On the other hand, at least a fraction of the Pt–Au nanoparticles are within the predicted range ($\sigma < 2.4$) of interparticle separation for interparticle coupling for all the seven combinations of Pt–Au bilayers. However, when the pitch ratio is 1.6, no EPB

observed, which seems to be correlated with the absence of apparent metal nanoparticles arrays with a $\sigma < 2.4$. These Pt–Au bilayer arrays demonstrate that block copolymer self-assembly is useful for synthesizing periodic arrays over large areas and could be used as a tool to probe and study the low-frequency vibrational modes for periodic arrays of nanoparticles.

Chapter 5

Thesis Summary and Outlook

5.1 Thesis Summary

The primary goal of this thesis is to study the optical properties of the mixed metal/oxide double layer nanopatterns developed by fully bottom up techniques for the self-assembly of block copolymer (BCP) and to develop a step-by-step procedure to form these systems by solvent vapor annealing, metallization, and reactive ion etching (RIE) of poly(styrene-*b*-vinyl-2-pyridine) (PS-*b*-P2VP). Moreover, a detailed optimization procedure of the self-assembly process of BCP, combined with machine learning approaches, were utilized to analyze, quantify, and minimize the defects observed in patterns fabricated using a BCP self-assembly. Highlights and breakthroughs for each chapter are summarized in the following sections.

5.1.1 Chapter 1

This chapter includes a brief introduction about BCPs, their chemistry, and selfassembly. The chapter began by introducing the limitations of Moore's law and photolithography. The next generation lithography techniques and current status of the semiconductor industry related to these techniques were introduced. Then, there is a brief explanation of the polymer chemistry, microphase segregation, and self-assembly of BCPs using different annealing techniques. Furthermore, a brief summary of high χ BCPs and their importance in pattern generation was discussed. Finally, potential applications of BCPs in the semiconductor industry were discussed.

5.1.2 Chapter 2

One of the major challenges to directed self-assembly (DSA) with BCP lithography is defect density and fast analysis of the defects over a large area. This chapter discusses the optimization of the solvent vapor annealing procedure for the self-assembly of poly(styrene-*b*-dimethysiloxane) (PS-*b*-PDMS) by combining machine learning approaches to quantify, analyze, and minimize the defect densities of a self-assembled BCP. The effect of the initial film thickness of the BCP and the swelling degree of the

solvent annealing step on phase defects and point defects of the resulting hexagonally ordered SiO_x dot patterns were studied in detail in this chapter. A controlled solvent vapor flow annealing system was utilized to ensure the reproducibility and control of the solvent annealing process. Machine learning approaches are not applied only to optimize simple self-assembly processes of BCP by analyzing the defects and finding the optimized parameters leading to minimum defect densities in the patterned surface. This approach of machine learning can be combined with any other annealing process as well as with the DSA process to optimize, analyze, and quantify the self-assembly process in an effective and efficient manner.

5.1.3 Chapter 3

This chapter addressed the problems and scientific solutions associated with the optimization of RIE for a single layer of metal-loaded BCP. This optimization is important in order to fabricate double layers of metal nanopatterns. Here, we used PS-*b*-P2VP with different molecular weights metallized with either Au or Pt as bottom and/or top layers. The major problem associated with the metal–metal double layers was the disordering of the bottom layer metal nanoparticles on the silicon substrate upon further RIE treatment due to incomplete annealing of metal ion loaded P2VP blocks during the first RIE step. Thermal annealing was used successfully to anneal these metal nanoparticles to withstand a second RIE step. However, the size of the resulting metal pattern was too small to induce the registration of the second layer. Thus, a chemical/wet electroless deposition of Ag(0) was used to increase the size of metal dots that suffered with variations in size distribution and poor reproducibility and can lead to random and unpredictable double layer metal–metal patterns.

5.1.4 Chapter 4

A fully bottom up self-assembly process of BCP was used to fabricate Pt−Au double layer metal patterns, and their optical properties were studied in this chapter. This sequential self-assembly of PS-*b*-P2VP with different and/or same molecular weight BCPs gives rise to a series of different pitch ratios with a wide range of non-native BCP morphologies of different compositions. Among these non-native patterns, honeycomb

patterns from commensurate pitch ratios and Moiré patterns from incommensurate pitch ratios are observed. However, the bimetallic Pt−Au nanopatterns showed interesting overlaps and/or contacts between the bottom Pt and top Au nanoparticles that are not observed in their respective single layer patterns. A more specific change in the LSPR of these Pt−Au double layers is the appearance of a new plasmon resonance band in the near-IR region, which attribute to an interparticle coupling of Au and Pt nanoparticles due to their close proximity.

5.2 Future Research Directions

5.2.1 Effect of Bottom Layer Height on Pt−Au Nanoparticle Overlap

As shown in Chapters 3 and 4, the height of the bottom layer has a strong influence on the resulting Moiré superstructures. However, this effect of the height of the bottom layer pattern on the registration of the top layer pattern is observed by Cong et al. in their study of Moiré superstructures of SiO_x dot patterns.[322] In Chapter 4, possible overlaps were observed between the bottom layer Pt nanoparticles and the top layer Au nanoparticles for several pitch ratios by closely monitoring the SEM micrographs, as shown in Figure 5.1. The direct overlaps between the top and bottom layer nanoparticles come with an energetic penalty and, to my knowledge,[76,322,344,368] were not observed in the majority of the field of multilayer self-assembly by other BCPs. Spatz and co-workers observed particle-on-particle patterns when they used a two-step dip-coating procedure to layer Au nanoparticles onto a surface coated by an array of titania nanoparticles.[353] The author states that they could not explain this observation easily.

One reasonable fact which allows these interlayer nanoparticle overlaps could be due to the considerably smaller heights of the bottom layer nanoparticles. To confirm these overlaps between Pt and Au nanoparticles further, a detailed analysis should be carried out to determine the height profiles of single layers of Au and Pt nanoparticles and Pt−Au bilayers where suspected overlaps are visible using atomic force microscopy (AFM). These overlaps can be supported further by using tilted SEM

micrographs (see Figure 5.2) and elemental mapping techniques, like energy dispersive x-ray analysis (EDX).

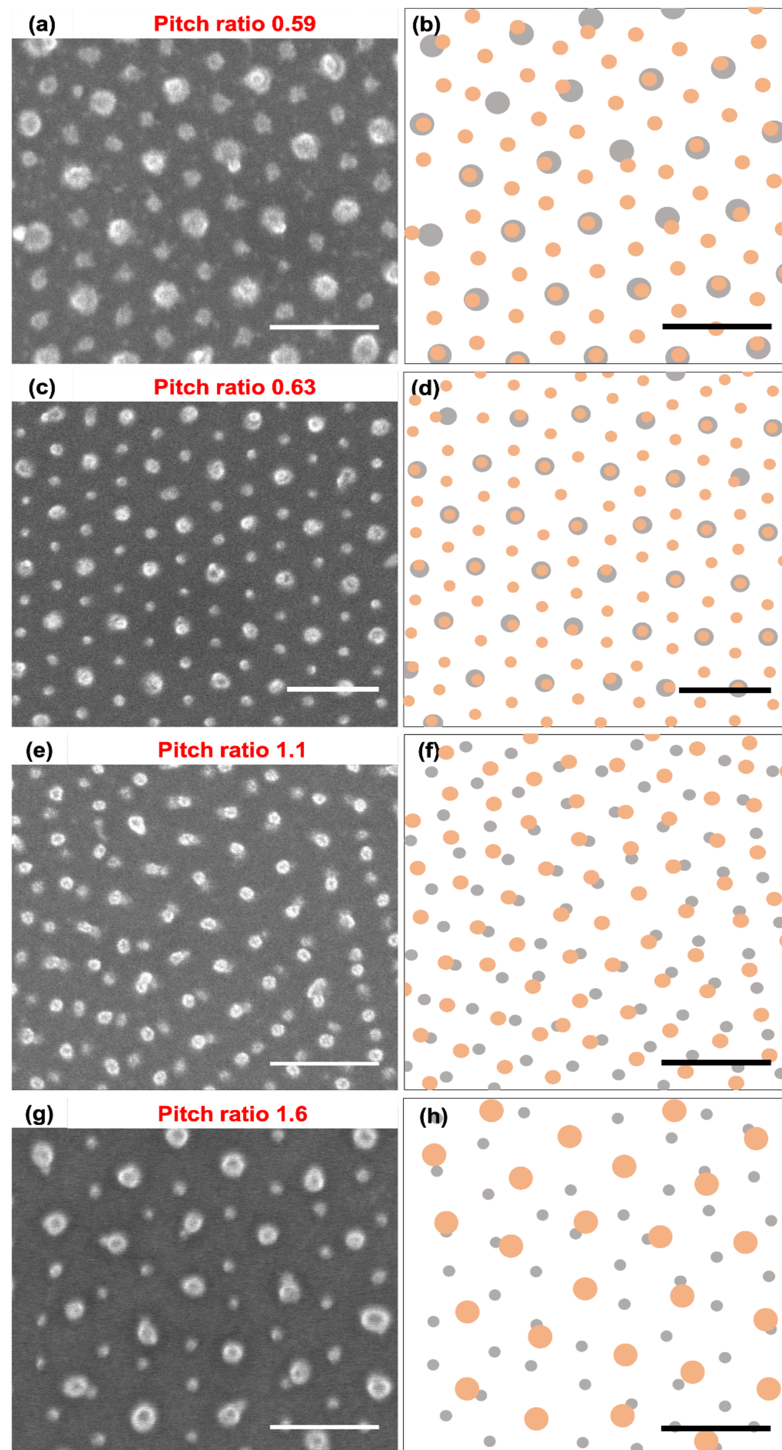

Figure 5.1. SEM micrographs and their manually drawn schematic representations of Pt–Au bilayers by self-assembly of PS-*b*-P2VP for pitch ratios (a) 0.59, (b) 0.63, (c) 1.1, and (d) 1.6. Orange and gray dots represent Au and Pt nanodots, respectively. All scale bars are 100 nm.

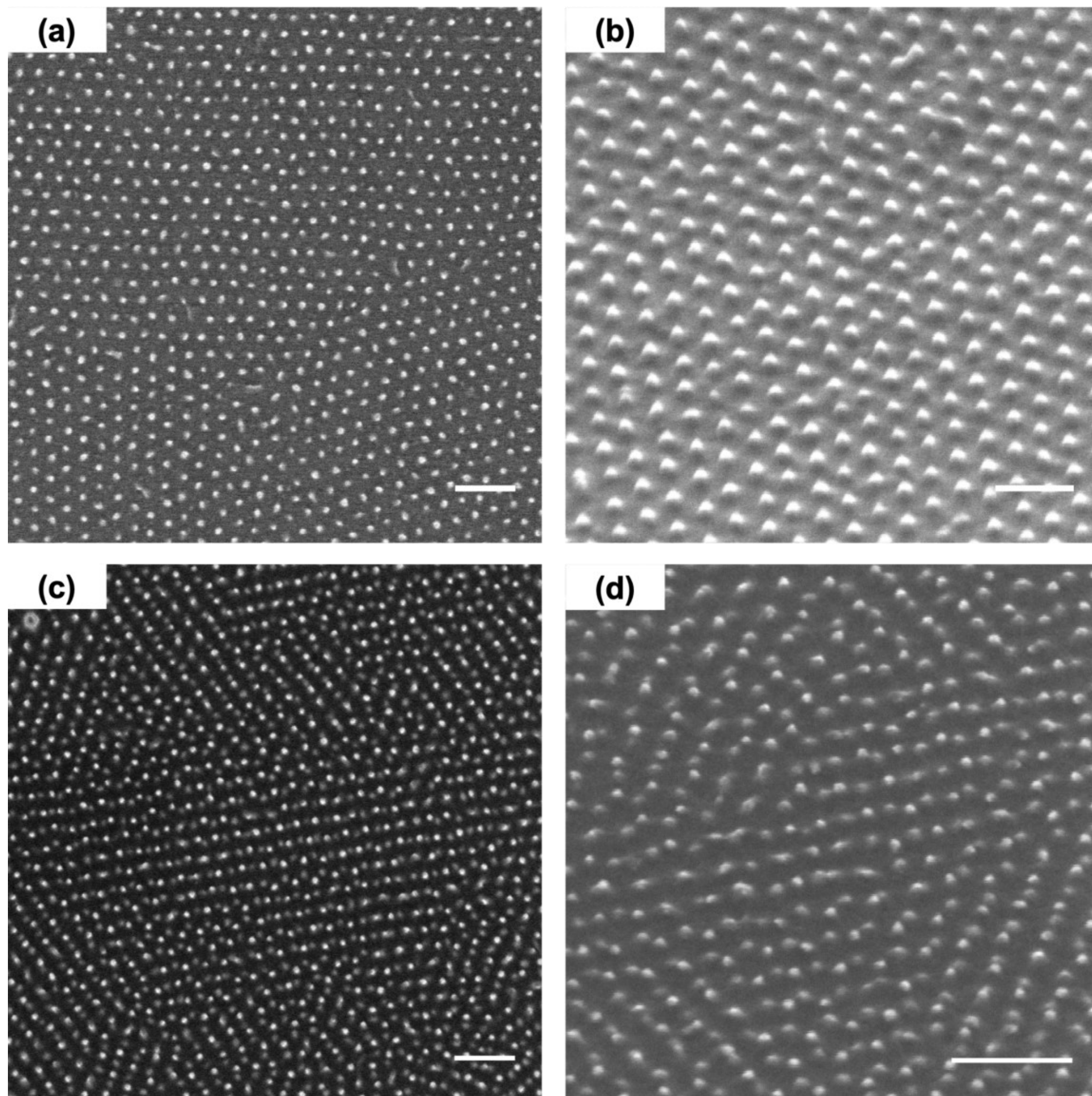

Figure 5.2. SEM micrographs of (a) planar and (b) tilted view of single layer of Pt nanoparticles self-assembled using PS-*b*-P2VP (44k-*b*-8.5k) and (c) planar and (b) tilted view of double layer of Pt–Pt nanopatterns by sequential self-assembled of PS-*b*-P2VP (44k-*b*-8.5k). All scale bars are 100 nm.

5.2.2 Finite-difference Time-domain (FDTD) Simulation of Pt–Au Bilayers

Finite-difference time-domain (FDTD) simulation is a popular computational electrodynamics modeling technique; it is easier to understand and implement in software packages. FDTD can cover a wide range of frequencies with a single simulation run, as it is a time-domain method.[395] The FDTD simulation method is used widely to estimate the plasmon resonance peaks locations, heights, scattering amplitude, and scattering cross sections of nano-scale geometries.[417] In the study of

Pt−Au bilayer patterns, the optical properties were investigated using the UV-vis absorption spectroscopy. However, a new peak formation in the near-IR region is attributed to the inter-particle coupling of Pt and Au nanoparticles that are in close proximity to each other; it was not supported by any theoretical calculations. Hence, FDTD simulations can be applied to determine how the nanogap between Pt and Au nanoparticles affects the resulting plasmon resonance peak of the Pt−Au bilayer patterns and the exact role of the Pt nanoparticles in the appearance of this new feature in the absorption spectrum.

5.2.3 Mixed Metal-metal Nanopattern and Their Optical Properties

Block copolymer self-assembly is a very useful bottom-up approach to fabricate highly uniform and dense hexagonal noble metal nanoparticle arrays over a large area. Among these noble metals, Au and Ag nanoparticles show interesting plasmonic properties and are used widely in different applications, including biosensing,[424] optical antennas,[425] and surface enhanced Raman spectroscopy (SERS).[308] Incorporation of these noble metal nanoparticles (Au, Ag, and Cu) into one single substrate to fabricate nanoparticles arrays of plasmon metals with different sizes and nanogaps between the particles could lead to interesting optical properties.

In Chapter 4, we used Pt and Au bilayers of nanoparticle arrays to study the optical properties of the combined system. We observed a possible interparticle coupling of these Pt and Au nanoparticles due to their close proximity in the bilayer patterns. However, Pt nanoparticles with a particle size less than 20 nm did not show LSPR in the visible region.[387,424,426] In future, the bottom and top layers can be substitute into several other metals, such as Au, Ag, and Cu, which show their LSPR (see Figure 5.3) in the visible region, and study how the variations of nanoparticle separations affect the resulting LSPR spectrum of the combined composition nanoparticle arrays.

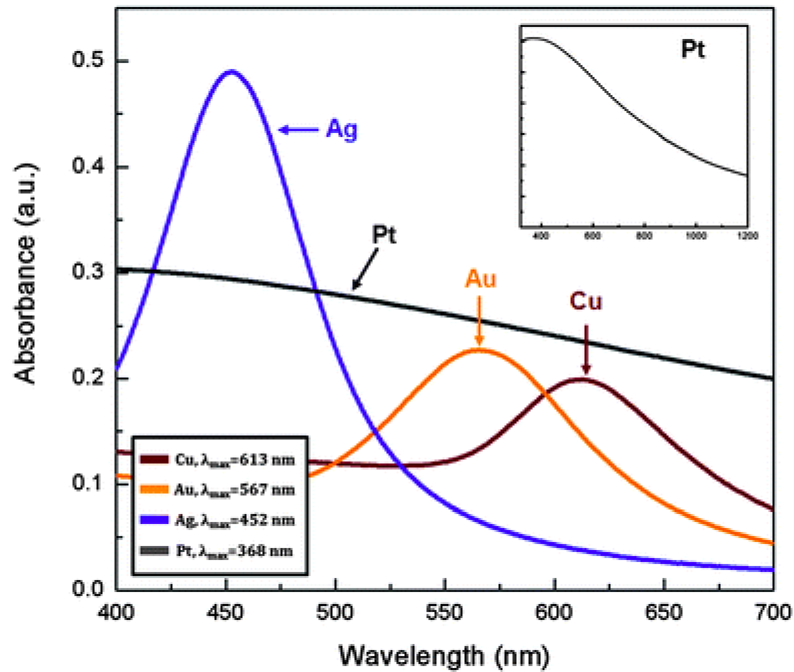

Figure 5.3. UV-vis absorbance spectra for Ag (blue), Pt (black), Au (orange), and Cu (brown) with the same geometry (size 40 nm and height 30 nm). The inset shows the extremely broad and weak absorbance band throughout the visible region. This image is from reference 424 with permission of the Royal Society of Chemistry.

5.2.4 Application of Mixed Metal–metal Bilayer Patterns

Various innovative metallic nanoarray structures have been fabricated owing to the advanced fabrication methods and processing techniques,[397–400] and they facilitate fine tuning the optical properties, such as resonance mode, spectral shape, and intensity. These metallic nanoarray structures can be used in several applications due to their optical properties. These include refractive index (RI) sensing by using narrow resonance linewidth,[427] surface-enhanced spectroscopies utilizing enhanced near-field,[308,428] plasmonic nanolasing due to the small mode volume and enhanced near-field,[394] and perfect light absorption as a result of strong optical confinement and increased light absorption.[429]

Plasmonic nanostructures can enhance near-fields at resonance frequencies greatly, and this can be used in surface enhanced Raman spectroscopy (SERS). Development of SERS relies on good reproducibility and high uniformity over a large area for quantitative analysis and high enhancement for trace amounts. Ren and co-workers fabricated reproducible periodic bowtie arrays with narrow nanogaps as an

SERS substrate, as shown in Figure 5.4.[428] The periodic Au bowtie was fabricated first using a holographic lithography technique with an 85 nm nanogap, and then the nanogap was reduced to 5 nm by electrodeposition of Ag. Both fabrication processes were monitored by in situ dark field spectroscopy for reproducibility.

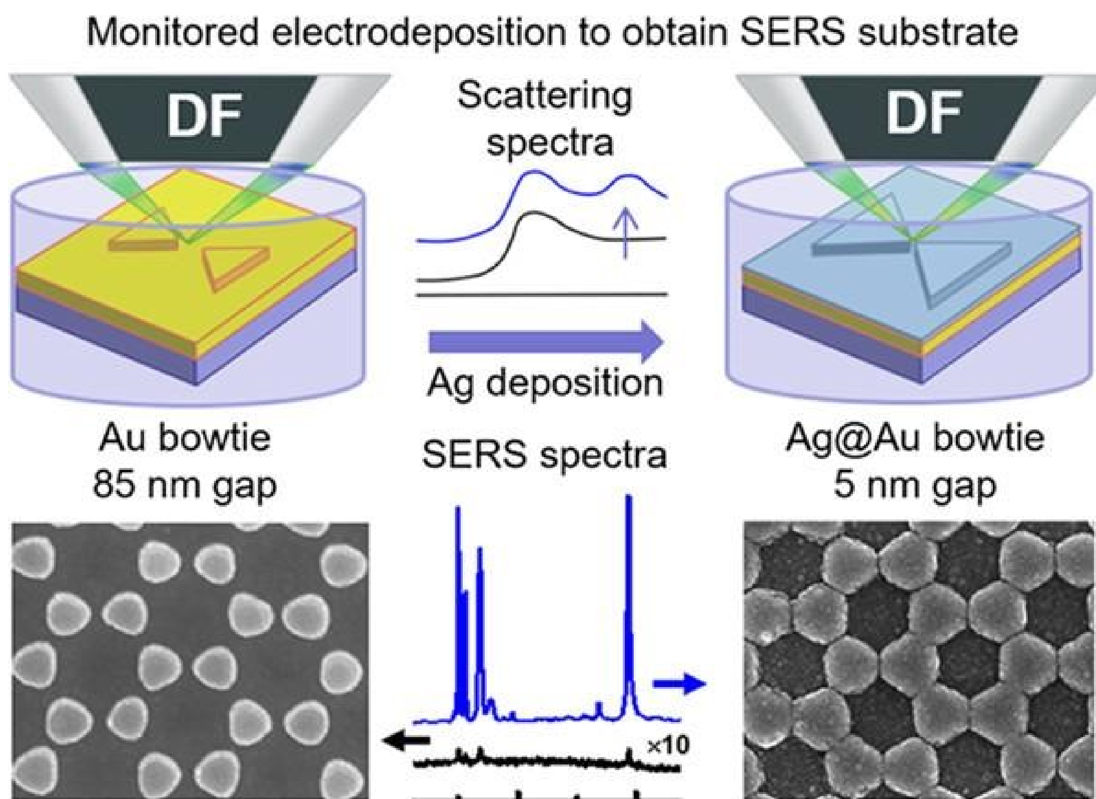

Figure 5.4. Morphology and SERS performance of Ag coated Au bowtie arrays. This image is from reference 428 with permission from the American Chemical Society.

Chapter 4 discusses the optical properties of Pt−Au bilayer arrays that deviate from their single layers of Pt and/or Au nanoparticle arrays owing to the changes in the nanoparticle gaps and interparticle plasmon coupling of Au due to the presence of Pt nanoparticles in close proximity. Most incommensurate pitch ratios of Pt−Au bilayers lead to variable interparticle gaps. However, the commensurate pitch ratio of 1.0 leads to a uniform interparticle gap of around 7 nm between Au and Pt nanoparticles with a honeycomb pattern over the substrate; it can be utilized successfully and tested as an SERS substrate, as shown in Figure 5.5. Au and Ag plasmonic nanostructures are considered as typical SERS substrates with a strong electromagnetic field enhancement. Hence, honeycomb patterns can be modified further by replacing the

bottom layer Pt nanoparticle arrays with Ag nanoparticles and keeping the top Au nanoparticles, as it also can be tested as an SERS substrate to see how the change of composition in the honeycomb pattern enhances the near-field plasmon resonance frequencies.

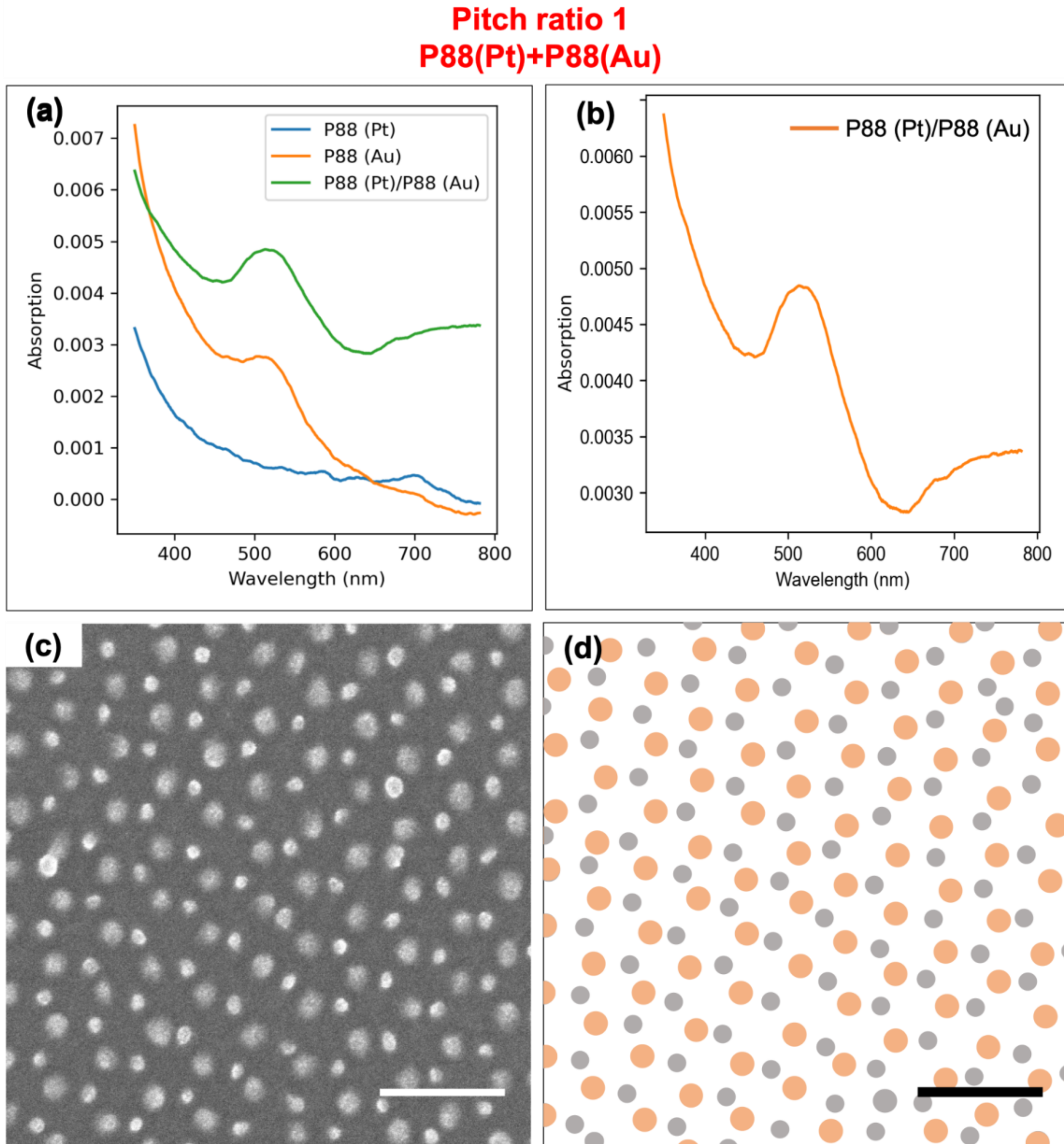

Figure 5.5. (a,b) UV-vis spectrum of the **P88** (Pt)/**P88** (Au) metal bilayer combination showing the distinct feature at wavelengths longer than 600 nm that could correspond to an extended plasmon band (EPB). (c) High magnification SEM micrographs and (d) high magnification schematic representation of the Pt–Au bilayer. Orange and gray dots represent Au and Pt nanodots, respectively. All scale bars are 100 nm.

References

(1) Moore, G. E. Cramming More Components onto Integrated Circuits, Reprinted from Electronics, Volume 38, Number 8, April 19, 1965, Pp.114 Ff. *IEEE Solid-State Circuits Soc. Newsl.* **2006**, *11* (3), 33–35. https://doi.org/10.1109/N-SSC.2006.4785860.

(2) Ostendorf, A.; König, K. Tutorial: Laser in Material Nanoprocessing. In *Optically Induced Nanostructures: Biomedical and Technical Applications*; König, K., Ostendorf, A., Eds.; De Gruyter: Berlin, 2015.

(3) *International Technology Roadmap for Semiconductors*, 2011th ed.; Semiconductor Industry Association: San Jose, CA, 2011.

(4) Likharev, K. Chapter 4 - Sub-20-Nm Electron Devices. In *Advanced Semiconductor and Organic Nano-Techniques*; Morkoç, H., Ed.; Academic Press: San Diego, 2003; pp 239–302. https://doi.org/10.1016/B978-012507060-7/50009-X.

(5) Beall, K. F. The Interdependence of Printer & Printmaker in Early 19th-Century Lithography. *Art J.* **1980**, *39* (3), 195–201. https://doi.org/10.1080/00043249.1980.10793579.

(6) Tallents, G.; Wagenaars, E.; Pert, G. Lithography at EUV Wavelengths. *Nat. Photonics* **2010**, *4* (12), 809–811. https://doi.org/10.1038/nphoton.2010.277.

(7) Mahmoodian, M.; Hajihoseini, H.; Mohajerzadeh, S.; Fathipour, M. Nano Patterning and Fabrication of Single Polypyrrole Nanowires by Electron Beam Lithography. *Synth. Met.* **2019**, *249*, 14–24. https://doi.org/10.1016/j.synthmet.2019.01.013.

(8) Wu, X.; Teng, F.; Libera, M. Functional Changes during Electron-Beam Lithography of Biotinylated Poly(Ethylene Glycol) Thin Films. *ACS Macro Lett.* **2019**, *8* (10), 1252–1256. https://doi.org/10.1021/acsmacrolett.9b00585.

(9) Randall, J. N.; Owen, J. H. G.; Lake, J.; Fuchs, E. Next Generation of Extreme-Resolution Electron Beam Lithography. *J. Vac. Sci. Technol. B* **2019**, *37* (6), 061605. https://doi.org/10.1116/1.5119392.

(10) Lewis, S. M.; Hunt, M. S.; DeRose, G. A.; Alty, H. R.; Li, J.; Wertheim, A.; De Rose, L.; Timco, G. A.; Scherer, A.; Yeates, S. G.; Winpenny, R. E. P. Plasma-Etched Pattern Transfer of Sub-10 Nm Structures Using a Metal–Organic Resist and Helium Ion Beam Lithography. *Nano Lett.* **2019**, *19* (9), 6043–6048. https://doi.org/10.1021/acs.nanolett.9b01911.

(11) Quan, Y.-J.; Kim, M.-S.; Kim, Y.; Ahn, S.-H. Colour-Tunable 50% Strain Sensor Using Surface-Nanopatterning of Soft Materials via Nanoimprinting with Focused Ion Beam Milling Process. *CIRP Ann.* **2019**, *68* (1), 595–598. https://doi.org/10.1016/j.cirp.2019.04.037.

(12) Liu, G.; Hirtz, M.; Fuchs, H.; Zheng, Z. Development of Dip-Pen Nanolithography (DPN) and Its Derivatives. *Small* **2019**, *15* (21), 1900564. https://doi.org/10.1002/smll.201900564.

(13) Ryu, Y. K.; Garcia, R. Advanced Oxidation Scanning Probe Lithography. *Nanotechnology* **2017**, *28* (14), 142003. https://doi.org/10.1088/1361-6528/aa5651.

(14) Liu, X.; Kumar, M.; Calo, A.; Albisetti, E.; Zheng, X.; Manning, K. B.; Elacqua, E.; Weck, M.; Ulijn, R. V.; Riedo, E. Sub-10 Nm Resolution Patterning of Pockets for Enzyme Immobilization with Independent Density and Quasi-3D Topography Control. *ACS Appl. Mater. Interfaces* **2019**, *11* (44), 41780–41790. https://doi.org/10.1021/acsami.9b11844.

(15) Sulkanen, A. R.; Sung, J.; Robb, M. J.; Moore, J. S.; Sottos, N. R.; Liu, G. Spatially Selective and Density-Controlled Activation of Interfacial Mechanophores. *J. Am. Chem. Soc.* **2019**, *141* (9), 4080–4085. https://doi.org/10.1021/jacs.8b10257.

(16) Roszkiewicz, A.; Jain, A.; Teodorczyk, M.; Nasalski, W. Formation and Characterization of Hole Nanopattern on Photoresist Layer by Scanning Near-Field Optical Microscope. *Nanomaterials* **2019**, *9* (10), 1452. https://doi.org/10.3390/nano9101452.

(17) Mulko, L. E.; Rossa, M.; Aranguren-Abrate, J. P.; Pino, G. A. Micropatterning of Fluorescent Silver Nanoclusters in Polymer Films by Laser Interference. *Appl. Surf. Sci.* **2019**, *485*, 141–146. https://doi.org/10.1016/j.apsusc.2019.04.149.

(18) Yulianto, E.; Chatterjee, S.; Purlys, V.; Mizeikis, V. Imaging of Latent Three-Dimensional Exposure Patterns Created by Direct Laser Writing in Photoresists. *Appl. Surf. Sci.* **2019**, *479*, 822–827. https://doi.org/10.1016/j.apsusc.2019.02.033.

(19) Handrea-Dragan, M.; Botiz, I. Multifunctional Structured Platforms: From Patterning of Polymer-Based Films to Their Subsequent Filling with Various Nanomaterials. *Polymers* **2021**, *13* (3), 445. https://doi.org/10.3390/polym13030445.

(20) Keyes, R. W. Physical Limits of Silicon Transistors and Circuits. *Rep. Prog. Phys.* **2005**, *68* (12), 2701–2746. https://doi.org/10.1088/0034-4885/68/12/R01.
(21) Shuler, K. Moore's Law is Dead: Long Live SoC Designers https://www.arteris.com/blog/moores-law-is-dead-long-live-soc-designers (accessed 2021 -09 -23).
(22) Moore, G. E. Cramming More Components onto Integrated Circuits. **1965**, *38* (8), 6.
(23) Fujikawa, S.; Takaki, R.; Kunitake, T. Fabrication of Arrays of Sub-20-Nm Silica Walls via Photolithography and Solution-Based Molecular Coating. *Langmuir* **2006**, *22* (21), 9057–9061. https://doi.org/10.1021/la061830e.
(24) Lin, B. J. The Ending of Optical Lithography and the Prospects of Its Successors. *Microelectron. Eng.* **2006**, *83* (4), 604–613. https://doi.org/10.1016/j.mee.2005.12.017.
(25) Sanders, D. P. Advances in Patterning Materials for 193 nm Immersion Lithography. *Chem. Rev.* **2010**, *110* (1), 321–360. https://doi.org/10.1021/cr900244n.
(26) Coughlin, T. A Road Map for Technologies That Drive Consumer Storage [The Art of Storage]. *IEEE Consum. Electron. Mag.* **2019**, *8* (2), 97–99. https://doi.org/10.1109/MCE.2018.2880855.
(27) Hoefflinger, B. IRDS—International Roadmap for Devices and Systems, Rebooting Computing, S3S. In *NANO-CHIPS 2030: On-Chip AI for an Efficient Data-Driven World*; Murmann, B., Hoefflinger, B., Eds.; The Frontiers Collection; Springer International Publishing: Cham, 2020; pp 9–17. https://doi.org/10.1007/978-3-030-18338-7_2.
(28) dcadmin. 2015 International Technology Roadmap for Semiconductors (ITRS) https://www.semiconductors.org/resources/2015-international-technology-roadmap-for-semiconductors-itrs/ (accessed 2021 -09 -08).
(29) Hierlemann, A.; Brand, O.; Hagleitner, C.; Baltes, H. Microfabrication Techniques for Chemical/Biosensors. *Proc. IEEE* **2003**, *91* (6), 839–863. https://doi.org/10.1109/JPROC.2003.813583.
(30) Bennett, H. S.; Pekarik, J. J.; Huang, M. RF and A/MS Technologies for Wireless Communications*+. No. 36, 7.
(31) Zhang, G. Q.; van Roosmalen, F.; Graef, M. The Paradigm of "More than Moore." In *2005 6th International Conference on Electronic Packaging Technology*; 2005; pp 17–24. https://doi.org/10.1109/ICEPT.2005.1564646.
(32) Tsai, C.-F.; Su, Y.-K.; Lin, C.-L. 01AG04 Further Improvement in the Light Output Power of InGaN-Based Light Emitting Diodes by Patterned Sapphire Substrate with KOH Wet-Chemical Etching on Sidewall. *Jpn. J. Appl. Phys.* **2012**, *51* (1).
(33) Chen, Y.-C.; Hsiao, F.-C.; Lin, B.-W.; Wang, B.-M.; Wu, Y. S.; Hsu, W.-C. The Formation and the Plane Indices of Etched Facets of Wet Etching Patterned Sapphire Substrate. *J. Electrochem. Soc.* **2012**, *159* (6), D362. https://doi.org/10.1149/2.095206jes.
(34) Ostrikov, K. *Plasma Nanoscience: Basic Concepts and Applications of Deterministic Nanofabrication*; John Wiley & Sons, 2008.
(35) Junior, F. G. de S. *Nanofabrication for Smart Nanosensor Applications*; Elsevier, 2020.
(36) Kumar, C. S. S. R.; Hormes, J.; Leuschner, C. *Nanofabrication Towards Biomedical Applications: Techniques, Tools, Applications, and Impact*; John Wiley & Sons, 2006.
(37) Choul Kim, B.; Moraes, C.; Huang, J.; D. Thouless, M.; Takayama, S. Fracture-Based Micro- and Nanofabrication for Biological Applications. *Biomater. Sci.* **2014**, *2* (3), 288–296. https://doi.org/10.1039/C3BM60276A.
(38) 2021IRDS_Litho.Pdf.
(39) Cutress, D. I. Intel's Process Roadmap to 2025: with 4nm, 3nm, 20A and 18A?! https://www.anandtech.com/show/16823/intel-accelerated-offensive-process-roadmap-updates-to-10nm-7nm-4nm-3nm-20a-18a-packaging-foundry-emib-foveros (accessed 2021 -09 -26).
(40) Chen, Y.; Xiong, S. Directed Self-Assembly of Block Copolymers for Sub-10 nm Fabrication. *Int. J. Extreme Manuf.* **2020**, *2* (3), 032006. https://doi.org/10.1088/2631-7990/aba3ae.
(41) Versolato, O. O. Physics of Laser-Driven Tin Plasma Sources of EUV Radiation for Nanolithography. *Plasma Sources Sci. Technol.* **2019**, *28* (8), 083001. https://doi.org/10.1088/1361-6595/ab3302.
(42) Demonstration of pattern transfer into sub-100 nm polysilicon line/space features patterned with extreme ultraviolet lithography: Journal of Vacuum Science & Technology B: Microelectronics and Nanometer Structures Processing, Measurement, and Phenomena: Vol 17, No 6 https://avs-scitation-org.login.ezproxy.library.ualberta.ca/doi/abs/10.1116/1.590936 (accessed 2021 -09 -24).
(43) Bjorkholm, J. E. EUV Lithography—The Successor to Optical Lithography? *EUV Lithogr.* 8.

(44) Moore, S. K. EUV Lithography Finally Ready for Fabs. *IEEE Spectr.* **2018**, *55* (1), 46–48. https://doi.org/10.1109/MSPEC.2018.8241736.
(45) Kim, S.-S.; Chalykh, R.; Kim, H.; Lee, S.; Park, C.; Hwang, M.; Park, J.-O.; Park, J.; Kim, H.; Jeon, J.; Kim, I.; Lee, D.; Na, J.; Kim, J.; Lee, S.; Kim, H.; Nam, S.-W. Progress in EUV Lithography toward Manufacturing. In *Extreme Ultraviolet (EUV) Lithography VIII*; SPIE, 2017; Vol. 10143, p 1014306. https://doi.org/10.1117/12.2264043.
(46) Thin Film Requirements for EUV Systems https://www.dentonvacuum.com/thin-film-requirements-extreme-uv-systems/ (accessed 2021 -09 -24).
(47) Improving the resolution of extreme-UV lithography scanners https://www.spie.org/news/6259-improving-the-resolution-of-extreme-uv-lithography-scanners (accessed 2021 -09 -29).
(48) Hasan, R. Md. M.; Luo, X. Promising Lithography Techniques for Next-Generation Logic Devices. *Nanomanufacturing Metrol.* **2018**, *1* (2), 67–81. https://doi.org/10.1007/s41871-018-0016-9.
(49) Hasan, R. Md. M.; Luo, X. Nanolithography: Status and Challenges. In *2017 23rd International Conference on Automation and Computing (ICAC)*; 2017; pp 1–6. https://doi.org/10.23919/IConAC.2017.8081979.
(50) Mulkens, J.; Hanna, M.; Wei, H.; Vaenkatesan, V.; Megens, H.; Slotboom, D. Overlay and Edge Placement Control Strategies for the 7nm Node Using EUV and ArF Lithography. In *Extreme Ultraviolet (EUV) Lithography VI*; SPIE, 2015; Vol. 9422, pp 572–584. https://doi.org/10.1117/12.2085761.
(51) Kerkhof, M. A. van de; Liu, F.; Meeuwissen, M.; Zhang, X.; Bayraktar, M.; Kruif, R. C. de; Davydova, N. V. High-Power EUV Lithography: Spectral Purity and Imaging Performance. *J. MicroNanolithography MEMS MOEMS* **2020**, *19* (3), 033801. https://doi.org/10.1117/1.JMM.19.3.033801.
(52) Mizoguchi, H.; Nakarai, H.; Abe, T.; Nowak, K. M.; Kawasuji, Y.; Tanaka, H.; Watanabe, Y.; Hori, T.; Kodama, T.; Shiraishi, Y.; Yanagida, T.; Yamada, T.; Yamazaki, T.; Okazaki, S.; Saitou, T. Performance of 250W High-Power HVM LPP-EUV Source. In *Extreme Ultraviolet (EUV) Lithography VIII*; SPIE, 2017; Vol. 10143, pp 330–337. https://doi.org/10.1117/12.2256652.
(53) Knight, W. The $150 Million Machine Keeping Moore's Law Alive. *Wired*.
(54) Pfeiffer, H. C. Recent Advances in Electron-Beam Lithography for the High-Volume Production of VLSI Devices. *IEEE Trans. Electron Devices* **1979**, *26* (4), 663–674. https://doi.org/10.1109/T-ED.1979.19475.
(55) Kumar, R.; Chauhan, M.; Moinuddin, M. G.; Sharma, S. K.; Gonsalves, K. E. Development of Nickel-Based Negative Tone Metal Oxide Cluster Resists for Sub-10 nm Electron Beam and Helium Ion Beam Lithography. *ACS Appl. Mater. Interfaces* **2020**, *12* (17), 19616–19624. https://doi.org/10.1021/acsami.9b21414.
(56) Pala, N.; Karabiyik, M. Electron Beam Lithography (EBL). In *Encyclopedia of Nanotechnology*; Bhushan, B., Ed.; Springer Netherlands: Dordrecht, 2016; pp 1033–1057. https://doi.org/10.1007/978-94-017-9780-1_344.
(57) Esashi, M.; Kojima, A.; Ikegami, N.; Miyaguchi, H.; Koshida, N. Development of Massively Parallel Electron Beam Direct Write Lithography Using Active-Matrix Nanocrystalline-Silicon Electron Emitter Arrays. *Microsyst. Nanoeng.* **2015**, *1* (1), 1–8. https://doi.org/10.1038/micronano.2015.29.
(58) Lin, S. Multiple Electron-Beam Direct-Write Lithography: An Overview; 2016; Vol. 9777, p 3.
(59) Asano, T.; Sakai, K.; Yamamoto, K.; Hiura, H.; Nakayama, T.; Hayashi, T.; Takabayashi, Y.; Iwanaga, T.; Resnick, D. J. The Advantages of Nanoimprint Lithography for Semiconductor Device Manufacturing. In *Photomask Japan 2019: XXVI Symposium on Photomask and Next-Generation Lithography Mask Technology*; SPIE, 2019; Vol. 11178, pp 131–140. https://doi.org/10.1117/12.2532522.
(60) Schift, H. Nanoimprint Lithography: 2D or Not 2D? A Review. *Appl. Phys. A* **2015**, *121* (2), 415–435. https://doi.org/10.1007/s00339-015-9106-3.
(61) Hasan, R. Md. M.; Luo, X. Promising Lithography Techniques for Next-Generation Logic Devices. *Nanomanufacturing Metrol.* **2018**, *1* (2), 67–81. https://doi.org/10.1007/s41871-018-0016-9.
(62) Kono, T.; Hatano, M.; Tokue, H.; Kobayashi, K.; Suzuki, M.; Fukuhara, K.; Asano, M.; Nakasugi, T.; Choi, E. H.; Jung, W. Study of Nanoimprint Lithography (NIL) for HVM of Memory Devices. In *Emerging Patterning Technologies*; SPIE, 2017; Vol. 10144, pp 19–25. https://doi.org/10.1117/12.2257951.
(63) Cummins, C.; Borah, D.; Rasappa, S.; Senthamaraikannan, R.; Simao, C.; Francone, A.; Kehagias, N.; Sotomayor-Torres, C. M.; Morris, M. A. Self-Assembled Nanofeatures in Complex Three-Dimensional

Topographies via Nanoimprint and Block Copolymer Lithography Methods. *ACS Omega* **2017**, *2* (8), 4417–4423. https://doi.org/10.1021/acsomega.7b00781.

(64) Mansky, P.; haikin, P.; Thomas, E. L. Monolayer Films of Diblock Copolymer Microdomains for Nanolithographic Applications. *J. Mater. Sci.* **1995**, *30* (8), 1987–1992. https://doi.org/10.1007/BF00353023.

(65) Ouk Kim, S.; Solak, H. H.; Stoykovich, M. P.; Ferrier, N. J.; de Pablo, J. J.; Nealey, P. F. Epitaxial Self-Assembly of Block Copolymers on Lithographically Defined Nanopatterned Substrates. *Nature* **2003**, *424* (6947), 411–414. https://doi.org/10.1038/nature01775.

(66) Stoykovich, M. P.; Müller, M.; Kim, S. O.; Solak, H. H.; Edwards, E. W.; Pablo, J. J. de; Nealey, P. F. Directed Assembly of Block Copolymer Blends into Nonregular Device-Oriented Structures. *Science* **2005**, *308* (5727), 1442–1446. https://doi.org/10.1126/science.1111041.

(67) Edwards, E. W.; Montague, M. F.; Solak, H. H.; Hawker, C. J.; Nealey, P. F. Precise Control over Molecular Dimensions of Block-Copolymer Domains Using the Interfacial Energy of Chemically Nanopatterned Substrates. *Adv. Mater.* **2004**, *16* (15), 1315–1319. https://doi.org/10.1002/adma.200400763.

(68) Liu, C.-C.; Han, E.; Onses, M. S.; Thode, C. J.; Ji, S.; Gopalan, P.; Nealey, P. F. Fabrication of Lithographically Defined Chemically Patterned Polymer Brushes and Mats. *Macromolecules* **2011**, *44* (7), 1876–1885. https://doi.org/10.1021/ma102856t.

(69) Wan, L.; Yang, X. Directed Self-Assembly of Cylinder-Forming Block Copolymers: Prepatterning Effect on Pattern Quality and Density Multiplication Factor. *Langmuir* **2009**, *25* (21), 12408–12413. https://doi.org/10.1021/la901648y.

(70) Cheng, J. Y.; Rettner, C. T.; Sanders, D. P.; Kim, H.-C.; Hinsberg, W. D. Dense Self-Assembly on Sparse Chemical Patterns: Rectifying and Multiplying Lithographic Patterns Using Block Copolymers. *Adv. Mater.* **2008**, *20* (16), 3155–3158. https://doi.org/10.1002/adma.200800826.

(71) Cheng, J. Y.; Rettner, C. T.; Sanders, D. P.; Kim, H.-C.; Hinsberg, W. D. Dense Self-Assembly on Sparse Chemical Patterns: Rectifying and Multiplying Lithographic Patterns Using Block Copolymers. *Adv. Mater.* **2008**, *20* (16), 3155–3158. https://doi.org/10.1002/adma.200800826.

(72) Claveau, G.; Quemere, P.; Argoud, M.; Hazart, J.; Pimenta-Barros, P.; Sarrazin, A.; Posseme, N.; Tiron, R.; Chevalier, X.; Nicolet, C.; Navarro, C. Surface Affinity Role in Graphoepitaxy of Lamellar Block Copolymers. *J. MicroNanolithography MEMS MOEMS* **2016**, *15* (3), 031604. https://doi.org/10.1117/1.JMM.15.3.031604.

(73) Doise, J.; Bekaert, J.; Chan, B. T.; Gronheid, R.; Cao, Y.; Hong, S.; Lin, G.; Fishman, D.; Chakk, Y.; Marzook, T. Implementation of Surface Energy Modification in Graphoepitaxy Directed Self-Assembly for Hole Multiplication. *J. Vac. Sci. Technol. B* **2015**, *33* (6), 06F301. https://doi.org/10.1116/1.4929884.

(74) Jeong, S.-J.; Kim, J. Y.; Kim, B. H.; Moon, H.-S.; Kim, S. O. Directed Self-Assembly of Block Copolymers for next Generation Nanolithography. *Mater. Today* **2013**, *16* (12), 468–476. https://doi.org/10.1016/j.mattod.2013.11.002.

(75) Kagan, C. R.; Hyeon, T.; Kim, D.-H.; Ruiz, R.; Tung, M. C.; Wong, H.-S. P. Self-Assembly for Electronics. *MRS Bull.* **2020**, *45* (10), 807–814. https://doi.org/10.1557/mrs.2020.248.

(76) Bita, I.; Yang, J. K. W.; Jung, Y. S.; Ross, C. A.; Thomas, E. L.; Berggren, K. K. Graphoepitaxy of Self-Assembled Block Copolymers on Two-Dimensional Periodic Patterned Templates. *Science* **2008**, *321* (5891), 939–943. https://doi.org/10.1126/science.1159352.

(77) Chang, J.-B.; Choi, H. K.; Hannon, A. F.; Alexander-Katz, A.; Ross, C. A.; Berggren, K. K. Design Rules for Self-Assembled Block Copolymer Patterns Using Tiled Templates. *Nat. Commun.* **2014**, *5* (1), 3305. https://doi.org/10.1038/ncomms4305.

(78) Gronheid, R.; Boeckx, C.; Doise, J.; Bekaert, J.; Karageorgos, I.; Ruckaert, J.; Chan, B. T.; Lin, C.; Zou, Y. EUV Patterned Templates with Grapho-Epitaxy DSA at the N5/N7 Logic Nodes. In *Extreme Ultraviolet (EUV) Lithography VII*; SPIE, 2016; Vol. 9776, pp 552–560. https://doi.org/10.1117/12.2219876.

(79) Torres, J. A.; Jiang, F.; Ma, Y.; Mellman, J.; Lai, K.; Raghunathan, A.; Xu, Y.; Liu, C.-C.; Chi, C. Directed Self Assembly on Resist-Limited Guiding Patterns for Hole Grapho-Epitaxy: Can DSA Help Lower EUV's Source Power Requirements? In *Extreme Ultraviolet (EUV) Lithography VI*; SPIE, 2015; Vol. 9422, pp 268–275. https://doi.org/10.1117/12.2085959.

(80) Pinto-Gómez, C.; Pérez-Murano, F.; Bausells, J.; Villanueva, L. G.; Fernández-Regúlez, M. Directed Self-Assembly of Block Copolymers for the Fabrication of Functional Devices. *Polymers* **2020**, *12* (10), 2432. https://doi.org/10.3390/polym12102432.

(81) Rademaker, G. J.; Pennec, A. L.; Giammaria, T. J.; Benotmane, K.; Pham, H.; Bouet, C.; Cacho, M. G. G.; Argoud, M.; Pourteau, M.-L.; Paquet, A.; Gharbi, A.; Navarro, C.; Nicolet, C.; Chevalier, X.; Sakavuyi, K.; Nealey, P.; Tiron, R. Establishing a Sidewall Image Transfer Chemo-Epitaxial DSA Process Using 193 nm Immersion Lithography. In *Advances in Patterning Materials and Processes XXXVII*; SPIE, 2020; Vol. 11326, pp 163–174. https://doi.org/10.1117/12.2552003.
(82) Ma, Y.; Wang, Y.; Word, J.; Lei, J.; Mitra, J.; Torres, J. A.; Hong, L.; Fenger, G.; Khaira, D.; Preil, M.; Yuan, L.; Kye, J.; Levinson, H. J. Directed Self Assembly (DSA) Compliant Flow with Immersion Lithography: From Material to Design and Patterning. In *Alternative Lithographic Technologies VIII*; SPIE, 2016; Vol. 9777, pp 117–127. https://doi.org/10.1117/12.2219505.
(83) Tsai, H.; Pitera, J. W.; Miyazoe, H.; Bangsaruntip, S.; Engelmann, S. U.; Liu, C.-C.; Cheng, J. Y.; Bucchignano, J. J.; Klaus, D. P.; Joseph, E. A.; Sanders, D. P.; Colburn, M. E.; Guillorn, M. A. Two-Dimensional Pattern Formation Using Graphoepitaxy of PS-b-PMMA Block Copolymers for Advanced FinFET Device and Circuit Fabrication. *ACS Nano* **2014**, *8* (5), 5227–5232. https://doi.org/10.1021/nn501300b.
(84) Liu, C.-C.; Franke, E.; Mignot, Y.; Xie, R.; Yeung, C. W.; Zhang, J.; Chi, C.; Zhang, C.; Farrell, R.; Lai, K.; Tsai, H.; Felix, N.; Corliss, D. Directed Self-Assembly of Block Copolymers for 7 Nanometre FinFET Technology and Beyond. *Nat. Electron.* **2018**, *1* (10), 562–569. https://doi.org/10.1038/s41928-018-0147-4.
(85) Li, D.; Chien, C.; Wei, X.; Huang, Y.; Qu, X.; Chang, T.; Xiong, S. Sub-10 nm Silicon FinFET Devices on SOI Substrate Made by Block Copolymer Lithography. In *2018 14th IEEE International Conference on Solid-State and Integrated Circuit Technology (ICSICT)*; 2018; pp 1–3. https://doi.org/10.1109/ICSICT.2018.8564952.
(86) Xiao, S.; Yang, X.; Steiner, P.; Hsu, Y.; Lee, K.; Wago, K.; Kuo, D. Servo-Integrated Patterned Media by Hybrid Directed Self-Assembly. *ACS Nano* **2014**, *8* (11), 11854–11859. https://doi.org/10.1021/nn505630t.
(87) Xiao, S.; Yang, X.; Lee, K. Y.; Hwu, J. J.; Wago, K.; Kuo, D. Directed Self-Assembly for High-Density Bit-Patterned Media Fabrication Using Spherical Block Copolymers. *J. MicroNanolithography MEMS MOEMS* **2013**, *12* (3), 031110–031110. https://doi.org/10.1117/1.JMM.12.3.031110.
(88) Pathangi, H.; Vaid, V.; Chan, B. T.; Vandenbroeck, N.; Li, J.; Hong, S. E.; Cao, Y.; Durairaj, B.; Lin, G.; Somervell, M.; Kitano, T.; Harukawa, R.; Sah, K.; Cross, A.; Bayana, H.; D'Urzo, L.; Gronheid, R. DSA Materials Contributions to the Defectivity Performance of 14nm Half-Pitch LiNe Flow at IMEC. In *Alternative Lithographic Technologies VIII*; SPIE, 2016; Vol. 9777, pp 84–89. https://doi.org/10.1117/12.2219936.
(89) Muramatsu, M.; Nishi, T.; You, G.; Saito, Y.; Ido, Y.; Ito, K.; Tobana, T.; Hosoya, M.; Chen, W.; Nakamura, S.; Somervell, M.; Kitano, T. Pattern Fidelity Improvement of Chemo-Epitaxy DSA Process for High-Volume Manufacturing. In *Alternative Lithographic Technologies VIII*; SPIE, 2016; Vol. 9777, pp 75–83. https://doi.org/10.1117/12.2218595.
(90) Hinsberg, W.; Cheng, J.; Kim, H.-C.; Sanders, D. P. Self-Assembling Materials for Lithographic Patterning: Overview, Status, and Moving Forward. In *Alternative Lithographic Technologies II*; SPIE, 2010; Vol. 7637, pp 101–111. https://doi.org/10.1117/12.852230.
(91) Li, W.; Müller, M. Thermodynamics and Kinetics of Defect Motion and Annihilation in the Self-Assembly of Lamellar Diblock Copolymers. *Macromolecules* **2016**, *49* (16), 6126–6138. https://doi.org/10.1021/acs.macromol.6b01088.
(92) Hur, S.-M.; Thapar, V.; Ramírez-Hernández, A.; Nealey, P. F.; de Pablo, J. J. Defect Annihilation Pathways in Directed Assembly of Lamellar Block Copolymer Thin Films. *ACS Nano* **2018**, *12* (10), 9974–9981. https://doi.org/10.1021/acsnano.8b04202.
(93) Doise, J.; Koh, J. H.; Kim, J. Y.; Zhu, Q.; Kinoshita, N.; Suh, H. S.; Delgadillo, P. R.; Vandenberghe, G.; Willson, C. G.; Ellison, C. J. Strategies for Increasing the Rate of Defect Annihilation in the Directed Self-Assembly of High-χ Block Copolymers. *ACS Appl. Mater. Interfaces* **2019**, *11* (51), 48419–48427. https://doi.org/10.1021/acsami.9b17858.
(94) DSA and EUV: Complementary Technologies to Enable Fine- Pitch Lithography | Semiconductor Digest.
(95) Hutchby, J. The Nanoelectronics Roadmap. In *Emerging Nanoelectronic Devices*; Chen, A., Hutchby, J., Zhirnov, V., Bourianoff, G., Eds.; John Wiley & Sons Ltd, 2014; pp 1–14.
(96) Herr, D. J. C. Directed Block Copolymer Self-Assembly for Nanoelectronics Fabrication. *J. Mater. Res.* **2011**, *26* (2), 122–139. https://doi.org/10.1557/jmr.2010.74.

(97) Park, S.; Lee, D. H.; Xu, J.; Kim, B.; Hong, S. W.; Jeong, U.; Xu, T.; Russell, T. P. Macroscopic 10-Terabit–per–Square-Inch Arrays from Block Copolymers with Lateral Order. *Science* **2009**, *323* (5917), 1030–1033. https://doi.org/10.1126/science.1168108.
(98) Hiemenz, P. C.; Lodge, T. P. *Polymer Chemistry*; CRC Press, 2007.
(99) Stille, J. K. Step-Growth Polymerization. *J. Chem. Educ.* **1981**, *58* (11), 862. https://doi.org/10.1021/ed058p862.
(100) Espinosa, L. M. de; R. Meier, M. A. Synthesis of Star- and Block- Copolymers Using ADMET: Head-to-Tail Selectivity during Step-Growth Polymerization. *Chem. Commun.* **2011**, *47* (6), 1908–1910. https://doi.org/10.1039/C0CC04161K.
(101) Nishimori, K.; Ouchi, M. AB-Alternating Copolymers via Chain-Growth Polymerization: Synthesis, Characterization, Self-Assembly, and Functions. *Chem. Commun.* **2020**, *56* (24), 3473–3483. https://doi.org/10.1039/D0CC00275E.
(102) Yokozawa, T.; Yokoyama, A. Chain-Growth Polycondensation: The Living Polymerization Process in Polycondensation. *Prog. Polym. Sci.* **2007**, *32* (1), 147–172. https://doi.org/10.1016/j.progpolymsci.2006.08.001.
(103) Hiorns, R. C.; Boucher, R. J.; Duhlev, R.; Kahovec, J. A Brief Guide to Polymer Nomenclature. *Int. Union Pure Appl. Chem.* **2012**, 2.
(104) Jones, reviewed by R. G. Compendium of Polymer Terminology and Nomenclature, IUPAC Recommendations 2008. *Chem. Int. -- Newsmag. IUPAC* **2009**, *31* (4), 32–33. https://doi.org/10.1515/ci.2009.31.4.32.
(105) Lutz, J.-F. Sequence-Controlled Polymerizations : The next Holy Grail in Polymer Science? *Polym. Chem.* **2010**, *1* (1), 55–62. https://doi.org/10.1039/B9PY00329K.
(106) Szwarc, M. ‘Living’ Polymers. *Nature* **1956**, *178* (4543), 1168–1169. https://doi.org/10.1038/1781168a0.
(107) Jones, R. A. L.; Jones, R. A. L.; Ph, R. J. *Soft Condensed Matter*; OUP Oxford, 2002.
(108) Dunn, A. S.; Melville, H. W. Synthesis of ‘Block’ Copolymers. *Nature* **1952**, *169* (4304), 699–700. https://doi.org/10.1038/169699a0.
(109) Szwarc, M.; Levy, M.; Milkovich, R. Polymerization Initiated by Electron Transfer to Monomer. A New Method of Formation of Block Polymers. *J. Am. Chem. Soc.* **1956**, *78* (11), 2656–2657. https://doi.org/10.1021/ja01592a101.
(110) Miyamoto, M.; Sawamoto, M.; Higashimura, T. Living Polymerization of Isobutyl Vinyl Ether with Hydrogen Iodide/Iodine Initiating System. *Macromolecules* **1984**, *17* (3), 265–268. https://doi.org/10.1021/ma00133a001.
(111) Otsu, T.; Yoshida, M.; Tazaki, T. A Model for Living Radical Polymerization. *Makromol. Chem. Rapid Commun.* **1982**, *3* (2), 133–140. https://doi.org/10.1002/marc.1982.030030209.
(112) Eastoe, J.; Cox, A. Colloids and Surfaces A: Physiochemical and Engineering Aspects. *Form PbS Nanoclusters Using Reversed Micelles Lead Sodium Aerosol-OT* **1995**, *101*, 63–76.
(113) Holden, G. Thermoplastic Elastomers. In *Rubber Technology*; Morton, M., Ed.; Springer US: Boston, MA, 1987; pp 465–481. https://doi.org/10.1007/978-1-4615-7823-9_16.
(114) Trimbach, D.; Feldman, K.; Spencer, N. D.; Broer, D. J.; Bastiaansen, C. W. M. Block Copolymer Thermoplastic Elastomers for Microcontact Printing. *Langmuir* **2003**, *19* (26), 10957–10961. https://doi.org/10.1021/la035214j.
(115) Nakamura, Y.; Sakai, Y.; Imamura, K.; Ito, K.; Fujii, S.; Urahama, Y. Effects of the Compatibility of a Polyacrylic Block Copolymer/Tackifier Blend on the Phase Structure and Tack of a Pressure-Sensitive Adhesive. *J. Appl. Polym. Sci.* **2012**, *123* (5), 2883–2893. https://doi.org/10.1002/app.34883.
(116) Okada, S.; Kashihara, Y.; Hirai, T.; Fujii, S.; Nakamura, Y.; Urahama, Y.; Ito, M.; Liang, X.; Nakajima, K. Adhesion Properties of Polyacrylic Block Copolymer Pressure-Sensitive Adhesives and Analysis by Pulse NMR and AFM Force Curve. *J. Appl. Polym. Sci.* **2019**, *136* (29), 47791. https://doi.org/10.1002/app.47791.
(117) Couvreur, P.; Barret, G. Critical Review in Therapeutic Drug Carrier System. *J Pediatr. Surg* **2005**, *5* (1), 1–20.
(118) Mizuno, H.; Buriak, J. M. Catalytic Stamp Lithography for Sub-100 nm Patterning of Organic Monolayers. *J. Am. Chem. Soc.* **2008**, *130* (52), 17656–17657. https://doi.org/10.1021/ja807708r.
(119) Liu, F.; Luber, E. J.; Huck, L. A.; Olsen, B. C.; Buriak, J. M. Nanoscale Plasmonic Stamp Lithography on Silicon. *ACS Nano* **2015**, *9* (2), 2184–2193. https://doi.org/10.1021/acsnano.5b00312.

(120) Zhu, G.; Ying, Y.; Li, X.; Liu, Y.; Yang, C.; Yi, Z.; Gao, C. Isoporous Membranes with Sub-10 nm Pores Prepared from Supramolecular Interaction Facilitated Block Copolymer Assembly and Application for Protein Separation. *J. Membr. Sci.* **2018**, *566*, 25–34. https://doi.org/10.1016/j.memsci.2018.08.033.
(121) Ahn, H.; Park, S.; Kim, S.-W.; Yoo, P. J.; Ryu, D. Y.; Russell, T. P. Nanoporous Block Copolymer Membranes for Ultrafiltration: A Simple Approach to Size Tunability. *ACS Nano* **2014**, *8* (11), 11745–11752. https://doi.org/10.1021/nn505234v.
(122) Wang, Y.; Li, F. An Emerging Pore-Making Strategy: Confined Swelling-Induced Pore Generation in Block Copolymer Materials. *Adv. Mater.* **2011**, *23* (19), 2134–2148. https://doi.org/10.1002/adma.201004022.
(123) Polymer Source https://www.polymersource.ca/ (accessed 2021 -09 -27).
(124) Feng, H.; Lu, X.; Zhang, W.; Kang, N.-G.; Mays, J. Block Copolymers: Synthesis, Self-Assembly, and Applications. *Polymers* **2017**, *9*, 494. https://doi.org/10.3390/polym9100494.
(125) Bates, F. S.; Fredrickson, G. H. Block Copolymers—Designer Soft Materials. *Phys. Today* **1999**, *52* (2), 32–38. https://doi.org/10.1063/1.882522.
(126) Lodge, T. P. Block Copolymers: Past Successes and Future Challenges. *Macromol. Chem. Phys.* **2003**, *204* (2), 265–273. https://doi.org/10.1002/macp.200290073.
(127) Meier, D. J. Theory of Block Copolymers. I. Domain Formation in A-B Block Copolymers. *J. Polym. Sci. Part C Polym. Symp.* **1969**, *26* (1), 81–98. https://doi.org/10.1002/polc.5070260106.
(128) Edwards, S. F. The Statistical Mechanics of Polymers with Excluded Volume. *Proc. Phys. Soc.* **1965**, *85* (4), 613–624. https://doi.org/10.1088/0370-1328/85/4/301.
(129) Helfand, E.; Sapse, A. M. Theory of Unsymmetric Polymer–Polymer Interfaces. *J. Chem. Phys.* **1975**, *62* (4), 1327–1331. https://doi.org/10.1063/1.430632.
(130) Helfand, E.; Wasserman, Z. R. Block Copolymer Theory. 4. Narrow Interphase Approximation. *Macromolecules* **1976**, *9* (6), 879–888. https://doi.org/10.1021/ma60054a001.
(131) Helfand, E.; Wasserman, Z. R. Block Copolymer Theory. 5. Spherical Domains. *Macromolecules* **1978**, *11* (5), 960–966. https://doi.org/10.1021/ma60065a023.
(132) Gennes, P.-G. de; Gennes, P. P.-G. *Scaling Concepts in Polymer Physics*; Cornell University Press, 1979.
(133) Flory, P. J. *Principles of Polymer Chemistry*; Cornell University Press, 1953.
(134) Leibler, L. Theory of Microphase Separation in Block Copolymers. *Macromolecules* **1980**, *13* (6), 1602–1617. https://doi.org/10.1021/ma60078a047.
(135) Khandpur, A. K.; Foerster, S.; Bates, F. S.; Hamley, I. W.; Ryan, A. J.; Bras, W.; Almdal, K.; Mortensen, K. Polyisoprene-Polystyrene Diblock Copolymer Phase Diagram near the Order-Disorder Transition. *Macromolecules* **1995**, *28* (26), 8796–8806. https://doi.org/10.1021/ma00130a012.
(136) Li, W.; Liu, M.; Qiu, F.; Shi, A.-C. Phase Diagram of Diblock Copolymers Confined in Thin Films. *J. Phys. Chem. B* **2013**, *117* (17), 5280–5288. https://doi.org/10.1021/jp309546q.
(137) Russell, T. P.; Hjelm, R. P.; Seeger, P. A. Temperature Dependence of the Interaction Parameter of Polystyrene and Poly(Methyl Methacrylate). *Macromolecules* **1990**, *23* (3), 890–893. https://doi.org/10.1021/ma00205a033.
(138) Cochran, E. W.; Morse, D. C.; Bates, F. S. Design of ABC Triblock Copolymers near the ODT with the Random Phase Approximation. *Macromolecules* **2003**, *36* (3), 782–792. https://doi.org/10.1021/ma020651a.
(139) Dai, K. H.; Kramer, E. J. Determining the Temperature-Dependent Flory Interaction Parameter for Strongly Immiscible Polymers from Block Copolymer Segregation Measurements. *Polymer* **1994**, *35* (1), 157–161. https://doi.org/10.1016/0032-3861(94)90065-5.
(140) Alberda van Ekenstein, G. O. R.; Meyboom, R.; ten Brinke, G.; Ikkala, O. Determination of the Flory−Huggins Interaction Parameter of Styrene and 4-Vinylpyridine Using Copolymer Blends of Poly(Styrene-Co-4-Vinylpyridine) and Polystyrene. *Macromolecules* **2000**, *33* (10), 3752–3756. https://doi.org/10.1021/ma992118+.
(141) Wan, L.; Ruiz, R.; Gao, H.; Patel, K. C.; Albrecht, T. R.; Yin, J.; Kim, J.; Cao, Y.; Lin, G. The Limits of Lamellae-Forming PS-*b*-PMMA Block Copolymers for Lithography. *ACS Nano* **2015**, *9* (7), 7506–7514. https://doi.org/10.1021/acsnano.5b02613.
(142) Lee, C.-J.; Cheng, J. Method for Integrated Circuit Manufacturing with Directed Self-Assembly (DSA). US10418245B2, September 17, 2019.

(143) Lo, T.-Y.; Krishnan, M. R.; Lu, K.-Y.; Ho, R.-M. Silicon-Containing Block Copolymers for Lithographic Applications. *Prog. Polym. Sci.* **2018**, *77*, 19–68. https://doi.org/10.1016/j.progpolymsci.2017.10.002.

(144) Böhme, S.; Girardot, C.; Garnier, J.; Arias-Zapata, J.; Arnaud, S.; Tiron, R.; Marconot, O.; Buttard, D.; Zelsmann, M. A Route for Industry Compatible Directed Self-Assembly of High-Chi PS-PDMS Block Copolymers. In *Alternative Lithographic Technologies VIII*; SPIE, 2016; Vol. 9777, pp 405–414. https://doi.org/10.1117/12.2219312.

(145) Bates, C. M.; Maher, M. J.; Janes, D. W.; Ellison, C. J.; Willson, C. G. Block Copolymer Lithography. *Macromolecules* **2014**, *47* (1), 2–12. https://doi.org/10.1021/ma401762n.

(146) Bates, F. S.; Fredrickson, G. H. Block Copolymer Thermodynamics: Theory and Experiment. *Annu. Rev. Phys. Chem.* **1990**, *41* (1), 525–557. https://doi.org/10.1146/annurev.pc.41.100190.002521.

(147) Yang, G.-W.; Wu, G.-P.; Chen, X.; Xiong, S.; Arges, C. G.; Ji, S.; Nealey, P. F.; Lu, X.-B.; Darensbourg, D. J.; Xu, Z.-K. Directed Self-Assembly of Polystyrene-b-Poly(Propylene Carbonate) on Chemical Patterns via Thermal Annealing for Next Generation Lithography. *Nano Lett.* **2017**, *17* (2), 1233–1239. https://doi.org/10.1021/acs.nanolett.6b05059.

(148) Williamson, L. D.; Seidel, R. N.; Chen, X.; Suh, H. S.; Rincon Delgadillo, P.; Gronheid, R.; Nealey, P. F. Three-Tone Chemical Patterns for Block Copolymer Directed Self-Assembly. *ACS Appl. Mater. Interfaces* **2016**, *8* (4), 2704–2712. https://doi.org/10.1021/acsami.5b10562.

(149) Kim, S.-W.; Kim, E.; Lee, H.; Berry, B. C.; Kim, H.-C.; Ryu, D. Y. Thickness-Dependent Ordering of Perpendicularly Oriented Lamellae in PS-b-PMMA Thin Films. *Polymer* **2015**, *74*, 63–69. https://doi.org/10.1016/j.polymer.2015.07.053.

(150) She, M.-S.; Lo, T.-Y.; Ho, R.-M. Long-Range Ordering of Block Copolymer Cylinders Driven by Combining Thermal Annealing and Substrate Functionalization. *ACS Nano* **2013**, *7* (3), 2000–2011. https://doi.org/10.1021/nn305725q.

(151) Lupi, F. F.; Giammaria, T. J.; Ceresoli, M.; Seguini, G.; Sparnacci, K.; Antonioli, D.; Gianotti, V.; Laus, M.; Perego, M. Rapid Thermal Processing of Self-Assembling Block Copolymer Thin Films. *Nanotechnology* **2013**, *24* (31), 315601. https://doi.org/10.1088/0957-4484/24/31/315601.

(152) Zhang, X.; Harris, K. D.; Wu, N. L. Y.; Murphy, J. N.; Buriak, J. M. Fast Assembly of Ordered Block Copolymer Nanostructures through Microwave Annealing. *ACS Nano* **2010**, *4* (11), 7021–7029. https://doi.org/10.1021/nn102387c.

(153) Jin, C.; Murphy, J. N.; Harris, K. D.; Buriak, J. M. Deconvoluting the Mechanism of Microwave Annealing of Block Copolymer Thin Films. *ACS Nano* **2014**, *8* (4), 3979–3991. https://doi.org/10.1021/nn5009098.

(154) Shang, X.; Yu, H.; Choi, W.; Lee, E. K.; Oh, J. H. Effects of Microwave-Assisted Annealing on the Morphology and Electrical Performance of Semiconducting Polymer Thin Films. *Org. Electron.* **2016**, *30*, 207–212. https://doi.org/10.1016/j.orgel.2015.12.027.

(155) Jin, C.; Olsen, B. C.; Luber, E. J.; Buriak, J. M. Nanopatterning via Solvent Vapor Annealing of Block Copolymer Thin Films. *Chem. Mater.* **2017**, *29* (1), 176–188. https://doi.org/10.1021/acs.chemmater.6b02967.

(156) Sinturel, C.; Vayer, M.; Morris, M.; Hillmyer, M. A. Solvent Vapor Annealing of Block Polymer Thin Films. *Macromolecules* **2013**, *46* (14), 5399–5415. https://doi.org/10.1021/ma400735a.

(157) Selkirk, A.; Prochukhan, N.; Lundy, R.; Cummins, C.; Gatensby, R.; Kilbride, R.; Parnell, A.; Baez Vasquez, J.; Morris, M.; Mokarian-Tabari, P. Optimization and Control of Large Block Copolymer Self-Assembly via Precision Solvent Vapor Annealing. *Macromolecules* **2021**. https://doi.org/10.1021/acs.macromol.0c02543.

(158) Ginige, G.; Song, Y.; Olsen, B. C.; Luber, E. J.; Yavuz, C. T.; Buriak, J. M. Solvent Vapor Annealing, Defect Analysis, and Optimization of Self-Assembly of Block Copolymers Using Machine Learning Approaches. *ACS Appl. Mater. Interfaces* **2021**, *13* (24), 28639–28649. https://doi.org/10.1021/acsami.1c05056.

(159) Borah, D.; Shaw, M. T.; Holmes, J. D.; Morris, M. A. Sub-10 nm Feature Size PS-b-PDMS Block Copolymer Structures Fabricated by a Microwave-Assisted Solvothermal Process. *ACS Appl. Mater. Interfaces* **2013**, *5* (6), 2004–2012. https://doi.org/10.1021/am302830w.

(160) Cummins, C.; Mokarian-Tabari, P.; Andreazza, P.; Sinturel, C.; Morris, M. A. Solvothermal Vapor Annealing of Lamellar Poly(Styrene)-*Block*-Poly(d,l-Lactide) Block Copolymer Thin Films for Directed Self-Assembly Application. *ACS Appl. Mater. Interfaces* **2016**, *8* (12), 8295–8304. https://doi.org/10.1021/acsami.6b00765.

(161) Majewski, P. W.; Yager, K. G. Millisecond Ordering of Block Copolymer Films via Photothermal Gradients. *ACS Nano* **2015**, *9* (4), 3896–3906. https://doi.org/10.1021/nn5071827.
(162) Leniart, A. A.; Pula, P.; Sitkiewicz, A.; Majewski, P. W. Macroscopic Alignment of Block Copolymers on Silicon Substrates by Laser Annealing. *ACS Nano* **2020**, *14* (4), 4805–4815. https://doi.org/10.1021/acsnano.0c00696.
(163) Jiang, J.; Jacobs, A. G.; Wenning, B.; Liedel, C.; Thompson, M. O.; Ober, C. K. Ultrafast Self-Assembly of Sub-10 nm Block Copolymer Nanostructures by Solvent-Free High-Temperature Laser Annealing. *ACS Appl. Mater. Interfaces* **2017**, *9* (37), 31317–31324. https://doi.org/10.1021/acsami.7b00774.
(164) Yong, D.; Jin, H. M.; Kim, S. O.; Kim, J. U. Laser-Directed Self-Assembly of Highly Aligned Lamellar and Cylindrical Block Copolymer Nanostructures: Experiment and Simulation. *Macromolecules* **2018**, *51* (4), 1418–1426. https://doi.org/10.1021/acs.macromol.7b02645.
(165) Zhang, C.; Cavicchi, K. A.; Li, R.; Yager, K. G.; Fukuto, M.; Vogt, B. D. Thickness Limit for Alignment of Block Copolymer Films Using Solvent Vapor Annealing with Shear. *Macromolecules* **2018**, *51* (11), 4213–4219. https://doi.org/10.1021/acs.macromol.8b00539.
(166) Luo, M.; Scott, D. M.; Epps, T. H. Writing Highly Ordered Macroscopic Patterns in Cylindrical Block Polymer Thin Films via Raster Solvent Vapor Annealing and Soft Shear. *ACS Macro Lett.* **2015**, *4* (5), 516–520. https://doi.org/10.1021/acsmacrolett.5b00126.
(167) Ruiz, R.; Kang, H.; Detcheverry, F. A.; Dobisz, E.; Kercher, D. S.; Albrecht, T. R.; de, P. J. J.; Nealey, P. F. Density Multiplication and Improved Lithography by Directed Block Copolymer Assembly. *Science* **2008**, *321* (5891), 936–939. https://doi.org/10.1126/science.1157626.
(168) Giammaria, T. J.; Ferrarese Lupi, F.; Seguini, G.; Perego, M.; Vita, F.; Francescangeli, O.; Wenning, B.; Ober, C. K.; Sparnacci, K.; Antonioli, D.; Gianotti, V.; Laus, M. Micrometer-Scale Ordering of Silicon-Containing Block Copolymer Thin Films via High-Temperature Thermal Treatments. *ACS Appl. Mater. Interfaces* **2016**, *8* (15), 9897–9908. https://doi.org/10.1021/acsami.6b02300.
(169) Chai, J.; Buriak, J. M. Using Cylindrical Domains of Block Copolymers To Self-Assemble and Align Metallic Nanowires. *ACS Nano* **2008**, *2* (3), 489–501. https://doi.org/10.1021/nn700341s.
(170) Welander, A. M.; Craig, G. S. W.; Tada, Y.; Yoshida, H.; Nealey, P. F. Directed Assembly of Block Copolymers in Thin to Thick Films. *Macromolecules* **2013**, *46* (10), 3915–3921. https://doi.org/10.1021/ma3025706.
(171) Borah, D.; Senthamaraikannan, R.; Rasappa, S.; Kosmala, B.; Holmes, J. D.; Morris, M. A. Swift Nanopattern Formation of PS-b-PMMA and PS-b-PDMS Block Copolymer Films Using a Microwave Assisted Technique. *ACS Nano* **2013**, *7* (8), 6583–6596. https://doi.org/10.1021/nn4035519.
(172) Han, J.; Kim, J.-S.; Man Shin, J.; Yun, H.; Kim, Y.; Park, H.; J. Kim, B. Rapid Solvo-Microwave Annealing for Optimizing Ordered Nanostructures and Crystallization of Regioregular Polythiophene-Based Block Copolymers. *Polym. Chem.* **2019**, *10* (36), 4962–4972. https://doi.org/10.1039/C9PY00871C.
(173) Hashimoto, T.; Bodycomb, J.; Funaki, Y.; Kimishima, K. The Effect of Temperature Gradient on the Microdomain Orientation of Diblock Copolymers Undergoing an Order−Disorder Transition. *Macromolecules* **1999**, *32* (3), 952–954. https://doi.org/10.1021/ma981249s.
(174) Bodycomb, J.; Funaki, Y.; Kimishima, K.; Hashimoto, T. Single-Grain Lamellar Microdomain from a Diblock Copolymer. *Macromolecules* **1999**, *32* (6), 2075–2077. https://doi.org/10.1021/ma981538g.
(175) Berry, B. C.; Bosse, A. W.; Douglas, J. F.; Jones, R. L.; Karim, A. Orientational Order in Block Copolymer Films Zone Annealed below the Order−Disorder Transition Temperature. *Nano Lett.* **2007**, *7* (9), 2789–2794. https://doi.org/10.1021/nl071354s.
(176) Basutkar, M. N.; Samant, S.; Strzalka, J.; Yager, K. G.; Singh, G.; Karim, A. Through-Thickness Vertically Ordered Lamellar Block Copolymer Thin Films on Unmodified Quartz with Cold Zone Annealing. *Nano Lett.* **2017**, *17* (12), 7814–7823. https://doi.org/10.1021/acs.nanolett.7b04028.
(177) Han, E.; Stuen, K. O.; Leolukman, M.; Liu, C.-C.; Nealey, P. F.; Gopalan, P. Perpendicular Orientation of Domains in Cylinder-Forming Block Copolymer Thick Films by Controlled Interfacial Interactions. *Macromolecules* **2009**, *42* (13), 4896–4901. https://doi.org/10.1021/ma9002903.
(178) Gu, X.; Gunkel, I.; Hexemer, A.; Russell, T. P. Controlling Domain Spacing and Grain Size in Cylindrical Block Copolymer Thin Films by Means of Thermal and Solvent Vapor Annealing. *Macromolecules* **2016**, *49* (9), 3373–3381. https://doi.org/10.1021/acs.macromol.6b00429.
(179) Gianotti, V.; Antonioli, D.; Sparnacci, K.; Laus, M.; Giammaria, T. J.; Ferrarese Lupi, F.; Seguini, G.; Perego, M. On the Thermal Stability of PS-*b*-PMMA Block and PS-r-PMMA Random Copolymers for

Nanopatterning Applications. *Macromolecules* **2013**, *46* (20), 8224–8234. https://doi.org/10.1021/ma401023y.
(180) Kim, E.; Ahn, H.; Park, S.; Lee, H.; Lee, M.; Lee, S.; Kim, T.; Kwak, E.-A.; Lee, J. H.; Lei, X.; Huh, J.; Bang, J.; Lee, B.; Ryu, D. Y. Directed Assembly of High Molecular Weight Block Copolymers: Highly Ordered Line Patterns of Perpendicularly Oriented Lamellae with Large Periods. *ACS Nano* **2013**, *7* (3), 1952–1960. https://doi.org/10.1021/nn3051264.
(181) Albalak, R. J.; Capel, M. S.; Thomas, E. L. Solvent Swelling of Roll-Cast Triblock Copolymer Films. *Polymer* **1998**, *39* (8), 1647–1656. https://doi.org/10.1016/S0032-3861(97)00497-7.
(182) Tu, K.-H.; Bai, W.; Liontos, G.; Ntetsikas, K.; Avgeropoulos, A.; Ross, C. A. Universal Pattern Transfer Methods for Metal Nanostructures by Block Copolymer Lithography. *Nanotechnology* **2015**, *26* (37), 375301. https://doi.org/10.1088/0957-4484/26/37/375301.
(183) Jung, Y. S.; Ross, C. A. Solvent-Vapor-Induced Tunability of Self-Assembled Block Copolymer Patterns. *Adv. Mater.* **2009**, *21* (24), 2540–2545. https://doi.org/10.1002/adma.200802855.
(184) Bai, W.; Yager, K. G.; Ross, C. A. *In Situ* Characterization of the Self-Assembly of a Polystyrene–Polydimethylsiloxane Block Copolymer during Solvent Vapor Annealing. *Macromolecules* **2015**, *48* (23), 8574–8584. https://doi.org/10.1021/acs.macromol.5b02174.
(185) Zhang, J.; Posselt, D.; Smilgies, D.-M.; Perlich, J.; Kyriakos, K.; Jaksch, S.; Papadakis, C. M. Lamellar Diblock Copolymer Thin Films during Solvent Vapor Annealing Studied by GISAXS: Different Behavior of Parallel and Perpendicular Lamellae. *Macromolecules* **2014**, *47* (16), 5711–5718. https://doi.org/10.1021/ma500633b.
(186) Onses, M. S.; Song, C.; Williamson, L.; Sutanto, E.; Ferreira, P. M.; Alleyne, A. G.; Nealey, P. F.; Ahn, H.; Rogers, J. A. Hierarchical Patterns of Three-Dimensional Block-Copolymer Films Formed by Electrohydrodynamic Jet Printing and Self-Assembly. *Nat. Nanotechnol.* **2013**, *8* (9), 667–675. https://doi.org/10.1038/nnano.2013.160.
(187) Kao, J.; Thorkelsson, K.; Bai, P.; Zhang, Z.; Sun, C.; Xu, T. Rapid Fabrication of Hierarchically Structured Supramolecular Nanocomposite Thin Films in One Minute. *Nat. Commun.* **2014**, *5*, 4053. https://doi.org/10.1038/ncomms5053.
(188) Hulkkonen, H.; Salminen, T.; Niemi, T. Automated Solvent Vapor Annealing with Nanometer Scale Control of Film Swelling for Block Copolymer Thin Films. *Soft Matter* **2019**, *15* (39), 7909–7917. https://doi.org/10.1039/C9SM01322A.
(189) Pester, C. W.; Liedel, C.; Ruppel, M.; Böker, A. Block Copolymers in Electric Fields. *Prog. Polym. Sci.* https://doi.org/10.1016/j.progpolymsci.2016.04.005.
(190) Kathrein, C. C.; Bai, W.; Currivan-Incorvia, J. A.; Liontos, G.; Ntetsikas, K.; Avgeropoulos, A.; Böker, A.; Tsarkova, L.; Ross, C. A. Combining Graphoepitaxy and Electric Fields toward Uniaxial Alignment of Solvent-Annealed Polystyrene– *b* –Poly(Dimethylsiloxane) Block Copolymers. *Chem. Mater.* **2015**, *27* (19), 6890–6898. https://doi.org/10.1021/acs.chemmater.5b03354.
(191) Ruppel, M.; Pester, C. W.; Langner, K. M.; Sevink, G. J. A.; Schoberth, H. G.; Schmidt, K.; Urban, V. S.; Mays, J. W.; Böker, A. Electric Field Induced Selective Disordering in Lamellar Block Copolymers. *ACS Nano* **2013**, *7* (5), 3854–3867. https://doi.org/10.1021/nn3059604.
(192) Liedel, C.; Pester, C. W.; Ruppel, M.; Lewin, C.; Pavan, M. J.; Urban, V. S.; Shenhar, R.; Bösecke, P.; Böker, A. Block Copolymer Nanocomposites in Electric Fields: Kinetics of Alignment. *ACS Macro Lett.* **2013**, *2* (1), 53–58. https://doi.org/10.1021/mz3005132.
(193) Majewski, P. W.; Gopinadhan, M.; Osuji, C. O. Magnetic Field Alignment of Block Copolymers and Polymer Nanocomposites: Scalable Microstructure Control in Functional Soft Materials. *J. Polym. Sci. Part B Polym. Phys.* **2012**, *50* (1), 2–8. https://doi.org/10.1002/polb.22382.
(194) Tran, H.; Gopinadhan, M.; Majewski, P. W.; Shade, R.; Steffes, V.; Osuji, C. O.; Campos, L. M. Monoliths of Semiconducting Block Copolymers by Magnetic Alignment. *ACS Nano* **2013**, *7* (6), 5514–5521. https://doi.org/10.1021/nn401725a.
(195) Raman, V.; Bose, A.; Olsen, B. D.; Hatton, T. A. Long-Range Ordering of Symmetric Block Copolymer Domains by Chaining of Superparamagnetic Nanoparticles in External Magnetic Fields. *Macromolecules* **2012**, *45* (23), 9373–9382. https://doi.org/10.1021/ma300500z.
(196) Keen, I.; Yu, A.; Cheng, H.-H.; Jack, K. S.; Nicholson, T. M.; Whittaker, A. K.; Blakey, I. Control of the Orientation of Symmetric Poly(Styrene)-Block-Poly(d,l-Lactide) Block Copolymers Using Statistical Copolymers of Dissimilar Composition. *Langmuir* **2012**, *28* (45), 15876–15888. https://doi.org/10.1021/la304141m.

(197) Kim, S.; Nealey, P. F.; Bates, F. S. Decoupling Bulk Thermodynamics and Wetting Characteristics of Block Copolymer Thin Films. *ACS Macro Lett.* **2012**, *1* (1), 11–14. https://doi.org/10.1021/mz2000169.
(198) Cheng, J.; Lawson, R. A.; Yeh, W.-M.; Jarnagin, N. D.; Tolbert, L. M.; Henderson, C. L. PS-b-PHEMA: Synthesis, Characterization, and Processing of a High X Polymer for Directed Self-Assembly Lithography. In *Alternative Lithographic Technologies V*; SPIE, 2013; Vol. 8680, pp 412–418. https://doi.org/10.1117/12.2021417.
(199) Suh, H. S.; Kim, D. H.; Moni, P.; Xiong, S.; Ocola, L. E.; Zaluzec, N. J.; Gleason, K. K.; Nealey, P. F. Sub-10-nm Patterning via Directed Self-Assembly of Block Copolymer Films with a Vapour-Phase Deposited Topcoat. *Nat. Nanotechnol.* **2017**, *12* (6), 575–581. https://doi.org/10.1038/nnano.2017.34.
(200) Bates, C. M.; Seshimo, T.; Maher, M. J.; Durand, W. J.; Cushen, J. D.; Dean, L. M.; Blachut, G.; Ellison, C. J.; Willson, C. G. Polarity-Switching Top Coats Enable Orientation of Sub–10-nm Block Copolymer Domains. *Science* **2012**, *338* (6108), 775–779. https://doi.org/10.1126/science.1226046.
(201) Nealey, P. F.; Kang, H.; Liu, G.; Yoshida, H.; Tada, Y.; Pablo, J. J. de; Ramirez-Hernandez, A. Directed Assembly of Block Copolymer Films between a Chemically Patterned Surface and a Second Surface. US9718250B2, August 1, 2017.
(202) Ebrahim Attia, A. B.; Ong, Z. Y.; Hedrick, J. L.; Lee, P. P.; Ee, P. L. R.; Hammond, P. T.; Yang, Y.-Y. Mixed Micelles Self-Assembled from Block Copolymers for Drug Delivery. *Curr. Opin. Colloid Interface Sci.* **2011**, *16* (3), 182–194. https://doi.org/10.1016/j.cocis.2010.10.003.
(203) Jeong, B.; Bae, Y. H.; Lee, D. S.; Kim, S. W. Biodegradable Block Copolymers as Injectable Drug-Delivery Systems. *Nature* **1997**, *388* (6645), 860–862. https://doi.org/10.1038/42218.
(204) Ke, W.; Zha, Z.; Mukerabigwi, J. F.; Chen, W.; Wang, Y.; He, C.; Ge, Z. Matrix Metalloproteinase-Responsive Multifunctional Peptide-Linked Amphiphilic Block Copolymers for Intelligent Systemic Anticancer Drug Delivery. *Bioconjug. Chem.* **2017**, *28* (8), 2190–2198. https://doi.org/10.1021/acs.bioconjchem.7b00330.
(205) Bodratti, A. M.; Alexandridis, P. Amphiphilic Block Copolymers in Drug Delivery: Advances in Formulation Structure and Performance. *Expert Opin. Drug Deliv.* **2018**, *15* (11), 1085–1104. https://doi.org/10.1080/17425247.2018.1529756.
(206) Ganda, S.; Dulle, M.; Drechsler, M.; Förster, B.; Förster, S.; Stenzel, M. H. Two-Dimensional Self-Assembled Structures of Highly Ordered Bioactive Crystalline-Based Block Copolymers. *Macromolecules* **2017**, *50* (21), 8544–8553. https://doi.org/10.1021/acs.macromol.7b01453.
(207) B. Darling, S. Block Copolymers for Photovoltaics. *Energy Environ. Sci.* **2009**, *2* (12), 1266–1273. https://doi.org/10.1039/B912086F.
(208) Fink, Y.; Urbas, A. M.; Bawendi, M. G.; Joannopoulos, J. D.; Thomas, E. L. Block Copolymers as Photonic Bandgap Materials. *J. Light. Technol.* **1999**, *17* (11), 1963–1969. https://doi.org/10.1109/50.802981.
(209) Guillorn, M.; Chang, J.; Bryant, A.; Fuller, N.; Dokumaci, O.; Wang, X.; Newbury, J.; Babich, K.; Ott, J.; Haran, B.; Yu, R.; Lavoie, C.; Klaus, D.; Zhang, Y.; Sikorski, E.; Graham, W.; To, B.; Lofaro, M.; Tornello, J.; Koli, D.; Yang, B.; Pyzyna, A.; Neumeyer, D.; Khater, M.; Yagishita, A.; Kawasaki, H.; Haensch, W. FinFET Performance Advantage at 22nm: An AC Perspective. In *2008 Symposium on VLSI Technology*; 2008; pp 12–13. https://doi.org/10.1109/VLSIT.2008.4588544.
(210) Liu, C.-C.; Franke, E.; Mignot, Y.; LeFevre, S.; Sieg, S.; Chi, C.; Meli, L.; Parnell, D.; Schmidt, K.; Sanchez, M.; Singh, L.; Furukawa, T.; Seshadri, I.; Silva, E. A. D.; Tsai, H.; Lai, K.; Truong, H.; Farrell, R.; Bruce, R.; Somervell, M.; Sanders, D.; Felix, N.; Arnold, J.; Hetzer, D.; Ko, A.; Metz, A.; Colburn, M.; Corliss, D. DSA Patterning Options for Logics and Memory Applications. In *Advances in Patterning Materials and Processes XXXIV*; SPIE, 2017; Vol. 10146, pp 15–27. https://doi.org/10.1117/12.2260479.
(211) Bruce, R. L.; Fraczak, G.; Papalia, J. M.; Tsai, H.; BrightSky, M.; Miyazoe, H.; Zhu, Y.; Engelmann, S. U.; Lung, H.-L.; Masuda, T.; Suu, K.; Liu, C.-C.; Tang, H.; Arnold, J. C.; Felix, N.; Lam, C. H. Directed Self-Assembly Patterning Strategies for Phase Change Memory Applications. In *Advanced Etch Technology for Nanopatterning VI*; SPIE, 2017; Vol. 10149, pp 25–34. https://doi.org/10.1117/12.2257829.
(212) Griffiths, R. A.; Williams, A.; Oakland, C.; Roberts, J.; Vijayaraghavan, A.; Thomson, T. Directed Self-Assembly of Block Copolymers for Use in Bit Patterned Media Fabrication. *J. Phys. Appl. Phys.* **2013**, *46* (50), 503001. https://doi.org/10.1088/0022-3727/46/50/503001.
(213) Albrecht, T. R.; Hellwing, O.; Ruiz, R.; Schabes, M. E.; Terris, B. D.; Wu, X. Z. Bit-Patterned Magnetic Recording: Nanoscale Magnetic Islands for Data Storage. In *Nanoscale Magnetic Materials and*

Applications; Liu, J. P., Fullerton, E., Gutfleisch, O., Sellmyer, D. J., Eds.; Springer US: Boston, MA, 2009; pp 237–274. https://doi.org/10.1007/978-0-387-85600-1_9.

(214) Yang, X.; Wan, L.; Xiao, S.; Xu, Y.; Weller, D. K. Directed Block Copolymer Assembly versus Electron Beam Lithography for Bit-Patterned Media with Areal Density of 1 Terabit/Inch2 and Beyond. *ACS Nano* **2009**, *3* (7), 1844–1858. https://doi.org/10.1021/nn900073r.

(215) Singh, A.; Nam, J.; Lee, J.; Chan, B. T.; Wu, H.; Yin, J.; Cao, Y.; Gronheid, R. Manufacturability of Dense Hole Arrays with Directed Self-Assembly Using the CHIPS Flow. In *Alternative Lithographic Technologies VIII*; SPIE, 2016; Vol. 9777, pp 135–143. https://doi.org/10.1117/12.2219261.

(216) Patel, K. C.; Ruiz, R.; Lille, J.; Wan, L.; Dobiz, E.; Gao, H.; Robertson, N.; Albrecht, T. R. Line-Frequency Doubling of Directed Self-Assembly Patterns for Single-Digit Bit Pattern Media Lithography. In *Alternative Lithographic Technologies IV*; SPIE, 2012; Vol. 8323, pp 157–165. https://doi.org/10.1117/12.916589.

(217) Black, C. T.; Ruiz, R.; Breyta, G.; Cheng, J. Y.; Colburn, M. E.; Guarini, K. W.; Kim, H.-C.; Zhang, Y. Polymer Self Assembly in Semiconductor Microelectronics. *IBM J. Res. Dev.* **2007**, *51* (5), 605–633. https://doi.org/10.1147/rd.515.0605.

(218) Ji, S.; Wan, L.; Liu, C.-C.; Nealey, P. F. Directed Self-Assembly of Block Copolymers on Chemical Patterns: A Platform for Nanofabrication. *Prog. Polym. Sci.* **2016**, *54–55*, 76–127. https://doi.org/10.1016/j.progpolymsci.2015.10.006.

(219) Xiong, S.; Chapuis, Y.-A.; Wan, L.; Gao, H.; Li, X.; Ruiz, R.; Nealey, P. F. Directed Self-Assembly of High-Chi Block Copolymer for Nano Fabrication of Bit Patterned Media via Solvent Annealing. *Nanotechnology* **2016**, *27* (41), 415601. https://doi.org/10.1088/0957-4484/27/41/415601.

(220) Doise, J.; Koh, J. H.; Kim, J. Y.; Zhu, Q.; Kinoshita, N.; Suh, H. S.; Delgadillo, P. R.; Vandenberghe, G.; Willson, C. G.; Ellison, C. J. Strategies for Increasing the Rate of Defect Annihilation in the Directed Self-Assembly of High-χ Block Copolymers. *ACS Appl. Mater. Interfaces* **2019**, *11* (51), 48419–48427. https://doi.org/10.1021/acsami.9b17858.

(221) Ren, J.; Zhou, C.; Chen, X.; Dolejsi, M.; Craig, G. S. W.; Rincon Delgadillo, P. A.; Segal-Peretz, T.; Nealey, P. F. Engineering the Kinetics of Directed Self-Assembly of Block Copolymers toward Fast and Defect-Free Assembly. *ACS Appl. Mater. Interfaces* **2018**, *10* (27), 23414–23423. https://doi.org/10.1021/acsami.8b05247.

(222) Li, W.; Müller, M. Defects in the Self-Assembly of Block Copolymers and Their Relevance for Directed Self-Assembly. *Annu. Rev. Chem. Biomol. Eng.* **2015**, *6* (1), 187–216. https://doi.org/10.1146/annurev-chembioeng-061114-123209.

(223) Tiron, R.; Chevalier, X.; Couderc, C.; Pradelles, J.; Bustos, J.; Pain, L.; Navarro, C.; Magnet, S.; Fleury, G.; Hadziioannou, G. Optimization of Block Copolymer Self-Assembly through Graphoepitaxy: A Defectivity Study. *J. Vac. Sci. Technol. B* **2011**, *29* (6), 06F206. https://doi.org/10.1116/1.3659714.

(224) Murphy, J. N.; Harris, K. D.; Buriak, J. M. Automated Defect and Correlation Length Analysis of Block Copolymer Thin Film Nanopatterns. *PLoS ONE* **2015**, *10* (7), e0133088. https://doi.org/10.1371/journal.pone.0133088.

(225) Pattern Coarsening in a 2D Hexagonal System. *EPL Europhys. Lett.* **2004**, *67* (5), 800. https://doi.org/10.1209/epl/i2004-10126-5.

(226) Black, C. T.; Forrey, C.; Yager, K. G. Thickness-Dependence of Block Copolymer Coarsening Kinetics. *Soft Matter* **2017**, *13* (18), 3275–3283. https://doi.org/10.1039/C7SM00212B.

(227) Knoll, A.; Magerle, R.; Krausch, G. 3. *J. Chem. Phys.* **2004**, *120* (2), 1105–1116. https://doi.org/10.1063/1.1627324.

(228) Wu, N. L. Y.; Harris, K. D.; Buriak, J. M. Conversion of Bilayers of PS-b-PDMS Block Copolymer into Closely Packed, Aligned Silica Nanopatterns. *ACS Nano* **2013**, *7* (6), 5595–5606. https://doi.org/10.1021/nn401968t.

(229) Park, S.; Kim, B.; Xu, J.; Hofmann, T.; Ocko, B. M.; Russell, T. P. Lateral Ordering of Cylindrical Microdomains Under Solvent Vapor. *Macromolecules* **2009**, *42* (4), 1278–1284. https://doi.org/10.1021/ma802480s.

(230) Gu, X.; Gunkel, I.; Hexemer, A.; Gu, W.; Russell, T. P. An In Situ Grazing Incidence X-Ray Scattering Study of Block Copolymer Thin Films During Solvent Vapor Annealing. *Adv. Mater.* **2014**, *26* (2), 273–281. https://doi.org/10.1002/adma.201302562.

(231) Gotrik, K. W.; Hannon, A. F.; Son, J. G.; Keller, B.; Alexander-Katz, A.; Ross, C. A. Morphology Control in Block Copolymer Films Using Mixed Solvent Vapors. *ACS Nano* **2012**, *6* (9), 8052–8059. https://doi.org/10.1021/nn302641z.

(232) Böhme, S.; Arias-Zapata, J.; Garnier, J.; Girardot, C.; Legrain, A.; Zelsmann, M. Annealing Treatments of Cylindrical Siloxane-Based Block Copolymers Optimized for Nanomanufacturing11Main Research Article. *Micro Nano Eng.* **2018**, *1*, 56–62. https://doi.org/10.1016/j.mne.2018.10.005.

(233) Chavis, M. A.; Smilgies, D.-M.; Wiesner, U. B.; Ober, C. K. Widely Tunable Morphologies in Block Copolymer Thin Films Through Solvent Vapor Annealing Using Mixtures of Selective Solvents. *Adv. Funct. Mater.* **2015**, *25* (20), 3057–3065. https://doi.org/10.1002/adfm.201404053.

(234) Nelson, G.; Drapes, C. S.; Grant, M. A.; Gnabasik, R.; Wong, J.; Baruth, A. High-Precision Solvent Vapor Annealing for Block Copolymer Thin Films. *Micromachines* **2018**, *9* (6), 271. https://doi.org/10.3390/mi9060271.

(235) Paik, M. Y.; Bosworth, J. K.; Smilges, D.-M.; Schwartz, E. L.; Andre, X.; Ober, C. K. Reversible Morphology Control in Block Copolymer Films via Solvent Vapor Processing: An in Situ GISAXS Study. *Macromolecules* **2010**, *43* (9), 4253–4260. https://doi.org/10.1021/ma902646t.

(236) Selkirk, A.; Prochukhan, N.; Lundy, R.; Cummins, C.; Gatensby, R.; Kilbride, R.; Parnell, A.; Baez Vasquez, J.; Morris, M.; Mokarian-Tabari, P. Optimization and Control of Large Block Copolymer Self-Assembly via Precision Solvent Vapor Annealing. *Macromolecules* **2021**. https://doi.org/10.1021/acs.macromol.0c02543.

(237) Kim, Y. C.; Shin, T. J.; Hur, S.-M.; Kwon, S. J.; Kim, S. Y. Shear-Solvo Defect Annihilation of Diblock Copolymer Thin Films over a Large Area. *Sci. Adv. 5* (6), eaaw3974. https://doi.org/10.1126/sciadv.aaw3974.

(238) Cheng, L.-C.; Bai, W.; Martin, E. F.; Tu, K.-H.; Ntetsikas, K.; Liontos, G.; Avgeropoulos, A.; Ross, C. A. Morphology, Directed Self-Assembly and Pattern Transfer from a High Molecular Weight Polystyrene-*Block*-Poly(Dimethylsiloxane) Block Copolymer Film. *Nanotechnology* **2017**, *28* (14), 145301. https://doi.org/10.1088/1361-6528/aa61c9.

(239) Lundy, R.; P. Flynn, S.; Cummins, C.; M. Kelleher, S.; N. Collins, M.; Dalton, E.; Daniels, S.; A. Morris, M.; Enright, R. Controlled Solvent Vapor Annealing of a High χ Block Copolymer Thin Film. *Phys. Chem. Chem. Phys.* **2017**, *19* (4), 2805–2815. https://doi.org/10.1039/C6CP07633E.

(240) Stein, A.; Wright, G.; Yager, K. G.; Doerk, G. S.; Black, C. T. Selective Directed Self-Assembly of Coexisting Morphologies Using Block Copolymer Blends. *Nat. Commun.* **2016**, *7*, 12366. https://doi.org/10.1038/ncomms12366.

(241) Kim, J. Y.; Liu, P.; Maher, M. J.; Callan, D. H.; Bates, C. M.; Carlson, M. C.; Asano, Y.; Blachut, G.; Rettner, C. T.; Cheng, J. Y.; Sunday, D. F.; Kline, R. J.; Sanders, D. P.; Lynd, N. A.; Ellison, C. J.; Willson, C. G.; Baiz, C. R. Spatial Control of the Self-Assembled Block Copolymer Domain Orientation and Alignment on Photopatterned Surfaces. *ACS Appl. Mater. Interfaces* **2020**, *12* (20), 23399–23409. https://doi.org/10.1021/acsami.0c02997.

(242) Li, J.; Rincon-Delgadillo, P. A.; Suh, H. S.; Mannaert, G.; Nealey, P. F. Understanding Kinetics of Defect Annihilation in Chemoepitaxy-Directed Self-Assembly. *ACS Appl. Mater. Interfaces* **2021**, *13* (21), 25357–25364. https://doi.org/10.1021/acsami.1c03830.

(243) Chen, Y.; Xiong, S. Directed Self-Assembly of Block Copolymers for Sub-10 nm Fabrication. *Int. J. Extreme Manuf.* **2020**, *2* (3), 032006. https://doi.org/10.1088/2631-7990/aba3ae.

(244) Ober, C. K. A Dress Code for Block Copolymers. *Nat. Nanotechnol.* **2017**, *12* (6), 507–508. https://doi.org/10.1038/nnano.2017.49.

(245) Arias-Zapata, J.; Böhme, S.; Garnier, J.; Girardot, C.; Legrain, A.; Zelsmann, M. Ultrafast Assembly of PS-PDMS Block Copolymers on 300 mm Wafers by Blending with Plasticizers. *Adv. Funct. Mater.* **2016**, *26* (31), 5690–5700. https://doi.org/10.1002/adfm.201601469.

(246) Li, W.; Müller, M. Directed Self-Assembly of Block Copolymers by Chemical or Topographical Guiding Patterns: Optimizing Molecular Architecture, Thin-Film Properties, and Kinetics. *Prog. Polym. Sci.* **2016**, *54–55*, 47–75. https://doi.org/10.1016/j.progpolymsci.2015.10.008.

(247) Michman, E.; Langenberg, M.; Stenger, R.; Oded, M.; Schvartzman, M.; Müller, M.; Shenhar, R. Controlled Spacing between Nanopatterned Regions in Block Copolymer Films Obtained by Utilizing Substrate Topography for Local Film Thickness Differentiation. *ACS Appl. Mater. Interfaces* **2019**, *11* (38), 35247–35254. https://doi.org/10.1021/acsami.9b12817.

(248) Shin, J. Y.; Oh, Y. T.; Kim, S.; Lim, H. Y.; Lee, B.; Ko, Y. C.; Park, S.; Seon, S. W.; Lee, S. G.; Mun, S. S.; Kim, B. H. Hierarchical Self-Assembly of Thickness-Modulated Block Copolymer Thin Films for Controlling Nanodomain Orientations inside Bare Silicon Trenches. *Polymers* **2021**, *13* (4), 553. https://doi.org/10.3390/polym13040553.

(249) Ham, S.; Shin, C.; Kim, E.; Ryu, D. Y.; Jeong, U.; Russell, T. P.; Hawker, C. J. Microdomain Orientation of PS-b-PMMA by Controlled Interfacial Interactions. *Macromolecules* **2008**, *41* (17), 6431–6437. https://doi.org/10.1021/ma8007338.

(250) Smith, A. P.; Douglas, J. F.; Meredith, J. C.; Amis, E. J.; Karim, A. Combinatorial Study of Surface Pattern Formation in Thin Block Copolymer Films. *Phys. Rev. Lett.* **2001**, *87* (1), 015503. https://doi.org/10.1103/PhysRevLett.87.015503.

(251) Kim, B. H.; Lee, H. M.; Lee, J.-H.; Son, S.-W.; Jeong, S.-J.; Lee, S.; Lee, D. I.; Kwak, S. U.; Jeong, H.; Shin, H.; Yoon, J.-B.; Lavrentovich, O. D.; Kim, S. O. Spontaneous Lamellar Alignment in Thickness-Modulated Block Copolymer Films. *Adv. Funct. Mater.* **2009**, *19* (16), 2584–2591. https://doi.org/10.1002/adfm.200900121.

(252) Olaya-Muñoz, D. A.; Nealey, P. F.; Hernández-Ortiz, J. P. Leveling of Polymer Grating Structures upon Heating: Dimension Dependence on the Nanoscale and the Effect of Antiplasticizers. *ACS Appl. Mater. Interfaces* **2018**, *10* (32), 27432–27443. https://doi.org/10.1021/acsami.8b06611.

(253) Rottler, J.; Müller, M. Kinetic Pathways of Block Copolymer Directed Self-Assembly: Insights from Efficient Continuum Modeling. *ACS Nano* **2020**, *14* (10), 13986–13994. https://doi.org/10.1021/acsnano.0c06433.

(254) Sunday, D. F.; Dolejsi, M.; Chang, A. B.; Richter, L. J.; Li, R.; Kline, R. J.; Nealey, P. F.; Grubbs, R. H. Confinement and Processing Can Alter the Morphology and Periodicity of Bottlebrush Block Copolymers in Thin Films. *ACS Nano* **2020**, *14* (12), 17476–17486. https://doi.org/10.1021/acsnano.0c07777.

(255) Kirkey, A.; Luber, E. J.; Cao, B.; Olsen, B. C.; Buriak, J. M. Optimization of the Bulk Heterojunction of All-Small-Molecule Organic Photovoltaics Using Design of Experiment and Machine Learning Approaches. *ACS Appl. Mater. Interfaces* **2020**, *12* (49), 54596–54607. https://doi.org/10.1021/acsami.0c14922.

(256) Cao, B.; Adutwum, L. A.; Oliynyk, A. O.; Luber, E. J.; Olsen, B. C.; Mar, A.; Buriak, J. M. How To Optimize Materials and Devices *via* Design of Experiments and Machine Learning: Demonstration Using Organic Photovoltaics. *ACS Nano* **2018**, *12* (8), 7434–7444. https://doi.org/10.1021/acsnano.8b04726.

(257) LeCun, Y.; Bengio, Y.; Hinton, G. Deep Learning. *Nature* **2015**, *521* (7553), 436–444. https://doi.org/10.1038/nature14539.

(258) Tsai, C. L.; Delaney, K. T.; Fredrickson, G. H. Genetic Algorithm for Discovery of Globally Stable Phases in Block Copolymers. *Macromolecules* **2016**, *49* (17), 6558–6567. https://doi.org/10.1021/acs.macromol.6b01323.

(259) Shim, S.; Cai, S.; Yang, J.; Yang, S.; Choi, B.; Shin, Y. Verification of Directed Self-Assembly (DSA) Guide Patterns through Machine Learning. In *Alternative Lithographic Technologies VII*; SPIE, 2015; Vol. 9423, pp 318–325. https://doi.org/10.1117/12.2085644.

(260) Khaira, G. S.; Qin, J.; Garner, G. P.; Xiong, S.; Wan, L.; Ruiz, R.; Jaeger, H. M.; Nealey, P. F.; de Pablo, J. J. Evolutionary Optimization of Directed Self-Assembly of Triblock Copolymers on Chemically Patterned Substrates. *ACS Macro Lett.* **2014**, *3* (8), 747–752. https://doi.org/10.1021/mz5002349.

(261) Tu, K.-H.; Huang, H.; Lee, S.; Lee, W.; Sun, Z.; Alexander-Katz, A.; Ross, C. A. Machine Learning Predictions of Block Copolymer Self-Assembly. *Adv. Mater.* **2020**, *32* (52), 2005713. https://doi.org/10.1002/adma.202005713.

(262) Trinh, T. B.; Upadhyaya, P.; Qian, Z.; Pei, D. Discovery of a Direct Ras Inhibitor by Screening a Combinatorial Library of Cell-Permeable Bicyclic Peptides. *ACS Comb. Sci.* **2016**, *18* (1), 75–85. https://doi.org/10.1021/acscombsci.5b00164.

(263) Nečas, D.; Klapetek, P. Gwyddion: An Open-Source Software for SPM Data Analysis. *Cent. Eur. J. Phys.* **2011**, *10* (1), 181–188. https://doi.org/10.2478/s11534-011-0096-2.

(264) Otsu, N. A Threshold Selection Method from Gray-Level Histograms. *IEEE Trans. Syst. Man Cybern.* **1979**, *9* (1), 62–66. https://doi.org/10.1109/TSMC.1979.4310076.

(265) Pedregosa, F.; Varoquaux, G.; Gramfort, A.; Michel, V.; Thirion, B.; Grisel, O.; Blondel, M.; Prettenhofer, P.; Weiss, R.; Dubourg, V.; Vanderplas, J.; Passos, A.; Cournapeau, D.; Brucher, M.; Perrot, M.; Duchesnay, É. Scikit-Learn: Machine Learning in Python. *J Mach Learn Res* **2011**, *12*, 2825–2830.

(266) Jeong, J. W.; Park, W. I.; Kim, M.-J.; Ross, C. A.; Jung, Y. S. Highly Tunable Self-Assembled Nanostructures from a Poly(2-Vinylpyridine-b-Dimethylsiloxane) Block Copolymer. *Nano Lett.* **2011**, *11* (10), 4095–4101. https://doi.org/10.1021/nl2016224.

(267) Leibler, L. Theory of Microphase Separation in Block Copolymers. *Macromolecules* **1980**, *13* (6), 1602–1617. https://doi.org/10.1021/ma60078a047.
(268) Jung, Y. S.; Ross, C. A. Solvent-Vapor-Induced Tunability of Self-Assembled Block Copolymer Patterns. *Adv. Mater.* **2009**, *21* (24), 2540–2545. https://doi.org/10.1002/adma.200802855.
(269) Helfand, E.; Tagami, Y. Theory of the Interface between Immiscible Polymers. II. *J. Chem. Phys.* **1972**, *56* (7), 3592–3601. https://doi.org/10.1063/1.1677735.
(270) Kimura, M.; Misner, M. J.; Xu, T.; Kim, S. H.; Russell, T. P. Long-Range Ordering of Diblock Copolymers Induced by Droplet Pinning. *Langmuir* **2003**, *19* (23), 9910–9913. https://doi.org/10.1021/la0351360.
(271) Kim, S. H.; Misner, M. J.; Xu, T.; Kimura, M.; Russell, T. P. Highly Oriented and Ordered Arrays from Block Copolymers via Solvent Evaporation. *Adv. Mater.* **2004**, *16* (3), 226–231. https://doi.org/10.1002/adma.200304906.
(272) Seppala, J. E.; Lewis, R. L.; Epps, T. H. Spatial and Orientation Control of Cylindrical Nanostructures in ABA Triblock Copolymer Thin Films by Raster Solvent Vapor Annealing. *ACS Nano* **2012**, *6* (11), 9855–9862. https://doi.org/10.1021/nn303416p.
(273) Sinturel, C.; Vayer, M.; Morris, M.; Hillmyer, M. A. Solvent Vapor Annealing of Block Polymer Thin Films. *Macromolecules* **2013**, *46* (14), 5399–5415. https://doi.org/10.1021/ma400735a.
(274) Baruth, A.; Seo, M.; Lin, C. H.; Walster, K.; Shankar, A.; Hillmyer, M. A.; Leighton, C. Optimization of Long-Range Order in Solvent Vapor Annealed Poly(Styrene)-Block-Poly(Lactide) Thin Films for Nanolithography. *ACS Appl. Mater. Interfaces* **2014**, *6* (16), 13770–13781. https://doi.org/10.1021/am503199d.
(275) Vega, D. A.; Harrison, C. K.; Angelescu, D. E.; Trawick, M. L.; Huse, D. A.; Chaikin, P. M.; Register, R. A. Ordering Mechanisms in Two-Dimensional Sphere-Forming Block Copolymers. *Phys. Rev. E* **2005**, *71* (6), 061803. https://doi.org/10.1103/PhysRevE.71.061803.
(276) Gasser, U.; Eisenmann, C.; Maret, G.; Keim, P. Melting of Crystals in Two Dimensions. *ChemPhysChem* **2010**, *11* (5), 963–970. https://doi.org/10.1002/cphc.200900755.
(277) Steinhardt, P. J.; Nelson, D. R.; Ronchetti, M. Bond-Orientational Order in Liquids and Glasses. *Phys. Rev. B* **1983**, *28* (2), 784–805. https://doi.org/10.1103/PhysRevB.28.784.
(278) Albrecht, T. R.; Arora, H.; Ayanoor-Vitikkate, V.; Beaujour, J.-M.; Bedau, D.; Berman, D.; Bogdanov, A. L.; Chapuis, Y.-A.; Cushen, J.; Dobisz, E. E.; Doerk, G.; Gao, H.; Grobis, M.; Gurney, B.; Hanson, W.; Hellwig, O.; Hirano, T.; Jubert, P.-O.; Kercher, D.; Lille, J.; Liu, Z.; Mate, C. M.; Obukhov, Y.; Patel, K. C.; Rubin, K.; Ruiz, R.; Schabes, M.; Wan, L.; Weller, D.; Wu, T.-W.; Yang, E. Bit-Patterned Magnetic Recording: Theory, Media Fabrication, and Recording Performance. *IEEE Trans. Magn.* **2015**, *51* (5), 1–42. https://doi.org/10.1109/TMAG.2015.2397880.
(279) Euclidean Distance Mapping. *Comput. Graph. Image Process.* **1980**, *14* (3), 227–248. https://doi.org/10.1016/0146-664X(80)90054-4.
(280) Kim, S.-W.; Kim, E.; Lee, H.; Berry, B. C.; Kim, H.-C.; Ryu, D. Y. Thickness-Dependent Ordering of Perpendicularly Oriented Lamellae in PS-b-PMMA Thin Films. *Polymer* **2015**, *74*, 63–69. https://doi.org/10.1016/j.polymer.2015.07.053.
(281) Williamson, L. D.; Seidel, R. N.; Chen, X.; Suh, H. S.; Rincon Delgadillo, P.; Gronheid, R.; Nealey, P. F. Three-Tone Chemical Patterns for Block Copolymer Directed Self-Assembly. *ACS Appl. Mater. Interfaces* **2016**, *8* (4), 2704–2712. https://doi.org/10.1021/acsami.5b10562.
(282) Surowiec, I.; Vikström, L.; Hector, G.; Johansson, E.; Vikström, C.; Trygg, J. Generalized Subset Designs in Analytical Chemistry. *Anal. Chem.* **2017**, *89* (12), 6491–6497. https://doi.org/10.1021/acs.analchem.7b00506.
(283) Guarini, K. W.; Black, C. T.; Zhang, Y.; Kim, H.; Sikorski, E. M.; Babich, I. V. Process Integration of Self-Assembled Polymer Templates into Silicon Nanofabrication. *J. Vac. Sci. Technol. B Microelectron. Nanometer Struct. Process. Meas. Phenom.* **2002**, *20* (6), 2788–2792. https://doi.org/10.1116/1.1521730.
(284) Park, S.-M.; Stoykovich, M. P.; Ruiz, R.; Zhang, Y.; Black, C. T.; Nealey, P. F. Directed Assembly of Lamellae- Forming Block Copolymers by Using Chemically and Topographically Patterned Substrates. *Adv. Mater.* **2007**, *19* (4), 607–611. https://doi.org/10.1002/adma.200601421.
(285) Black, C. T.; Guarini, K. W.; Breyta, G.; Colburn, M. C.; Ruiz, R.; Sandstrom, R. L.; Sikorski, E. M.; Zhang, Y. Highly Porous Silicon Membrane Fabrication Using Polymer Self-Assembly. *J. Vac. Sci. Technol. B Microelectron. Nanometer Struct. Process. Meas. Phenom.* **2006**, *24* (6), 3188–3191. https://doi.org/10.1116/1.2366700.

(286) Thurn-Albrecht, T.; Steiner, R.; DeRouchey, J.; Stafford, C. M.; Huang, E.; Bal, M.; Tuominen, M.; Hawker, C. J.; Russell, T. P. Nanoscopic Templates from Oriented Block Copolymer Films. *Adv. Mater.* **2000**, *12* (11), 787–791. https://doi.org/10.1002/(SICI)1521-4095(200006)12:11<787::AID-ADMA787>3.0.CO;2-1.

(287) Chai, J.; Wang, D.; Fan, X.; Buriak, J. M. Assembly of Aligned Linear Metallic Patterns on Silicon. *Nat. Nanotechnol.* **2007**, *2* (8), 500–506. https://doi.org/10.1038/nnano.2007.227.

(288) Aizawa, M.; Buriak, J. M. Block Copolymer Templated Chemistry for the Formation of Metallic Nanoparticle Arrays on Semiconductor Surfaces. *Chem. Mater.* **2007**, *19* (21), 5090–5101. https://doi.org/10.1021/cm071382b.

(289) Farrell, R. A.; Petkov, N.; Shaw, M. T.; Djara, V.; Holmes, J. D.; Morris, M. A. Monitoring PMMA Elimination by Reactive Ion Etching from a Lamellar PS-b-PMMA Thin Film by Ex Situ TEM Methods. *Macromolecules* **2010**, *43* (20), 8651–8655. https://doi.org/10.1021/ma101827u.

(290) Liu, C.-C.; Nealey, P. F.; Ting, Y.-H.; Wendt, A. E. Pattern Transfer Using Poly(Styrene-Block-Methyl Methacrylate) Copolymer Films and Reactive Ion Etching. *J. Vac. Sci. Technol. B Microelectron. Nanometer Struct. Process. Meas. Phenom.* **2007**, *25* (6), 1963–1968. https://doi.org/10.1116/1.2801884.

(291) Chang, S.-W.; Chuang, V. P.; Boles, S. T.; Ross, C. A.; Thompson, C. V. Densely Packed Arrays of Ultra-High-Aspect-Ratio Silicon Nanowires Fabricated Using Block-Copolymer Lithography and Metal-Assisted Etching. *Adv. Funct. Mater.* **2009**, *19* (15), 2495–2500. https://doi.org/10.1002/adfm.200900181.

(292) Huang, Y.; Kim, T. W.; Xiong, S.; Mawst, L. J.; Kuech, T. F.; Nealey, P. F.; Dai, Y.; Wang, Z.; Guo, W.; Forbes, D.; Hubbard, S. M.; Nesnidal, M. InAs Nanowires Grown by Metal–Organic Vapor-Phase Epitaxy (MOVPE) Employing PS/PMMA Diblock Copolymer Nanopatterning. *Nano Lett.* **2013**, *13* (12), 5979–5984. https://doi.org/10.1021/nl403163x.

(293) Rasappa, S.; Borah, D.; Faulkner, C. C.; Lutz, T.; Shaw, M. T.; Holmes, J. D.; Morris, M. A. Fabrication of a Sub-10 nm Silicon Nanowire Based Ethanol Sensor Using Block Copolymer Lithography. *Nanotechnology* **2013**, *24* (6), 065503. https://doi.org/10.1088/0957-4484/24/6/065503.

(294) Bas, S. Z.; Cummins, C.; Selkirk, A.; Borah, D.; Ozmen, M.; Morris, M. A. A Novel Electrochemical Sensor Based on Metal Ion Infiltrated Block Copolymer Thin Films for Sensitive and Selective Determination of Dopamine. *ACS Appl. Nano Mater.* **2019**, *2* (11), 7311–7318. https://doi.org/10.1021/acsanm.9b01794.

(295) Jung, Y. S.; Jung, W.; Tuller, H. L.; Ross, C. A. Nanowire Conductive Polymer Gas Sensor Patterned Using Self-Assembled Block Copolymer Lithography. *Nano Lett.* **2008**, *8* (11), 3776–3780. https://doi.org/10.1021/nl802099k.

(296) Murugesan, M.; Fukushima, T.; Bea, J. C.; Hashimoto, H.; Koyanagi, M. Intra- and Inter-Chip Electrical Interconnection Formed by Directed Self Assembly of Nanocomposite Containing Diblock Copolymer and Nanometal. In *2018 IEEE International Reliability Physics Symposium (IRPS)*; 2018; p 4D.2-1-4D.2-7. https://doi.org/10.1109/IRPS.2018.8353589.

(297) Ng Cheong Chan, Y.; Schrock, R. R.; Cohen, R. E. Synthesis of Single Silver Nanoclusters within Spherical Microdomains in Block Copolymer Films. *J. Am. Chem. Soc.* **1992**, *114* (18), 7295–7296. https://doi.org/10.1021/ja00044a051.

(298) Spatz, J. P.; Mößmer, S.; Möller, M. Mineralization of Gold Nanoparticles in a Block Copolymer Microemulsion. *Chem. – Eur. J.* **1996**, *2* (12), 1552–1555. https://doi.org/10.1002/chem.19960021213.

(299) Cavalcanti-Adam, E. A.; Micoulet, A.; Blümmel, J.; Auernheimer, J.; Kessler, H.; Spatz, J. P. Lateral Spacing of Integrin Ligands Influences Cell Spreading and Focal Adhesion Assembly. *Eur. J. Cell Biol.* **2006**, *85* (3), 219–224. https://doi.org/10.1016/j.ejcb.2005.09.011.

(300) Arnold, M.; Cavalcanti-Adam, E. A.; Glass, R.; Blümmel, J.; Eck, W.; Kantlehner, M.; Kessler, H.; Spatz, J. P. Activation of Integrin Function by Nanopatterned Adhesive Interfaces. *ChemPhysChem* **2004**, *5* (3), 383–388. https://doi.org/10.1002/cphc.200301014.

(301) Klingelhöfer, S.; Heitz, W.; Greiner, A.; Oestreich, S.; Förster, S.; Antonietti, M. Preparation of Palladium Colloids in Block Copolymer Micelles and Their Use for the Catalysis of the Heck Reaction. *J. Am. Chem. Soc.* **1997**, *119* (42), 10116–10120. https://doi.org/10.1021/ja9714604.

(302) Mizuno, H.; Buriak, J. M. Building Upon Patterned Organic Monolayers Produced via Catalytic Stamp Lithography. *ACS Appl. Mater. Interfaces* **2010**, *2* (8), 2301–2307. https://doi.org/10.1021/am100348f.

(303) Mizuno, H.; Buriak, J. M. Nanoscale Patterning of Organic Monolayers by Catalytic Stamp Lithography: Scope and Limitations. *ACS Appl. Mater. Interfaces* **2009**, *1* (12), 2711–2720. https://doi.org/10.1021/am900602m.

(304) Wu, N. L. Y.; Zhang, X.; Murphy, J. N.; Chai, J.; Harris, K. D.; Buriak, J. M. Density Doubling of Block Copolymer Templated Features. *Nano Lett.* **2012**, *12* (1), 264–268. https://doi.org/10.1021/nl203488a.

(305) Jin, C.; Olsen, B. C.; Wu, N. L. Y.; Luber, E. J.; Buriak, J. M. Sequential Nanopatterned Block Copolymer Self-Assembly on Surfaces. *Langmuir* **2016**, *32* (23), 5890–5898. https://doi.org/10.1021/acs.langmuir.6b01365.

(306) Cha, S. K.; Mun, J. H.; Chang, T.; Kim, S. Y.; Kim, J. Y.; Jin, H. M.; Lee, J. Y.; Shin, J.; Kim, K. H.; Kim, S. O. Au–Ag Core–Shell Nanoparticle Array by Block Copolymer Lithography for Synergistic Broadband Plasmonic Properties. *ACS Nano* **2015**, *9* (5), 5536–5543. https://doi.org/10.1021/acsnano.5b01641.

(307) Akinoglu, G. E.; Mir, S. H.; Gatensby, R.; Rydzek, G.; Mokarian-Tabari, P. Block Copolymer Derived Vertically Coupled Plasmonic Arrays for Surface-Enhanced Raman Spectroscopy. *ACS Appl. Mater. Interfaces* **2020**, *12* (20), 23410–23416. https://doi.org/10.1021/acsami.0c03300.

(308) Jin, H. M.; Kim, J. Y.; Heo, M.; Jeong, S.-J.; Kim, B. H.; Cha, S. K.; Han, K. H.; Kim, J. H.; Yang, G. G.; Shin, J.; Kim, S. O. Ultralarge Area Sub-10 nm Plasmonic Nanogap Array by Block Copolymer Self-Assembly for Reliable High-Sensitivity SERS. *ACS Appl. Mater. Interfaces* **2018**, *10* (51), 44660–44667. https://doi.org/10.1021/acsami.8b17325.

(309) Lin, C.-W.; Chang, S.-H.; Huang, C.-C.; Lin, C.-H. Plasmonic Nanocavities Fabricated by Directed Self-Assembly Lithography and Nanotransfer Printing and Used as Surface-Enhanced Raman Scattering Substrates. *Microelectron. Eng.* **2020**, *227*, 111309. https://doi.org/10.1016/j.mee.2020.111309.

(310) Chung, C.-K. Plasma Etching. In *Encyclopedia of Microfluidics and Nanofluidics*; Li, D., Ed.; Springer: New York, NY, 2015; pp 2766–2781. https://doi.org/10.1007/978-1-4614-5491-5_1251.

(311) Plasma Assisted Etching http://ieeexplore.ieee.org/abstract/document/5271350/ (accessed 2021 -11 -10).

(312) Madou, M. J. Pattern Transfer with Dry Etching Techniques. In *Fundamentals of microfabrication*; CRC Press, 2018; pp 101–146.

(313) Terekhin, V. V.; Dement'eva, O. V.; Rudoy, V. M. Formation of Ordered Nanoparticle Assemblies by Block Copolymer Lithography Methods. *Russ. Chem. Rev.* **2011**, *80* (5), 453. https://doi.org/10.1070/RC2011v080n05ABEH004183.

(314) Spatz, J. P.; Herzog, T.; Mößmer, S.; Ziemann, P.; Möller, M. Micellar Inorganic–Polymer Hybrid Systems—A Tool for Nanolithography. *Adv. Mater.* **1999**, *11* (2), 149–153. https://doi.org/10.1002/(SICI)1521-4095(199902)11:2<149::AID-ADMA149>3.0.CO;2-W.

(315) Brodie, I.; Muray, J. J. Particle Beams. In *The Physics of Micro/Nano-Fabrication*; Brodie, I., Muray, J. J., Eds.; Microdevices; Springer US: Boston, MA, 1992; pp 55–257. https://doi.org/10.1007/978-1-4757-6775-9_2.

(316) Guenther, G.; Guillon, O. Models of Size-Dependent Nanoparticle Melting Tested on Gold. *J. Mater. Sci.* **2014**, *49* (23), 7915–7932. https://doi.org/10.1007/s10853-014-8544-1.

(317) Gao, F.; Gu, Z. Melting Temperature of Metallic Nanoparticles. In *Handbook of Nanoparticles*; Aliofkhazraei, M., Ed.; Springer International Publishing: Cham, 2016; pp 661–690. https://doi.org/10.1007/978-3-319-15338-4_6.

(318) Guisbiers, G.; Abudukelimu, G.; Hourlier, D. Size-Dependent Catalytic and Melting Properties of Platinum-Palladium Nanoparticles. *Nanoscale Res. Lett.* **2011**, *6* (1), 396. https://doi.org/10.1186/1556-276X-6-396.

(319) Glass, R.; Arnold, M.; Blümmel, J.; Küller, A.; Möller, M.; Spatz, J. p. Micro-Nanostructured Interfaces Fabricated by the Use of Inorganic Block Copolymer Micellar Monolayers as Negative Resist for Electron-Beam Lithography. *Adv. Funct. Mater.* **2003**, *13* (7), 569–575. https://doi.org/10.1002/adfm.200304331.

(320) Kong, P.-C.; Rochon, F. D. Reactions of K_2PtCl_4 with Pyridine Derivatives in Dimethylformamide and Synthesis of Potassium Trichloro(Pyridine)Platinum(II). *Can. J. Chem.* **1978**, *56* (4), 441–445. https://doi.org/10.1139/v78-070.

(321) Chang, J.-B.; Son, J. G.; Hannon, A. F.; Alexander-Katz, A.; Ross, C. A.; Berggren, K. K. Aligned Sub-10-nm Block Copolymer Patterns Templated by Post Arrays. *ACS Nano* **2012**, *6* (3), 2071–2077. https://doi.org/10.1021/nn203767s.

(322) Jin, C.; Olsen, B. C.; Luber, E. J.; Buriak, J. M. Preferential Alignment of Incommensurate Block Copolymer Dot Arrays Forming Moiré Superstructures. *ACS Nano* **2017**, *11* (3), 3237–3246. https://doi.org/10.1021/acsnano.7b00322.

(323) Wang, D.; Li, Y. Bimetallic Nanocrystals: Liquid-Phase Synthesis and Catalytic Applications. *Adv. Mater.* **2011**, *23* (9), 1044–1060. https://doi.org/10.1002/adma.201003695.

(324) Matsen, M. W.; Schick, M. Stable and Unstable Phases of a Diblock Copolymer Melt. *Phys. Rev. Lett.* **1994**, *72* (16), 2660–2663. https://doi.org/10.1103/PhysRevLett.72.2660.

(325) Matsen, M. W. Effect of Architecture on the Phase Behavior of AB-Type Block Copolymer Melts. *Macromolecules* **2012**, *45* (4), 2161–2165. https://doi.org/10.1021/ma202782s.

(326) Karim, A.; Singh, N.; Sikka, M.; Bates, F. S.; Dozier, W. D.; Felcher, G. P. Ordering in Asymmetric Poly (Ethylene–Propylene)–Poly (Ethylethylene) Diblock Copolymer Thin Films. *J. Chem. Phys.* **1994**, *100* (2), 1620–1629. https://doi.org/10.1063/1.466589.

(327) Radzilowski, L. H.; Carvalho, B. L.; Thomas, E. L. Structure of Minimum Thickness and Terraced Free-Standing Films of Block Copolymers. *J. Polym. Sci. Part B Polym. Phys.* **1996**, *34* (17), 3081–3093. https://doi.org/10.1002/(SICI)1099-0488(199612)34:17<3081::AID-POLB20>3.0.CO;2-2.

(328) Knoll, A.; Horvat, A.; Lyakhova, K. S.; Krausch, G.; Sevink, G. J. A.; Zvelindovsky, A. V.; Magerle, R. Phase Behavior in Thin Films of Cylinder-Forming Block Copolymers. *Phys. Rev. Lett.* **2002**, *89* (3), 035501. https://doi.org/10.1103/PhysRevLett.89.035501.

(329) Stein, G. E.; Kramer, E. J.; Li, X.; Wang, J. Layering Transitions in Thin Films of Spherical-Domain Block Copolymers. *Macromolecules* **2007**, *40* (7), 2453–2460. https://doi.org/10.1021/ma0625509.

(330) Bates, F. S.; Hillmyer, M. A.; Lodge, T. P.; Bates, C. M.; Delaney, K. T.; Fredrickson, G. H. Multiblock Polymers: Panacea or Pandora's Box? *Science* **2012**, *336* (6080), 434–440. https://doi.org/10.1126/science.1215368.

(331) Functional nanostructured materials based on self-assembly of block copolymers | MRS Bulletin | Cambridge Core https://www.cambridge.org/core/journals/mrs-bulletin/article/functional-nanostructured-materials-based-on-selfassembly-of-block-copolymers/9A2EC1CA307B51A760DD08DF0AE9145F (accessed 2018 -02 -01).

(332) S. Doerk, G.; G. Yager, K. Beyond Native Block Copolymer Morphologies. *Mol. Syst. Des. Eng.* **2017**, *2* (5), 518–538. https://doi.org/10.1039/C7ME00069C.

(333) Kim, J. H.; Jin, H. M.; Yang, G. G.; Han, K. H.; Yun, T.; Shin, J. Y.; Jeong, S.-J.; Kim, S. O. Smart Nanostructured Materials Based on Self-Assembly of Block Copolymers. *Adv. Funct. Mater.* **2020**, *30* (2), 1902049. https://doi.org/10.1002/adfm.201902049.

(334) Hayashida, K.; Takano, A.; Arai, S.; Shinohara, Y.; Amemiya, Y.; Matsushita, Y. Systematic Transitions of Tiling Patterns Formed by ABC Star-Shaped Terpolymers. *Macromolecules* **2006**, *39* (26), 9402–9408. https://doi.org/10.1021/ma0618474.

(335) Matsushita, Y. Creation of Hierarchically Ordered Nanophase Structures in Block Polymers Having Various Competing Interactions. *Macromolecules* **2007**, *40* (4), 771–776. https://doi.org/10.1021/ma062266h.

(336) Sveinbjörnsson, B. R.; Weitekamp, R. A.; Miyake, G. M.; Xia, Y.; Atwater, H. A.; Grubbs, R. H. Rapid Self-Assembly of Brush Block Copolymers to Photonic Crystals. *Proc. Natl. Acad. Sci.* **2012**, *109* (36), 14332–14336. https://doi.org/10.1073/pnas.1213055109.

(337) Gu, W.; Huh, J.; Hong, S. W.; Sveinbjornsson, B. R.; Park, C.; Grubbs, R. H.; Russell, T. P. Self-Assembly of Symmetric Brush Diblock Copolymers. *ACS Nano* **2013**, *7* (3), 2551–2558. https://doi.org/10.1021/nn305867d.

(338) Aissou, K.; Kwon, W.; Mumtaz, M.; Antoine, S.; Maret, M.; Portale, G.; Fleury, G.; Hadziioannou, G. Archimedean Tilings and Hierarchical Lamellar Morphology Formed by Semicrystalline Miktoarm Star Terpolymer Thin Films. *ACS Nano* **2016**, *10* (4), 4055–4061. https://doi.org/10.1021/acsnano.5b06728.

(339) Antoine, S.; Aissou, K.; Mumtaz, M.; Pécastaings, G.; Buffeteau, T.; Fleury, G.; Hadziioannou, G. Nanoscale Archimedean Tilings Formed by 3-Miktoarm Star Terpolymer Thin Films. *Macromol. Rapid Commun.* **2019**, *40* (7), 1800860. https://doi.org/10.1002/marc.201800860.

(340) Tavakkoli, K. G. A.; Gotrik, K. W.; Hannon, A. F.; Alexander-Katz, A.; Ross, C. A.; Berggren, K. K. Templating Three-Dimensional Self-Assembled Structures in Bilayer Block Copolymer Films. *Science* **2012**, *336* (6086), 1294–1298.

(341) Tavakkoli K. G., A.; Nicaise, S. M.; Hannon, A. F.; Gotrik, K. W.; Alexander-Katz, A.; Ross, C. A.; Berggren, K. K. Sacrificial-Post Templating Method for Block Copolymer Self-Assembly. *Small* **2014**, *10* (3), 493–499. https://doi.org/10.1002/smll.201301066.

(342) Kim, J. Y.; Kim, B. H.; Hwang, J. O.; Jeong, S.-J.; Shin, D. O.; Mun, J. H.; Choi, Y. J.; Jin, H. M.; Kim, S. O. Flexible and Transferrable Self-Assembled Nanopatterning on Chemically Modified Graphene. *Adv. Mater.* **2013**, *25* (9), 1331–1335. https://doi.org/10.1002/adma.201204131.

(343) Majewski, P. W.; Rahman, A.; Black, C. T.; Yager, K. G. Arbitrary Lattice Symmetries via Block Copolymer Nanomeshes. *Nat. Commun.* **2015**, *6* (1), 7448. https://doi.org/10.1038/ncomms8448.

(344) Demazy, N.; Cummins, C.; Aissou, K.; Fleury, G. Non-Native Block Copolymer Thin Film Nanostructures Derived from Iterative Self-Assembly Processes. *Adv. Mater. Interfaces* **2020**, *7* (5), 1901747. https://doi.org/10.1002/admi.201901747.

(345) Jung, Y. S.; Chang, J. B.; Verploegen, E.; Berggren, K. K.; Ross, C. A. A Path to Ultranarrow Patterns Using Self-Assembled Lithography. *Nano Lett.* **2010**, *10* (3), 1000–1005. https://doi.org/10.1021/nl904141r.

(346) Mansky, P.; Liu, Y.; Huang, E.; Russell, T. P.; Hawker, C. Controlling Polymer-Surface Interactions with Random Copolymer Brushes. *Science* **1997**, *275* (5305), 1458–1460. https://doi.org/10.1126/science.275.5305.1458.

(347) Jung, H.; Hwang, D.; Kim, E.; Kim, B.-J.; Lee, W. B.; Poelma, J. E.; Kim, J.; Hawker, C. J.; Huh, J.; Ryu, D. Y.; Bang, J. Three-Dimensional Multilayered Nanostructures with Controlled Orientation of Microdomains from Cross-Linkable Block Copolymers. *ACS Nano* **2011**, *5* (8), 6164–6173. https://doi.org/10.1021/nn2006943.

(348) Kim, E.; Shin, C.; Ahn, H.; Yeol Ryu, D.; Bang, J.; J. Hawker, C.; P. Russell, T. Size Control and Registration of Nano-Structured Thin Films by Cross-Linkable Units. *Soft Matter* **2008**, *4* (3), 475–479. https://doi.org/10.1039/B717903K.

(349) Jeong, J. W.; Park, W. I.; Do, L.-M.; Park, J.-H.; Kim, T.-H.; Chae, G.; Jung, Y. S. Nanotransfer Printing with Sub-10 nm Resolution Realized Using Directed Self-Assembly. *Adv. Mater.* **2012**, *24* (26), 3526–3531. https://doi.org/10.1002/adma.201200356.

(350) Abate, A. A.; Vu, G. T.; Pezzutti, A. D.; García, N. A.; Davis, R. L.; Schmid, F.; Register, R. A.; Vega, D. A. Shear-Aligned Block Copolymer Monolayers as Seeds To Control the Orientational Order in Cylinder-Forming Block Copolymer Thin Films. *Macromolecules* **2016**, *49* (19), 7588–7596. https://doi.org/10.1021/acs.macromol.6b00816.

(351) Ruiz, R.; Sandstrom, R. L.; Black, C. T. Induced Orientational Order in Symmetric Diblock Copolymer Thin Films. *Adv. Mater.* **2007**, *19* (4), 587–591. https://doi.org/10.1002/adma.200600287.

(352) Smith, A. P.; Douglas, J. F.; Meredith, J. C.; Amis, E. J.; Karim, A. Combinatorial Study of Surface Pattern Formation in Thin Block Copolymer Films. *Phys. Rev. Lett.* **2001**, *87* (1), 015503. https://doi.org/10.1103/PhysRevLett.87.015503.

(353) Polleux, J.; Rasp, M.; Louban, I.; Plath, N.; Feldhoff, A.; Spatz, J. P. Benzyl Alcohol and Block Copolymer Micellar Lithography: A Versatile Route to Assembling Gold and in Situ Generated Titania Nanoparticles into Uniform Binary Nanoarrays. *ACS Nano* **2011**, *5* (8), 6355–6364. https://doi.org/10.1021/nn201470f.

(354) Rahman, A.; Majewski, P. W.; Doerk, G.; Black, C. T.; Yager, K. G. Non-Native Three-Dimensional Block Copolymer Morphologies. *Nat. Commun.* **2016**, *7*, 13988. https://doi.org/10.1038/ncomms13988.

(355) Son, J. G.; Hannon, A. F.; Gotrik, K. W.; Alexander-Katz, A.; Ross, C. A. Hierarchical Nanostructures by Sequential Self-Assembly of Styrene-Dimethylsiloxane Block Copolymers of Different Periods. *Adv. Mater.* **2011**, *23* (5), 634–639. https://doi.org/10.1002/adma.201002999.

(356) Amidror, I. *The Theory of the Moiré Phenomenon: Volume I: Periodic Layers*; Springer Science & Business Media, 2009.

(357) Chiang, F.-P. Moiré Methods of Strain Analysis. *Exp. Mech.* **1979**, *19* (8), 290–308. https://doi.org/10.1007/BF02324290.

(358) Post, D. The Moir Grid-Analyzer Method for Strain Analysis. 10.

(359) Mühlberger, M.; Bergmair, I.; Schwinger, W.; Gmainer, M.; Schöftner, R.; Glinsner, T.; Hasenfuß, Ch.; Hingerl, K.; Vogler, M.; Schmidt, H.; Kley, E. B. A Moiré Method for High Accuracy Alignment in Nanoimprint Lithography. *Microelectron. Eng.* **2007**, *84* (5), 925–927. https://doi.org/10.1016/j.mee.2007.01.081.

(360) Bassett, G. A.; Menter, J. W.; Pashley, D. W.; Bowden, F. P. Moiré Patterns on Electron Micrographs, and Their Application to the Study of Dislocations in Metals. *Proc. R. Soc. Lond. Ser. Math. Phys. Sci.* **1958**, *246* (1246), 345–368. https://doi.org/10.1098/rspa.1958.0144.

(361) Cadarso, V. J.; Chosson, S.; Sidler, K.; Hersch, R. D.; Brugger, J. High-Resolution 1D Moirés as Counterfeit Security Features. *Light Sci. Appl.* **2013**, *2* (7), e86–e86. https://doi.org/10.1038/lsa.2013.42.

(362) Aggarwal, A. K.; Kaura, S. K.; Chhachhia, D. P.; Sharma, A. K. Concealed Moiré Pattern Encoded Security Holograms Readable by a Key Hologram. *Opt. Laser Technol.* **2006**, *38* (2), 117–121. https://doi.org/10.1016/j.optlastec.2004.10.010.

(363) Chen, K.; Rajeeva, B. B.; Wu, Z.; Rukavina, M.; Dao, T. D.; Ishii, S.; Aono, M.; Nagao, T.; Zheng, Y. Moiré Nanosphere Lithography. *ACS Nano* **2015**, *9* (6), 6031–6040. https://doi.org/10.1021/acsnano.5b00978.

(364) Wu, Z.; Zheng, Y. Moiré Chiral Metamaterials. *Adv. Opt. Mater.* **2017**, *5* (16), 1700034. https://doi.org/10.1002/adom.201700034.

(365) Lubin, S. M.; Zhou, W.; Hryn, A. J.; Huntington, M. D.; Odom, T. W. High-Rotational Symmetry Lattices Fabricated by Moiré Nanolithography. *Nano Lett.* **2012**, *12* (9), 4948–4952. https://doi.org/10.1021/nl302535p.

(366) Karademir, E.; Balci, S.; Kocabas, C.; Aydinli, A. Lasing in a Slow Plasmon Moiré Cavity. *ACS Photonics* **2015**, *2* (7), 805–809. https://doi.org/10.1021/acsphotonics.5b00168.

(367) Ibbotson, L. A.; Demetriadou, A.; Croxall, S.; Hess, O.; Baumberg, J. J. Optical Nano-Woodpiles: Large-Area Metallic Photonic Crystals and Metamaterials. *Sci. Rep.* **2015**, *5* (1), 8313. https://doi.org/10.1038/srep08313.

(368) Jin, C.; Olsen, B. C.; Luber, E. J.; Buriak, J. M. Van Der Waals Epitaxy of Soft Twisted Bilayers: Lattice Relaxation and Mass Density Waves. *ACS Nano* **2020**, *14* (10), 13441–13450. https://doi.org/10.1021/acsnano.0c05310.

(369) Wu, Z.; Zheng, Y. Moiré Metamaterials and Metasurfaces. *Adv. Opt. Mater.* **2018**, *6* (3), 1701057. https://doi.org/10.1002/adom.201701057.

(370) Bedoya-Pinto, A.; Pandeya, A. K.; Liu, D.; Deniz, H.; Chang, K.; Tan, H.; Han, H.; Jena, J.; Kostanovskiy, I.; Parkin, S. S. P. Realization of Epitaxial NbP and TaP Weyl Semimetal Thin Films. *ACS Nano* **2020**, *14* (4), 4405–4413. https://doi.org/10.1021/acsnano.9b09997.

(371) Fu, W.; Qiao, J.; Zhao, X.; Chen, Y.; Fu, D.; Yu, W.; Leng, K.; Song, P.; Chen, Z.; Yu, T.; Pennycook, S. J.; Quek, S. Y.; Loh, K. P. Room Temperature Commensurate Charge Density Wave on Epitaxially Grown Bilayer 2H-Tantalum Sulfide on Hexagonal Boron Nitride. *ACS Nano* **2020**, *14* (4), 3917–3926. https://doi.org/10.1021/acsnano.0c00303.

(372) Bae, S.-H.; Kum, H.; Kong, W.; Kim, Y.; Choi, C.; Lee, B.; Lin, P.; Park, Y.; Kim, J. Integration of Bulk Materials with Two-Dimensional Materials for Physical Coupling and Applications. *Nat. Mater.* **2019**, *18* (6), 550–560. https://doi.org/10.1038/s41563-019-0335-2.

(373) Alvarez-Fernandez, A.; Cummins, C.; Saba, M.; Steiner, U.; Fleury, G.; Ponsinet, V.; Guldin, S. Block Copolymer Directed Metamaterials and Metasurfaces for Novel Optical Devices. *Adv. Opt. Mater.* **2021**, *9* (16), 2100175. https://doi.org/10.1002/adom.202100175.

(374) Bukhari, S. S.; Vardaxoglou, J. (Yiannis); Whittow, W. A Metasurfaces Review: Definitions and Applications. *Appl. Sci.* **2019**, *9* (13), 2727. https://doi.org/10.3390/app9132727.

(375) Vallecchi, A.; Albani, M.; Capolino, F. Collective Electric and Magnetic Plasmonic Resonances in Spherical Nanoclusters. *Opt. Express* **2011**, *19* (3), 2754–2772. https://doi.org/10.1364/OE.19.002754.

(376) Qian, Z.; Hastings, S. P.; Li, C.; Edward, B.; McGinn, C. K.; Engheta, N.; Fakhraai, Z.; Park, S.-J. Raspberry-like Metamolecules Exhibiting Strong Magnetic Resonances. *ACS Nano* **2015**, *9* (2), 1263–1270. https://doi.org/10.1021/nn5050678.

(377) Sheikholeslami, S. N.; Alaeian, H.; Koh, A. L.; Dionne, J. A. A Metafluid Exhibiting Strong Optical Magnetism. *Nano Lett.* **2013**, *13* (9), 4137–4141. https://doi.org/10.1021/nl401642z.

(378) Kravets, V. G.; Kabashin, A. V.; Barnes, W. L.; Grigorenko, A. N. Plasmonic Surface Lattice Resonances: A Review of Properties and Applications. *Chem. Rev.* **2018**, *118* (12), 5912–5951. https://doi.org/10.1021/acs.chemrev.8b00243.

(379) Ok Shin, D.; Jeong, J.-R.; Hee Han, T.; Min Koo, C.; Park, H.-J.; Taik Lim, Y.; Ouk Kim, S. A Plasmonic Biosensor Array by Block Copolymer Lithography. *J. Mater. Chem.* **2010**, *20* (34), 7241–7247. https://doi.org/10.1039/C0JM01319F.

(380) Tang, L.; Li, J. Plasmon-Based Colorimetric Nanosensors for Ultrasensitive Molecular Diagnostics. *ACS Sens.* **2017**, *2* (7), 857–875. https://doi.org/10.1021/acssensors.7b00282.

(381) Dong, Y.; Itoh, T. Metamaterial-Based Antennas. *Proc. IEEE* **2012**, *100* (7), 2271–2285. https://doi.org/10.1109/JPROC.2012.2187631.

(382) Akselrod, G. M.; Argyropoulos, C.; Hoang, T. B.; Ciracì, C.; Fang, C.; Huang, J.; Smith, D. R.; Mikkelsen, M. H. Probing the Mechanisms of Large Purcell Enhancement in Plasmonic Nanoantennas. *Nat. Photonics* **2014**, *8* (11), 835–840. https://doi.org/10.1038/nphoton.2014.228.

(383) Stefik, M.; Guldin, S.; Vignolini, S.; Wiesner, U.; Steiner, U. Block Copolymer Self-Assembly for Nanophotonics. *Chem. Soc. Rev.* **2015**, *44* (15), 5076–5091. https://doi.org/10.1039/C4CS00517A.
(384) Glybovski, S. B.; Tretyakov, S. A.; Belov, P. A.; Kivshar, Y. S.; Simovski, C. R. Metasurfaces: From Microwaves to Visible. *Phys. Rep.* **2016**, *634*, 1–72. https://doi.org/10.1016/j.physrep.2016.04.004.
(385) Deng, S.; Zhang, B.; Choo, P.; Smeets, P. J. M.; Odom, T. W. Plasmonic Photoelectrocatalysis in Copper–Platinum Core–Shell Nanoparticle Lattices. *Nano Lett.* **2021**, *21* (3), 1523–1529. https://doi.org/10.1021/acs.nanolett.0c05029.
(386) Cao, D.; Wang, Q.; Wu, Y.; Zhu, S.; Jia, Y.; Wang, R. Solvothermal Synthesis and Enhanced Photocatalytic Hydrogen Production of Bi/Bi_2MoO_6 Co-Sensitized TiO_2 Nanotube Arrays. *Sep. Purif. Technol.* **2020**, *250*, 117132. https://doi.org/10.1016/j.seppur.2020.117132.
(387) Zorić, I.; Zäch, M.; Kasemo, B.; Langhammer, C. Gold, Platinum, and Aluminum Nanodisk Plasmons: Material Independence, Subradiance, and Damping Mechanisms. *ACS Nano* **2011**, *5* (4), 2535–2546. https://doi.org/10.1021/nn102166t.
(388) Knight, M. W.; Liu, L.; Wang, Y.; Brown, L.; Mukherjee, S.; King, N. S.; Everitt, H. O.; Nordlander, P.; Halas, N. J. Aluminum Plasmonic Nanoantennas. *Nano Lett.* **2012**, *12* (11), 6000–6004. https://doi.org/10.1021/nl303517v.
(389) Zhou, W.; Gao, X.; Liu, D.; Chen, X. Gold Nanoparticles for In Vitro Diagnostics. *Chem. Rev.* **2015**, *115* (19), 10575–10636. https://doi.org/10.1021/acs.chemrev.5b00100.
(390) Kasani, S.; Curtin, K.; Wu, N. A Review of 2D and 3D Plasmonic Nanostructure Array Patterns: Fabrication, Light Management and Sensing Applications. *Nanophotonics* **2019**, *8* (12), 2065–2089. https://doi.org/10.1515/nanoph-2019-0158.
(391) Yang, K.; Yao, X.; Liu, B.; Ren, B. Metallic Plasmonic Array Structures: Principles, Fabrications, Properties, and Applications. *Adv. Mater. n/a* (n/a), 2007988. https://doi.org/10.1002/adma.202007988.
(392) Wang, B.; Yu, P.; Wang, W.; Zhang, X.; Kuo, H.-C.; Xu, H.; Wang, Z. M. High-Q Plasmonic Resonances: Fundamentals and Applications. *Adv. Opt. Mater.* **2021**, *9* (7), 2001520. https://doi.org/10.1002/adom.202001520.
(393) Volk, K.; Honold, T.; Feller, D.; Karg, M. Surface Lattice Resonances in Self-Templated Plasmonic Honeycomb and Moiré Lattices. *Adv. Mater. Interfaces* **2021**, *8* (13), 2100317. https://doi.org/10.1002/admi.202100317.
(394) Deng, S.; Li, R.; Park, J.-E.; Guan, J.; Choo, P.; Hu, J.; Smeets, P. J. M.; Odom, T. W. Ultranarrow Plasmon Resonances from Annealed Nanoparticle Lattices. *Proc. Natl. Acad. Sci.* **2020**, *117* (38), 23380–23384. https://doi.org/10.1073/pnas.2008818117.
(395) Ghosh, S. K.; Pal, T. Interparticle Coupling Effect on the Surface Plasmon Resonance of Gold Nanoparticles: From Theory to Applications. *Chem. Rev.* **2007**, *107* (11), 4797–4862. https://doi.org/10.1021/cr0680282.
(396) Ponomareva, E.; Volk, K.; Mulvaney, P.; Karg, M. Surface Lattice Resonances in Self-Assembled Gold Nanoparticle Arrays: Impact of Lattice Period, Structural Disorder, and Refractive Index on Resonance Quality. *Langmuir* **2020**, *36* (45), 13601–13612. https://doi.org/10.1021/acs.langmuir.0c02430.
(397) Hulteen, J. C.; Van Duyne, R. P. Nanosphere Lithography: A Materials General Fabrication Process for Periodic Particle Array Surfaces. *J. Vac. Sci. Technol. A* **1995**, *13* (3), 1553–1558. https://doi.org/10.1116/1.579726.
(398) Kasani, S.; Zheng, P.; Wu, N. Tailoring Optical Properties of a Large-Area Plasmonic Gold Nanoring Array Pattern. *J. Phys. Chem. C* **2018**, *122* (25), 13443–13449. https://doi.org/10.1021/acs.jpcc.7b11660.
(399) Colburn, M.; Johnson, S. C.; Stewart, M. D.; Damle, S.; Bailey, T. C.; Choi, B.; Wedlake, M.; Michaelson, T. B.; Sreenivasan, S. V.; Ekerdt, J. G.; Willson, C. G. Step and Flash Imprint Lithography: A New Approach to High-Resolution Patterning. In *Emerging Lithographic Technologies III*; SPIE, 1999; Vol. 3676, pp 379–389. https://doi.org/10.1117/12.351155.
(400) Broers, A. N.; Molzen, W. W.; Cuomo, J. J.; Wittels, N. D. Electron-beam Fabrication of 80-Å Metal Structures. *Appl. Phys. Lett.* **1976**, *29* (9), 596–598. https://doi.org/10.1063/1.89155.
(401) Juodėnas, M.; Tamulevičius, T.; Henzie, J.; Erts, D.; Tamulevičius, S. Surface Lattice Resonances in Self-Assembled Arrays of Monodisperse Ag Cuboctahedra. *ACS Nano* **2019**, *13* (8), 9038–9047. https://doi.org/10.1021/acsnano.9b03191.
(402) Plimpton, S. Fast Parallel Algorithms for Short-Range Molecular Dynamics. *J. Comput. Phys.* **1995**, *117* (1), 1–19. https://doi.org/10.1006/jcph.1995.1039.

(403) Malynych, S.; Luzinov, I.; Chumanov, G. Poly(Vinyl Pyridine) as a Universal Surface Modifier for Immobilization of Nanoparticles. *J. Phys. Chem. B* **2002**, *106* (6), 1280–1285. https://doi.org/10.1021/jp013236d.

(404) Shafiqa, A. R.; Abdul Aziz, A.; Mehrdel, B. Nanoparticle Optical Properties: Size Dependence of a Single Gold Spherical Nanoparticle. *J. Phys. Conf. Ser.* **2018**, *1083*, 012040. https://doi.org/10.1088/1742-6596/1083/1/012040.

(405) Dusemund, B.; Hoffmann, A.; Salzmann, T.; Kreibig, U.; Schmid, G. Cluster Matter: The Transition of Optical Elastic Scattering to Regular Reflection. 4.

(406) Halas, N. J.; Lal, S.; Chang, W.-S.; Link, S.; Nordlander, P. Plasmons in Strongly Coupled Metallic Nanostructures. *Chem. Rev.* **2011**, *111* (6), 3913–3961. https://doi.org/10.1021/cr200061k.

(407) Fagan, A. M.; Jeffries, W. R.; Knappenberger, K. L.; Schaak, R. E. Synthetic Control of Hot-Electron Thermalization Efficiency in Size-Tunable Au–Pt Hybrid Nanoparticles. *ACS Nano* **2021**, *15* (1), 1378–1387. https://doi.org/10.1021/acsnano.0c08661.

(408) Lim, S. I.; Varon, M.; Ojea-Jiménez, I.; Arbiol, J.; Puntes, V. Pt Nanocrystal Evolution in the Presence of Au(III)-Salts at Room Temperature: Spontaneous Formation of AuPt Heterodimers. *J. Mater. Chem.* **2011**, *21* (31), 11518–11523. https://doi.org/10.1039/C1JM10313J.

(409) Grant, C. D.; Schwartzberg, A. M.; Norman, T. J.; Zhang, J. Z. Ultrafast Electronic Relaxation and Coherent Vibrational Oscillation of Strongly Coupled Gold Nanoparticle Aggregates. *J. Am. Chem. Soc.* **2003**, *125* (2), 549–553. https://doi.org/10.1021/ja028532y.

(410) Reeler, N. E. A.; Lerstrup, K. A.; Somerville, W.; Speder, J.; Petersen, S. V.; Laursen, B. W.; Arenz, M.; Qiu, X.; Vosch, T.; Nørgaard, K. Gold Nanoparticles Assembled with Dithiocarbamate-Anchored Molecular Wires. *Sci. Rep.* **2015**, *5* (1), 15273. https://doi.org/10.1038/srep15273.

(411) Zhang, Y.; Gu, C.; Schwartzberg, A. M.; Chen, S.; Zhang, J. Z. Optical Trapping and Light-Induced Agglomeration of Gold Nanoparticle Aggregates. *Phys. Rev. B* **2006**, *73* (16), 165405. https://doi.org/10.1103/PhysRevB.73.165405.

(412) Cherqui, C.; Bourgeois, M. R.; Wang, D.; Schatz, G. C. Plasmonic Surface Lattice Resonances: Theory and Computation. *Acc. Chem. Res.* **2019**, *52* (9), 2548–2558. https://doi.org/10.1021/acs.accounts.9b00312.

(413) Li, W.; Sun, Z.; Tian, D.; Nevirkovets, I. P.; Dou, S.-X. Platinum Dendritic Nanoparticles with Magnetic Behavior. *J. Appl. Phys.* **2014**, *116* (3), 033911. https://doi.org/10.1063/1.4890506.

(414) Sennuga, A.; Marwijk, J. van; Whiteley, C. G. Ferroxidase Activity of Apoferritin Is Increased in the Presence of Platinum Nanoparticles. *Nanotechnology* **2011**, *23* (3), 035102. https://doi.org/10.1088/0957-4484/23/3/035102.

(415) Cai, S.-C.; Li, J.-J.; Yu, E.-Q.; Chen, X.; Chen, J.; Jia, H.-P. Strong Photothermal Effect of Plasmonic Pt Nanoparticles for Efficient Degradation of Volatile Organic Compounds under Solar Light Irradiation. *ACS Appl. Nano Mater.* **2018**, *1* (11), 6368–6377. https://doi.org/10.1021/acsanm.8b01578.

(416) Wang, J.; Duan, Q.; Yang, M.; Zhang, B.; Guo, L.; Li, P.; Zhang, W.; Sang, S. Rapid Controlled Synthesis of Gold–Platinum Nanorods with Excellent Photothermal Properties under 808 nm Excitation. *Beilstein J. Nanotechnol.* **2021**, *12* (1), 462–472. https://doi.org/10.3762/bjnano.12.37.

(417) Berry, K. R.; Romo, R. L.; Mitchell, M.; Bejugam, V.; Roper, D. K. Controlled Gold Nanoparticle Placement into Patterned Polydimethylsiloxane Thin Films via Directed Self-Assembly. *J. Nanomater.* **2019**, *2019*, e5390562. https://doi.org/10.1155/2019/5390562.

(418) Auguié, B.; Barnes, W. L. Diffractive Coupling in Gold Nanoparticle Arrays and the Effect of Disorder. *Opt. Lett.* **2009**, *34* (4), 401–403. https://doi.org/10.1364/OL.34.000401.

(419) Jin, C.; Olsen, B. C.; Luber, E. J.; Buriak, J. M. Preferential Alignment of Incommensurate Block Copolymer Dot Arrays Forming Moiré Superstructures. *ACS Nano* **2017**, *11* (3), 3237–3246. https://doi.org/10.1021/acsnano.7b00322.

(420) Shin, D. O.; Jeong, J.-R.; Han, T. H.; Koo, C. M.; Park, H.-J.; Lim, Y. T.; Kim, S. O. A Plasmonic Biosensor Array by Block Copolymer Lithography. *J. Mater. Chem.* **2010**, *20* (34), 7241–7247. https://doi.org/10.1039/C0JM01319F.

(421) Shin, D. O.; Mun, J. H.; Hwang, G.-T.; Yoon, J. M.; Kim, J. Y.; Yun, J. M.; Yang, Y.-B.; Oh, Y.; Lee, J. Y.; Shin, J.; Lee, K. J.; Park, S.; Kim, J. U.; Kim, S. O. Multicomponent Nanopatterns by Directed Block Copolymer Self-Assembly. *ACS Nano* **2013**, *7* (10), 8899–8907. https://doi.org/10.1021/nn403379k.

(422) Langhammer, C.; Yuan, Z.; Zorić, I.; Kasemo, B. Plasmonic Properties of Supported Pt and Pd Nanostructures. *Nano Lett.* **2006**, *6* (4), 833–838. https://doi.org/10.1021/nl060219x.

(423) Yanik, A. A.; Cetin, A. E.; Huang, M.; Artar, A.; Mousavi, S. H.; Khanikaev, A.; Connor, J. H.; Shvets, G.; Altug, H. Seeing Protein Monolayers with Naked Eye through Plasmonic Fano Resonances. *Proc. Natl. Acad. Sci.* **2011**, *108* (29), 11784–11789. https://doi.org/10.1073/pnas.1101910108.

(424) Yao, X.; Jiang, S.; Luo, S.; Liu, B.-W.; Huang, T.-X.; Hu, S.; Zhu, J.; Wang, X.; Ren, B. Uniform Periodic Bowtie SERS Substrate with Narrow Nanogaps Obtained by Monitored Pulsed Electrodeposition. *ACS Appl. Mater. Interfaces* **2020**, *12* (32), 36505–36512. https://doi.org/10.1021/acsami.0c09357.

(425) Landy, N. I.; Sajuyigbe, S.; Mock, J. J.; Smith, D. R.; Padilla, W. J. Perfect Metamaterial Absorber. *Phys. Rev. Lett.* **2008**, *100* (20), 207402. https://doi.org/10.1103/PhysRevLett.100.207402.